Topological Development of Homogeneous-Charge and Stratified-Charge Flames in an Internal Combustion Engine

by

Peter Mark Lillo

A dissertation submitted in partial fulfillment
of the requirements for the degree of
Doctor of Philosophy
(Mechanical Engineering)
In the University of Michigan
2016

Doctoral Committee:

Professor Volker Sick, Chair
Professor André L. Boehman
Professor James F. Driscoll
Assistant Research Scientist Jason B. Martz
Research Scientist David L. Reuss

DEDICATION

This thesis is dedicated to my father Mark Lillo and my grandfather Robert Lillo who are both medical doctors. Their work has saved and improved countless lives. My choice to pursue higher education and impactful work stems directly from my admiration for them and their careers.

ACKNOWLEDGEMENTS

I would like to thank all those who made this possible, starting with my advisor Dr. Volker Sick who has supplied me with all of the knowledge and resources needed to succeed in graduate school. He fearlessly allowed me to subject his glass engine to all sorts of abuses. Then on the "rare" occasions when I pushed his engine too hard and scatter broken pieces of equipment across his lab, he always remained supportive and encouraging. His experimental resilience and devotion to science is contagious and I'm grateful for all that he's done for me. He also deserves a lot of credit for the work presented here.

I would also like to thank Dr. Dave Reuss who has been a daily source of wisdom and guidance. It has been an honor to learn from him. I would like to thank the rest of my committee, including Dr. Jim Driscoll, Dr. André Boehman and Dr. Jason Martz. The collective depth of technical knowledge held by the committee is truly staggering and it has been a privilege receiving their council.

I would also like to thank Rick Davis, Dr. Tang-Wei Kuo, Dr. Xiaofeng Yang and Norm Maasshoff from General Motors for providing a great deal of support and technical guidance for my research. Without them this work would not have been possible.

I would also like to thank Dr. Hao Chen and Hanyang Zhuang who acted as copilots during the engine experiments. Dr. Hao Chen provided pivotal experimental support throughout the course of my studies. Hanyang processed the particle image velocity data presented in this

document. I truly appreciate the efforts that they made and they deserve credit for their physical and academic contributions to this thesis.

I would also like to thank my other labmates and coworkers at the University of Michigan including, but not limited to, Philipp Schiffmann, Mark Greene, Dr. Preeti Abraham, Ivan Tibavinsky, Ahmet Mazacioglu, Dr. Michael Mosburger, Dr. Michael Cundy, Dr. Michael Gross, Kent Pruss, Jim Elkins, Melissa McGeorge. Ryan Benedict, Dave Odell and Phil Kim.

I am deeply indebted to the National Science Foundation, and indirectly to the US taxpayers for providing financial support for my research in the form of an NSF GRFP fellowship. As such, the following should also be acknowledged.

This material is based upon work supported by the National Science Foundation Graduate Research Fellowship Program under Grant No. DGE 1256260. Any opinion, findings, and conclusions or recommendations expressed in this material are those of the authors and do not necessarily reflect the views of the National Science Foundation.

I would like to thank my wife Marina Lillo. She selflessly left her family and friends on the west coast to follow me to Michigan. She has been a constant source of encouragement and joy. She even put her own career on hold to raise our son while I finished this very document. She deserves more praise and thanks then I have to give.

I would like to thank the rest of my family including my son Andrey. He has motivated me in a manner that only a baby can. I would also like to thank my parents, siblings, grandparents and friends for thirty-one years of support and care.

I would also like to thank Dr. Robert Dibble from UC Berkeley. He was the first person to recognize the applicability of my automotive background towards the field of combustion research and he readily converted me from a mechanic into a scientist. He made great efforts

to share his unique perspective on the field and he instilled in me a technical foundation that continues to guide the way that I understand and work with flames. He deserves a lot of credit for guiding my career and research endeavors.

I would also like to thank Dr. Charles Mueller and Dr. Lyle Pickett from Sandia National Laboratories for introducing me to the field of optical engine research. They taught me, by example, how to design, execute and disseminate high impact scientific studies. They motivated me to continue investigating engine combustion phenomena in glass engines and helped inspire me to pursue graduate studies

Finally, I would like to thank all of the employers, educators and co-workers who took part in the miraculous transformation that was my early career. I was, once, an incredibly uninspired teenager that didn't know the sky from the ground. A few automotive mechanics and community college educators taught me which way was up. They set me off onto the professional trajectory that has taken me to where I am now and I'll always be thankful to them for it. In particular, I would like to thank John Popylisen from JP Automotive and the entire De Anza College Automotive faculty including Michael Brandt, Pete Vernazza, Gary Lewis, Randy Bryant and Rick Maynard. Without them, I certainly would not be publishing this.

TABLE OF CONTENTS

LIST OF TABLES

LIST OF FIGURES

LIST OF APPENDICES

LIST OF ACRONYMS

A: Area

aTDCc: After top-dead-center compression

BDC: Bottom-dead-center

bTDCc: Before top-dead-center compression

CCV: Cycle-to-cycle variability

CAxx: Crank angle degree of xx mass fraction

CAD: Crank angle degree

CFD: Computational fluid dynamics

COV: Coefficient of variability

CI: Compression ignition

DI: Direct-injection

DISI: Direct- injection spark-ignition

DNS: Direct numerical simulation

EOInj: End of injection

EVC: Exhaust valve closed

EVO: Exhaust valve open

FFT: Fast Fourier transform

G4VDI: Gasoline four-valve direct-injection engine

HC: Hydrocarbon

IVC: Intake valve closed

IVO: Intake valve open

IC: Internal combustion

IMEP: Indicated mean effective pressure

LES: Large eddy simulation

MAP: Manifold absolute pressure

Nd:YAG : Neodymium-doped yttrium aluminum garnet lasing medium

NMEP: Net indicated mean effective pressure

P: Pressure

PIV: Particle image velocimetry

PLIF: Planar laser induced fluorescence

PMEP: Pumping mean effective pressure

PolyC: Polytropic coefficient of compression

PolyE: Polytropic coefficient of exhaust

R: Radius

RANS: Reynolds averaged Navier-Stokes

SI: Spark ignition

SGSC: Spray-guided stratified-charge

SIDI: Spark-ignited direct-injected

SOIgn: Start of ignition

SOInj: Start of injection

T: Temperature

TDC: Top-dead-center

V: Volume

W: Work

WGSC: Wall-guided stratified-charge

LIST OF SYMBOLS

α (alpha): Thermal diffusivity

C_i: Molecular concentration of species i

C_p: Specific heat at constant pressure

χ (chi): Scalar dissipation

D: Molecular diffusivity

Da: Damköhler number

δ (delta): Thickness

$\emptyset_{fl}$: Fluorescent quantum yield

I_o: Flame stretch factor

γ (gamma): Ratio of specific heats

I: Image

$I_{background}$: Background image

$I_{flatfield}$: Flat-field image

Λ (lambda): Integral length scale

λ: Taylor microscale

ℓ: Length

$\mathcal{L}$: Markstein length

Le: Lewis number

m: Mass

n_i: Number density of species i

Φ (phi): Equivalence ratio

ρ (rho): Density

Re: Reynolds number

s: Strain

S: Flame speed

S_L^o: Un-stretched laminar flame speed

S_L: Laminar flame speed

S_t: Turbulent flame speed

σ_{abs}: Light absorption cross section

Σ (sigma): Flame surface density

τ (tao): Characteristic time scale

t: Time

u: X-direction (horizontal) velocity

u': Root-mean-square of velocity variance

v: Y-direction (vertical) velocity

Ξ (Xi): Wrinkled-ness factor

ABSTRACT

No technology can currently replace fossil fuel powered internal combustion engines as the primary source of transportation power. For better or worse, the next generation of automobiles will continue to be powered by combustion. As such, it is in our best interest to learn how to burn fuel in the smartest manner. There are many advanced combustion strategies that promise efficiency improvements over conventional strategies, most of which have failed to make it onto the road due to technical deficiencies. Many of these strategies, such as spray-guided stratified-charge combustion, rely upon the precise partial mixing of fuel with oxidizer inside the combustion chamber. Advanced computational tools are being developed to aid such challenging designs. However, a lack of understanding of in-cylinder flame physics and computational power limitations continues to hinder the predictive abilities of engine models.

In this work, engine flame topological development is studied. Flame wrinkled-ness is both one of the most important and poorly understood engine combustion phenomena. Generally, a flame may wrinkle for two reasons: (i) its own naturally instabilities and/or (ii) through interaction with turbulent flow. The relative contribution of these two causes towards flame wrinkled-ness in the engine environment was unclear so targeted experiments were performed to provide some clarity. The development of flame wrinkled-ness within an optically accessible engine was measured with a combination of planar laser induced fluorescence and stereo particle image velocimetry under homogeneous-charge and stratified-charge conditions. From this, equivalence ratio, charge velocities, and flame wrinkled-ness were quantified and analyzed. For the iso-octane/toluene mixtures studied the flame wrinkling was insensitive to

thermo-diffusive flame front instabilities. The relative contribution of wrinkles of various spatial scales towards overall flame wrinkled-ness was also measured. Homogeneous-charge flames generally had lower wrinkling factors than stratified-charge flames. Overall, flame wrinkled-ness increased with flame size under both modes of engine operation. Large flames demonstrated an ability to maintain more large scale wrinkles than small flames, which contributed to their overall higher levels of wrinkled-ness. Based on the observations, suggestions are provided for those who are developing advanced homogeneous and stratified-charge engine models.

Chapter 1: INTRODUCTION

Motivation

From 1960 to 2010 the world population increased from three to almost seven billion people. The United Nations estimates that 9 billion people will inhabit earth by 2050 [1]. The quantity of energy that an average person consumes has increased by 150% since 1960 and is expected to continue growing for the foreseeable future. Continuing to meet the global demand for energy is and will continue to be a challenge.

In total, the world's current energy use is about 500 quadrillion Btu's per year [2] . This is the energy equivalent of burning 250 billion trees[1]. 90% of this energy is supplied by combusting a combination of oil, natural gas, coal and biofuels [2].

There is no technology that is currently capable of replacing fossil fuel combustion from producing the lion share of the world's power. For better or worse, the next generation will continue to be powered by combustion. While fire continues to power our lives, it is in our best interest to learn how to burn fuel in the smartest manner.

Over the last century many health and environmental issues associated with combustion have been recognized. For example, the growth in automobile ownership in the first half of the 20th century led to large amounts of engine generated smog and emissions in densely populated

[1] There are only 400 billion trees on earth.

cities such as Los Angeles, CA. Such health hazards led to the Clean Air Act of 1970 which regulated HC, CO and NOx emissions from automobiles and forced the auto manufacturers to produce cleaner burning engines [3]. Similar regulations were formed for the coal burning power industry as the dangers of their flue gasses became evident. More recently, the detrimental effects of global warming due to combustion born CO2 has become a concern. The primary means of reducing CO2 emissions from a combustion device is to burn more efficiently. In the automotive industry new fuel mileage regulations are being implemented across the world.

Fuel resources such as petroleum are being consumed at unsustainable rates. Particularly in light of the global trends of increasing population and energy consumption per capita, this is a great concern. It is clear now more than ever that we need to get the most out of our fuel resources and burn them responsibly.

Increasing the cleanliness and efficiency from combustion devices is challenging. It has taken decades of mostly trial-and-error based design to build the combustion devices used today. Pushing the limits of combustion technology often requires a greater understanding and control of flames than exists. Combustion theory has been slow to develop and difficult to apply in practical design due to the complexity of flames. We are only beginning to enter an age where our understanding of combustion science can readily be applied to design through the medium of computational modeling.

In the late 1950s scientific groups such as the Combustion Institute formed, recognizing the value in acquiring a fundamental understanding of flames [4]. As combustion science has progressed, so has the performance of combustion devices such as IC engines. There still remains room for improvement in our understanding of fundamental combustion phenomenon and the design of practical devices.

Internal combustion (IC) engines found on roads today are still less than 35% efficient, largely due to combustion related limitations. There are promising advanced combustion strategies capable of pushing IC engines towards higher efficiencies. One example of such a strategy is the spray-guided stratified-charge (SGSC) approach, which has demonstrated improvements of more than 20% over its conventional SI counterpart. Homogeneous-charge compression ignition (HCCI), partially premixed compression ignition (PPCI), reactivity controlled compression ignition (RCCI) are a few other examples of such promising technologies that are not yet realized in practice today. Advanced strategies usually require a higher degree of control and understanding over in-cylinder combustion processes than currently exists.

Of the advanced strategies mentioned above, three out of four involve the partially premixing (SGSC,PPCI,RCCI) of the fuel/air charge prior to combustion. There are many advantages to partial premixing. For example, in the SGSC strategy partial-premixing enables un-throttled engine operation which provides a thermodynamic advantage (minimal pumping losses). PPCI engines use partial-premixing as a means of producing a fast, well timed, reliable burn event which is also beneficial for efficiency. Even conventionally diesel engines have become increasingly more partially-premixed as it has become recognized as an effective means of reducing soot emissions. Unfortunately; partially-premixed flame physics are poorly understood and design of such combustion systems is particularly challenging. Hence, none of the advanced combustion strategies mentioned above have found large scale commercial success.

In this new age of computational power, engine manufacturers desire predictive computer models that allow them to explore and test combustion strategies. The use of zero and one dimensional engine models is common practice. Such models do not attempt to resolve flame phenomenon and are therefore not well suited to the investigation of engine combustion issues. For example, a zero-dimensional modeling program such as GT-power may be used to design engine components that surround the combustion chamber such as intake, exhaust or turbocharging systems. It may also be used to optimize engine operation. However, such a model is of little use in aiding piston contour or cylinder head design. Low dimensional models

are ineffective at identifying in-cylinder sources of pollutant generation, abnormal combustion (knock or super-knock) and cyclic variability.
Three-dimensional reactive CFD models are well suited to such investigations of in-cylinder phenomenon. The use of multi-dimensional models in design is increasing, but is still limited. Such models combine turbulent CFD, spray and flame models. Individually, none of these three topics is fully understood and when combined the challenge is amplified.

Combustion phenomenon spans too many time and length scales to be simulated at a practical computational expense. Therefore, out of necessity the processes that are understood are modeled and those which aren't are often neglected. There is an ongoing effort to improve the physicality of such models so that they can be used in a truly predictive, yet practical manner.

The multi-scale nature of flames in particular makes combustion modeling a challenge. Reactions occur on the atomic scales (10^{-10} m) whereas flame dimensions (such as height) are on the macro scales (10^{-2}-10^{0} m). It is too computationally expensive to simulate real engine flames which may grow to be 100 mm wide on a nanometer spaced grid. Considering the large number of computations required at each grid point to account for chemistry as well as heat and mass transport, the computational demand is great.

Grid spacing for 3-D engine models being used today is on the order of 1 mm. Engine flame thicknesses are usually about 0.1 mm. Therefore, most current models cannot resolve flame structure phenomenon. Effects of local chemistry, topology, etc. are approximated in sub-grid models.

Some combustion phenomenon can be well characterized through sub-grid modeling, such as the calculation of heat release rates (HRR) in 0-D engine models. For many years empirical relationships have been used to accurately describe the HRR of combustion in a conventional SI engine. With complete neglect for flame physics, such a model can be used to test the global performance of an engine computationally. However, such a model only works because the

detail of such phenomenon that is modeled can be characterized rather simply and consistently for many engines.

Most combustion phenomenon is not simple and cannot be easily characterized through sub-grid modeling. For example, the interactions that occur between turbulent in-cylinder flows and flames are yet to be accurately described through empirical relationships over a large range of conditions. How to best deal with such processes in engine combustion modeling remains unclear.

Many complex engineering problems have been solved through computational modeling. For example, it was once a daunting task to perform thermal analysis on structures that exhibited elaborately curved contours. However, Finite Element Analysis (FEA) methods have made such heat transfer analysis simple and common practice. One may naively view the task of analyzing flames as being similar in nature and expect predictive computational modeling to become a reliable common practice in combustion design. However, the two problems are very different.

Successful, predictive 3-D engineering models are almost always based upon first principles. In FEA heat transfer analysis, complex structures are approximated by fine computational meshes. The well-established, fundamental equations of thermodynamics and heat transfer are then applied between grid points. In combustion simulations; most of the fundamental equations are understood but there is little to no hope of performing calculations on a fine enough mesh to approximate processes well. Therefore, combustion models are forced to abandon first principles and focus on approximations which are often empirical. In that, it is not surprising that combustion models struggle to achieve the high fidelity results achieved in other engineering simulation applications.

Since it is not possible to simulate engine combustion processes across all 10^{10} relevant scales, it is important to recognize what phenomenon/scales are suitable for sub-grid modeling. The successes of “flamelet” modeling suggest that it might be appropriate to approximate engine flames as thin, moving contours. This allows for the chemical/flame scales to be modeled

separately from larger scale transport processes and eliminates the necessity of gridding on the atomic scale.

The smallest in-cylinder turbulent eddies tend to be on the order of 10-100 μm in diameter. Engine flames tend to wrinkle on scales ranging from about 0.1 mm all the way up to scales that are only a small fraction of the bore.

It is unclear as to whether the interactions that occur between turbulent eddy and flames can be represented well by sub-grid models. The complexity of such interactions might demand fine grid resolution and first-principle based modeling techniques. An increase in computational grid spacing from 1 mm to 10 μm would require a 10^6 increase in computational power, which if Moore's law of computing[2] persists will take about 45 years to occur.

The importance of turbulent eddy-to-flame interactions and wrinkling on flame physics is unquestionable. As early as the late 19th century, Zel'dovich demonstrated that flame's consume fuel/oxidizer at a rate comparable to their surface area. A flames surface area density is closely related to its degree of wrinkled-ness and wrinkles are primarily caused by eddy-flame interactions. For a combustion model to accurately capture important flame features, such as propagation speed, it must account for flow-flame interactions and topological effects.

There has been very little research on the topology of stratified[3] engine flames. This is concerning being that so many advanced combustion strategies rely upon partial-premixing. The way for which stratified flames wrinkle in the turbulent environment is unique and not understood. Most stratified flame models are based upon homogeneous and heterogeneous combustion theory. The extent for which either class of flame theory applies to stratified flames

[2] Moore's law of computing states that the number of transistors on integrated circuits (and therefore computational power) doubles approximately every two years. This trend held from 1971-2010 but has slowed slightly since. The power of supercomputers is in part limited by software, not hardware. Therefore supercomputers do not adhere to Moore's law and can be expected to improve in computational speed much more rapidly (10^6 increase in computations power feasible in 10-20 years).

[3] Stratified flames are partially premixed flames.

is unclear. Further, even under simplified homogeneous-charge (premixed) engine conditions, flame topological phenomenon is incompletely understood.

For these reasons, this study focused on providing a better understanding of engine flame wrinkling processes. In particular, the study focused on recognizing the relative contribution of wrinkles of various scales towards the flame surface area development under both conventional homogeneous-charge and stratified-charge engine conditions. From the insights gained in this study, engine modelers can make more informed decisions with regards to choice of flame wrinkled-ness models, computational grid-spacing requirements and to temper their expectations of such models. Further, advanced engine researchers can use the results presented here to assess the benefits and challenges of employing SGSC combustion strategies.

In this study, optical diagnostics were performed within an engine and the physical insights gained help to answer the following questions,

Do thermo-diffusive instabilities play an important role in the early flame wrinkled development process in homogeneous-charge engines?

What flow scales have the greatest influence over homogeneous-charge engine flame topology?

How steady is the early flame wrinkled-ness process under homogeneous-charge conditions?

Do equivalence ratio based flame instability effects, such as those caused by thermo-diffusive instabilities play an important role in the wrinkle development process in stratified-charge engines?

What flow scales have the greatest influence over stratified-charge flame topology?

How are the flame wrinkled-ness development processes similar and different under spray-guided stratified-charge engine conditions from that of conventional homogeneous-charge engine conditions?

Wrinkled-ness aside, how are the flame spread processes different under spray-guided stratified-charge engine conditions from that of conventional homogeneous-charge engine conditions?

Is it worthwhile attempting to resolve topological flame features or should they be subject to sub-grid modeling for the foreseeable future?

Before discussing the research performed to answer these questions, a background on engines and flames will be provided. The first section provides a basic description of common and advanced internal combustion engines, as well as their advantages. Discussion is provided on advanced combustion design, as it relates to the motivation for these studies. Combustion theory is then presented. First non-premixed and premixed flame theory is discussed, followed by partially-premixed flame theory. It is necessary to have a background in the former two topics in order to discuss the latter. Following the background section, an experimental approach section is provided to outline all of the mechanical and optical diagnostics techniques employed in the study.

The results of the study are presented throughout three different sections. The first results section is titled “Engine Performance” (Chapter 4) and it demonstrates both the efficiency advantages and functional challenges that were encountered while operating an engine under SGSC conditions. The section offers no scientific contributions but provides a lot of practical information that may be used by those who wish to design or operate similar engines. It also provides necessary documentation on the engine conditions used throughout the following sections.

The second and third results sections (Chapters 5 and 6) present two complementary studies titled “Homogeneous-Charge Flame Wrinkled-ness Study” and “Stratified-Charge Flame Wrinkled-ness Study”. In these studies, a combination of planar laser induced fluorescence and stereo particle image velocimetry imaging techniques were employed to monitor the development of homogeneous and stratified-charge flames with particular focus on the development of flame wrinkled-ness; the results of which provide the bulk of the scientific contributions of this thesis.

At the very end of this document the overall conclusions of the study are outlined and all of the previously stated research questions are answered directly.

Chapter 2: BACKGROUND THEORY

2.1 Engines

This section will review a few engine concepts including the spray-guided stratified-charge (SGSC) combustion strategy. Many great books have been published on internal combustion (IC) engines, including the following references [5-7]. For more complete IC engine theory please refer to them. This section will begin with a description of conventional spark ignited (SI) and compression ignition (CI) engines. The motivation to move beyond conventional and towards advanced combustion strategies will be discussed. SGSC engines will be introduced and their differences from conventional engines will be highlighted. Finally, discussion will be provided on the combustion processes inside a SGSC engine and the scientific and practical benefits of studying stratified flames.

There are two types of engine which dominate the automotive fleet and they are typically classified by the type of fuel that they use, gasoline or Diesel. There exist many types of engines that utilize one or both of these fuels, but there has been so little variety in engine design over the last 50 years that the term “gasoline engine” has become synonymous with a 4-stroke, homogeneous, spark-ignited engine. Similarly, the term “Diesel engine” with a 4-stroke, heterogeneous, compression ignited engine. These two common engine designs will be referred to as conventional; the terms “conventional SI” or a “conventional Diesel” engine will be used to designate the industry norm as defined above.

Conventional SI engines are clean but inefficient. Diesel engines are efficient but emit high levels of engine out pollutants. Both conventional SI and Diesel engines have continued to improve with time and technology but are becoming increasingly difficult to improve. After-treatment systems have cleaned up the tailpipe emissions of Diesel engines, but at the detriment of efficiency. Hybrid powertrains have enabled SI engines to better operate near their optimum efficiency, but only through greater complexity and cost.

The general consensus is that automotive fuel efficiency needs to be improved in the near future. The U.S. government has regulated aggressive increases Corporate Average Fuel Economy (CAFE) Standards. Alternative combustion strategies exist that may provide both the fuel efficiency and cleanliness that is desired; but none without technical challenges. In light of the increasing demand for fuel efficiency alternative advanced combustion strategies are being considered more seriously.

Of the engine combustion strategies currently being researched, many aim to combine the best of both worlds; the efficiency of a Diesel engine with the cleanliness of a conventional SI engine. Often these strategies utilize fuel/air mixtures that are neither homogeneous nor heterogeneous; they are partially-premixed. Some examples of such strategies are partially-premixed compression ignition (PPCI), reactivity-controlled compression ignition (RCCI), lean lifted-Diesel spray combustion and the stratified-charge (SC) combustion concepts. Even conventional Diesel engines have become progressively less heterogeneous and more partially-premixed over time as the cleanliness benefits of partial-premixing have been realized.

2.1.1 Efficiency

Thermodynamics tells us that engines efficiency is limited and that it is impossible to build a perfect, 100% efficient engine. It is worthwhile to compare real engine cycles with ideal theoretical cycles in order to gauge just how efficient an engine is in relation to its theoretical limit. There have been many detailed studies based on the second law of thermodynamics but

here I will show a very basic analysis to demonstrate the potential for improvement. Please refer to [8-10] if more on the topic is desired.

Conventional SI engines are often compared to the ideal Otto cycle. This cycle is illustrated in the pressure-volume diagram in Figure 2-1 below provided by Borgnakke et al. [11]. Isentropic compression occurs between 1-2, isochoric heat release (combustion) between 2-3, isentropic expansion between 3-4 and an isochoric expansion between 4-1. Obviously real processes cannot occur so ideally; friction and heat transfer will produce entropy during the compression and expansion strokes. Further; combustion takes time and cannot occur isochorically. IC engines operate on an open cycle and experience losses due to pumping and scavenging. Therefore, the Otto cycle is known to only provide a rough, conservative estimate for the upper limits of SI engine efficiency.

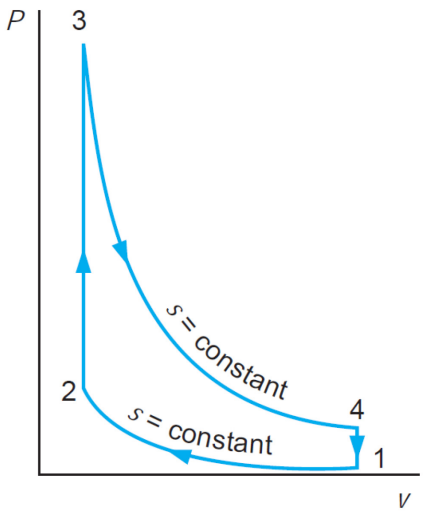

Figure 2-1: Pressure vs. Volume diagram of the ideal Otto cycle from Borgnakke et al. [11]

The Otto cycle efficiency is found to be,

$$\eta_{th} = 1 - (r_c)^{1-\gamma}$$

Where,

η_{th} = thermal efficiency

r_c = compression ratio
γ = ratio of specific heats

Therefore, an ideal Otto cycle engine with a compression ratio (r_c) of 10 with air as the working fluid (γ=1.4) should be able to achieve about 60% thermal efficiency. Conventional SI engines only realize about 35% efficiency at their peak. Rarely do conventional SI engines operate near their peak. Average efficiencies of automotive SI engines on the road today are about 20% [12].

This qualitative comparison suggests that the thermal efficiency of SI engines can be substantially improved. Researchers have found that real SI engine fuel efficiency can be increased by at least 50% over what is currently realized [13].

A more realistic pressure-volume diagram for a conventional SI engine is shown below in Figure 2-2,which has been borrowed from Heywood's book on IC engines [5].

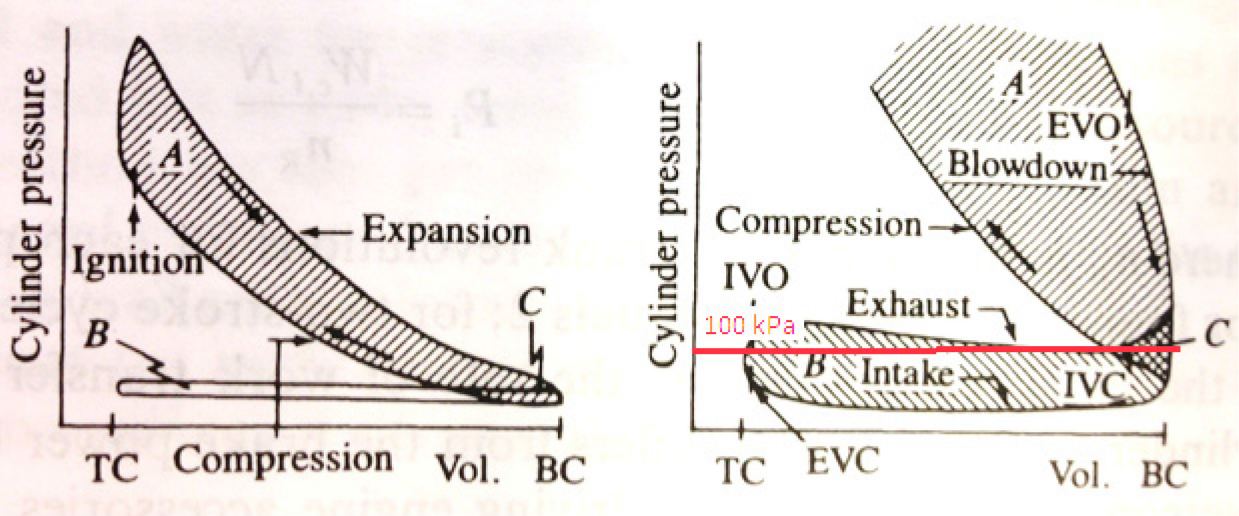

Figure 2-2: Cylinder pressure vs. Volume diagram for a SI engine. Provided by Heywood [5]

Note that the compression and expansion curves do not follow an isentropic path, combustion does not occur isochorically and a second loop which is labeled B is present. The B loop traces the exhaust and intake strokes, which is often referred to as the "pumping loop".

Indicated work per cycle, $W_{c,I}$, is equal to

$$W_{c,i} = \oint p\, dV$$

Where,
p = cylinder pressure
V = cylinder volume

Graphically, the area in loop A represents indicated work output, whereas the area in loop B represents the pumping work consumed to scavenge the in-cylinder charge. The total indicated work output is the difference between the areas of the two loops. Obviously it is never favorable to have a large pumping loop as it detracts from power output and efficiency.

Engine power output is controlled either through intake air flow throttling or fuel mass flow regulation. Conventional SI engines throttle inlet air, whereas Diesel and SGSC engines control load via fuel flow. Air throttling comes at the cost of increased pumping work whereas fuel flow regulation is performed with minimal losses. Revisiting Figure 2-2, notice that the area of the pumping loop is strongly dependent on the cylinder pressure during the intake stroke. When a throttle valve is used to regulate an engine intake air flow then both intake system and engine cylinder charging pressures remain lower than atmospheric due to the pressure drop that occurs across the throttle valve. In a typical SI engine intake pressures range from 25 kPaa at idle to 100 kPaa at wide open throttle. Figure was drawn by Heywood to represent such a throttled condition and the pumping loop is significantly large – detracting from the cycle efficiency. For un-throttled, naturally-aspirated engine operation, the pressure would remain near 100 kPaa for the entirety of the intake stroke and pumping losses would be minimal.

One might then ask; why don't conventional SI engines throw the throttle valve into the trash and regulate load via fuel flow like Diesel engines? The answer is twofold. Firstly, operating in

such a manner requires the engine to operate over a range of global equivalence ratio's (Φ)[4]. Such operation requires globally fuel-lean conditions, which is not feasible in a premixed environment under low load due to flammability limits. Further; conventional SI engines emissions after treatment systems dictate that they operate stoichiometrically. SGSC and Diesel engines are able to control load via fuel flow because they rely upon partial-premixing; whereas fuel is burned locally at flammable conditions despite the globally lean environment. This concept will become more evident when images of SGSC engines are shown in future sections.

Globally lean engines, which are often referred to as "lean burn engines" have an inherent advantage over stoichiometric engines in terms of the effectiveness of the lean charge as a working fluid. To illustrate this, review the Otto cycle efficiency equation. From this equation, it can be seen that for the Otto cycle efficiency, η_{th} increases along with γ. Hence, it is favorable to have a high γ working fluid during the expansion stroke. Pure air has a higher γ than do most combustion mixtures so lean mixtures tend to be thermodynamically favorable.

Another inherent advantage of lean burn engine strategies such as SGSC is that they tend to have lower in-cylinder temperatures relative to stoichiometric engines. Therefore, heat transfer losses are minimal.

There are a wide variety of combustion strategies offering higher efficiencies than conventional SI engines, including those previously mentioned in the discussion of engine basics. Many of these strategies utilize compression ignition (CI) instead of SI and are able to take advantage of higher compression ratios. Looking back once again to the ideal Otto cycle efficiency equation η_{th} increases with r_c. SI engines are limited in their ability to increase compression ratio due to the phenomenon of engine knock. Modern SI compression ratios are typically about 9-12. CI engines are not knock limited and typically operate at r_c = 15-22. This compression ratio advantage, along with reduced throttling losses, mostly explains the efficiency advantage of a

[4] $\Phi = \frac{F/O}{(\frac{F}{O})_{stoich}}$ where F/O is the fuel-air ratio. Φ=1 is stoichiometric, Φ<1 is fuel lean, Φ>1 is fuel rich.

Diesel relative to a conventional SI engine. There are prospects for both advanced CI strategies such as PCCI as well as for SI strategies such as SGSC. The focus of much of the work in this thesis focuses on SGSC and a lot of discussion will be given to stratified combustion throughout. However, it should be recognized that most advanced combustion strategies promising high efficiency utilize partial-premixing.

The intent of most current engine combustion research is to improve combustion efficiency while maintaining low pollutant emissions. Here I've discussed some of the basics of engine efficiency and it should be recognized that there are significant efficiency benefits to non-conventional combustion strategies; many of which burn partially-premixed fuel/air charges.

2.1.2 Stratified-Charge Engines

Stratified-charge engines differ greatly from conventional SI engines mostly in operational strategy but only slightly in physical hardware. The differences and similarities between stratified and conventional engines will be highlighted here. The sources of efficiency advantages for the SGSC strategy will also be discussed in detail; as it is this advantage that has driven the field of research.

Figure 2-3 below provided by Drake et al. [8] shows three different engine configurations. The first of which is Homogeneous Spark-Ignited Port Fuel Injection (SI PFI), which has been the industry standard for almost 20 years. Fuel is injected into the intake port just outside of the cylinder. This fuel is targeted at the intake valve region and a liquid film develops around the valve and port. Upon intake valve opening, the engine is charged with air/fuel charge. By late in the compression stroke the fuel/air charge is completely homogenized. A spark is initiated shortly before top dead center (TDC) compression and flame propagation consumes the mixture. The in-cylinder flow around ignition can be strong; it's not unusual for a newly formed flame cornel to encounter flows on the order of 10 m/s. This flow convects and stretches the

growing flame. The flame is distorted and wrinkled by turbulence. Through interaction with local flow it accelerates to speeds at least double the laminar flame speed.

The newest generation of homogeneous SI engines utilizes direct injection (DI) as opposed to port fuel injection. These SIDI engines are often equipped with similar hardware to the two stratified charge engines shown in Figure 2-3. Conventional SIDI engines also offer improved economy over their PFI counterparts.

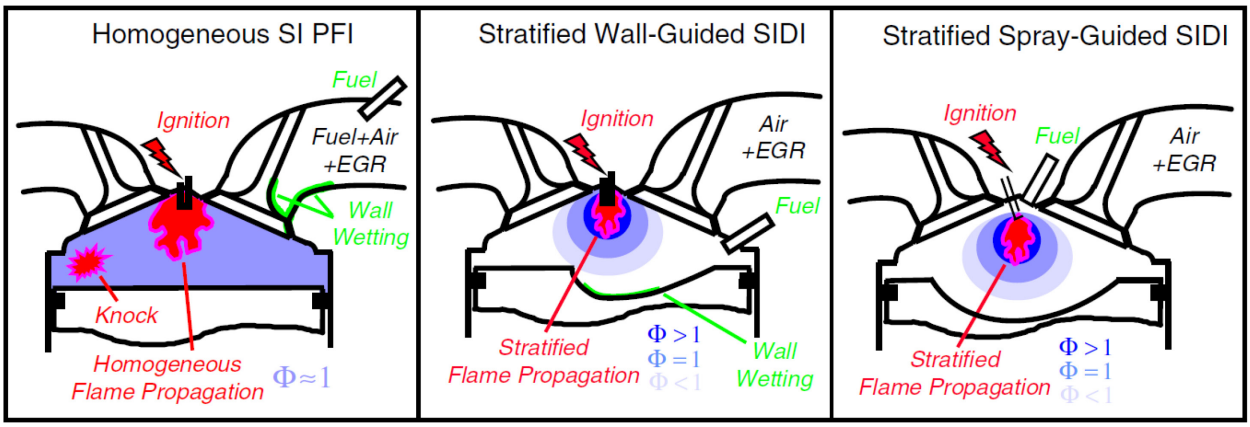

Figure 2-3: Gasoline engine types classified by fuel-injector location, mixture-formation process, ignition mode, and combustion mode. Figure by Drake et al.. [14]

A convenient feature of the homogeneous SI engine is that flame speed increases nearly proportional to engine speed[5]. It typically takes 40-50 crank angle degrees (CAD) for combustion to complete in a gasoline SI engine, and this occurs almost independent of engine speed. Therefore, the rate of burn for an engine running full speed at 6000 RPM is about six times that of the same engine idling at 1000 RPM. The flame acceleration is attributed to an increase in in-cylinder turbulence which causes a higher degree of flame wrinkled-ness and corrugation. This trend is typical of homogeneous but not necessarily partially premixed engine flames.

The center and right configurations in the figure illustrate typical stratified-charge engine architecture. Notice the similarity in architecture between all three engines, even between the

[5] Engine speed is a measure of rotational speed, commonly reported in units of rotations per minute (RPM).

homogeneous and stratified engines. They all have a piston, valves, spark plug (at the location of the ignition lightning bolt) and an injector. For both the wall and spray-guided engines, fuel injection is performed directly into the cylinder. Unique to the stratified charge engines is that the fuel/air charge is intentionally not fully mixed prior to ignition. A flammable, partially-premixed fuel cloud is created in the vicinity of the spark plug. Upon ignition, the stratified fuel cloud burns; but the combustion process is more complex than the homogeneous flame propagation that occurred in the PFI engine. The stratified flame must propagate through a cloud of varied equivalence ratio whereas some regions of the chamber air/fuel are very well mixed where in other regions not so much. The rich regions for which fuel is in excess will continue to burn late into the cycle.

The difference between the wall and spray-guided stratified charge architectures lies in the method for which they create an ignitable fuel cloud. In the wall-guided configuration the fuel injector is targeted at the piston bowl. In the spray-guided configuration the spark plug is directly targeted by the fuel spray. Both systems create the stratified cloud around the spark plug, but the wall guided does so indirectly deflecting spray off of the piston bowl. Whereas the spray-guided engine directly targets the plug.

Both wall and spray guided strategies have been tried and there is a general consensus that the spray-guided approach to stratification is superior. It is difficult, if not impossible, in a wall-guided stratified-charge (WGSC) engine to prevent excessive soot and hydrocarbon (HC) emissions while targeting and wetting the piston with the fuel spray [15]. Although the spray-guided approach does also have challenges of its own, most ongoing stratified charge engine research is focused upon the SGSC approach. Therefore, further discussion will be focused upon the spray-guided approach, not the wall-guided approach.

Stratified-charge strategies have been shown to improve thermal efficiency of an SI engine by 20% or more over conventional SIDI engines; the degree of improvement depending on the specifics of the engine and application [16]. Alkides et al. [17] performed a set of experiments

and modeling studies in order to determine the sources of fuel economy improvement over for a SGSC engine relative to a comparable PFI engine over the Federal Test Procedure (FTP) city cycle. The results of this test are summarized by Alkides in Figure 2-4 below.

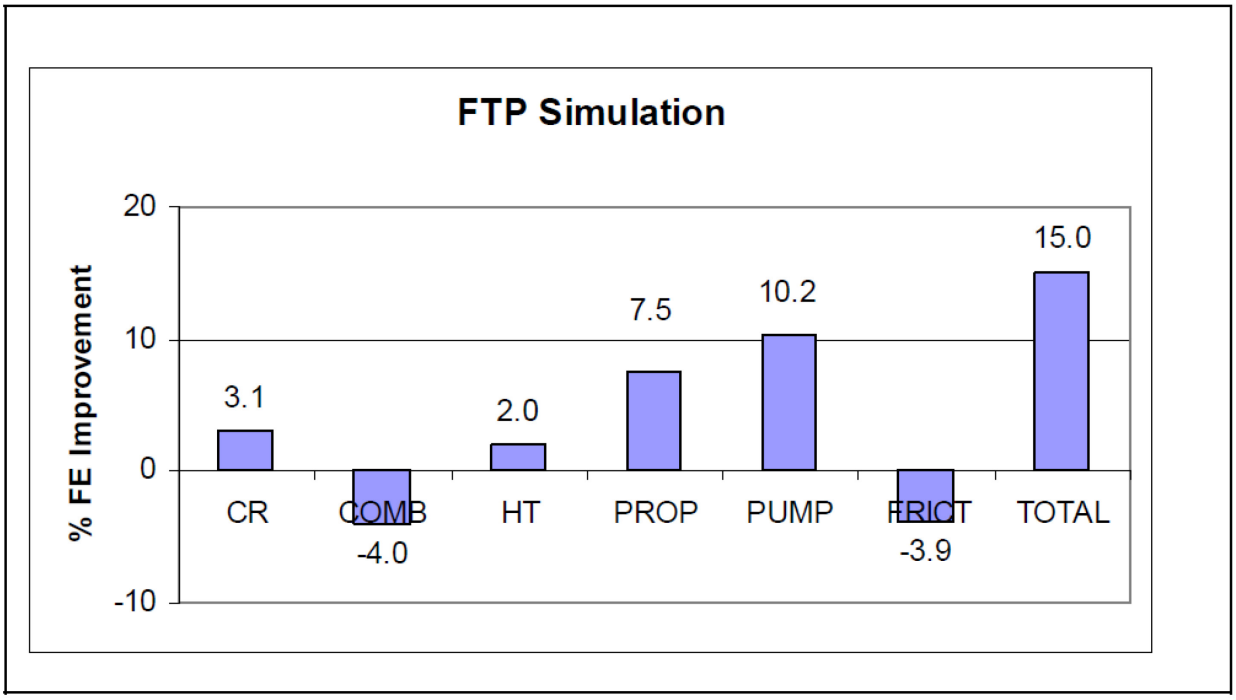

Figure 2-4: The contributions of various factors to the total % improvement in brake efficiency of the DISI engine over the baseline PFI engine, for the 7-point FTP simulation [10]. CR = compression ratio, COMB = combustion efficiency, HT = heat transfer, PROP = gas thermal properties, PUMP = pumping work, FRICT = friction.

The total efficiency improvement over the FTP cycle was 15%. Under the lowest load conditions tested (850 RPM, 115 kPa BMEP[6]) the efficiency improvement was 39%. Under the highest load condition tested (1750 RPM, 550 kPa BMEP) the efficiency improvement was only 3%. Typically, SGSC engines are operated in a dual mode manner; whereas SC operation is utilized only during low load when its efficiency benefit over conventional homogeneous SI operation can be realized. Under high load conditions conventional homogeneous SI operation is then used for best engine performance.

[6] Brake Mean Effective Pressure (BMEP) is the brake work per cycle divided by the cylinder volume displaced. It is a common engine performance measure for load.

From Figure 2-4, the reasons for the efficiency gains can be seen to be those already discussed; reduced pumping losses and favorable thermal gas properties. SGSC engines do also gain a little bit of efficiency from reduced heat transfer due to lower in-cylinder temperatures, but such gains remain minimal. The combination of all of these fuel saving effects motivates SGSC engine research and development.

2.1.3 Spray-Guided Stratified-Charge Challenges

Although SGSC engines are promising in terms of efficiency, they do come with their challenges. The two issues that inhibit SGSC technology the most are related to reliability and emissions [18]. Firstly; SGSC engines are prone to misfire[7] and partial-burn cycles [19]. Secondly; SGSC engines produce a significant amount of pollutant emissions that require expensive after treatment [16]. Emissions issues will be discussed first, then reliability.

Unburned hydrocarbons (uHC), carbon monoxide (CO), oxides of nitrogen (NO_x) and soot are all pollutants formed inside a SGSC engine that are undesirable for public health and the environment. These pollutants must be cleaned to acceptable levels by exhaust after treatment system prior to being emitted into the environment. Conventional SI engines are able to use a 3-way catalytic converter to clean up more than 98% of the uHC, CO and NO_x pollutants. 3-way catalyst technology is proven and has become a relatively affordable means of both oxidizing rich products and reducing NO_x through a single piece of equipment [20] . However, the 3-way catalyst that has been so pivotal in the wide scale success of conventional SI engines is incapable of reducing NO_x to acceptable levels when there is O_2 of significant concentrations in the exhaust flow. Therefore, lean burn strategies such as SGSC cannot utilize a 3-way catalyst and necessarily incorporate alternative NO_x reducing strategies to meet emissions standards [21]. SGSC engine also produce larger quantities of particulate emissions than do conventional

[7] A misfire is an engine cycle for which there is a complete ignition failure and nearly all of the fuel/air mixture is exhausted without being burnt.

SI engines. Particulate matter exhaust after-treatment may become necessary for SGSC engines in the future [18].

The pollutant issues associated with SGSC engines may be solvable through the implementation of exhaust after-treatment systems. Diesel engine manufacturers already use a combination of oxidation catalysts, particulate traps and selective catalyst reduction systems or lean NO_x traps to reduce pollutants to acceptable levels. SGSC engines may adapt a similar strategy. However, the cost of such systems in terms of both cost and efficiency is significant. It is desirable, if possible, to reduce emissions to engine-out levels low enough to require less after-treatment.

A natural question to ask is, could a SGSC engine in a manner as to avoid particulate (smoke) and NO_x emissions as to avoid the need for expensive after treatment? The answer is probably not when considering upcoming emissions requirements. However, the better SGSC engines can do at reducing engine out pollutant levels the less burden lies on expensive after-treatment systems. Figure 2-5 below was generated by Akihama et al. from a zero dimensional Diesel engine simulation using detailed chemical kinetics [22]. Akihama's analysis and this figure is thought to be generally relevant for most combustion strategies and hydrocarbon fuels. This diagram shows the intensity of soot and NO_x emission formation over a range of equivalence ratio's (Φ) and in-cylinder temperatures relevant to engines. Soot formation can be avoided by maintaining $\Phi < 2$ and NO_x formation can be avoided by maintaining low temperatures.

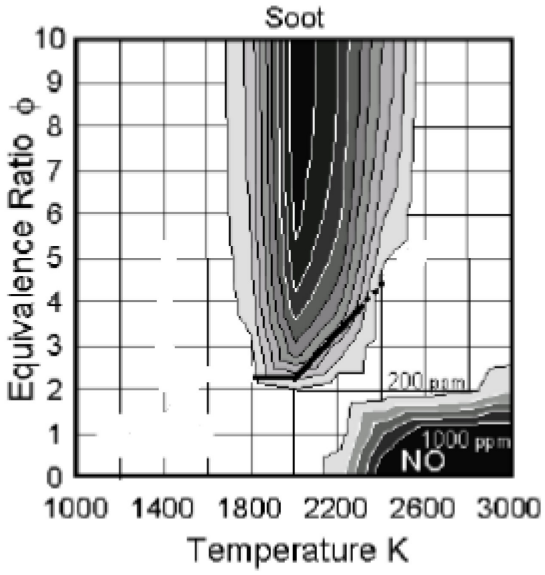

Figure 2-5: Emissions formation regime diagram generated by Akihama et al. [22]

A SGSC engine cannot operate within these low emission regimes. SGSC engine flames encounter very rich (Φ > 2) regions and occur at temperatures above 2200 K.

Figure 2-6 below by Peterson et al. [23] shows what a stratified charge fuel jet looks like in the SGSC environment. These images show both the Φ distribution through biacetyl planar laser induced fluorescence (PLIF) as well as the flow field velocity via particle image velocimetry (PIV). They were acquired in the same gasoline, 4-valve direct injection (G4VDI) engine used for this study at the University of Michigan Quantitative Laser Diagnostics Laboratory (QLDL). In fact, very similar equivalence ratio distributions will be shown from this study in Chapter 6.

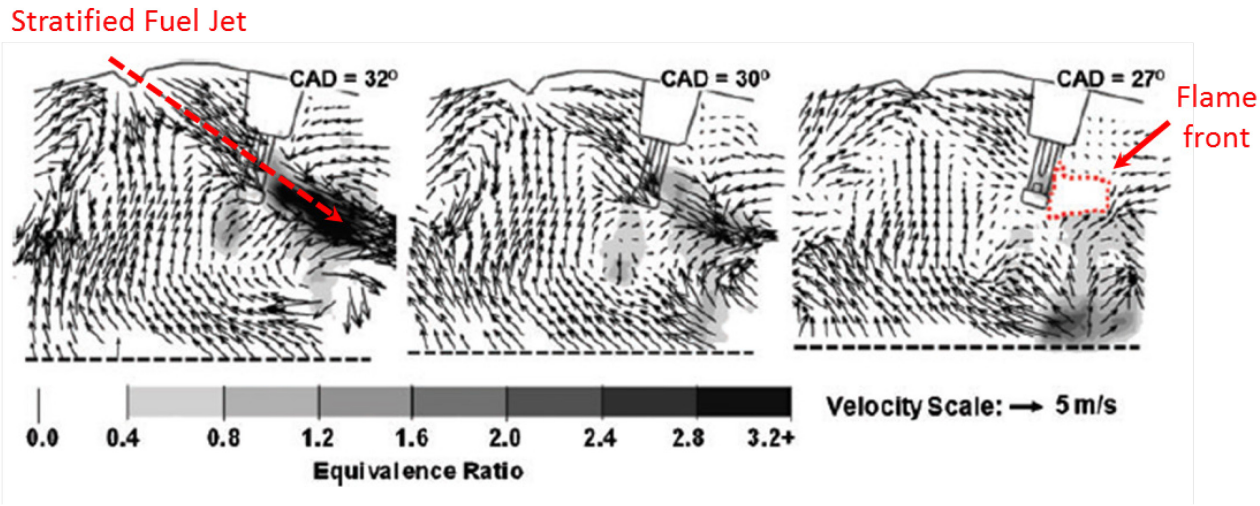

Figure 2-6: Simultaneously acquired PIV and PLIF images of equivalence ratio and flow field velocity in a SGSC engine provided by Peterson et al. [23]

The SGSC engine hardware and configuration shown in Figure 2-6 is common. However, it should be recognized that there exists a wide variety of SGSC configurations. Differences can be found in combustion chamber, piston and injector design between manufacturers. For example, the G4VDI engine shown utilizes a multi-hole injector. Many SGSC engines utilize an outwardly-opening pintle injector [24]. A more detailed description of SGSC technology and design is provided by Zhao in ref. [18] and for the sake of brevity further discussion will be limited to the SGSC hardware shown.

In the first image of Figure 2-6 the jet trajectory has been highlighted by the red arrow. The fuel spray emanating from the fuel injector is directed close to the spark plug. It is clear that near the center of the fuel jet core is very rich at $\Phi>3$. A small fraction of the jet likely persists as liquid ($\Phi=\infty$) but most of the jet is partially-premixed ($0<\Phi<\infty$) and is surrounded by pure air ($\Phi=0$). The persistent liquid portion of the jet is not well visualized by the PLIF technique but is known to exist near the injector tip, spark plug and other engine surfaces subject to spray impingement. In the third image a small flame cornel has formed and is outlined by the red dotted line. Further images would reveal that this small cornel grows into a larger, highly turbulent flame as the engine cycle progresses [25].

The flame that consumes this mixture experiences a variety of equivalence ratio's and inevitably, some of the mixture will burn around Φ=1 where flame temperatures are high and subsequently significant quantities of NO_x will form. Sometimes mixture dilution is used in the form of exhaust gas recirculation (EGR) to lower in-cylinder temperatures and NO_x. However, even with dilution flames must exist at approximately $\Phi < 0.7$ in order to completely avoid the NO_x formation temperature threshold that exists around 1800 K [26]. Such operation is not practical so the necessity for NO_x after treatment is a reality for SGSC engines.

Researchers have found that SGSC engines tend to produce more soot than conventional homogeneous engines [27]. As Figure 2-5 showed, soot forms in regions of $\Phi > 2$. This relationship has been verified extensively with n-heptane [28]. In order to avoid soot formation in the G4VDI engine shown in Figure 2-6, far better pre-mixing would have to be achieved prior to ignition if the $\Phi>2$ threshold were to be avoided. SGSC mixtures ignite optimally in rich regions of $1.5 < \Phi < 3$ [29] and so premixing to such a soot-free level would likely degrade ignition quality. Therefore, it's unlikely that SGSC engines will be able to achieve robust ignition and soot free operation simultaneously.

Luckily, not all soot formed from rich engine combustion survives to be exhausted. Hot soot is oxidized throughout the cycle and only the remaining particles make it into the exhaust. SGSC engine are best operated in a manner whereas soot formation is minimized and oxidation is maximized so that tailpipe particulate levels are low. Such goals can only be achieved by optimizing fuel/air mixing and combustion; a task which is greatly challenging.

SGSC engines typically demonstrate comparable HC and CO emissions relative to conventional SI engines [16]. Sometimes these pollutants are increased due to wall/plug wetting and excessive rich combustion. Smart engine geometry design and operational strategy can reduce HC emissions. The generation of both HC and CO emissions is detrimental to engine efficiency, but both pollutants be cleaned up prior to exhausting by an oxidation catalyst, provided the catalyst is kept at a reasonable temperature.

As emissions standards tighten, it is unlikely that SGSC engines will be able to avoid utilizing more complex and expensive after-treatment hardware. Some after-treatment technologies such as particulate and lean NO_x traps require frequent rich engine operation for regeneration, which reduces engine efficiency. Using after-treatment technologies in a SGSC engine environment can also be a technical challenging; particularly under low load when exhaust temperatures are too low for proper catalyst function. So for SGSC strategies to succeed, it is important that in-cylinder mixing and combustion processes are optimized to relieve the burden from the exhaust after-treatment system.

Emissions aside, one of SGSC engines most challenging problems is high cycle-to-cycle variability (CCV). SGSC engines are subject to abnormally frequent miss-fires and partial burn cycles. A common metric of cyclic variability is coefficient of variance (COV) of indicated mean effective pressure (IMEP). Whereas IMEP is an indicated measure of work performed on the piston during an engine cycle. A conventional SI engine will experience a COV of IMEP less than 2% under stable, low-load operating conditions [30]. SGSC engines have difficulty achieving less than 5% COV of IMEP under similar conditions [31]. Differing levels and causes of cycle-to-cycle variability have been observed in different engine setups. Such high variability is bad for vehicle drive-ability, longevity, noise and emissions.

CCV in conventional SI engines has been researched since the 1980's [32] and sources of normal SI combustion variations are generally attributed, rather generically, to turbulence [33-35]. Engine in-cylinder flows are moderately turbulent and turbulence is stochastic in nature; therefore, engine flames are also stochastic in nature. The degree for which combustion varies within an engine tends to scale with the turbulence intensity of the in-cylinder flow.

In a conventional SI engine ignition occurs robustly and CTC variability is a lesser cause for concern. During ignition, there is always a favorable $\Phi=1$ mixture around the spark plug that tends form a resilient flame kernel. This kernel is subject to in-cylinder currents and may be transported across the cylinder before growing to substantial size. Early extinction causing a

misfire rarely occurs in conventional SI engines. However, flame propagation will vary spatially cycle-to-cycle based upon the random convection of the flame kernel [36], contributing to the <2% COV in IMEP that is normally observed. Natural luminosity images of conventional SI flames tend to show unique, but robust flame growth on almost every engine cycle.

CCV is a larger problem in the SGSC environment because a robust ignition event is not guaranteed. The stochastic in-cylinder flow is not merely convecting the flame kernel, but is also altering the trajectory and mixing of the fuel jet [37]. For ignition to even occur, a favorable cloud needs to form locally by the spark plug. Not only does the cloud need be favorable in the region of the spark plug, but the fuel cloud and flow field surrounding the newly formed kernel must be favorable to promote flame propagation. The stochastic in-cylinder flow and fuel-spray do not always create suitable conditions.

Researchers have found that misfires occur in SGSC engines largely due to unfavorable Φ and velocity distributions local to the spark plug during ignition [15]. Partial burns cycles have been seen to occur when an early flame kernel forms but propagates sluggishly; never growing large enough to consume the mixture before the end of the cycle. CCV is known to increase in a SGSC engine with engine speed [38]as does in-cylinder turbulence. Hence, it is known that in-cylinder flow variations drive combustion variations in SGSC engines.

The sources of misfires and partial-burns in the G4VDI engine were studied extensively by Peterson [39]. Peterson found that most poorly burned cycles occurred due to a combination of unfavorable fuel cloud distributions and high local strain around the spark-plug. Others have observed misfires due to ignition system related failures [40] or plug wetting.

Every engine is unique and subject to its own failure modes. Whether the problem is excessive emissions formation or high cycle-to-cycle variability; engine manufacturers need a means of understanding such problems and implementing solutions.

2.1.4 Advanced Engine Design

Historically, engines have been designed by trial-and-error approaches and empirical theory. In the early days of IC engines there was very little combustion theory for engineers to draw from. A lot has been achieved through design based upon experimentation and conventional engines have thrived. However, the field is no longer young and the challenges have become more complex in nature. Advanced strategies such as SGSC require a far greater degree of control and smart design than do conventional strategies. Advanced concepts demand a clear understanding of in-cylinder processes; the foundation of which is best based upon scientific first principles, not empiricism.

Foundational engine combustion research has brought about a conceptual understanding of conventional engine processes and led to design improvement. For example, Dec presented a conceptual model of the diesel engine flame structure [41] based upon optical imaging studies. This work presented flame pictures and images which provide a physically intuitive understanding of in-cylinder processes. From this, modern diesel engine engineers can better consider the effects that implementing hardware changes might have on the engine combustion performance. Similarly; conceptual descriptions were developed as early as the 1960's for the conventional SI engine combustion process, also through in-cylinder imaging studies [42-44]. SGSC engine processes have been characterized [14, 18, 45-50] but are not understood in the same depth as conventional strategies.

Many of the fundamental processes that drive engine combustion such as flow development, spray development, mixing and combustion, are only superficially understood. Even in the absence of completely formulated fundamentals, numerical computer models have been developed to aid in engine design. A wide variety of models exist; from simplified zero and one dimensional models [51-54] to full 3-D computational fluid-dynamics (CFD) models that incorporate flame physics [15, 55]. With computational and combustion science ever

advancing, the fidelity and usefulness of combustion models is rapidly improving. Engines are slowly being developed more by computers and less by iterative experimentation.

In order to be useful in combustion design, 3-D CFD combustion models must be capable of approximating real combustion processes to a reasonable accuracy. Real flame physics cannot be directly simulated in the engine environment. Resolving engine flames requires consideration of an unreasonably large range of spatial and temporal scales. Approximations are necessarily and readily applied to engine models. These approximations are often empirical in nature and require tuning.

In reference [14] Drake and Haworth discuss the value of using optical diagnostics and numerical modeling symbiotically to develop advanced engines. Model accuracy can be assessed when compared to comparable experiments. Optical diagnostics can both validate modeling assumptions as well as provide invaluable insight into the relative importance of in-cylinder processes. Through collaboration between experimentalists and modelers, high fidelity computational models are being developed into powerful design tools. Such models are particularly appealing in advanced engine development. It is desirable, whenever possible, to explore changes in engine geometry or operating strategies on a computer rather than building and testing a large number of prototypes.

A lot of experimental work has been done in the past identified key in-cylinder combustion processes and features in conventional engines. Models have been designed to capture these key features. However, since these models are based on approximations their fidelity is always questionable outside of the validated regime. It is difficult to assess the limits of 3-D CFD engine combustion models and therefore engine designers are necessarily hesitant to use them outside of validated regimes. Until engine models are truly predictive experimental design techniques cannot be completely replaced by computational modeling. The predictive abilities of partially-premixed flame models is particularly questionable being that most of these models are comprised of an aggregate of fully premixed and non-premixed models despite many

experiments having demonstrated physics intrinsically unique to the partially premixed environment.

Real engines are currently being designed through a combination of both experimentation and modeling. The balance between the two is not well documented in literature.

Despite the challenges, a few manufacturers have produced commercial SGSC engines. Mitsubishi introduced a WGSC engine in 1996 in Japan and Europe [56]. Mercedes Benz produced a SGSC engine [57] in 1997. Many other manufactures including Toyota, Nissan, Ford, Isuzu, Audi, Honda, Subaru, General Motors and Fiat have also designed prototype stratified engines since [18]. The CLS 350 CGI spray-guided engine was introduced into the market in 2006 by Mercedes-Benz [58]. This engine offers a 10% efficiency benefit[8] in comparison to a conventional baseline version of the same v-6 engine. An outwardly opening piezo-electric injector system is credited for enabling the engines success.

The small scale success of these few commercial SGSC engines demonstrates that it's currently possible to design a SGSC engine worthy of production. Yet, most automotive manufacturers refrain. To the best of the author's knowledge, neither Mercedes nor any other manufacturer is still continuing to produce SGSC engines commercially. From this it can be reasoned that the current drawbacks of SGSC technology still outweigh the benefits; at least in the view of engine manufacturers.

Through acquiring an improved understanding of the processes that drive SGSC engines, better tools can be developed to enable smarter design so that the full benefits of SGSC engines can be realized on a larger scale. If predictive computations are to be used than the relative importance of in-cylinder processes must be recognized so that the appropriateness of their inclusion or exclusion in a model can be assessed.

[8] Efficiency benefit measured throughout the European combined driving cycle.

2.1.5 Engines Summary

In this section the importance of burning fuel cleanly and efficiently in engines was highlighted. Conventional SI and diesel engines were discussed, along with their benefits and downsides. It was shown that conventional SI engines leave much to be desired in terms of efficiency and that alternative combustion strategies such as spray-guided stratified-charge (SGSC) are capable of improvement. Following some general discussion on efficiency, SGSC engine hardware was introduced.

The sources of efficiency improvement in the SGSC engine relative to conventional SI engines were outlined. The challenges relating to SGSC engine emissions and cycle-to-cycle variability were discussed. Advanced engine design was discussed; highlighting the need for both experimentation and numerical modeling in the design of future engines. However, it was pointed out that numerical models necessarily apply approximations of important phenomenon that compromises the predictive abilities and accuracy of the model. Therefore, all models must be extensively validated before deemed trustworthy. Some in-cylinder phenomenon is still poorly understood, particularly with regard to turbulent partially-premixed combustion. A recognition and understanding of important flame physics is prerequisite to predictive model development.

SGSC engines are only one example of many promising advanced combustion strategies. The physical phenomenon that drives most these strategies is similar. Understanding stratified flames in the engine environment has value far beyond SGSC engines.

The motivation for the research performed here was primarily to achieve a greater understanding of homogeneous-charge and stratified-charge combustion physics and secondarily to move forward SGSC engine technology. It should be recognized that the engine is a very difficult environment to perform truly fundamental studies. It is never possible to hold a single test parameter constant in an engine. Inevitably, any change in engine operation, such as

increasing engine speed, load or combustion phasing, affects the entire spatial and temporal evolution of the combustion process. Rarely can one physical effect be isolated from another to the degree that a scientist would desire.

For these reasons fundamental combustion research has historically been performed on bench tops and not inside practical combustion devices. The problem with this of course is that flames in real devices can act quite different than a simplified experiment. Engine combustion physics are particularly unique due to the peculiarities of engine flows caused by the expansion, compression and scavenging processes. The work that is presented here was intended to be about as fundamental as possible within the limitations of the engine environment. The flame studies here are commercially relevant. With this will come the benefits of realism but also the challenges of working within a poorly controlled scientific environment.

Independent of whether or not the current engine combustion theories are correct, modeling of conventional SI and diesel engines has been relatively successful. One could make the argument that this is so because SI and diesel combustion have been so well characterized through years of study. The properties of a conventional SI flame are well documented, so combustion models can be made to look like a flame, somewhat independent of the physicality of the model. For practical reasons this may be acceptable, dependent on what information is to be extracted from such a model. However, only physically based models can be relied upon for truly predictive results.

The same degree of characterization and understanding does not exist for less conventional combustion strategies such as SGSC. Theory based upon conventional SI engines or homogeneous flames is not necessarily relevant in the SGSC environment. For example, prior to this document there is almost no published work on the wrinkling of flames in the SGSC environment. However, as will be later discussed, understanding wrinkling is a prerequisite to modeling flames well.

This section has been written to introduce engines, the SGSC strategy and the reasons why engine combustion research is important. The next sections will focus upon flame theory. Through the combination of these two background sections it should become clear why the flame wrinkling studies performed here in a spray-guided stratified-charge engine are relevant and just how challenging and complex the field of engine combustion is as a whole.

2.2 Combustion

Fire has existed as an essential force of nature on earth for the last 540 million years, but it wasn't practically utilized until about 2.5 million years ago when our early ancestors began using it to cook [59]. Over the last 30,000 years a phenomenological understanding of combustion has developed and enabled a variety of technologies, including automobiles, airplanes and power generation [60]. The vast majority of the theoretical background currently accepted in the field has been formulated over the last century. Despite being such an old science turbulent flame physics remains a field in discovery.

Flames may be fully premixed (homogenous), completely non-premixed (heterogeneous) or of partial mixed-ness (partially-premixed). Turbulent flame "regimes" may be defined based upon properties of the flame and the turbulent flow. In the absence of turbulence flames are laminar. Flames of differing mixed-ness or turbulent regimes tend to behave differently; therefore combustion theory is often categorized based upon both regime and mixed-ness. A recent review of the field by Bilger et al. [4] highlights many important questions that remain in the field of combustion. Most of the remaining questions pertain to turbulent premixed and partially-premixed flames.

Turbulence tends to accelerate combustion processes. Industrial burners and engines usually desire high burn rates. Therefore, flames found in combustion devices are almost always turbulent.

Unfortunately; the interactions between turbulent flows and flames is complex enough that turbulent flame theory remains incomplete. Laminar flame physics is relatively simple in comparison. The structure and properties of laminar flames are mostly understood, but the same cannot be said for turbulent flames. Throughout most combustion regimes, the underlying structure of laminar and turbulent flames remains similar; therefore some laminar flame theory can be borrowed by turbulent flame theory.

Flame fronts undergo distortion due to aerodynamic stretch and intrinsic instabilities [61]. Such effects are greatly important for flames that fall within turbulent regimes, but less so under laminar conditions where aerodynamic forces are minimal. Turbulence eddies can interact and wrinkle flame fronts, causing flame area growth. Flame surface area growth is the mechanism that drives flame speeds to increase along with turbulence levels. Therefore, turbulent flame speed and flame surface topology phenomenon such as wrinkling are closely related.

Non-premixed turbulent flames have been extensively studied and modeled. Although scientific questions still remain, the theory behind non-premixed flames has developed to a level where multidimensional CFD codes can be used predictively. That is not to say that such non-premixed flame models are physically accurate, or that the science behind non-premixed flames is fully understood; but that methods for modeling non-premixed flames have proven useful and predictive in design. Therefore, turbulent non-premixed flame physics are generally considered better understood then their premixed or partially premixed counterpart.

Premixed turbulent flames are actively being studied and there is an improving understanding of the science. The strong coupling between turbulence and flame topology in turbulent premixed flames makes the topic particularly challenging. Phenomenological descriptions of such complicated flame-flow interactions have not proven successful. None the less, premixed flame models are commonly used in the engine design. When properly validated and used within their relevant regimes, such models have proven their utility in design.

Partially premixed flames are formed in mixtures that exhibit fuel/air mixture stratification; hence they are sometimes referred to as stratified flames. Partially premixed flame physics are poorly understood in comparison to either (non-premixed or premixed flame) mixed-ness regimes. Stratified engine combustion modeling has found limited success in practice.

Stratified flame physics is often considered to be an aggregate of premixed and non-premixed flame physics. However, it is not clear that premixed or non-premixed theory can readily be applied to stratified mixtures. In stratified flames, propagation can occur in a “premixed like” manner in adequately mixed regions. However, mixture fraction gradients are known to modify flame properties such as wrinkle growth rate [62] . Rich stratified mixtures can exhibit both premixed and non-premixed like burn characteristics. These flames often exhibit a “trailing diffusion flame” region where partially oxidized rich combustion products are consumed in a “non-premixed like” manner. The details of such flames will be discussed in depth later but it is important to recognize that it remains unclear to what extent premixed and non-premixed flame theory need be modified or combined to account for stratification. Partially premixed flames have shown intrinsic uniqueness’s which complicate the application of premixed and non-premixed flame theory towards the stratified environment.

Prior to discussion on partially-premixed flames, a background will be provided on non-premixed flames and premixed flames as the theory of these two regimes is pre-requisite. The non-premixed flame theory section is brief since non-premixed flames were not a direct focus of this study. The premixed and partially-premixed flames theory sections are more in depth, as is necessary as a primer for the study to follow.

2.2.1 Non-Premixed Flames

Most natural combustion occurs between fuels and oxidizers that are initially separate. The most common oxidizer on earth is gaseous Oxygen. Fuels tend to be found in the solid or liquid form. For example, wood, coal and oil. Both fuel and oxidizer must be in gaseous form and

adequately mixed to react. Most non-engineered combustion events (eg. disasters such as forest and house fires) are non-premixed in nature.

There are properties of non-premixed flames that cause them to be desirable in application. They tend to be stable and reliable which is mandatory in applications where blowout is unacceptable, such as airplane propulsion systems. They are also more easily controlled than their premixed counterpart. For example, the rate of heat release from a non-premixed flame can often be easily regulated by limiting the rate of reactants supplied.

An example of a non-premixed combustion device is the common candle. Prior to being lit, wick and wax rest spatially separated from ambient Oxygen. Once lit, the solid candle core vaporizes and mixes with ambient O_2. In a thin mixing region just above the candle a flame front forms where the fuel and oxidizer join to react. The flame is driven by an influx of vaporized wax and Oxygen. The wax vaporization is driven by heat transfer backwards from the flame (feedback from the flame). At the flame front, mixing occurs primarily by diffusion. Many chemical reactions occur within the flame front very quickly. Rapid reactivity is characteristic of all combustion processes.

In the case of the candle the rate for which combusting occurs is limited by mixing processes. Such is true for all non-premixed combustion processes. It may take a few hours to burn a candle because it takes so long for the solid candle core to melt and gasify. Once gaseous, the wax is consumed almost instantly by the flame (hence the flame sits very close to the candle body). Accelerating the chemical reaction processes within the non-premixed flame front would not increase the rate for which the candle was consumed. Ultimately, it is the pace for which the wick melts, evaporates and mixes that limits the burn rate of the candle.

To demonstrate the importance of non-premixed combustion in the SGSC environment, review Figure 2-6 and notice the abundance of rich regions within the engine. Some of the combustion in these regions is mixing controlled (i.e. will require further mixing with Oxidizer in order to

react), and therefore non-premixed in nature. Highly rich regions where the local equivalence ratio is beyond flammability limits will burn in a completely non-premixed manner, like a candle (a candle in a tornado might be a better description). Flammable rich regions will experience mixed mode combustion, whereas a "premixed like" flame will consume as much fuel as possible but will be unable to complete the oxidation due to lack of oxidizer. Partial oxidation products such as CO and H_2 will form and a non-premixed "trailing diffusion flame" will usually complete the oxidation process. Such a trailing flame will burn in a non-premixed manner. Hence, non-premixed flames can be recognized in both completely non-premixed and partially-premixed fuel-oxidizer environment.

2.2.1.1 Diffusion and Mixing

Non-premixed flames are mixing rate limited [26]. Molecular mixing processes are driven by diffusion. In recognition of the importance of the diffusion process in heterogeneous combustion, non-premixed flames are often referred to as "diffusion flames". Therefore, the term diffusion flame will be used synonymously with non-premixed flame throughout this document.

Molecular diffusion occurs as described by Fick's 2nd law,

$$\frac{\partial C_i}{\partial t} = \nabla \cdot (D \nabla C_i)$$

A steady, molecular diffusive flux can be described by

$$J_i = D \nabla C_i$$

Where J_i = molecular flux
D = molecular diffusivity of species i in medium
C_i = molecular concentration of species i

As Ficks law shows, molecular diffusion is driven by species concentration gradients. Molecular diffusion is the only means for which species mix on the atomic level necessary for chemical reaction. It is therefore a critical process in all reacting systems. Diffusion is highly effective at mixing across small distances but is inefficient at mixing on larger scales. Therefore, most mixing processes are performed through a combination of large scale convective stirring (for which turbulence is effective) and small scale diffusive mixing.

A characteristic mixing length of diffusion can be defined as

$$L_d = \sqrt{4Dt}$$

Where L_d = characteristic mixing length
t = mixing time

For a given amount of time, concentration gradient may smooth on the same spatial scale as L_d. Within engines, combustion processes occur rapidly and characteristic mixing lengths tend to be very short (on the order of 10^{-5} m)

In an environment where convection occurs on a faster scale than diffusion (diffusion rate limited), mixture fraction gradients remain sharp. Here, the interface between the two dissimilar fluids can be viewed as a mixing sheet. Since the concentration gradient remains similar across all regions of such a mixing sheet, so does the diffusive flux. Therefore, the rate of diffusive mixing in such an environment is controlled entirely by the surface area of the mixing sheet.

The surface area of such a mixing sheet can be stretched by aerodynamic forces. Turbulence is particularly effective at stretching fluid sheets and promoting mixing in this manner. Diffusion flames can largely be viewed as thin sheets that are mixed in the manner described above. The burn rate of a diffusion flame is strongly influenced by a coupling between turbulent convection and diffusion; whereas turbulent eddies tend to stretch the flames surface and generate

surface area. Diffusion is then able to mix (supply) reactants into the flame front at a rate comparable to the flames surface area, which is generally done more effectively when the surface area is large.

Modeling mixing processes is a challenge, even in a non-reactive environment. The conservation of mass, momentum and energy equations must all be considered in three dimensions, as is commonly done in the field of computational fluid dynamics (CFD). One approach is to utilize the Reynolds Averaged Navier-Stokes (RANS) equations. In RANS, the fluctuating (turbulent) portion of the equation is separated from the time averaged portion. The averaged portion may then be solved and the turbulence modeled. Large Eddy Simulation (LES) is another common approach, whereas the Navier-Stokes equations are solved on a limited range of spatial scales. The resulting solution is similar to a low-pass filtered version of the flow field. Direct numerical simulation (DNS) can be used to numerically solve the Navier-Stokes equation for very simplified flow configurations for which the Reynolds number is relatively low. However, rarely is DNS practical for mixing simulations relevant to realistic combustion devices.

Using such approaches, mixing processes (such as non-premixed flames) may be modeled. Scalar's quantities (ψ_i) include species mass fractions and temperatures may be tracked as they mix. Almost all scalar mixing models are based upon passive mixing, whereas effects of mixture reactivity are ignored. Warhaft [63] describes a passive scalar as a diffusive contaminant in a fluid flow that is present in such low concentration that it has no dynamical effect (such as buoyancy) on the fluid motion itself. An example of such a passive mixing process would be the mixing of two inert gasses (such as He and Ar)

Flames are by nature, reactive. The diffusion process feeding a non-premixed flame is affected by the flames reactivity and heat release. It is not correct, but common, for passive scalar mixing concepts to be applied to flame modeling [64]. In fact most diffusion flame models, such

as those most commonly used for diesel engine development, are based upon passive scalar models. Surprisingly, many such models have found utility.

In the description of non-premixed combustion systems it is common to introduce a mixture fraction variable Z [65],

$$Z = \frac{m_f}{m_f + m_{ox}}$$

Z_{st} can then be defined as the value for a stoichiometric fuel/oxidizer mixture. The masses associated with Z are elemental, not molecular, so they are considered passive. Z therefore is a measure of mixed-ness. On the fuel side of a diffusion flame Z = 1, whereas on the oxidizer side Z = 0. In-between a flame exists with a reaction zone residing near Z_{st}.

A commonly used mixing metric is the instantaneous scalar dissipation rate (χ),

$$\chi = 2D|\nabla Z|^2$$

The scalar dissipation rate is commonly viewed as the inverse of the diffusional time scale. χ appears frequently in non-premixed combustion models.

The importance of convective-diffusive mixing processes on non-premixed flame physics cannot be understated. In the non-premixed environment, estimates of important flame properties such as burn rate can only be made based upon accurate estimates of mixing processes. Whether the mixing process is characterized by χ or another method, fundamentally it is driven by diffusion and topology, the latter of which is the focus of this study. Many of the same concepts with regards to mixing and surface area generation will be later discussed and shown to be similar for premixed and partially-premixed flames.

2.2.1.2 Turbulent Non-Premixed Flames

Due to a combination of natural instabilities and/or interaction with local flow, most non-premixed flames become turbulent. The difference between a laminar and turbulent diffusion flame is visually recognizable. The contour of laminar diffusion flames usually looks smooth, whereas turbulent flames contours exhibit significant levels of wrinkling and corrugation due to flow/flame interactions.

The normal state of fluid motion (or flames) is turbulent. Any flow field can be broken into its average and random components, respectably,

$$\vec{u} = \overline{\vec{u}} + \vec{u}'$$

Where $\vec{u}'$ = fluctuating velocity components

Turbulence causes a portion of the flow ($\vec{u}'$) to be random, chaotic and unpredictable in nature. Laminar flows are therefore just the subgroup of flows for which $\vec{u}'$ is negligibly small. Although stochastic, turbulence flow contributions often self-organize into vortex structures which are generally referred to as “eddies”. Such structures span many scales and are particularly effective at imposing aerodynamic strain.

The characterization of a flame as turbulent vs. laminar can generally be evaluated using the Reynolds number definition,

$$Re = \frac{\rho L V}{\mu}$$

Where Re = Reynolds number
L = characteristic length
V = flow velocity
μ = fluid dynamic viscosity

At a critical Reynolds number (geometry dependent, and never exact) flow transitions from laminar to turbulent regimes. The Re number can be viewed as a ratio of inertial to viscous forces. At high Re number flow, inertial forces and turbulent contributions dominant the flow. At low Re number viscous forces dominate, eddies are rapidly dissipated, and flow remains laminar.

There exists a range of Reynolds numbers for which the flow is "transitioning" from laminar into turbulence. In this regime the $\vec{u}'$ flow contributions are significant, but do not dominate flow dynamics.

The various turbulent regimes of a non-premixed flame can be observed by the classic "bending" phenomenon illustrated in Figure 2-7 below by McAllister et al. [66]. This figure shows the progression of a jet flame as the nozzle velocity (and turbulence intensity) is continually increased.

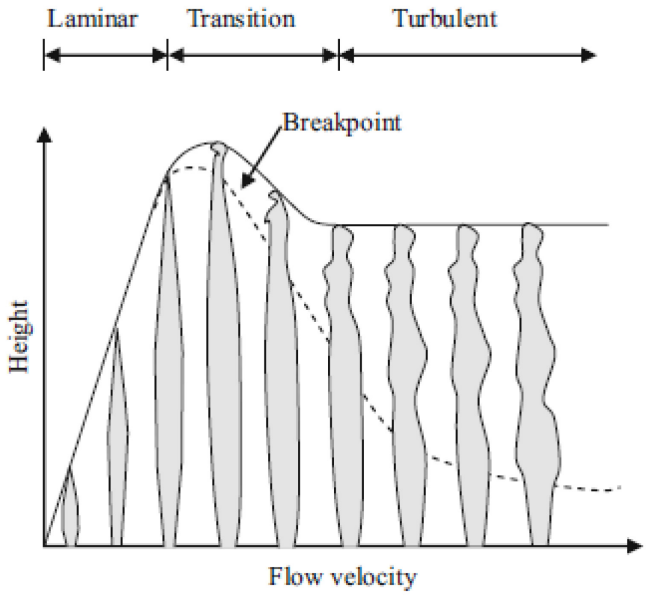

Figure 2-7: Flame height vs. nozzle velocity trend for jet diffusion flame provided by McAllister et al. [66]

Notice that flame height increases linearly with flow rate throughout the laminar regime. Then a transition occurs where the flame height reaches a maximum, followed by a constant height throughout the turbulent regime. Within the turbulent regime the diffusion flame height is independent of flow rate. When these results were originally recognized through experiment, they were thought to be counterintuitive. One may reason that diffusion flame height should continue to grow with increasing jet mass and momentum as the total burn rate of the flame must increase. As will be shown, it is surface area phenomenon that allows such a flame to maintain height throughout the turbulent regime.

A drawing of the jet flow is shown in Figure 2-8 below. The mass flow rate of fuel ($\dot{m}_f$) ejected from the nozzle scales linearly with the flow velocity (V_{nozzle}) since the nozzle area (A_{nozzle}) is fixed,

$$\dot{m}_f = \rho_f A_{nozzle} V_{nozzle}$$

Therefore, as V_{nozzle} increases the jet flame needs to accommodate this with a proportionally larger total burn rate. All of the fuel mass must pass through the flame contour at some portion of the flames surface (∂A) at approximately the local flame speed (S) and density (ρ)

$$\dot{m}_f\big|_{\partial A} = (\rho S \cdot \delta A)|_{\delta A}$$

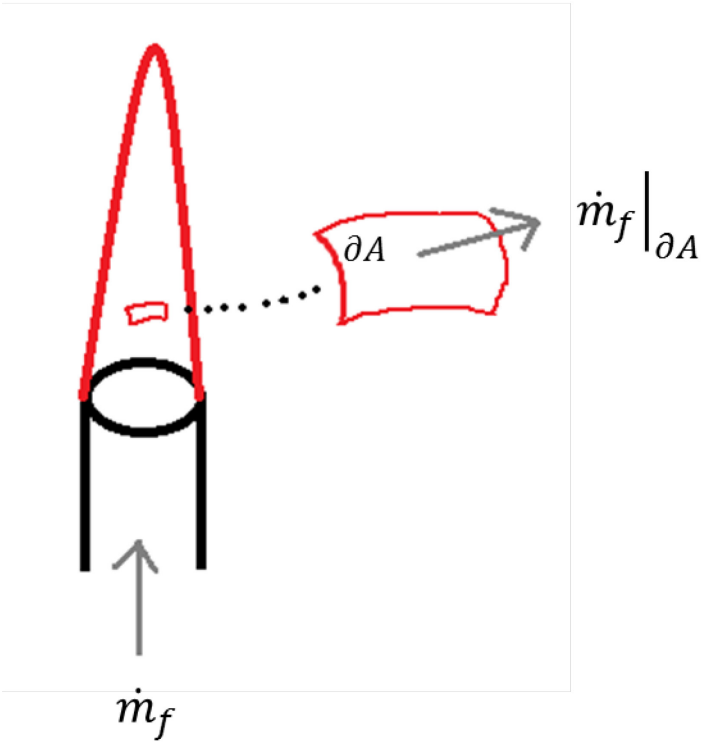

Figure 2-8: Laminar Jet flame

The ρ of the gas leaving the flame surface will be similar throughout the flame contour. As discussed previously, diffusion flames tend to rest along a Φ=1 contour with similar properties, such as flame speed (S) throughout. Therefore, with both ρ and S being similar at every point that fuel passes through the flame front,

$$\dot{m}_f = \sum_{\partial A} (\rho S \cdot \delta A)|_{\delta A} \sim \rho S A_{total}$$

$\dot{m}_f$ is proportional to the total flame area (A_{total}). The turbulent jet flame can only compensate for the extra fuel by increasing its total surface area. It does so by wrinkling. Within the turbulent regimes, eddies stretch the diffusion flame causing surface area growth and diffusion flame burn rates are therefore driven largely by flame-flow interactions and topological phenomenon.

In the “bending” example the flame maintains height throughout the turbulent regime because mixing intensity scales with the flow velocity. Turbulence stretches the front, increasing the surface area and enhancing the diffusive flux of fuel and oxidizer into the flame.

Figure 2-9 below shows the same diffusion jet flame that has now become turbulent. Notice that the wrinkled front has a much longer perimeter than would a laminar front of equal area. The local flame surface area per volume, commonly referred to as surface area density (Σ) is larger for the turbulent flame than it was for the laminar flame.

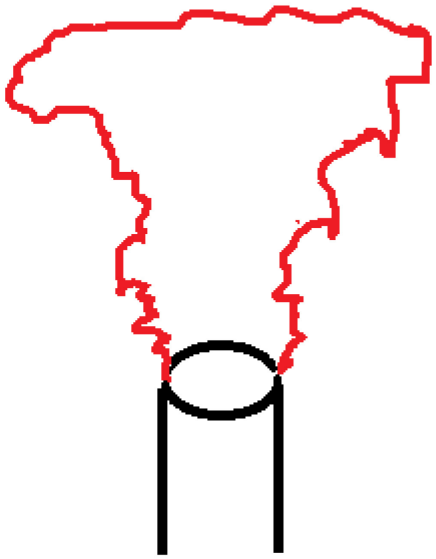

Figure 2-9: Turbulent Jet Flame

As previously mentions, diffusion flames wrinkled due to both natural instabilities and turbulent flow/flame interaction; the combination of which is highly complex. The jet flame geometry presented here is of rather simple geometry in comparison to those found in real combustion devices. The richness of diffusion flame topology can be observed in everyday life (such as pulsating log flame in a fireplace) or in engineered devices, such as engines.

If more is desired on the topic of non-premixed flame wrinkling please refer to references [67, 68] or on non-premixed flames in general refer to any of the following textbooks [26, 65, 66, 69, 70]. Many of the same concepts just presented with regards to diffusion, mixing, surface area generation and turbulent flow-to-flame interactions are relevant for premixed and partially-premixed flames alike.

2.2.2 Premixed Flames

Flames can occur in fuel/oxidizer mixtures of a wide range of mixed-ness. In the previous section the one extreme of completely non-premixed flames was discussed. This section will focus on just the opposite, flames where the fuel and oxidizer are completely mixed prior to combustion. In-between lies a partially premixed regime of mixed-ness, which will be discussed later. Throughout this document the term “premixed flames” will be used exclusively for flames occurring in a completely homogeneous fuel/oxidizer mixture. Such mixtures are by definition free of unburned reactant concentration gradients.

Premixed flames are utilized in conventional SI engines. There, fuel and oxidizer are typically fully premixed to $\Phi = 1$ prior to being ignited. The popularity of conventional SI engines has motivated a few decades of premixed engine combustion studies. Premixed flames are also used in Bunsen burners. Beyond these two examples it becomes difficult to identify premixed flame applications as they are uncommon.

For a premixed flame to occur, reactants must be first mixed and then ignited. Following ignition, a flame typically propagates through the mixture until the charge is consumed or the flame is quenched. Premixed combustion events tend to occur quickly and violently. Usually flames propagate at sub-sonic speeds (deflagration), but sometimes they can transition into a detonation wave which propagates at super-sonic speeds. Stellar explosions are a rare and awe inspiring example of such a naturally occurring premixed detonation. Fortunately, no detonations of that sort occurred in the experiments performed in this study.

Premixed flames are free of unburned gas Φ concentration gradients and are therefore less sensitive to the fuel/oxidizer mixing processes. Recall that fuel/oxidizer mixing processes were rate-limiting in diffusion flames. Therefore, the physics which limit burn rate in a premixed flame differ from those of a diffusion flame. Based upon common chemical engineering terminology, premixed flames are usually labeled as “kinetically limited”. Such a label insinuates that reaction rate is limited by reactivity and not mixing processes. As it is true that premixed flames are insensitive to reactant mixing processes, they are sensitive to turbulent stretch and their stability may depend upon diffusive effects. The rate for which a premixed flame propagates is largely controlled by a combination of the flames aero-thermo-diffusively controlled structure and its topology.

The combustion community has struggled to fully understand premixed flame phenomenon because the flame physics are so closely and complexly coupled to turbulence which is itself is a field in discovery.

Laminar premixed flame structures are fairly well understood; largely because their physics can be understood in the absence of turbulence-flame interactions. Fortunately, some laminar flames theory remains applicable to turbulent flames. Therefore, laminar premixed flame theory is foundational in turbulent flame theory and will be discussed. The importance of flame topology and wrinkling will be emphasized throughout this section as it relates directly to the research performed. Some common modeling techniques for premixed flames will also be discussed with an emphasis on engine applications.

2.2.2.1 Un-stretched Laminar Premixed Flames

Premixed flames consume fuel/oxidizer through the process of flame propagation. An outwardly expanding premixed flame is shown in Figure 2-10. After being centrally ignited, the flame propagates outwards towards the unburned portion of the charge. Eventually the whole charge will be consumed and the flame will extinguish.

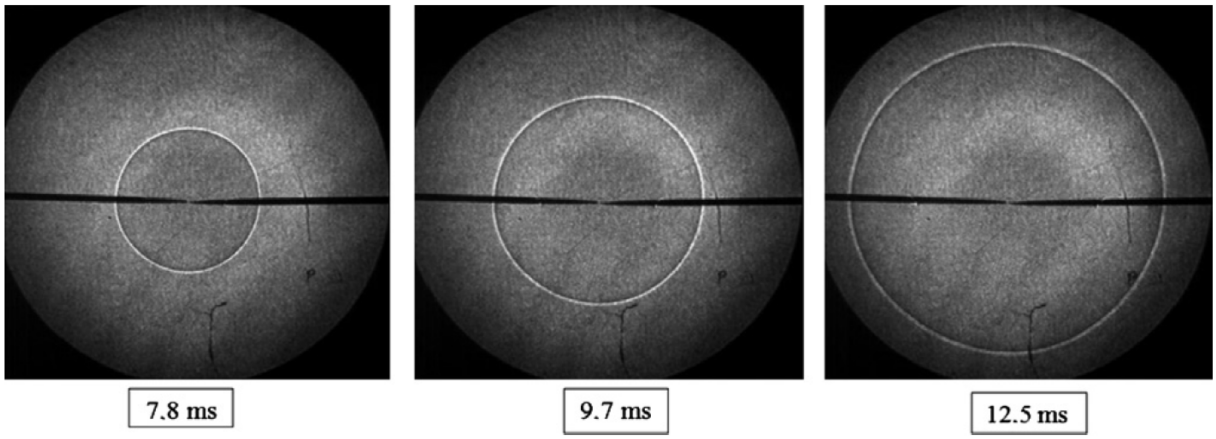

Figure 2-10: Laminar flame propagating spherically through a premixed iso-octane/butane/air charge. Shadowgraphy images provided by Guillaume et al. [71].

Notice that the flame propagates normal to its own surface and that its contour is smooth, these two properties are characteristic of laminar flames.

Some of the earliest combustion theories were capable of qualitatively capturing the key features of premixed flames. Zel'dovich et al. [72] presented an asymptotic analysis titled "A theory of thermal propagation of a flame" in 1938. In this analytic study combustion was assumed to occur as a single step, irreversible reaction. Also, the unburned reactants Lewis (Le) number was assumed unity and thermal properties (C_p) were considered constant. The Le number is defined as the ratio of thermal to mass diffusivity (of limiting reactant) as follows,

$$Le = \frac{thermal\ diffusivity}{mass\ diffusivity\ of\ limiting\ reactant} = \frac{\alpha}{D_u}$$

Zel'dovichs analysis suggested that premixed flames exhibit a two-part flame structure. Assuming that the chemical activation energy of the reactive mixture is large (Activation Energy Asymptotic theory), then reactions are limited to a thin region of the flame called the "reaction zone". This region is preceded by a thicker non-reactive "preheat zone", where heat from reaction prepares the incoming mixture for combustion.

Through a combination of the continuity and Navier-Stokes equations the structure and velocity of an unstrained laminar premixed flame can be solved. The results of such an analysis are demonstrated in Figure 2-11 below by Lipatnikov [60]. A complete summary of the analysis techniques and assumptions in the AEA analysis can also be found in the same reference.

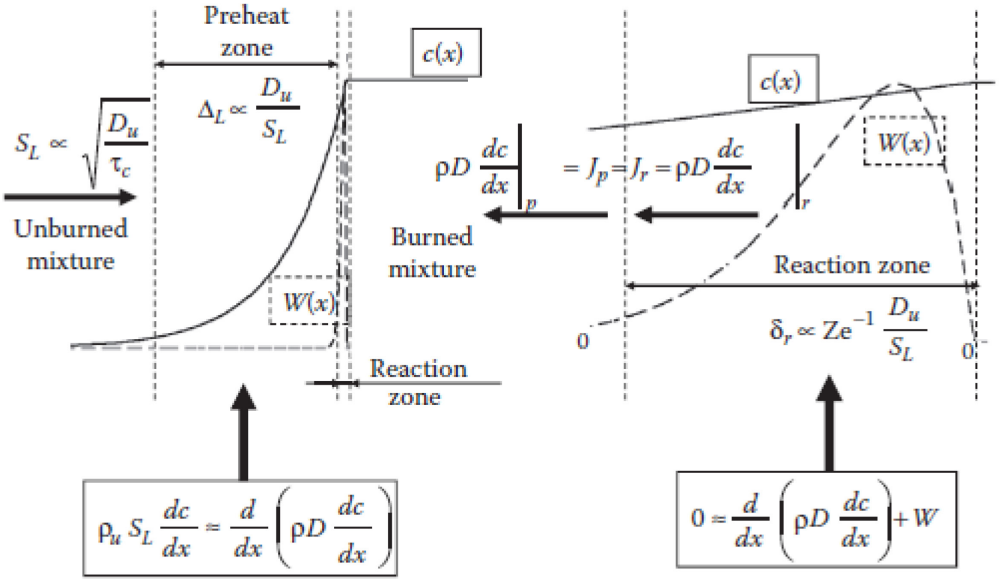

Figure 2-11: A summary of AEA theory by Lipatnikov [60]

c = temperature progress variable (unity in burned gas, zero in unburned gas)
S_L = laminar flame speed
W = reaction rate
δ_r = reaction zone thickness
δ_p = preheat zone thickness
$\Delta_L = \delta_f$ laminar flame thickness (reaction zone neglected as $\delta_p >> \delta_r$)
Θ = chemical activation temperature
Ze = Zel'dovich number = $\Theta(T_b-T_u)$
J = mass flux
τ_c= chemical reaction time scale = $\frac{1}{2\int_0^1 \frac{W}{\rho_u} dc}$

Notice that δ_r decreases as Ze increases. Therefore the "thin reaction zone" assumption becomes more reasonable at high Θ. Total flame thickness (Δ_L in Figure 2-11 which will be referred to as δ_f) decreases with flame speed and scales as,

$$\delta_f \propto \sqrt{D_u \tau_c}$$

Therefore, flames with high molecular diffusivity or slow chemical reactions are thick. The appearance of mass diffusivity in the flame thickness proportionality seems counterintuitive being that the reaction is kinetically limited; however, remember that at uniform Le number $D_u = \alpha$. The same proportionality may be written as $\delta_f \propto \sqrt{\alpha \tau_c}$. Higher thermal diffusivity causes a lengthier preheat zone. Although the AEA model is based upon a highly simplified analysis, the general results agree qualitatively well with experiments.

In the reaction zone of real flames hundreds to thousands of reactions occur. The thickness of such a zone is not as negligibly thin as the AEA model may suggest; it's typical for $\delta_r \approx 0.1\delta_f$. The Lewis number of reactants is also not generally unity.

It is becoming less common for laminar premixed flame structure and speed to be evaluated in an analytical manner and more common for computational techniques to be employed. For example, commercial programs such as CHEMKIN-PRO [73] can readily solve the continuity and Navier-Stokes equations along with detailed chemical kinetics to provide good estimates of laminar flame structures and speeds while employing minimal assumptions.

In order for such a solver to evaluate detailed chemistry, the chemical kinetic equations must be recognized. There are too many reactions occurring in a flame for a simple global reaction rate equation to be defined, at least for any realistic fuel. Therefore, the chemical species concentrations, including radicals must be tracked throughout the flame considering the effect all elementary reactions.

An elementary reaction may be generically described in the form,

$$aA + bB \leftrightarrow cC + dD$$

Where A, B, C, D = chemical species
a, b, c, d = stoichiometric coefficients

Reaction rate can then be described by the Arrhenius equation,

$$\frac{dC_A}{dt} = A(-e^{\frac{-\Theta_{AB}}{T}} C_A^a C_B^b + e^{\frac{-\Theta_{CD}}{T}} C_C^c C_D^d)$$

Where A = collisional frequency factor
Θ_{ij}= chemical activation temperature of reaction between species i and j

In the Arrhenius rate equation, ($AC_I^i C_j^j$) quantifies the rate for which molecular collisions occur and the ($e^{\frac{-\Theta_{ij}}{T}}$) the probability that such a collision results in reaction. The number of reactants participating in an elementary reaction is not limited; however almost all reactions occur in a unimolecular or bimolecular manner as the probability of three or more molecules colliding is very small.

For iso-octane, there are about 3600 reactions and 860 species that participate in combustion [74]. To model the structure of such a flame considering detailed chemistry, a mechanism must be specified that includes all relevant reactions and species. The constants Θ_{ij} and A must be known for every reaction over the modeled range of conditions. Luckily, not all of the reactions within a flame front are important; some reactions contribute negligibly towards reactivity. Therefore, it is common for mechanisms to be reduced so that they only include the most important reactions and species. For example, the iso-octane mechanism most commonly used in CHEMKIN-PRO contains 2820 reactions and 463 species [75]; 800 reactions and 400 species were neglected as their contribution was deemed minimal. Some researchers have further reduced the iso-octane mechanisms to 69 reactions and 38 species [76], but modeling accuracy is compromised at this level of reduction. Generally, when possible (computationally feasible and practically appropriate) the less reduced mechanisms are best used for premixed flame calculations.

Chemical mechanisms are typically validated through comparison with experiments. Confidence is gained in such mechanisms when they demonstrate the ability to accurately predict ignition delay times and flame speeds. A variety of experimental hardware configurations can be used to provide experimental data for comparison. Shock tubes, rapid

compression machines and flow reactors can all be used to measure ignition delay time and flame speed. Such comparisons between experiment and model do provide a good validation of the models global behavior. However, they do not provide a measure individual elementary reaction rate constants or flame structure for evaluation of the mechanism/model details. Therefore, reaction constants such as Θ and A often must be determined through chemical thermodynamics or empirical trial/error.

Chemical reaction pathways differ based upon the fuel used. Generally, hydrocarbon fuels start as large chains and are broken down into smaller chains through combustion. Larger fuels (by molecular count) require lengthier chemical mechanisms. However, once partially oxidized, larger hydrocarbon molecules tend to follow the same pathways as do smaller hydrocarbon fuels. Therefore, large fuel chemical kinetic mechanisms can be built upon the foundation of smaller fuels. For example, the mechanism for iso-octane (C_8H_{18}) can be developed by starting with the established mechanism for butane (C_4H_{10}), and adding to it the reactions that occur due to C_5 to C_8 sized species.

Commercial fuels that are used in vehicles are blends containing hundreds of species. The kinetics of such a "soup like" mixture is complex. Therefore, developing accurate mechanisms for real fuels is a challenge. The combustion community has chosen to focus its effort upon developing a few high fidelity mechanisms for "surrogate" fuels, such as iso-octane and n-heptane, and using the surrogates to approximate real fuels. However, it remains challenging to reproduce real fuels using surrogate fuel blends, as inevitably, there will be physical differences between the two.

Recognizing the complexity of chemical kinetics within flames, it is impressive that flame structures and speeds can be actually be modeled through programs such as CHEMKIN-PRO quite accurately. For example, Figure 2-12 below shows a comparison between the predicted ignition delay time calculated from a mechanism developed by Curran et al. [74] and experimental shock tube data provided by Fieweger et al. [77] at Φ=1.

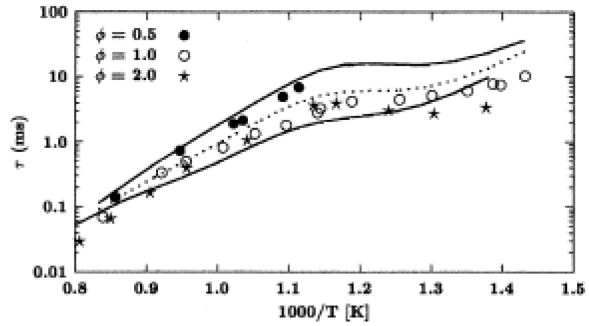

Figure 2-12: Iso-octane ignition delay time comparison of experiment (dotted line) and chemical kinetics model calculations of Curran et al. [74] at Φ=1.

This shows, at least qualitatively, that such kinetics models are capable of capturing the chemical reactivity of iso-octane mixtures. Davis et al. [78] used Curran's kinetic mechanism discussed above to calculate and compare iso-octane flame speeds over a range of equivalence ratio's. These results are shown below in Figure 2-13.

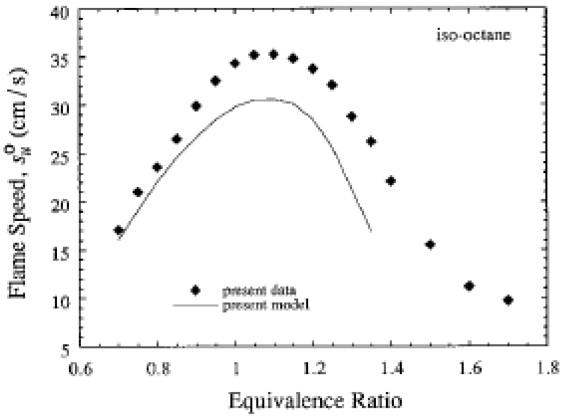

Figure 2-13: Iso-octane flame speed comparison between experiment (diamonds) and a chemical kinetic mechanism by Curran et al. [74]. Figure and experimental data by Davis et al. [78].

The Curran mechanism and PREMIX[9] code used to calculate the flame speeds in Figure 2-13 is state of the art. Notice that the measured flame speeds differ from calculated flame speeds by as much as 20%. Similar errors have also been reported between different flame speed measurement techniques [79], suggesting that the uncertainty in the experimentally measured flame speed is on the same order. This iso-octane mechanism validation has been used as an

[9] Developed by Sandia National Laboratories

example, but such levels of uncertainty are common across the field. It remains a challenge to computationally quantify laminar flame speeds and ignition delays much more accurately.

Chemical kinetics aside, recognize how laminar flame speed changes with Φ for iso-octane in Figure 2-13. S_L peaks just slightly rich of stoichiometric, as is common. Most flames propagate their fastest at near Φ=1, independent of fuel composition. Further, the trend of adiabatic flame temperature vs. Φ is shown in Figure 2-14 for a few different fuels.

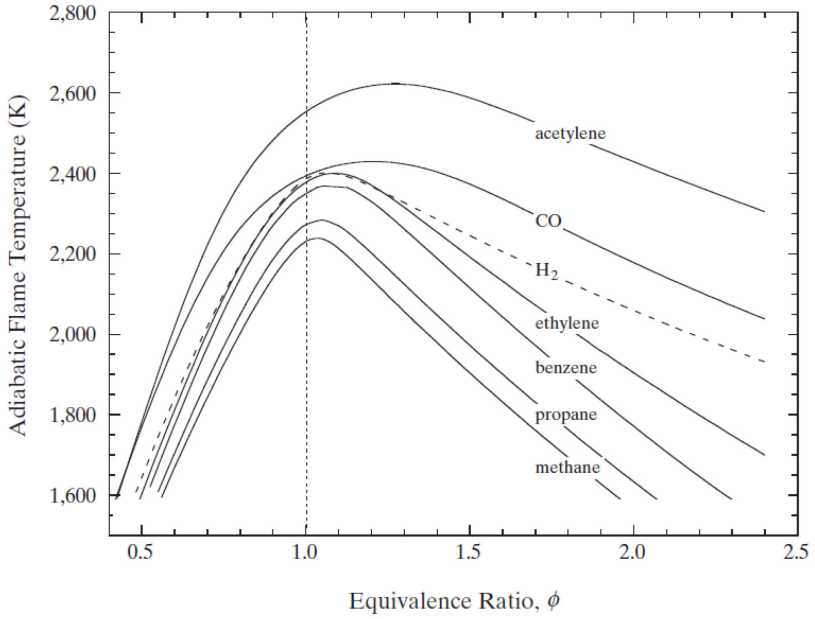

Figure 2-14: Adiabatic flame temperature vs Φ. Figure by Law [26].

Flame temperature, like speed, peaks close to Φ=1. In the previous AEA analysis it was shown that $S_L \propto \sqrt{\frac{D_u}{\tau_c}}$ and τ_c decreases with increasing reactivity. Through the Arrhenius equation $W \propto e^T$, so reactivity, and subsequently flame speed are both highly sensitive to temperature. Near stoichiometric flames propagate quickly largely because their flame temperature is high.

Fast flames tend to resist extinction and tend to be robust in application. Highly lean or rich flames burn slowly and have more of a tendency to extinguish than do near stoichiometric flames, particularly when subject to aerodynamic stretch.

Laminar flame speed computations such as those performed by the PREMIX code provide flame front species and temperature profiles. The detailed chemical structure of laminar premixed flames can be examined in detail. Such an analysis will be excluded for brevity. Radicals such as OH, H, CH_2O and others participate in reactions throughout the front in a complex manner. Reactivity is mostly confined to a narrow zone which is similar to the thin reaction zone concept utilized by the AEA model. However, the transition between the pre-heat and reaction zone is not discrete and defining a bordering location requires the definition of an arbitrary threshold. Particularly for some fuels which undergo multiple stages of ignition. Such fuels exhibit significant reactivity at lower temperature (~700K), which by most asymptotic type analysis is considered well into the preheat zone. Therefore, the two-zone model is only to be used conceptually. Flame zone measurement (such as δ_r) must be considered with ambiguous definition and their respective uncertainty.

Qualitatively, analytical analysis such as that originally developed by Zel'dovich provides a useful conceptual model for how laminar premixed flames structure and propagate speed. Qualitatively, computational analysis is capable of providing much better estimates of important properties such as flame speed and ignition delay for use in engineering application. Even with the state of the art calculations, uncertainty in any such estimates still remains uncomfortably high for many engine design applications.

2.2.2.2 Stretched Laminar Premixed Flames

Flames are affected by aerodynamic stretch. It generally leads to flame surface area growth. It is also capable of altering flame front internal structure and subsequently, stretch can affect a flames temperature profile and propagation speed. High amounts of stretch can extinguish a flame. Stretch is caused by a combination of aerodynamic strain and curvature, which can be recognized in the following relation,

$$\dot{s} = \frac{1}{A}\frac{dA}{dt}$$

Where $\dot{s}$ = stretch rate. Hence, flame stretch and surface area growth are directly related to each other. The local stretch rate of a flame front can be further broken up into its respective components [60],

$$\dot{s} = a_t + Sa_c$$

Where a_t= local strain rate
a_c= local stretch due to curvature
S = speed of self-propagation

The strain component of stretch is caused by fluid interaction with the front and is quantified as the tangential divergence of the velocity vector,

$$a_t = \nabla_t \cdot \vec{v}$$

Curvature induced stretch is found to be [60],

$$a_c = \nabla \cdot \vec{n} = \frac{1}{R_1} + \frac{1}{R_2}$$

Where $\vec{n}$ = vector normal to flame front
R_1 and R_2 = principal radii of surface

Because high levels of flame stretch lead to extinction, flames are limited in their ability to curve sharply or survive in strong flows. Stretch extinction is thought to occurs due to either flame front cooling or reduced reactant residence time [80].

Curvature induced stress (a_c) arises for a number of reasons, one of which being that flames must propagate in a direction for which air/fuel reside, which often necessitates curvature. For

example, a flame that is ignited in the center of a premixed fuel/oxidizer charge must expand outwardly. It does so in a spherical manner and as it grows in size it will experience a decreasing a_c (due to increasing R_1 and R_2). Obviously such curvature will increase flame surface area through positive $\dot{s}$, however, the effect of $\dot{s}$ on internal flame structure and local propagation speed is not self-evident.

The AEA analysis presented earlier is ignorant of stretch because it was performed on a one-dimensional flame. In three-dimensions, curvature affects heat and mass transfer processes in a manner for which one-dimensional models cannot capture. Particularly when considering differential diffusion effects (Le≠1), as will be discussed.

Flame curvature is defined to be positive when convex and negative when concave in the direction of travel. This has been illustrated in Figure 2-15 below.

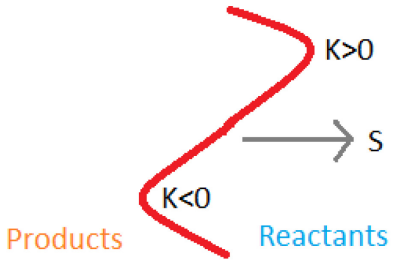

Figure 2-15: Curvature of a flame front

Diffusive process are more effective on positively curved surfaces (κ>0) than flat or negatively curved surfaces ($\kappa \leq 0$). When $\kappa \neq 0$ diffusive transfer occurs in both the normal and tangential directions which promotes transfer for κ>0 and hinders transfer for κ<0.
Flame fronts are hindered by increased heat diffusivity (heat losses) but are aided by increased mass diffusivity rates (fuel flow rate), as the total energy input and outputs are quantified respectably. Flame front curvature can increase (κ>0) or decrease (κ<0) both rates simultaneously; but not one individually.

If Le<1 and (κ>0) then diffusive transfer of the limiting reactant (burn rate) will increase into the front relative to heat transfer losses out due to curvature and above adiabatic flame temperatures will result. If Le>1 and (κ<0) then just the opposite will occur and the flame front will cool. The flame speed will increase or decrease with flame temperature accordingly. Le = 1 flames are relatively insensitive to curvature. The effect of Lewis number on flame speed is summarized in Table 2-1 below.

Table 2-1: Speed relative to unstrained laminar flame speed (S_L) for a curved flame front

	$\kappa < 0$	$\kappa = 0$	$\kappa > 0$
Le < 1	$S < S_L$	$S = S_L$	$S > S_L$
Le = 1	$S = S_L$	$S = S_L$	$S = S_L$
Le > 1	$S > S_L$	$S = S_L$	$S < S_L$

For any given mixture of fixed Lewis non-unity number, flame speed will be inversely affected depending on the direction of curvature. Because flames propagate normal to themselves, positive curvature fronts propagate divergently whereas negative fronts converge. Convergent regions of a flame front (κ < 0) tend to close up due to propagation. Outwardly propagating flames are positively curved on average, whereas inwardly propagating flames are negatively curved. Therefore, Le<1 flames tend to burn fast in expansion and Le>1 flames burn fast in contraction.

If Le < 1 then the fastest local flame regions are found at the most positive and the slowest in the most negative regions of curvature. Concave regions of the front (κ < 0) will tend to close slowly. Convex regions (κ > 0) will accelerate with the flame tip propagating the fastest. Therefore, Le < 1 flames are relatively unstable and slow to reduce flame front curvature if perturbed. More will be discussed on flame stability later.

Although the qualitative description summarized in Table 2-1 is generally correct the real effects of stretch and curvature on laminar flame wrinkling is more complex and cannot be explained through Le number alone.

The effect of curvature due to Lewis number is often termed “differential diffusion” [26]. Similarly, differences in molecular diffusivity between the fuel and oxidizer can also affect flame structure and speed is termed “preferential diffusion”. If the limiting reactant preferentially diffuses into the front ($D_{\substack{limiting \\ reactant}} > D_{\substack{excess \\ reactant}}$) then super adiabatic flame temperatures and high flame speeds will occur. If ($D_{\substack{limiting \\ reactant}} < D_{\substack{excess \\ reactant}}$) then the opposite trend is observed. Because preferential and differential diffusion occur simultaneously it is difficult to isolate the effects of either effect individually in a Le≠1, ($D_{\substack{limiting \\ reactant}} \neq D_{\substack{excess \\ reactant}}$) curved flames; as is generally the case.

There have been numerous studies that have shown that stretched laminar flame speed cannot accurately be quantified in terms of just S_L, κ, a_t and Le. One example being a DNS simulation of a methane flame by Echekki et al. [81] for which it was found that curvature effects highly diffusive intermediate species, such as H and H_2 in a manner not described by Lewis number descriptions alone.

Flaws in the very definition of Lewis number have been recognized. For example, Haq et al. [82] published a review paper that noted that the Lewis number is ambiguous at Φ=1 where there is no deficient reactant. The step change that occurs in Le number value in the transition from lean to rich mixtures was also discussed to be unphysical. Therefore, Lewis number remains as a useful and commonly used combustion mixture metric, but is not expected to be present in truly fundamental derivations.

As early as 1964 Markstein observed a linear relation between laminar flame stretch and speed [83]. Since then, a great number of analytical, computational and experimental studies have

observed the same relationship [84]. Markstein's suggested the following relationship between local flame velocity, unperturbed laminar flame velocity and stretch,

$$\frac{S}{S_L} = 1 - \mathcal{L}\tau_c\dot{s} = 1 - \mathcal{L} \cdot Ka$$

Where $\mathcal{L}$ = Markstein length
Ka = Karlovitz number

Markstein lengths can be experimentally measured. Often, different Markstein lengths are defined for different flame speed definitions (flame velocity, consumption rate, etc.). Here, $\mathcal{L}$ is defined in terms of velocity. One method for measuring $\mathcal{L}$ is to monitor the radial evolution of a spherically expanding laminar flame in a quiescent chamber. For such a configuration both a_c and a_t can be estimated based on the simple spherical geometry. $\mathcal{L}S_L$ can then be found as the slope of S vs. $\tau_c\dot{s}$. An example of such a procedure for iso-octane and n-heptane can be found in ref [85].

Since $\mathcal{L}$ is experimentally determined, all stretched flame physics should be captured in the linear Markstein relationship for as long as the relation remains valid. $\mathcal{L}$ is a mixture property and is usually assumed to be constant for a mixture at a given thermodynamic state.

Theoretical derivations that support the linear S-$\mathcal{L}$ relationship are based upon weakly stretched flames (Ka <<1) [60]. Most measurements that support the theory are also based under weakly stretched conditions [86]. Therefore, the linear relationship is only thought to hold true under weakly stretched flames. Some researchers have recognized that the linear S-$\mathcal{L}$ relationship tends to over predict flame speeds and have suggested the following corrected relationship be used [86, 87],

$$\left(\frac{S}{S_L}\right)^2 \ln\left(\frac{S}{S_L}\right)^2 = -2\frac{\mathcal{L}\dot{s}}{S_L}$$

All empirical S-$\mathcal{L}$ relations, be them linear or non-linear, are questionable in accuracy. No simple S-$\mathcal{L}$ relation is known to fully capture all of the physics involved in the stretching of laminar flames. However, such empirical relations have proven their worth in practice.

Perhaps the most accurate way to characterize the effect of stretch on premixed laminar flames is direct numerical simulation. One such example by Echekki was previously discussed [81]. However, DNS simulations are computationally expensive and rarely performed. They can only be performed at relatively low turbulence intensities.

Changes in local flame velocity due to stretch are typically < 20% S_L in application. In contrast to topological effects such as turbulent flame surface area growth which may increase flame velocities by an order of magnitude, such local stretch induced changes in velocity are of second order importance. However, stretch effects on local flame velocity influences topology through hydrodynamic stability, which may promote wrinkling and lead to physical flame acceleration effect of flame stretch of first order importance. Therefore, flame stretch physics is a very important branch of combustion research.

2.2.2.3 Turbulent Premixed Flames

Premixed flames are almost always turbulent. Even within a perfectly quiescent environment laminar flames develop wrinkles due to flame front instabilities. Eventually such laminar flames transition into turbulent flames. In most applications, such as engines, turbulence is desirable as it tends to increase the burn rate.

Turbulent premixed flames are classified as reaction (or kinetically) limited based upon the flames Damköhler number (Da >> 1). Where Da is conventionally defined by chemical engineers as,

$$Da = Damkohler\ Number = \frac{reaction\ rate}{mass\ transfer\ rate}$$

In the turbulent reacting environment it is common to define the Da number in terms of characteristic turbulent mixing and reaction times,

$$Da_{\substack{turb \\ rxn}} = \frac{\tau_t}{\tau_c}$$

Where τ_t = turbulent scale (commonly the flows integral scale is used). The Da number represents the ratio of reaction rate to mixing rate. In the turbulent environment the mixing timescale is associated with the properties of the turbulence. At Da >> 1 chemical reactions are fast relative to mixing. Therefore it is reasonable to assume that reaction occurs quickly, within a thin reaction zone a high Da number. Most practical combustion devices operate within the high Da regimes where it is appropriate to view the flame as being a thin contour.

Under highly turbulent conditions it is possible for mixing to be enhanced to high rates so that ($Da \propto 1$). Under such conditions thin flame theory (flamelet concept) loses applicability and thick flame theory is required. Such flames may lack a dominant rate limiting processes which increases the challenge in describing their physics simply. This document will focus mainly on thin flame (flamelet) theory.

Regime diagrams are commonly used to classify turbulent premixed flames. Borghi [88] was one of the first to present such a diagram. An updated version of his diagram by Peters [65] is shown in Figure 2-16 below,

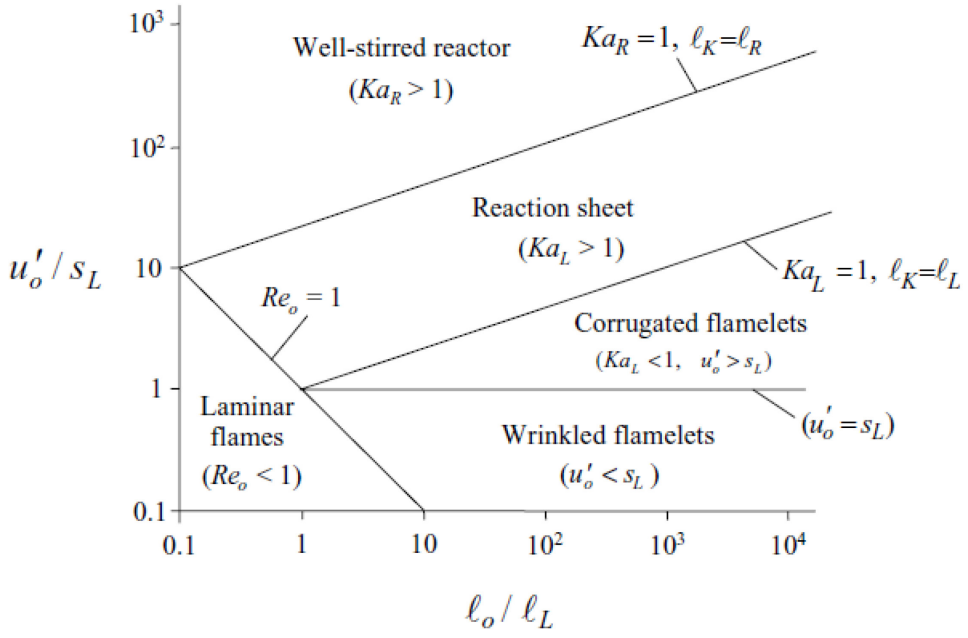

Figure 2-16: Regime diagram (also known as Borghi diagram) for premixed turbulent combustion. This figure was provided by Peters [65].

Where u'_0 = rms velocity

Re_o = Reynolds number

Ka_L = Karlovitz number

Ka_R = reaction-zone Karlovitz number

ℓ_K= Kolmogorov scale

ℓ_L= flame thickness

ℓ_R= reaction zone thickness

The y-axis is labeled as normalized turbulence intensity and the x-axis as the ratio of integral length scale to flame thickness. The Karlovitz number has been previously introduced as Ka = $\tau_c \dot{s}$. However, it may be introduced more formally as a ratio of turbulence to flame scales,

$$Ka_L = (\frac{\ell_L}{\ell_K})^2 = \frac{\tau_L}{\tau_K}$$

$$Ka_R = (\frac{\ell_R}{\ell_K})^2 = \frac{\tau_R}{\tau_K} = \frac{Ka_L}{Ze^2}$$

Physically, the Ka number represents the ratio of a flame thickness (reaction or preheat zone) to the Kolmogorov length scale. The Komogorov length scale is characteristic of the smallest eddy sustained by the flow[10].

The Borghi diagram suggests the following occurs to a laminar flame as turbulence intensity is increased. At modest turbulence intensities the flame wrinkles. As turbulence is further increased the flame corrugates but still retains its thin, laminar like (flamelet) structure. A further increase in turbulence causes the flame to become a reaction sheet; whereas the flame maintains a sheet like figure but its internal structure becomes mixed and thickened by turbulent eddies. As turbulence intensity is further increased the flame becomes "well stirred", or practically, extinct.

Throughout all of the turbulent regimes eddies interact with the flame front and the manner/degree for which the flame is effected by eddies varies based upon the properties of the flame and the flow. Large scale eddies ($\ell_{Eddy} \gg \ell_L$) are capable of distorting flame fronts, whereas small scale eddies ($\ell_{Eddy} < \ell_L$) tend to mix the internal structure of flame.

The "Laminar flame" regime lies in the lower left of the diagram where the Re < 1. The properties of laminar flames have been discussed in detail previously and will not be revisited. In the lower right of the Borghi diagram the "Wrinkled flamelet" region is characterized by (Re > 1, u' < S_L). Under such mild turbulent conditions premixed flames wrinkle but remain "flamelet like". Because the length scales of the flow (size of eddies) is large relative to the flames thickness (Ka << 1), the flow is able to wrinkle, but not mix the preheat or reaction zones of the front.

The "corrugated flamelet" regime exists directly above the wrinkled regime on the Borghi diagram. In this regime turbulent fluctuations are larger in magnitude than flame velocities (u' >

[10] Eddies smaller than the Komogorov scale cannot exist due to viscous dissipation.

S_L) and flow folds and wrinkles the front more intensely. The flame retains the "flamelet like" structure as turbulent eddies remain larger in scale than the flame itself.

When turbulence is increased further beyond the corrugated regime into the "reaction sheet" regime, the structure of the flame begins to become mixed due to small eddy intrusion since $\ell_K < \ell_L$. Peters provides Figure 2-17 to demonstrate how such eddies might interact with a flame front,

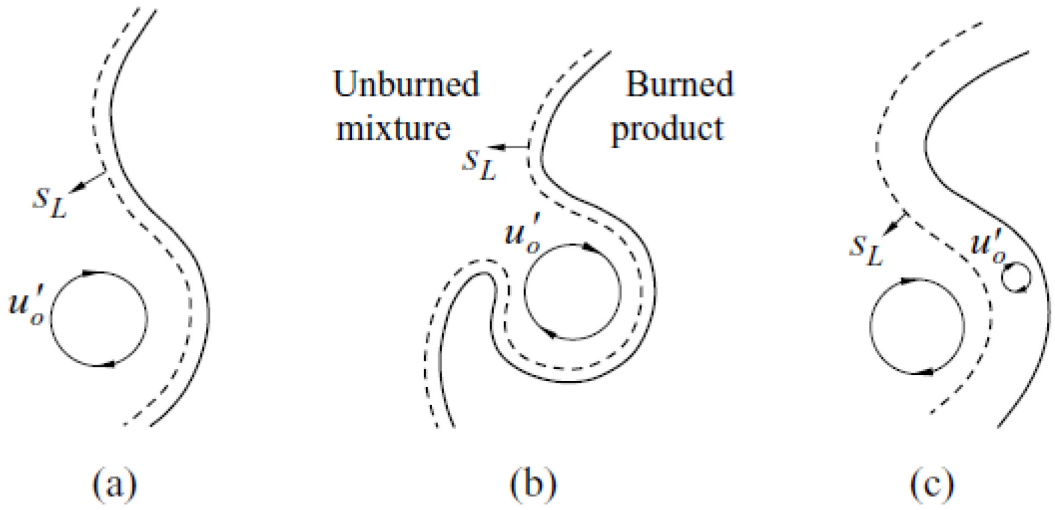

Figure 2-17: (a) Weak flame-vortex interaction ($u' < S_L$) resulting in a wrinkled flamelet. (b) Strong flame-vortex interaction ($u' > S_L$) resulting in a corrugated flamelet (c) Strong flame-vortex interaction with the smaller eddies penetrating into and broadening the preheat zone of the flame. Figure provided by Peters [65]

A weak eddy interacts with a flame front in (a) causing it to wrinkle. A stronger eddy corrugates the front in (b). In (c) both a large and small eddy interact with the front. The larger eddy perturbs the front but the smaller eddy is able to penetrate the flame. In penetrating the flame, the small eddy in (c) is able to mix and alter the flame structure.

In (a) and (b), the thin flame front is stretched but not mixed. It is therefore reasonable to assume that the flame structure is locally that of a stretched laminar flame (flamelet). Therefore, for (a) and (b) S_L can be determined anywhere along the front based upon the

stretched laminar flame theory discussed in the previous section. In (c) it is not reasonable to assume the flame structure is “laminar flamelet like”, as the small eddy that penetrates the front alters the heat and species distribution throughout the front. Determination of S_L in (c) is challenging as laminar flame theory is not applicable.

If a small eddy is able to enter the front, as shown in (c), it might only mix the preheat zone ($\ell_{Eddy} < \ell_L$ and $\ell_{Eddy} > \ell_R$ So, Ka_L>1 but Ka_R<1). Or, if the eddy is small enough ($\ell_{Eddy} < \ell_R$ So, Ka_R>1) it can penetrate both the preheat and reaction zones; altering the complete inner structure of the flame. The former occurs in the “reaction sheet” and the latter in the “well mixed” regimes. When such fine scale eddies penetrate the reaction zone extinction is probable to occur.

Although the general trends shown in the Borghi diagram are correct, the location of borders between regimes is not as exact or discrete. For example, if the turbulence intensity of a corrugated flame is increased the Borghi diagram suggests that the flame will undergo a bimodal transition to a reaction sheet when Ka_L=1. Such transitions never occur so rapidly or exactly. A flame near Ka_L=1 may exhibit properties associated with both the corrugated and reaction sheet regimes. After all, there is no reason why an eddy slightly larger than the flame ($\ell_{Eddy} = \ell_L + d\ell$) would not mix the inner structure of the flame almost as effectively as an equal-scale eddy ($\ell_{Eddy} = \ell_L$). Since there is such uncertainty surrounding the borders of the Borghi diagram (or other similar turbulent combustion regime diagrams), particularly between the reaction sheet and well stirred regimes, such diagram should only be used conceptually and qualitatively.

For an eddy on scale with the reaction zone ($\ell_{Eddy} \leq \ell_R$) to penetrate the reaction zone, it must first traverse the preheat zone. Often, such small eddies are dissipated by the hot preheat zone and never reach the reaction zone. Therefore, a flame may exist well above Ka_R>1 and still not be within the “well mixed” regime. Therefore, impractically high turbulence intensities are required in order to achieve “well mixed” flames.

Many researchers have shown that highly turbulent flames (Ka_L>1) can maintain laminar flame thicknesses despite being classified in the distributed (reaction sheet and well mixed) reaction regimes based on Karlovitz criterion. For example, Sheperd et al. [89] observed a turbulent premixed methane flame all the way up to Ka_L=17 and found no significant flame broadening. Therefore, it is likely that the "flamelet" concept is applicable at turbulent intensities higher than predicted by the Borghi diagram.

Accepting the "flamelet" viewpoint (which is usually accurate within engine regimes); flamelet fronts can be treated as wrinkled/ corrugated contours that propagate normal to themselves. The speed for which any region of the contour propagates at can be calculated based upon the stretched laminar flame speed estimation methods already discussed. The direction of local flame propagation is dictated by topology. Topological development is driven by a combination of flame-flow interaction and flame front instabilities. The stochastic nature of eddy-flame interactions tends to lead to stochastic topology.

Fundamentally, the physics of combustion are the same within all regimes which would suggest that there only need be a single description for all flames. However, such an exact description of premixed flames based solely on conserved quantities (mass, atoms, energy, momentum) and chemical kinetics is not achievable. Most of the governing equations of a premixed flame can be written down but not solved either analytically or numerically. For very thin, laminar like flamelets, chemical and transport physics can be treated separately which is very convenient in practice.

Due to the stochastic nature of flames flame properties are often quantified in a statistical manner. Flame contours may by superimposed onto each other [60] as is shown in Figure 2-18 below.

Figure 2-18: Superimposed contours of instantaneous flamelets. Provided by Fox and Weinberg [90]

The region traced out by the contours is commonly called a “flame brush”. Flame properties can be characterized across the flame brush. A global turbulent flame speed can be defined normal to the brush (S_T); as is shown in Figure 2-19 provided by Driscoll [91].

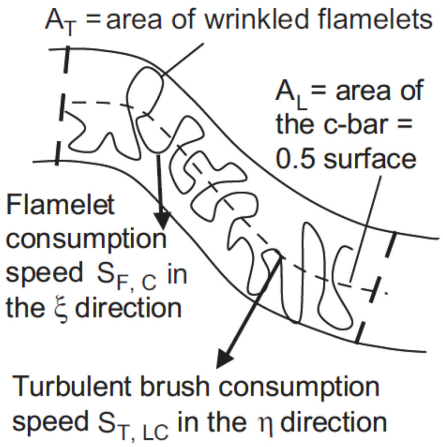

Figure 2-19: Schematic of the wrinkled flamelet. Provided by Driscoll [91]

In this figure a reactiveness (c) metric is defined as

$$c = \frac{T - T_R}{T_P - T_R}$$

Where c = 0.5 contour is commonly chosen to represent the flame contour location. The temperature distribution is discovered through many flame realizations. The probability that a flame exists anywhere within the brush can be quantified. Such a characterization is particularly useful in comparisons between models and experiment.

Locally, the flame propagates at a speed normal to itself. Globally, the flame tends to propagates at the turbulent flame speed (S_T), normal to the brush in the direction of the unburnt reactants.

Although the physics that drives turbulent flames is highly complex, many researches have tried to develop empirical turbulent flame speed relationships that may be used with practical ease. There have been a wide variety of such relationships developed in attempt to characterize (S_T) for various geometries. The simplest of which is [60],

$$S_t = S_L + Cu'$$

Where C = constant

Early combustion vessel studies by Abdel-Gayed and Bradley found a relationship of the form for spherically propagating flames [92],

$$\frac{S_t}{S_L} = C_1(Re_t)^{C_2}$$

Where C_1 and C_2 = constants and Re_t = turbulent Reynolds number.
Most proposed relationships for S_t are of the form $S_t = f(Re, Da)$ or $S_t = f(Pr, Da, u')$ or $S_t = f(Ka, Le)$. The exact formulations vary based upon the specific test conditions and geometries used for the models development. No empirical flame speed relationships have found wide scale applicability. However, many have found utility within the regimes and geometries for which the model was developed and validated.

Notice that all of the empirical relationships presented attempt to relate turbulent flow metrics (u', Re, Ka) to turbulent flame speed. Such relationships are unsuccessful at predicting flame speeds beyond the limited regime largely because flows and flames are highly geometry dependent. Interactions between flames and turbulence are more complex than can be described in a simple algebraic manner. Retroactive effects are known to be important in premixed flame topological development which suggests that time derivatives and a transport equation best be in a proper flame speed model.

Since flame phenomenon tends to be geometry dependent (at least on the macro-scales), many studies classify turbulent premixed flames based upon geometry. A few examples of common geometries being envelope, oblique, flat and spherical flames [91, 93]. However, there is nothing fundamental about flame geometry that should warrant its classification. Therefore, flame models best be free of geometric parameters.

2.2.2.4 Flame Surface Area Density

Within the flamelet regime the mean flame front reaction rate can be expressed as [94],

$$\langle w \rangle = \rho_u \Sigma S_L^o I_o$$

Where $\langle w \rangle$ = mean conversion rate of reactants per unit volume
S_L^o = un-streteched laminar burning velocity
I_o = stretch factor
Σ = flame surface density

This relationship is in the form of the continuity equation ($\dot{m} = \rho A V$). The I_o term is used to correct the local S_L^o for stretch. Σ quantifies local flame surface area per unit volume. For an infinitely thin flame, the local value of Σ is defined by [60],

$$\Sigma = |\nabla c|$$

For a flame of finite thickness the following definition is suggested by Pope [95]

$$\Sigma(c^*, \vec{x}, t) = \overline{|\nabla c|\delta(c - c^*)}$$

Σ can be experimentally measured across a flame brush and related to flame speed through [91],

$$\frac{S_T}{S_L^o} = I_o \int_{-\infty}^{\infty} \Sigma d\eta = I_o \Sigma_{max} \delta_t$$

Where η = direction normal to the flame brush
δ_t = flame brush thickness

Turbulent flame speed can also be related to laminar flame speed by the wrinkling factor through [96],

$$\frac{S_T}{S_L^o} = I_o \Xi$$

Where Ξ is the wrinkled-ness factor; a parameter which is commonly measured and discussed in this study.

Turbulent flame consumption rate (and subsequently velocity) scales with flame speed and surface area. Flame surface area is closely related to the degree of wrinkled-ness. For a given fuel/air mixture, $S_L^o I_o$ might vary on the order of 20% [97] due to turbulent stretching primarily from preferential and differential diffusion effects. Turbulence can increase Σ and Ξ by a factor of ten; mostly through wrinkling and corrugating the flame front. Hence, turbulence increases speed of a premixed flame primarily by wrinkling and increasing the surface area of the reactive front. Hence, this works focus on flame wrinkled-ness.

2.2.2.5 Premixed Flame Wrinkling and Corrugation

Premixed flames can wrinkle on their own due to natural instabilities or through interaction with turbulent eddies. Once induced, the magnitude of a flame front perturbation can either grow or shrink depending both on the both the response of the flame front and the flame fronts further interactions with local flow. The underlying physics that drives flame wrinkling, although not fully understood, will now be discussed.

2.2.2.5.1 Instability Induced Wrinkling

The hydrodynamic instability that is thought to play the largest role in wrinkling premixed flames has been named after two scientists, Darrieus and Landau (DL) [98, 99], who were some of the first to investigate the phenomenon. They performed a hydrodynamic flame analysis whereas the flame was considered to be an infinitely thin contour propagating at a constant local velocity always normal to itself. They concluded that all flames are unconditionally unstable to perturbations of all wavenumbers.

The reason for unconditional instability is illustrated in Figure 2-20 below by Law et al. [80].

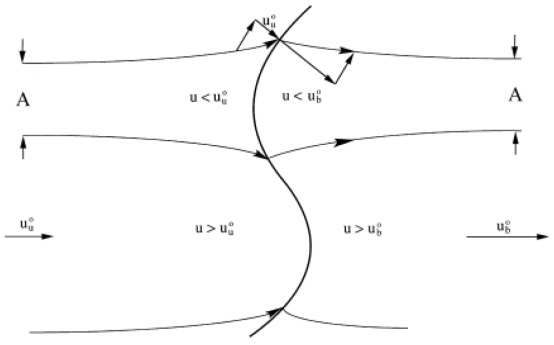

Figure 2-20: Schematic showing the mechanism of hydrodynamic cellular instability.(u = flow velocity, u_u° = unstretched laminar flame velocity, u_b°=burned gas velocity) Provided by Law et al. [80]

In convex ($\kappa > 0$) regions the incoming flow diverges and local flow velocity is low; therefore the flame velocity is high relative to the flow. In concave ($\kappa < 0$) regions local flow converges and flow velocity is high; therefore the flame velocity is low relative to the flow. This causes the concave regions of the flame to race ahead of the convex regions accentuating the perturbation.

The DL instability predicts a perturbation growth rate of [100],

$$\omega = S_L k\left(\frac{-\sigma + \sqrt{\sigma^3 + \sigma^2 - \sigma}}{\sigma + 1}\right)$$

Where ω = perturbation growth rate
k = transverse wave number
$\sigma = \frac{\rho_u}{\rho_b}$

This implies that small perturbations (large wave numbers) should grow much more rapidly than do large perturbations. The bracketed density ratio (σ) term suggests that thermal expansion at the flame front also plays a role in instability growth (or flame stabilization).

An example of how a Landau instability would develop on a propagating flame front (based upon the assumptions imposed by Darrieus and Landau) is illustrated by Law et al. [80] in Figure 2-21 below,

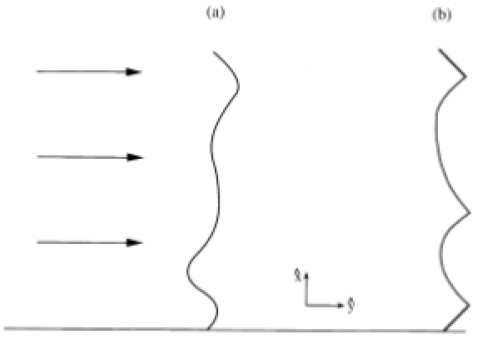

Figure 2-21: Schematic of flame propagation (a) before cusp formation (b) after cusp formation. Provided by Law et al. [80]

The curved front progresses to form steep cusps. This cusp like phenomenon has also been observed experimentally. However, the conclusion of Darrieus and Landau that all flames are unconditionally unstable is known to be false [60]. Flames can remain stable over a wide range of conditions. There are further mechanisms of instability that were not recognized by Darrieus and Landau, which can promote or reduce flame front stability.

As discussed previously in section 2.2.2.2, flame front structure and speed is affected by curvature primarily due to differential or preferential diffusion. The assumption that Darrieus and Landau made that local flame speed is unaffected by perturbation is not reasonable for most flames, particularly if Le≠1. Changes in local flame speed due to curvature can cause flames to either be more or less stable than Darrieus and Landau predicted.

If Le < 1 then differential diffusion assists in cusp formation and compounded with the DL instability, tends to cause flame front perturbations to grow. If Le > 1 then differential diffusion slows convex regions of the flame and assists the closure of concave regions, therefore leading to a more stable flame. Therefore, Lewis number effects (differential diffusion) can either accentuate or counteract perturbation growth due to DL (or any) instability.

In the same manner, preferential diffusion can either accentuate or counteract small flame perturbations growth. If ($D_{\underset{reactant}{limiting}} > D_{\underset{reactant}{excess}}$) than convex flame regions will propagate faster than concave regions, leading to perturbation growth. If ($D_{\underset{reactant}{limiting}} < D_{\underset{reactant}{excess}}$) then the opposite will occur, leading to a more stable flame. The term “thermo-diffusive instability” is used to refer to the combined contribution of differential and preferential diffusion towards flame front instability.

A complete description of flame stability includes more than the DL and thermo-diffusive instabilities discussed above. Local heat release, gravitational forces and acoustic wave-flame interactions are only a few examples of phenomenon that can also effect flame front

perturbation growth. Such influences are not fully understood and beyond the scope of this document. A more in depth discussion on premixed flame instability can be found in ref. [100].

Flame wrinkles require time and space to develop. The images in Figure 2-22 below by Jomaas et al. [101] show the cellular surface development of a spherically expanding premixed flame via Schlieren imaging.

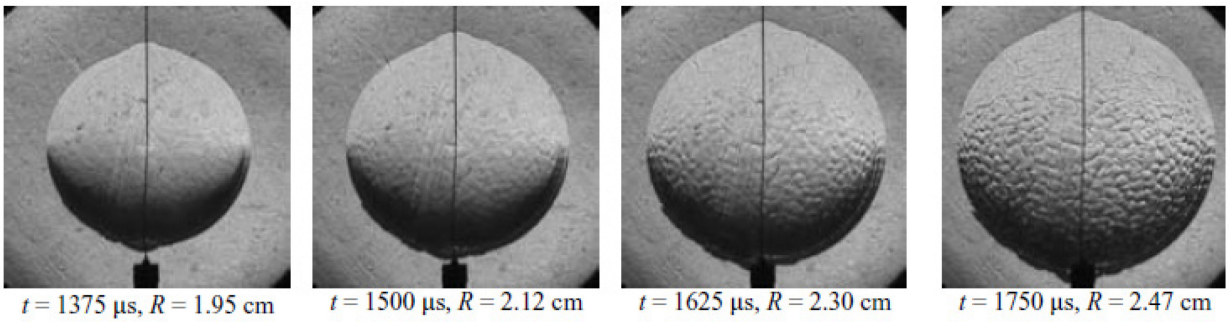

Figure 2-22: Schlieren image sequence of a typical flame propagation showing the transition from smooth to cellular flame. Provided by Jamaas et al. [101]

In the first image of the sequence the flame is small and its contour is smooth. However, very rapidly as its size exceeds 2 cm the flame develops cellular structures on the surface which continue to grow in size. A variety of fuels were imaged in the study over a wide range of conditions and the scale for which the front became unstable was found to correlate well with a critical Peclet number,

$$Pe_c = \frac{R_{flame}}{\ell_L}$$

Jomaas et al. chose conditions that enabled the individual influences preferential and differential diffusion to be isolated. They found that fuels of high Lewis number tended to become unstable at low Pe_c. Equidiffusive fuels became unstable at a Pe_c that was almost independent of Φ. The stability of non-equidiffusive fuels was highly dependent on Φ, as would be expected due to Lewis number effects. All of these observations agree with the previous discussion on the role of thermo-diffusive stability.

2.2.2.5.2 Turbulence Induced Wrinkling

Turbulent flows are irregular and contain a variety of coherent structures that span a wide range of scales [102]. Flames can become wrinkled by interacting with such turbulent structures (eddies).

Large flow structures primarily convect and distort flame fronts. Very small flow structures ($O(\ell_{eddy})\sim O(\ell_R)$) are easily dissipated in preheat zones and are thought to be incapable of interacting with flame fronts. Flow structures of the in-between scales are thought to be responsible for the bulk of flow induced wrinkling that occurs on flames.

The inner cutoff scale (ε_i) is commonly defined as the smallest scale of interaction between turbulent eddies and a premixed flame front. Experiments performed on moderately turbulent ($u'/S_L<10$) burners have shown a range of $\varepsilon_i=10\ell_L$-$15\ell_L$ [103] based upon fractal flame front analysis [104]. Therefore, the smallest wrinkles on a flame tend to be at least an order of magnitude larger in scale than the flame thickness.

Most turbulent flame wrinkling is caused by interactions occurring between the flame front and vortex structures that are larger than ε_i but smaller than the flame. Such interactions are local and stochastic in nature. The stretch induced by an eddy can be quantified as [91],

$$\dot{s}_{eddy} = \frac{1}{A}\frac{dA}{dt}$$

The ability of an eddy to cause a flame front to grow in area is dependent on both the strength of the eddy as well as the duration (t_{eddy}) for the which it interacts with the front,

$$\ln(A) = \int_0^{t_{eddy}} \dot{s}_{eddy} dt \approx \bar{s}_{eddy} t_{eddy}$$

A small eddy, even of equal strength to a large eddy, will be less effective in wrinkling a flame front [105] than a large eddy due to the conciseness of its interaction with a flame front [91].

Many researchers have studied single and multiple (two or three) eddy interactions with flames under simplified conditions, both experimentally and numerically. The results of such idealized studies have not proven to be widely applicable across differing geometries. There remains much to be learned about the manner for which eddies interact with flames, particularly in the complex engine environment.

Peters et al. [106] performed an asymptotic analysis of a single vortex interacting with a flame front. For very high Peclet number[11], his analysis predicted that vortices roll up and form a reactive core. Such spiraled flames have not been experimentally observed and it has been suggested that eddy-flame interaction residence times are too short for such roll up to occur [107].

Poinsot et al. [108] performed DNS of single vortex-flame interactions including non-unity Lewis number, curvature, heat-release and non-constant viscosity effects. It was concluded that not only stretch, but also curvature, viscous dissipation and transient dynamics have a large effect on the quenching of premixed flames. It was discussed that curvature based stretch may offset eddy induced strain, particularly for small eddies which try to form small scale wrinkles. Poinsot et al. suggested alterations to the location of the borders between combustion regimes in the classic Borghi diagram.

Wu et al. [107] performed flame interface numerical simulations of a vortex covected through a laminar flame. They found that increasing the eddy convective velocity reduces the residence time and subsequently the degree for which the eddy wrinkled the flame. Eddies were shown to induce extensive strain more often than compressive strain on the flame front.

[11] Pe = $\frac{advective\ transport\ rate}{diffusive\ transport\ rate} = \frac{LU}{D}$
Where L = characteristic length, U = velocity

Many other numerical studies have been performed on vortex-flow interactions, for example see ref. [109-112]. From these much has been learned but it remains a challenge to model or simulate realistic flame-flow interactions; particularly in realistic environments where large numbers of eddy-flame interactions occur both simultaneously and spatially/temporally separated. DNS studies are limited to studies where only one or two eddies interact. Models necessarily apply questionable approximations in order to study more complex flames; however they typically do so by neglecting important physics such as those due to thermal expansion, differential/preferential diffusion and complex chemistry.

Modeling results suggest that eddy-flame interactions are highly complex in nature and that many small scale physics best not be neglected. For example, eddy-flame interactions are not likely to be understood without considering local curvature development (time history) and the effects of viscous dissipation within the flame front. High spatial and temporal resolution of the flame front is required to resolve either of these effects. Increased computational power is required before turbulent eddy-flame interactions, as they would take place in a combustion device, can be fully understood through modeling or simulation.

Eddy-flame interactions have been researched through experiment as well. Roberts and Driscoll [113] studied pocket formation of a premixed flame interacting with a laminar vortex through Mie scattering tomography. The importance of viscous attenuation and flame stretch on diffusional unstable flames were recognized. The DNS results by Poinsot et al. [108] were verified by Roberts and Driscoll's study as well as by experiments performed by Poinsot et al. [114]. Roberts et al. [115] observed vortex induced quenching and found that small vortices were less effective at quenching a premixed flame front than most *a priori* estimates such as the Borghi diagram generally suggest. Different fuels were shown to exhibit different extinction Karlovitz numbers demonstrating the importance of detailed chemistry.
Nye et al. [116] performed simultaneous PIV and OH PLIF measurements on an unsteady V-flame and found local strain rate and curvature on the flame front to be statistically independent of each other.

Driscoll et al. [117] imaged torroidal vortex-flame interactions with PIV and determined the aerodynamic strain distribution on the front. It was found that strain is not maximum near the forward stagnation point of the vortex as was previously theorized. Small vortices were shown to exert a different strain rate distribution over the flame front than large vortices. Driscoll et al. concluded the strain process (and wrinkling process) cannot be modeled as being self-similar. In this same study [117] it was shown that vortices can be produced in the products of a premixed flame. Pindera and Talbot [118] performed numerical studies prior that also suggested that such vortices may be produced by a flame.

Mueller et al. studied the interactions of between vortices of differing strengths and a premixed flames [119]. Weak vortices were observed to attenuate due to volume expansion. Strong eddies survived passage through the flame but weakened the flame in the process. A flame was shown to generate intense vortices and induce a product side flow velocity that tended to stabilize the front. Mueller et al. [120] also studied the effects of unsteady vortex induced stretch on a premixed flame. The propane flame front was rapidly strengthened by negative stretch but responded slowly to positive stretch. Mueller's results suggest that flame chemistry is sensitive to negative strain and that unsteadiness best be considered when modeling flow induced flame stretching processes.

Sinbaldi et al. [121] studied the ability of buoyance to suppress vortex-flame induced wrinkling. Buoyancy was found to be capable of reducing vortex-induced wrinkle amplitude by a factor of 2-3. Flames were observed to propagate at about twice the speed under zero gravity as 1-g conditions. The Rayleigh-Taylor and baroclinic mechanisms were given as an explanation for the stabilization under normal gravity conditions. Such results highlight the important role buoyancy can play in stabilizing premixed flames.
Many other experiments have revealed the richness of eddy-flame interactions. More information and references on the topic can be found in the review paper by Renard et al. [105].

In review, consider all of the factors that affect wrinkle formation due to eddy-flame interaction. The impact of an eddy on a flame depends on the size and strength of the eddy, the duration of eddy-flame interaction, as well as the condition (existing curvature, speed, thickness, etc.) of the flame front. The curvature induced on the front by the eddy will also depend upon preferential diffusion, differential diffusion, heat transfer (including radiative losses), thermal expansion, DL and other thermo-diffusive instabilities, viscous dissipation, as well as baroclinic and gravitational effects that occur within the front. In the turbulent environment many such eddy-flame interactions may occur simultaneously. Interactions which occur spatially and temporally close are likely to be coupled. Interactions occur so quickly that unsteady physics best be considered; sometimes detailed chemistry as well.

Needless to say, there has been no successful characterization of eddy-flame interactions which is global in nature. Many models, some of which will be discussed in the modeling section, attempt to capture the wrinkling of flames due to eddy-flame interactions through empirical correlations based upon global turbulence properties (such as ε and κ) or by tracking the transport of topological features such as flame surface density. However, any such model is questionable considering the complex, small scale physics involved. Much of which is neither understood nor resolved on the scale of most modeling grids.

To what extent any empirical model “sub-grid” type model can be improved upon to capture the full physics of premixed flame wrinkling remains equally unclear. However, as computational power continues to increase it becomes more feasible that computational models be run on fine enough grids to capture wrinkling phenomenon, as wrinkles tend to occur on a scale which is an order of magnitude larger than the flame thickness (and an order of magnitude or two smaller than most current engine models grid). Therefore, achieving a fundamental understanding of eddy-flame interactions is important, as such an understanding may be directly applied to improve premixed flame modeling in the coming years.

2.2.2.6 Turbulent Premixed Flame Modeling

Turbulent premixed engine flames are usually modeled by either the G-equation or coherent flame approaches. Reitz [13] suggests that the G-equation because he claims that it is the most practical in terms of the computational time/accuracy tradeoff, for the purpose of engine design. Both modeling approaches are classified as "flame area evolution" models. Such models track surface area growth through either the wrinkling factor or flame surface density.

Beyond these two common approaches, large varieties of techniques have been developed and are used within the combustion community. Here, only three modeling approaches will be discussed: the G-equation, then the Bray-Moss-Libby and Coherent Flame methods. All of these models are based upon the "flamelet" assumption. Many of the models excluded from discussion are empirical in nature, such as the Eddy Breakup Model. Others, such as fractal based approaches, are excluded because they aren't commonly used in modern engine applications. More can be found on turbulent flame modeling in any of the following references [26, 65, 70, 122-124] .

2.2.2.6.1 Turbulent Premixed Flame G-Equation Modeling

The G-equation approach utilizes a non-reactive scalar, G, to track flame evolution. The flame is represented by an infinitely thin surface that separates the burnt (G > 0) from the unburnt gas (G < 0) regions. The flames iso-surface lies at

$$G(\vec{x}, t) = G_0$$

This is illustrated in Figure 2-23 below by Peters [65]. Williams was the first to develop such a level-set approach [125].

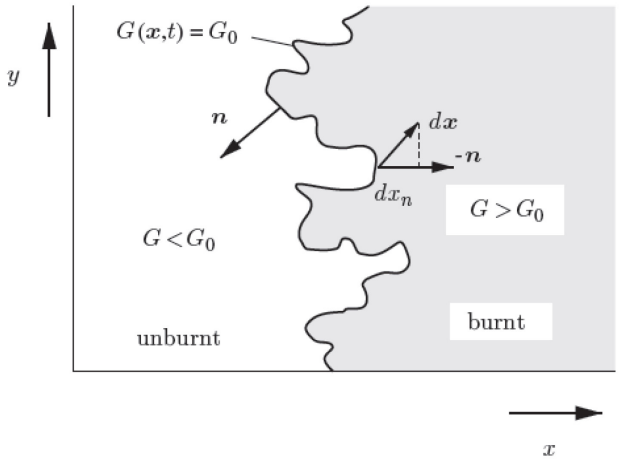

Figure 2-23: A schematic representation of the flame front as an iso-scalar surface by Peters[65].

Although the front is considered to be infinitely thin, the G scalar field is continuous. This allows the flame to be accurately tracked even when the model grid-size exceeds the flames dimensions. Values of G anywhere other than on the front's surface are meaningless.

Various authors have derived forms of the G transport equation for both RANS and LES models. The following G transport equation is suggested by Peters [65],

$$\frac{\partial G}{\partial t} + \vec{v} \cdot \nabla G = s_L^{\circ} |\nabla G|(1 - \kappa \mathcal{L}) - \mathcal{L} S |\nabla G|$$

Where S = strain rate imposed by the velocity gradient = $-\vec{n} \cdot \nabla \vec{v} \cdot \vec{n}$

The flames self-propagation rate is dependent on curvature, Markstein length, aerodynamic strain and the maximum increase rate in G.

Remember that for an infinitely thin flame front local surface area density is defined as

$$\Sigma = |\nabla c|$$

G is by definition an infinitely thin contour, therefore $|\nabla \mathrm{G}|\big|_{G=G_0} = \Sigma$, if, and only if, the G-equations provides an accurately representation of flame topology. Rarely is this the case and

often a wrinkling factor is used in order to correct the flame speed for unresolved or incorrect topological features (curvature/surface area density). For example, a G-equation flame evolution model presented by Weller [126] in 1993 was of the form [70],

$$\frac{\partial \bar{\rho}\tilde{G}}{\partial t} + \frac{\partial\left(\rho \tilde{u}_i \tilde{G}\right)}{\partial x_i} - \frac{\partial}{\partial x_i}\left(\bar{\rho}\overline{D}_G \frac{\partial \tilde{G}}{\partial x_i}\right) = -\left[\bar{\rho}\Xi + (\bar{\rho}_u - \bar{\rho}) \cdot \min\left(\Xi, \Xi_{eq}\right)\right] \cdot s_L \left|\nabla \tilde{G}\right|$$

Where Ξ_{eq} = equilibrium wrinkled-ness factor, as can be estimated many empirical ways. The definition of Ξ is further expanded,

$$\Xi = \frac{s_t}{s_l} = \frac{\Sigma}{\left|\nabla \tilde{G}\right|}$$

In such a formulation, the wrinkled-ness factor is proportional to the ratio of turbulent to laminar flame speeds. The wrinkling factor is often limited to an equilibrium level. Here, the wrinkling factor has been defined proportional to the ratio of the actual flames surface area to the surface area of the G contour (at the infinitely thin contour limit). Therefore, Ξ can be used to correct the modeled flame speed for the inaccuracy induced by under-resolving the surface area of the iso-contour of G (i.e. inaccurately wrinkled flame). In this manner, Ξ as it has been defined here (and is often used) is ill defined in that its value may depend on the flame contour resolution itself.

There are many ways for which Ξ can be modeled. Algebraic type relationships between Ξ and flow/flame properties have been tried, but none have found widespread success. The physics of wrinkling is complex and it is generally agreed that wrinkle generation, transport and destruction are important and must be taken into account in estimating Ξ or Σ. Some choose to assume that wrinkling processes occur fast enough so that wrinkle production and destruction balance and $\Xi = \Xi_{eq}$ always. Although often used, such an assumption is clearly questionable as unsteady wrinkling effects have been shown important. However, if the equilibrium assumption is to be used Ref. [127] provides an example of how Ξ_{eq} may be estimated.

Full Ξ and Σ transport equations are becoming common practice in engine combustion modeling and will be discussed in more detail when the coherent flame model is introduced.

In the G-equation transport above, the flame is convected by the flow field through the $\vec{v} \cdot \nabla G$ term. Accurate modeling of the $\vec{v}$ field is prerequisite to accurate flame modeling. Modeling in-cylinder flows is a difficult task itself, particularly when a flame is present as the flame itself interacts with the flow field. Generally, all engine modeling techniques continue to struggle to estimate the $\vec{v}$ field with high fidelity and the accuracy of flame models suffer. Whether it be in the context of RANS or LES modeling environment, developing models that can capture the physics of flow-flame interactions on both the large and small (usually unresolved) scales is an ongoing challenge.

2.2.2.6.2 BML and Surface Area Density Premixed Flame Modeling

Bray, Moss and Libby developed a premixed flame model in 1977 (BML model) based upon a eddy crossing frequency [128, 129]. Borrowing some of the concepts, "Coherent Flame Models" were developed shortly after by Marble and Broadwell [130]. Both approaches utilize the flamelet assumption and are therefore relevant within the flamelet regimes. The base equations for the two approaches are similar but methods for which reaction rates and flame speeds are calculated differ.

The BML model estimates reaction rates by solving an algebraic relationship. This relationship is based upon physical analysis and reasoning. The coherent flame model uses flame surface density estimates to determine reaction rate. The coherent flame model tracks Σ through a transport equation which fully considers surface area development, propagation and destruction; but requires many of such effects to be modeled. Such "flame area models" can be used in conjunction with the G-equation approach previously discussed. The difference between the coherent flame and the G-equation approaches is primarily the method for which

the front is tracked. Most BML or coherent flame models do not utilize a scalar field (such as G); instead they solve the conservation equations while accounting for reactivity. Although more physically correct, such approaches can be challenging as the flame front is often thinner than can be resolved on the computational grid. Sometimes this problem is overcome by artificially thickening the flame front.

The BML model is rarely used in engine applications anymore as there are now more accurate alternatives. However, some of the theories used to develop the model, such as crossing frequency, are still relevant. Flame surface area density (FSAD) models similar to the coherent flame model are most commonly often used in engine combustion modeling. Therefore, the BML model will only be briefly introduced as background material. Then the coherent flame model will be discussed.

Both of these models solve the conservation equations for mass, momentum and energy. These equations are often written in terms of a progress variable, such as reduced temperature, $\Theta = \frac{C_p(T-T_u)}{(\Delta H)_{Rxn} Y_{fuel}}$. For example, the following RANS conservation equations given in Poinsot and Veynante's book [68] for isobaric and adiabatic conditions.

$$\frac{\partial \bar{\rho}}{\partial t} + \frac{\partial}{\partial x_i}(\bar{\rho}\tilde{u}_i) = 0$$

$$\frac{\partial \bar{\rho}\tilde{u}_j}{\partial t} + \frac{\partial}{\partial x_i}\left(\rho \tilde{u}_i \tilde{u}_j\right) + \frac{\partial \bar{p}}{\partial x_i} = \frac{\partial}{\partial x_i}\left(\bar{\tau}_{ij} - \bar{\rho}\widetilde{u_i'' u_j''}\right)$$

$$\frac{\partial \bar{\rho}\widetilde{\Theta}}{\partial t} + \frac{\partial}{\partial x_i}\left(\rho \widetilde{\Theta} \tilde{u}_i\right) = \frac{\partial}{\partial x_i}\left(\bar{\rho}\bar{D}\frac{\partial \widetilde{\Theta}}{\partial x_i} - \bar{\rho}\widetilde{u_i'' \Theta''}\right) + \bar{\dot{\omega}}_\Theta$$

Where $\bar{\dot{\omega}}_\Theta$ = mean reaction rate

$\bar{\dot{\omega}}_\Theta$, along with the two other unclosed terms must be modeled. $\bar{\dot{\omega}}_\Theta$ is modeled differently for the BML model than for the coherent flame model.

Bray, Moss and Libby proposed the following relationships for $\bar{\dot{\omega}}_\theta$ based upon statistical analysis of the telegraphic signal. They suggested that $\bar{\dot{\omega}}_\theta$ depends mostly on a flame crossing (or passing) frequency, $\int_c$, as,

$$\bar{\dot{\omega}}_\theta = \dot{\omega}\int_c$$

Where $\dot{\omega}$ = reaction rate per flame crossing. By analyzing the intermittency between unburnt and burnt gasses at a location within the reaction zone through a bimodal pdf and the telegraphic signal [68] $\int_c$ is found to be,

$$\int_c = \frac{\bar{\theta}(1-\bar{\theta})}{\hat{T}}$$

Where $\hat{T}$ = mean period of telegraphic signal, which is often estimated based upon turbulent scaling so that the mean reaction rate takes the algebraic form of,

$$\bar{\dot{\omega}}_\theta = 2\rho_0 {s_L^0}^2 \frac{\varepsilon}{\mathrm{k}}\bar{\theta}(1-\bar{\theta})$$

Alternatively; the coherent flame model uses a flame surface density based approach for closing $\bar{\dot{\omega}}_\theta$. Remember that reaction rate can be quantified by,

$$\dot{\omega} = \rho_u \Sigma S_L^o I_o$$

The effects of topology on flame speed are recognized though Σ and I_o(stretch factor). Due to the intrinsic complexity of both instability and flame-eddy interaction induced wrinkling, it is not thought adequate to describe flame surface density through algebraic equations. Nevertheless, algebraic closures are common (examples in ref. [68, 131, 132]). Σ generation, propagation and destruction best be captured through a Σ transport model. A commonly used form of Σ transport equation in 2-D take the following form [91, 133],

$$\frac{\partial \Sigma}{\partial t} + \tilde{U}\frac{\partial \Sigma}{\partial x} + \tilde{V}\frac{\partial \Sigma}{\partial y} = \nu_T \frac{\partial^2 \Sigma}{\partial y^2} + \bar{K}\Sigma - \bar{M} - \bar{Q}$$

Where $\bar{K}$ = time averaged stretch rate
$\bar{M}$ = mean merging rate
$\bar{Q}$ = mean quenching rate

All three of which can be modeled [133-135]. Sometimes the effect of aerodynamic strain, as would be included in a $\bar{K}$ model, is broken up into mean and turbulent contributions [136-138]. Such an approach is well summarized in Poinsot and Veynante's book [68].

The usage of Σ transport based combustion models has become common in engine applications. How to best model transport terms is an active area of research.

2.2.2.7 Premixed Flame Summary

A premixed flame is one for which fuel and oxidizer are fully premixed prior to combustion. Premixed flames are used to power most gasoline powered vehicles. Laminar premixed flames are well understood but turbulent premixed flames remain an active area of research.

The burn rate of a premixed flame is aero-thermo-diffusively limited. Within the front of a premixed flame chemical reactions occur very rapidly and so flames tend to be very thin. Fronts propagate normal to themselves in the direction of unburned reactants. The combined effects of turbulence and natural instabilities cause flames to wrinkle. Such wrinkling drastically affects the propagation process. Turbulent premixed flames often propagate an order of magnitude faster than their laminar counterpart, primarily due to the effects of wrinkling. Therefore, an understanding of flame front topology is prerequisite towards accurately predicting turbulent premixed flame speed.

Within a laminar premixed flame front, most reactions occur within a thin “reaction zone” that occupies only about 1/10 of the flame thickness. Preceding this reaction zone is a “preheat zone” where fuel and oxidizer are heated prior to reaction. Hundreds to thousands of reactions take place within the reaction zone simultaneously. The structure and speed of laminar premixed flames can be modeled by commercial programs. Flame speeds have been tabulated for common surrogate fuels such as iso-octane and n-heptane over a wide range of conditions. Engine combustion models often draw upon flamelet flame speed “look up tables” to improve computational speed.

Premixed flames are sensitive to stretch. Stretch is caused by a combination of aerodynamic strain and curvature. Laminar flame speed and structure is sensitive to flame front curvature, mostly due to “differential diffusion” (also known as Le number) effects. At low stretch rates a linear relationship between stretch and laminar flame speed has been observed and is often characterized by a Markstein length. The effects of stretch on local flame speed are typically smaller than 20%; an order of magnitude smaller than topological effects.

Premixed flames are categorized into one of the following regimes (listed in order of increased turbulence intensity): laminar, wrinkled, corrugated, reaction sheet or well stirred reactor. The latter four regimes are turbulent and within those regimes eddy-flame interactions strongly affect the combustion process. The wrinkled and corrugated regimes are often referred to as “flamelet” regimes. Here, the flame is distorted by the flow but remains thin. Such a flame retains the local structure of a stretched, laminar flame. At higher turbulence intensities, such as those experienced in the reaction sheet or well stirred reactor regimes, turbulent eddy’s of comparable scale to the preheat or reaction zones are able to penetrate and mix the inner structure of the flame. At such high turbulence intensities the intrinsic structure of the flames becomes affected by eddy intrusion and laminar flame concepts loose applicability. Most engine flames lie within the wrinkled and corrugated “flamelet” regimes, where strained laminar flame theory can be drawn upon.

The flamelet assumption conveniently allows the chemistry to be decoupled from other flame front physics. Local flame speed can be estimated based upon established laminar flame theory and flame surface topological development can be considered separately. However, in the turbulent environment it is topological features, such as flame surface area density development, that are known to be a primary driver of turbulent flame acceleration. Unfortunately, flame wrinkling and corrugation processes are not only important but also highly complex.

Turbulent flame-flow interactions are only becoming understood. When an eddy interacts with a flame the effect that the two entities have on each other depends not only on both the properties of the eddy and flame, but also on the duration of interaction. A small eddy might dissipate upon collision with a flame front, whereas a larger eddy is likely to stretch the front. The reaction of a flame front to perturbation during and after an eddy-flame interaction will depend on the stability of the front. Perturbations can be damped or accentuated by flame front hydrodynamic and thermo-diffusive instabilities. A wide variety of physics is known to contribute or detract from flame front stability; including those driven by buoyancy, thermal expansion and baroclinic effects. A turbulent flame may experience hundreds or thousands of eddy-flow interactions at any given time; sometimes within close proximity. Premixed flame topological development is naturally unsteady and therefore sensitive to retroactive effects.

Despite the challenge, turbulent premixed flame models have been developed and successfully used in engineering design; particularly in the optimization of conventional SI gasoline engines. The “G-equation” or “Coherent Flame” models are popular for use in engine applications. Both of these flame surface area based modeling approaches relies upon the flamelet assumption as well as surface area development models. It remains a challenge to accurately model flame surface area development due to the complexity of turbulent-flame interactions.
The wrinkled-ness development of premixed engine flames was observed and analyzed in this study. Much of the theory just discussed, particularly with regards to the thermo-diffusive

stability of premixed flames and flame-to-flow turbulent interactions will be drawn upon in later sections.

2.2.3 Partially Premixed Flames

Partially premixed flames exist within fuel/oxidizer charges that are neither spatially separated nor fully mixed. The process of molecular diffusion always seeks to eliminate the species concentration gradients that are so characteristic of the partially-premixed state; therefore stratified flames occur in a naturally unsteady and transient environment of fuel/air mixing. The term stratified flame will be used synonymously with partially premixed flame through-out this document.

Fully premixed and non-premixed flames, as they have been discussed, represent the upper and lower limits of the combustion reactant mixed-ness spectrum. Partially premixed encompass all states of mixed-ness that lie between the two. It is becoming increasingly more common for partially premixed combustion to be utilized in engine applications; largely because such mixtures tend to offer a fair tradeoff between efficiency and emissions.

When the reactants of a partially premixed flame are well, but incompletely, mixed prior to combustion, the stratified flame that occurs tends to act similar to a premixed flame. When a stratified flames reactants are poorly mixed the flame tends to act similar to a diffusion flame. For median levels of mixed-ness, the flame may not act like either a premixed nor non-premixed flame and it demands to be considered by its own (non-existent) branch of combustion theory.

Most SGSC engines achieve a high degree of partial mixed-ness between fuel and oxidizer prior to ignition. Therefore SGSC combustion occurs in a mostly “premixed like” manner with conventionally propagating flames. Alternatively; diesel engines achieve a relatively low degree of fuel/air mixed-ness prior to combustion. Therefore, they burn most of their fuel in a in a

“non-premixed like” mass transfer rate-limited manner. PPCI engines achieve a median degree of mixed-ness prior to combustion. Their flames are more “premixed like” than a diesel, but still dominantly “non-premixed like”. To what extent classic combustion theory, based upon premixed and non-premixed flames, may be applied to such mixed mode combustion regimes remains unclear.

Stratified flames are commonly understood through an aggregate of premixed and non-premixed flame theory. However, there are unique effects observed in the stratified environment not addressed by either branch of theory.

The partially premixed state is more general than the fully premixed and non-premixed states. When evaluating partially premixed flame theory, conventional combustion theory should always be recovered at the upper (premixed) and lower (non-premixed) limits of mixed-ness. If partially premixed flames were to become fully understood (based upon first principles), so should premixed and non-premixed flames. Such a global flame theory is not likely in the near future. However, being the most general state of combustion there is great value in studying partially premixed flames.

In order to recognize the richness of stratified combustion, consider a few different stratified flames. First imagine a flame burning through a completely lean stratified charge. Such a flame propagates in an aero-thermo-diffusively limited manner which will appear similar to a premixed flame, at least superficially. Perhaps the only notable visual differences between the lean stratified flame and a conventional premixed flame will be the flames tendency to wrinkle excessively. Less visible, but notable, is that such a flame might exhibit hyper-extended flammability limits relative to an equivalent homogeneous flame. These effects are attributed to Φ-gradient based physics, which are unique to stratification.

Now consider as similar stratified flame, only now through a rich stratified charge. A premixed like flame front will propagate through the mixture, similar to that described for the lean flame.

However, unique to the rich flame, a secondary (trailing diffusion) flame will form in the wake of the propagating front. The role of this secondary flame is to complete the oxidation of rich products (mostly CO and H_2) left behind by the propagating front. The trailing diffusion flame should appear “non-premixed like”. However, its location and composition (mostly CO and HC’s) are a bit peculiar.

Both lean and rich stratified flames exist simultaneously in a SGSC engine. Sometimes, concurrent to a normal diffusion flame (very rich jet region that has not been mixed within flammability limits, droplet combustion, or surface pool fires due to wall wetting). Therefore, nearly all of combustion mixture regimes exist and interact within a SGSC engine, making the SGSC combustion environment one of the most complex imaginable.

For those trying to model SGSC combustion, the existence of both kinetically and mixing-controlled combustion regions provides a challenge. Whereas premixed flame models may be suitable for “premixed flame like” regions, the existence of trailing “diffusion flame like” regions demands models that are capable of spanning combustion regimes. Modeling techniques, such as the G-equation approach, must be able to smoothly transitioning between the two modes (if a two mode model is found appropriate). Further, if premixed and non-premixed flame theory are to be combined for the modeling of stratified flames then the physics that are unique to the stratified environment must also be incorporated into the theory. The effects of stratification on flames has not been fully recognized or characterized in the engine environment.

Adding further challenge, the theory behind turbulent premixed and turbulent non-premixed flames is still being developed. In particular, turbulent premixed flame physics remains an active area of research and has only recently provided a foundation for stratified combustion theory to build upon. Partially premixed combustion remains a young field of study. To the authors’ knowledge, there are no textbooks published on the topic yet.
As the value of partially-premixed combustion has become recognized in application, the motivation to understand the science that drives such flames has grown. Many scientists are

actively researching partially premixed flames; some studies of which will be discussed in the following section on partially premixed flame theory. The work presented here addresses the wrinkling of partially-premixed flames, as they are recognized under SGSC engine conditions.

2.2.3.1 Partially Premixed Flame Theory

Partially premixed flames can take many geometric forms. An example of a partially premixed flame in a stratified environment has been illustrated in Figure 2-24 below by Helie and Trouvé [139].

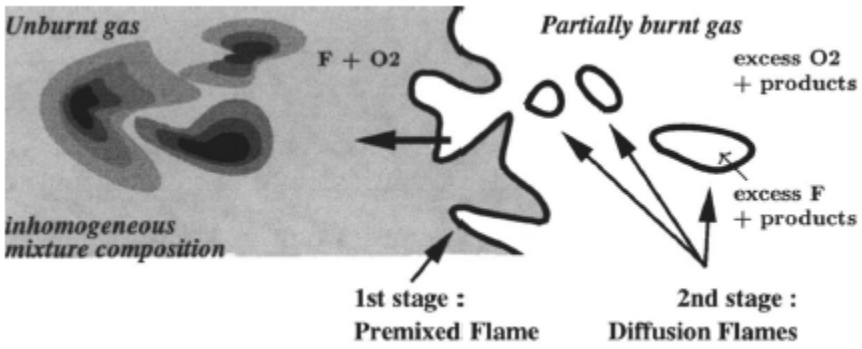

Figure 2-24: A representation of turbulent flame propagation into partially premixed reactants. Provided by Helie and Trouvé [139]

Figure 2-24 reveals a two stage combustion process. A premixed flame is propagating through the flammable regions of the stratified charge. In its wake, a secondary diffusion flame is oxidizing the remaining rich product species. There remain unburnt regions ahead of the front which are highly stratified. When the premixed flame encounters these regions, the portion of the charge which is mixed well enough to be flammable will burn in a “premixed like” manner. The poorly mixed core regions of the charge are too rich for flame propagation, so they will burn diffusely.

As drawn, the fuel/air charge immediately upstream of the flame front is nearly homogeneous. Therefore, the premixed flame will propagate through this region in a manner consistent with homogeneous flame theory.

The trailing diffusion flame will burn as non-premixed flame theory predicts. However, local conditions and composition of the 2nd stage diffusion flame are unusual. Being that the flame exists in the wake of a premixed flame; the fuel will be composed of high temperature rich products. Most of the nearby Oxygen will have been consumed by the premixed flame so the diffusion flame will therefore burn slowly. Under certain conditions a significant fraction of the 2nd stage diffusion flame will fail to burn at all (extinguish).

When the premixed flame reaches the stratified region further ahead of the front (labeled inhomogeneous mixture in Figure 2-24), the flame structure will become more complex due to the Φ distribution and gradients. The flame will propagate much more rapidly through the near stoichiometric regions than the off-stoichiometric regions of the charge. The inner structure, topology and burn rate of the flame will depend upon the local Φ structure and distribution in a manner that cannot predicted well based upon conventional (premixed and non-premixed) combustion theory.

One of the most studied partially premixed flame geometries is known as a “tribrachial” or “triple” flame, as has been illustrated in below by Kionio et al. [140].

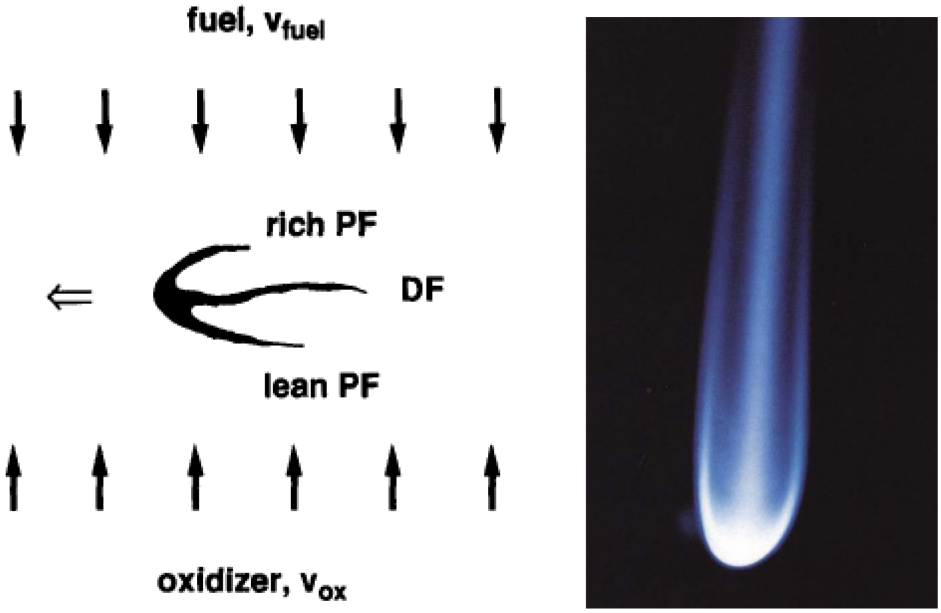

Figure 2-25: Drawing and Image of a laminar tribrachial (triple) flame. Images provided by Kioni et al. [140].

As can be seen, the triple flame contains a rich premixed (rich PF) branch, a lean premixed (lean PF) branch and trailing diffusion flame (DF). The leading tip of the triple flame burns stoichiometrically, and therefore most rapidly. The stoichiometric point where all three branches meet is often referred to as the "triple point."

Triple flames have been extensively studied [140-145], largely because such structures play an important role in the stabilization of lifted jet flames. In the SGSC engine, triple flame structures exist in regions where lean and rich mixtures intersect; typically near the leading edge of the flame.

It has been shown experimentally that the leading edge of a triple flame is capable of propagating at speeds double that of the equivalent stoichiometric premixed flame [60]. This acceleration has been attributed to both an increased local flame burning rate as well as a "perceived" acceleration due to the redirection of reactants towards the leading tip of the flame [146].

When tribachial flames are highly curved, as in figure Figure 2-25, their local flame speeds are naturally influenced by preferential and differential (Le) diffusion effects[147]. Lewis number gradients are inherent along the fronts due to the Φ gradients present. Therefore, an effective "instability gradient" across the front complicates the turbulent wrinkling process. Depending on the properties of the fuel, differential/preferential diffusion leads to either a local increase or decrease in flame speed around the triple point. The thickness and topology of the lean and rich braches will generally differ [148], primarily due to flame speed and species gradients effects. The manner for which the different branches interact with turbulent structures [148] will be unconventional. At times, the premixed and non-premixed branches of triple flames have been seen to contact and merge. Such direct interactions between a trailing diffusion flame and a propagating partially premixed flame have not been well studied.

Triple flames are only one of many edge flame structures that may arise in the partially premixed environment. The more general class of edge flames has also been a common topic of research [141, 149-151].

In a partially premixed environments such as are found in a SGSC engine, a complex combination of all flame types discussed throughout this document exists and interacts.

There is evidence indicating that zones within a stratified flame of differing mixture strength (Φ) interact [152]. Gradients in Φ across a stratified flame front lead to heat and radical transport which is known extend the flammability limits of both lean [153-156] and rich [157] flame regions. Stratification can increase surface area density [155, 158] and wrinkled-ness [152, 157-159] due to both large and small scale mixture fraction inhomogeneity effects. Generally, stratified flames tend to travel at higher local velocities than homogeneous flames of equal Φ [155, 160, 161]; and rarely the inverse has also been observed[157].

Hydrodynamic instabilities unique to stratified flames have been recognized [161]. The degree of wrinkled-ness across a stratified flame front has been shown to be dependent on Φ; as

regions of differing Φ tend to exhibit differing degrees of thermo-diffusive instability (Le or $\mathcal{L}$) [152, 159].

Stratified flames have been shown to wrinkle in a manner different than homogeneous flames [158]. Stable flame regions interact with unstable flame regions creating topological effects noticeably unique [158, 159]. Further, stratified-flame can form along initially wrinkled fuel/air mixing fronts. For example, within SGSC engines fuel jets are often given a significant amount of time to mix prior to combustion and tend form an inhomogeneous, wrinkled fuel cloud prior to ignition. In such an environment, the early flame that initially spreads and engulfs the cloud must conform to the shape of the cloud itself which can lead to a highly wrinkled early flame. Although this may not be considered a flame wrinkling process in itself, it does lead to a wrinkled flame front through means not previously discussed that is unique to the stratified environment.

Retro-active effects are known to be important in stratified flame propagation. Certain topological features observed in stratified flames studied have only be described through knowledge of the flames history [154]. Flames have shown sensitivity to both the instantaneous and mean behavior of stratification [155, 162].

Stratification affects the intrinsic behavior of a flame, which suggest that models, particularly those based upon homogeneous flame theory, need to be modified to include such Φ gradient effects [158]. However, the degree for which such effects are important is not fully understood or agreed upon, particularly in the engine environment.

High fidelity modeling studies have tended to disagree with the experimental conclusion that Φ gradient effects are significantly important in stratified flames. 2-D DNS studies of triple flame propagation concluded that Φ gradient effects such as heat and radical transfer across the flame front were minor [135]. High resolution 2-D engine simulations performed by Haworth [163] in 2000 concluded that differences in flame area between homogeneous and non-

homogeneous reactants having the same overall stoichiometry were small. 2-D DNS performed by Lopez [161] in 2005 showed that Φ gradient effects were significant at low turbulence levels, but were minimal under highly turbulent conditions.

The modeling study by Haworth [163] is the only study performed under engine like conditions. All stratified flame experiments known to the author have found Φ gradients to significantly affects flame speed, surface area density, and usually topology. However, all such experiments have also been performed on simplified setups such as burners or constant volume spray vessels. These results may not translate into the engine environment which is uniquely complex. The relative importance of equivalence ratio effects of flame topology (i.e. wrinkled-ness) in the SGSC engine environment is addressed in this study.

2.2.3.2 Partially Premixed Flame Modeling

Partially premixed combustion models have been developed largely through the combination of previously developed premixed and non-premixed models. However, as mentioned before, phenomenon unique to the stratified combustion environment has been recognized that might be considered for inclusion in such models. In his turbulent combustion book [60], Lipatnikov separates partially premixed combustion phenomenon into two categories, (i) effects taken into account by contemporary RANS or LES models, (ii) effects that have not yet been addressed by such models but were documented in experimental and DNS studies.

Under category (i), effects that are accounted for by contemporary models, Lipatnikov lists [60] mean mixture composition inhomogeneity, local burning fluctuation due to pulsations in Φ and mixing controlled afterburning as effects captured by contemporary models. “Back-support”, extension of flammability limits and increase in surface area due to mixture inhomogeneity are listed as (ii) phenomenon not yet addressed by RANS or LES models. “Transverse support” (heat and radicals transported transversely across the flame front) would fall under the same category.

Stratified flame models typically introduce premixed and non-premixed models separately [164]. The extent for which each burning mode contributes to local reactivity is then estimated and used to weight the contribution of each burning mode respectively. Often a progress variable or a flame index is used to quantify the role of each mode.

Domingo et al. [165] suggested using a modified form of the normalized reaction variable c in the partially premixed environment, as follows,

$$c(Z;\vec{x},t) = \frac{Y_{F,o}Z - Y_F(\vec{x},t)}{Y_{F,o}Z - Y_F^{Eq}(\vec{x},t)}$$

Where Y_F^{Eq} = equilibrium fuel mass fraction
Z = mixture fraction in terms of concentration of reactants (passive scalar)

From this formulation, c = 0 for unburned gasses, c = 1 for completely equilibrated (burned) gasses, and c assumed values in-between in partially reacted regions. Using this definition, conventional techniques can be combined. The transport equation for premixed flame portions can be modeled by,

$$\frac{\partial \rho c}{\partial t} + \nabla \cdot (\rho \vec{u} c) = \nabla \cdot (\rho D \nabla c) + \dot{\omega}_c$$

$\dot{\omega}_c$ requires modeling, the many methods for can be used have already been discussed in the turbulent premixed flame modeling section.

The transport equation for the non-premixed combustion regions can be modeled by,

$$\frac{\partial \rho c}{\partial t} + \nabla \cdot (\rho \vec{u} c) = \nabla \cdot (\rho D \nabla c) + \dot{\omega}_c + \left(\frac{2}{Y_{F,o}Z - Y_F^{Eq}(Z)}\right)\left(Y_{F,o} - \frac{dY_F^{Eq}(Z)}{dZ}\right)\rho\, \chi_{Z,c} - \left(\frac{c}{Y_{F,o}Z - Y_F^{Eq}(Z)}\right)\frac{d^2 Y_F^{Eq}(Z)}{dZ^2}\rho\, \chi_{Z,c}$$

The latter two terms that include Z and $\chi_{Z,c}$ (scalar dissipation) require closure. Forms of this model have been used in both the RANS and LES environments [165]. Domingo et al. [166] further verified the validity of the "two zone" type model through a combined experimental and DNS study of a weakly turbulent lifted jet flames. $\dot{\omega}_c$ also must be modeled through methods previously discussed in the turbulent non-premixed flame section.

Presumed PDF models are common in non-premixed but uncommon in premixed combustion models. Such models presume the mean reaction rate of a region to be of a certain distribution as,

$$\overline{W}(x,t) = \int_0^1 W(c)P(x,t,c)dc$$

Where P(x,t,c) is a pdf function that is often based upon the beta function. A great amount of computational effort and complexity is saved by assuming such a heat release distribution across the flame front. Due to the sensitivity of premixed flames to turbulence it is difficult to develop accurate pdf's for premixed flames and hence, presumed pdf models are scarcely applied to premixed flames within the flamelet regime [60]. However, such an approach is convenient in practice and commonly used for partially premixed flames.

Libby et al. [167] developed a presumed pdf model for which $P = fn(f, Y_f, x, t)$, where mixture fraction (f) and fuel mass fraction (Y_f) are used to differentiate between premixed and non-premixed regimes so that the proper beta function constants may be applied. This model was later improved upon by Ribert et al. [168] and then Robin et al. [169].

Premixed coherent flame models have been modified for the stratified environment by a number of researchers. Veynante et al. [170] were some of the first to adapt the CFM to account for mixture non-uniformity. Baritaud et al. [171] further modified the CFM for the stratified charge engine environment and accurately predicted CO production trends. However,

both models only applied to the premixed portion of the cycle and neglected any diffusive afterburning. Duclos et al. [172] demonstrated the usage of a similar stratified engine model in KIVA, as may be useful for engine design.

Colin et al. [173] combined a modified coherent flame model with a presumed PDF model in order to capture both the "premixed like" and non-premixed phenomenon occurring within a stratified charge engine. This flame model was validated by comparing calculated pressure traces with experimental pressure traces.

A G-equation based SGSC flame model was recently developed by Dahms et al. [15, 29, 174-176], based upon extensive optical imaging studies. This model represents the state-of-the-art in industry. The G-contour was transported equation was defined by,

$$\langle\rho\rangle\frac{\partial\tilde{G}}{\partial t}+\langle\rho\rangle\nabla\tilde{G}\cdot\tilde{\vec{u}}=-\langle\rho\rangle\widetilde{D}_t'\tilde{\kappa}\left|\nabla\tilde{G}\right|+\widetilde{(\rho s_t)}\left|\nabla\tilde{G}\right|$$

Where $\widetilde{(\rho s_t)}$ is determined by a combining of a flame surface area based turbulent flame speed estimate with the probability of finding a flame front within a given region,

$$\widetilde{(\rho s_t)}=\int_0^1\rho_u\cdot\max\left[s_L,s_L(\tilde{\sigma}_t+1)-\widetilde{D}_t'\tilde{\kappa}\right]\tilde{P}(\tilde{Z};\tilde{Z},\widetilde{Z''^2})dZ$$

Where the mean turbulent flame surface area ratio is defined to be, $\tilde{\sigma}_t=\frac{s_t-s_L}{s_L}$, which is modeled by the following algebraic relationship,

$$\tilde{\sigma}_t\left(Z,\widetilde{H}(Z),\tilde{\kappa}\right)=-\frac{b_3^2}{4b_1}\sqrt{\frac{3c_\mu c_s}{Sc_t}}\frac{\ell_{f,t}}{\ell_f^0}\left(1-\mathcal{L}\ell_f^0\tilde{\kappa}\right)\left(\frac{\ell_{f,t}}{\ell_{f,t,alg}}\right)^{\frac{2}{3}}$$
$$+\sqrt{\frac{b_3^4}{16b_1^2}\frac{3c_\mu c_s}{Sc_t}\left(\frac{\ell_{f,t}}{\ell_f^0}\right)^2\left(1-\mathcal{L}\ell_f^0\tilde{\kappa}\right)^2\left(\frac{\ell_{f,t}}{\ell_{f,t,alg}}\right)^{\frac{4}{3}}+\frac{c_s b_3^2}{2s_L^0\ell_f^0}\ell_{f,t}^2\frac{\tilde{\varepsilon}}{\tilde{k}_{SFK}}}$$

Where b_1, b_3, c_μ, c_s and Sc_t are all modeling constants. $\ell_{f,t,alg}$ is a quantity obtained by neglecting the temporal derivative in the G variance equation which can be approximated as,

$$\ell_{f,t,alg} = b_2 \ell_t$$

Were b_2 is a modeling constant. The $\tilde{\sigma}_t$ relasionship was originally derived by Peters [65] for premixed flames but was modified for stratification. The pdf defined for $\tilde{P}(\tilde{Z}; \tilde{Z}, \widetilde{Z''^2})$ is of Gaussian form. It is suggested, but not demonstrated that the G-equation based model can be coupled with a non-premixed model in order to capture the diffusive after-burn. For more information on the Dahms et al. model please refer to the previously listed references as the details are his techniques are well documented.

Whether through a combination of presumed pdf, coherent flame, G-equation, or any other modeling technique discussed throughout this document; all partially-premixed models approach the challenge of capturing stratified flame physics in the same manner - by patching and modifying previously developed premixed and non-premixed models. In this, intrinsic differences between a stratified flame and completely premixed or non-premixed flames are usually not recognized or rectified. However, that has not hindered some models from achieving limited success.

In the engine environment, stratified flame models have generally been validated by comparison with experimental pressure traces. Validation in this manner ensures that global flame properties, such as total heat release rate, are being modeled accurately. However, important flame details such as degree of wrinkled-ness, curvature or flame surface area density have not been extensively validated for any partially premixed engine flame model. Such local properties influence flame path, combustion reliability and pollutant emissions generation.

Partially-premixed combustion modeling is a developing field. A lot of progress has been made in the last decade and more is to be expected. As the combustion communities theoretical understanding of partially premixed flames improves, so should the models and so should SGSC engines.

Chapter 3: EXPERIMENTAL APPROACH

3.1 Optical Engine

The optical engine utilized for these studies is nicknamed and will be commonly referred to throughout this document as the G4VDI engine. The name was chosen based upon the engines mechanical features. It is a gasoline engine (G) that houses four valves (4V) and a high-pressure direct in-cylinder injector (DI). The engine offers superb optical access through its fully transparent cylinder liner as well as its multiple cylinder head and piston bowl windows.

Every sensor, system, nut and bolt on the G4VDI engine was engineered to ensure excellent engine characterization abilities and test-to-test repeatability. The motivation for such a design was twofold. Firstly, to provide certain experimental data for this study. Secondly, to provide high fidelity data for the purpose of comparing G4VDI engine experiments and models in a meaningful manner. The latter motivation requires a much higher standard of equipment quality, control and characterization than the first and years of design, setup and testing were devoted towards the cause. By doing so the data collected for this study will continue to provide value far beyond the final pages of this document; it will serve as a benchmark for future G4VDI modeling collaborations for years to come.

This section will discuss the G4VDI engine's hardware, instrumentation and quality control practices. The G4VDI engine has been used to produce impactful theses and papers by many previous researchers at the Quantitative Laser Diagnostics Laboratory [39, 177]. However, an extensive amount of hardware changes has been made since. The engine has been the focus of

a few recent publications [178, 179] and readers are encouraged to consult these papers and the many to follow to learn more about the G4VDI engine.

3.1.1 Engine Hardware

The engines most relevant mechanical parameters are listed in Table 3-1 below.

Table 3-1: Engine Parameters

Engine Name	G4VDI (Gasoline Four Valve Direct Injection Engine)
Geometric Compression Ratio	8.7
Bore	86.1 mm
Stroke	86 mm
Connecting Rod/Stroke Ratio	1.85
Head Design	Pent-Roof
Piston Design	Custom, optically accessible with bowl
Cylinder Design	Completely optically accessible (fused silica)
Compression Ring Design	Single piece (gapless)
Valves	2 intake (1 throttled near port), 2 exhaust
Primary, Secondary Intake Valve Opening Times	-357, -357 aTDCc
Primary, Secondary Intake Valve Closing Times	-140, -129 aTDCc
Exhaust Valve Opening Time	137 aTDCc
Exhaust Valve Closing Time	-348 aTDCc
Fuel Injector	8-hole, 90° angle
Fuel Injector Orientation	Center of combustion chamber directed slightly off-axis to target spark plug
Fuel Rail Pressure (held constant through testing)	12 MPa

Many of the engines basic features that are listed in Table 3-1 such as its bore, stroke and displacement are production like. It's four-valve, pent-roof cylinder head was specially designed to target the fuel spray from the centrally mounting DI injector towards the spark plug in a

favorable manner as to enable spray-guided stratified-charge operation. The 8-hole, 90° umbrella angle high pressure fuel injector was operated at 12 MPa fuel rail pressure.

The engine was equipped with a “swirl control” throttling valve in one of its two intake ports. When the valve is closed the engines intake charge is restricted to only one of two ports which induced high levels of swirl and tumble into the in-cylinder airflow. When the control valve was wide open the in-cylinder swirl and tumble levels were much lower. These two swirl valve conditions, fully closed and fully open, were both tested in this study and will be referred to as high and low swirl conditions respectively.

A front view of the G4VDI engine can be seen in Figure 3-1 below,

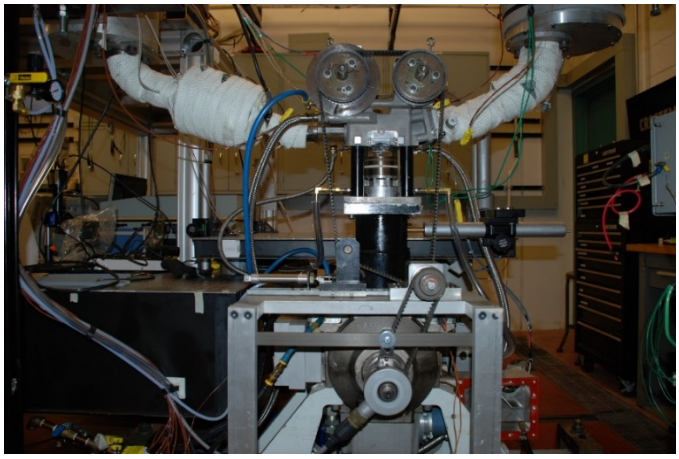

Figure 3-1: Front view of G4VDI engine

Large plenums were mounted to the intake and exhaust runners to stabilize the inlet and exhaust boundary conditions during the tests. The exhaust system was fitted with a mixing can/muffler.

The engine’s roller bearing crankcase and large Bowditch connecting rod were atypical. Hence, only indicated engine performance parameters will be discussed throughout this document. A hydraulic dyno head was attached directly to the rear end of the engine and was used to drive the engine under motored conditions and to provide rolling resistance as needed under fired

conditions. The engine was limited to relatively low speeds (~ <2500 RPM). All of the testing performed in this study was done at 1300 RPM.

The entire cylinder head and liner assembly was removed between tests for cleaning. To enable this, the cylinder head and liner assembly was designed to be easily decapitated and the intake and exhaust systems were mounted to sliding mechanisms that allowed them to be moved away from the head.

The engines optical access was enabled by a transparent cylinder liner, cylinder head and piston windows. All of the windows were machined out of fused silica. The optical components were made out of fused silica and were capable of withstanding very high temperatures. However, the burst pressure of the cylinder liner was about 50 bar peak so engine testing was limited to low loads.

A rear view of the engine is shown in Figure 3-2 below. As will be seen, this is the viewing perspective used by the cameras in this study and will be shown time and time again in this document.

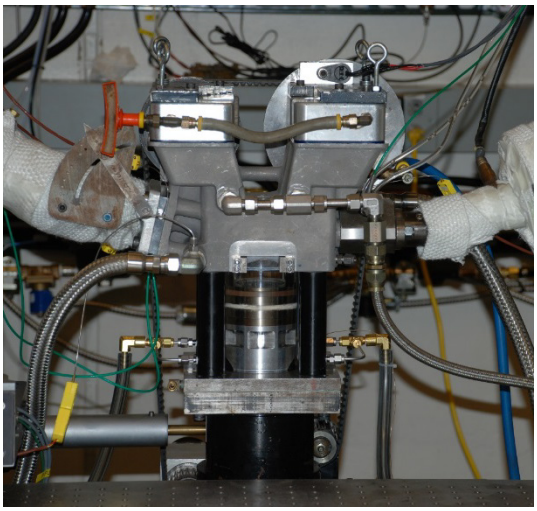

Figure 3-2: Rear view of G4VDI engine

The rear optical access is further magnified Figure 3-3 below. In this image the piston is set at BDC. As can be seen, the top most window (cylinder head window) provides an excellent view of much of the region of the combustion chamber that's contained within the cylinder head. The transparent liner provided superb optical access everywhere below the fire deck. The piston side windows provided optical access into the piston bowl. A head gasket separates the liner from the cylinder head and obstructs a small region of the field-of-view.

Figure 3-3: Optical access from camera side view

A close up view of the optical piston is provided in Figure 3-4. In this study, one of the piston side windows was used for viewing. The larger, centrally located piston window was used to bring the laser sheet illumination into the cylinder.

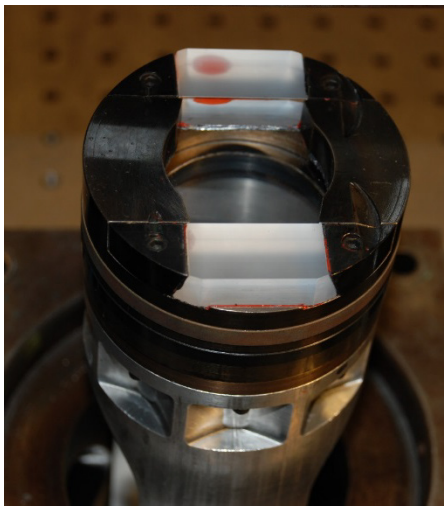

Figure 3-4: G4VDI optical piston

The single piece piston ring was made out of Rulon. It was sized to provide an excellent seal against the glass cylinder liner. The piston and the cylinder liner were constantly cooled by diffuse air cooling jets. Doing so enabled lengthened (2-20 minute) tests.

For safety reasons, the engine was operated and controlled from a control room next-door to the engine itself. Cameras and microphones allowed the engine to be head and viewed from the control room. A variety of acquisition and control system allowed the engine to be piloted and monitored as well as for the mechanical and optical data to be recorded in a synchronized manner.

The engines instrumentation will now be discussed in the mechanical engine diagnostics section.

3.1.2 Mechanical Engine Diagnostics and Control

The engine was extensively instrumented with more than twenty thermocouples, half a dozen low-speed pressure transducers, half a dozen high-speed pressure transducers and an in-

cylinder pressure transducer, mass airflow and fuel-flow meters and an optical crankshaft encoder. The engine test cell was wired with sound signal grounding and EMF noise-reduction procedures to ensure that the signal to noise ratio of all of the sensors was as high as possible.

Although much of the G4VDI engines mechanical instrumentation was installed as standard test cell design practice; the abundance of high speed pressure transducers installed throughout the engines intake and exhaust system, which have been shown in Figure 3-5 below, is unique.

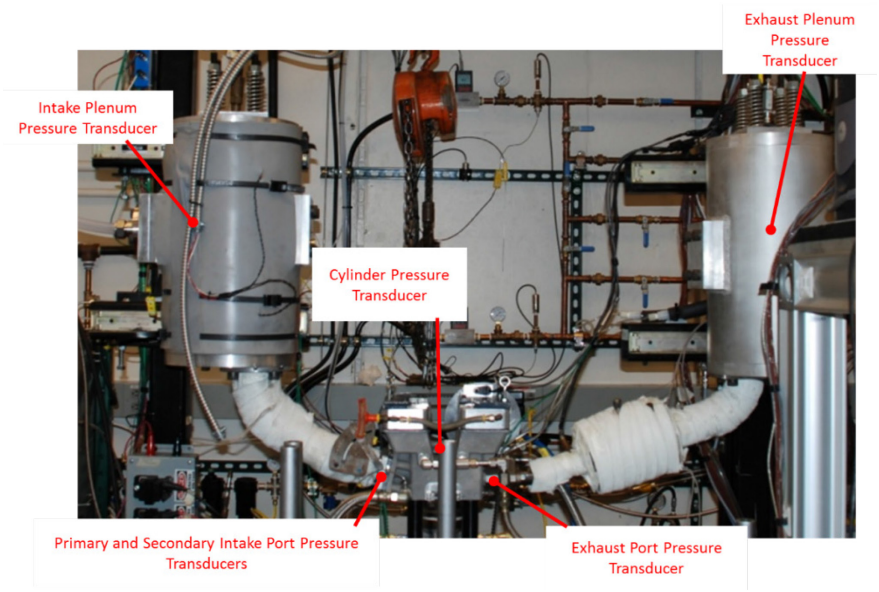

Figure 3-5: High speed pressure transducer locations

Every transducer labeled in Figure 3-5 was complimented by a thermocouple. Together, they enabled the thermal boundary conditions of the engine to be characterized at the temporal resolution (0.5 CAD) of the engine encoder. As will be shown in section 4.1, these boundary condition measurements are of great value in experiment-to-model comparisons. In this study they were used to validate a GT Power model which was used as a tool throughout the study.

During operation, the engine was fed by a critical orifice air-charge system that was designed to provide a constant, highly quantifiable (uncertainty of 0.1% FSV) flow rate to the engines intake system. The fuel system was fit with a mass fuel flow meter for monitoring the engines fueling

flow. From the combination of the two systems, the engines air/fuel mixture (equivalence ratio) could be well quantified during testing. However, being a direct injection engine, the total mass fuel flow scaled with engine speed (approx. +/- 5%). The engine was always operated in an open-loop mode and the fuel injector was always driven at a constant injection duration throughout a given test.

As will be discussed in more detail in 3.2.4.1, a silicon based oil was seeded into the intake system as a tracer for the airflow. The seed oil also acted as an engine lubricant and helped minimize compression ring scuffing and prevent piston seizures. Because the inside of the fused silica cylinder liner could not be temperature controlled, the cylinder wall and piston temperatures during operation are thought to be ever changing. With knowledge of this, testing procedures and combustion based metrics were used in order to assure that the engines steady-state operation was as steady as could be practically achieved. Stable (<2% COV of IMEP) engine operation was common when robust combustion strategies were employed.

Many of the engines most important operational parameters, such as injection and spark timing, was commanded by a prototype General Motors engine controller. The hydraulic dynamometer was also controlled by custom hardware and software that was designed specifically for the application by the manufacturer. The dynamometer was only capable of holding the engine speed constant to within about +/- 30 RPM during a typical fired test.

The thirty-five low speed sensors, including thermocouples, mass flow meters and select pressure transducers (such as those that oversaw critical oiling and fuel systems) were monitored and recorded by a National Instruments (NI) based data acquisition system. The system consisted of a NI CompactDAQ module and an in-house LabView based code. The cDAQ chassis was populated with the appropriate modules to enable the desired input and output signals. The LabView based code displayed sensor values in real time and also recorded them on demand at a rate of 2 Hz.

The high speed sensors, such as the intake, exhaust and cylinder pressure transducers were all monitored and recorded by a Phoenix Combustion Analysis System (CAS) which is an A&D Technologies product. The CAS system was temporally paced via the engine encoders and operated on a crank angle basis.

3.1.3 Post-Processing of Mechanical Engine Data

Mechanical engine data from both the high speed (CAS based) and low speed (LabView based) data acquisition programs was saved and later combined by a MATLAB based algorithm in a common, convenient format. The combined data was then further post-processed within MATLAB as needed.

Since the two data acquisition systems were always started and stopped within a few seconds of each other, the low and high speed data sets were treated as synchronous.

The CAS system automatically calculated and saved many of the in-cylinder pressure based metrics used throughout this study; such as heat release rates, burn fraction profiles and mean effective pressures. Documentation on the algorithms that were used by CAS to perform the calculation can be found in the software's user manual.

In order to calculate indicated heat release calculations CAS required a few parameters to be specified; namely, the start of calculation time and the crank angle ranges for which the compression and expansion polytropic coefficients were to be averaged over. In this study, the heat release calculation was always initiated at the start of ignition, the compression polytropic was always calculated from intake valve closing until 30 bTDCc (just before ignition) and the exhaust polytropic was always calculated from 55 to 130 aTDCc (just before IVO). Heat transfer was neglected in all heat release calculations. Further, since detailed emissions measurements were not made combustion efficiency based corrections to the heat release rates and burn fractions could not be made.

An entire library of MATLAB codes was developed and used to perform a large variety of post-processing tasks, ranging from statistical analysis of engine data, to generating engine data summaries, to verifying that select engine parameters within a given test measured within a given range. The post-processing infrastructure was designed primarily for quality control purposes but also proved great value as a data exploration tool.

3.1.4 Quality Control of Engine Experiments

The G4VDI engine was built to produce exceptionally high quality mechanical data. Quality control procedures were developed to ensure that it did just that.

All engine tests were performed multiple times and the mechanical results were verified to be reasonably consistent. Baseline conditions were chosen, re-run and compared on a regular basis to ensure that engine remained in good health throughout the study. Engineering judgements were necessarily made as to what level of test-to-test consistency was acceptable. There are simply too many monitor able engine parameters to discuss the tolerances for test-to-test repeatability for each sensor in this document. Generally, the repeatability tolerances were specified to be as low as was reasonably possible for the experiments. For example, the intake and exhaust MAP's were maintained within 1 kPa, mass airflows within 0.02 g/s and airflow temperatures at the intake ports within 5 C of specified.

Extensive control charting practices were implemented which enabled day-to-day operational changes in engine performance, if they were to arise, to rapidly be recognized and rectified. Critical engine system flows and leakage rates were measured and verified acceptable regularly. The engines high speed intake and exhaust transducers were re-calibrated daily (relative to an extremely accurate barometric pressure sensor) to compensate for signal drift. Since the engine was completely re-instrumented for this study, all of the engines sensors were in great condition and their performance was verified from their first day in operation until the completion of this study.

Experimental data was compared regularly with a well built and validated GT-Power model. Acceptable ranges for engine operating parameters, such as peak engine pressure, indicated mean affective pressures and mass inlet airflow (per prescribed intake MAP) became well known and were monitored daily. Therefore, by comparison, the mechanical data produced by the engine during the tests included in this study was able to be repeatable and of high quality.

3.2 Optical Diagnostics

Two different optical diagnostic techniques, planar laser induced fluorescence (PLIF) and stereo-particle image velocimetry (PIV) were combined in order to measure in-cylinder equivalence ratio distributions, burned/un-burned gas locations and flow velocities within the optical engine.

Small (~1 micron) silicon oil droplets were introduced into the engines intake air as an in-cylinder tracer for burned/unburned gas regions and a seed for the PIV system. Toluene was introduced into the fuel mixture as a fluorescent fuel dopant which enabled the PLIF system to recognize in-cylinder equivalence ratio distributions.

The optical imaging systems were both low speed and could only operate at speeds below 20 Hz. Both systems also used Nd:YAG lasers for in-cylinder illumination. The PIV laser was fit with frequency doubling crystals which converted its native 1064 nm light into a 532 nm green beam, which was directed into the engine in order to illuminate the airborne silicon oil droplets. It featured a dual cavity design which enabled rapid (10-100 microsecond temporal spacing) double pulsed operation which enabled the PIV system to track the oil particles via the well-developed imaging technique known as frame straddling.

The PLIF system utilized a single cavity, frequency quadrupled Nd:YAG laser which produced a 266 nm ultra-violet beam for Toluene excitation. The UV laser power was measured to be 70 +/- 20 mJ per pulse just upstream of the Bowditch mirror. The UV energy delivered to the

engine was always a little less than measured due to Bowditch mirror reflection and piston window transmission losses. These losses could not be quantified but are expected to be on the order of 10%.

Cylindrical lenses were used to form both beams into thin sheets of nearly constant height of 30 mm of converging thickness. The green and UV beams were overlapped before being directed into the engine. The PLIF and PIV beam thicknesses were focused down to 0.5 mm and 1.5 mm, respectively, inside the cylinder.

The scattered green light (PIV) and fluorescent Toluene signal (PLIF) were captured and recorded by scientific cameras. The stereo-PIV system utilized two s-CMOS cameras and the PLIF system a single CCD camera and intensifier. Both cameras viewed select wavelengths through optical filters which were mounted in front of the camera lenses.

DaVis software [180] which was developed by LaVision GmbH was used to control the lasers and cameras and to synchronize the optical systems with the engine. At the imaging rate of once per every other cycle the cameras were operating at about 5 Hz and the lasers were operating at 10-20 Hz. The exact rate of operation varied by about +/- 5% due to engine speed transients. The DaVis software made the necessary on-the-fly timing adjustments to the imaging systems to ensure that all three laser pulses and the five camera exposures always occurred at the correct engine timing (CAD).

Collectively, the cameras provided a single PLIF image and four PIV images (double frame sets from both cameras) at a single prescribed crank-angle-degree at a recording rate of one image set per every second cycle.

Once analyzed, the four PIV images provided a planar estimate of the in-cylinder flow field that considered all three velocity dimensions. The single PLIF image provided an estimate of the in-cylinder equivalence ratio distribution throughout the cylinder. When combined, the two

systems provided adequate information to discern burned vs unburned gas regions and flame contour information, even under stratified conditions where the disappearance of one tracer or another was not indicative of a flame.

A schematic of the optical hardware setup is shown in Figure 3-6 below,

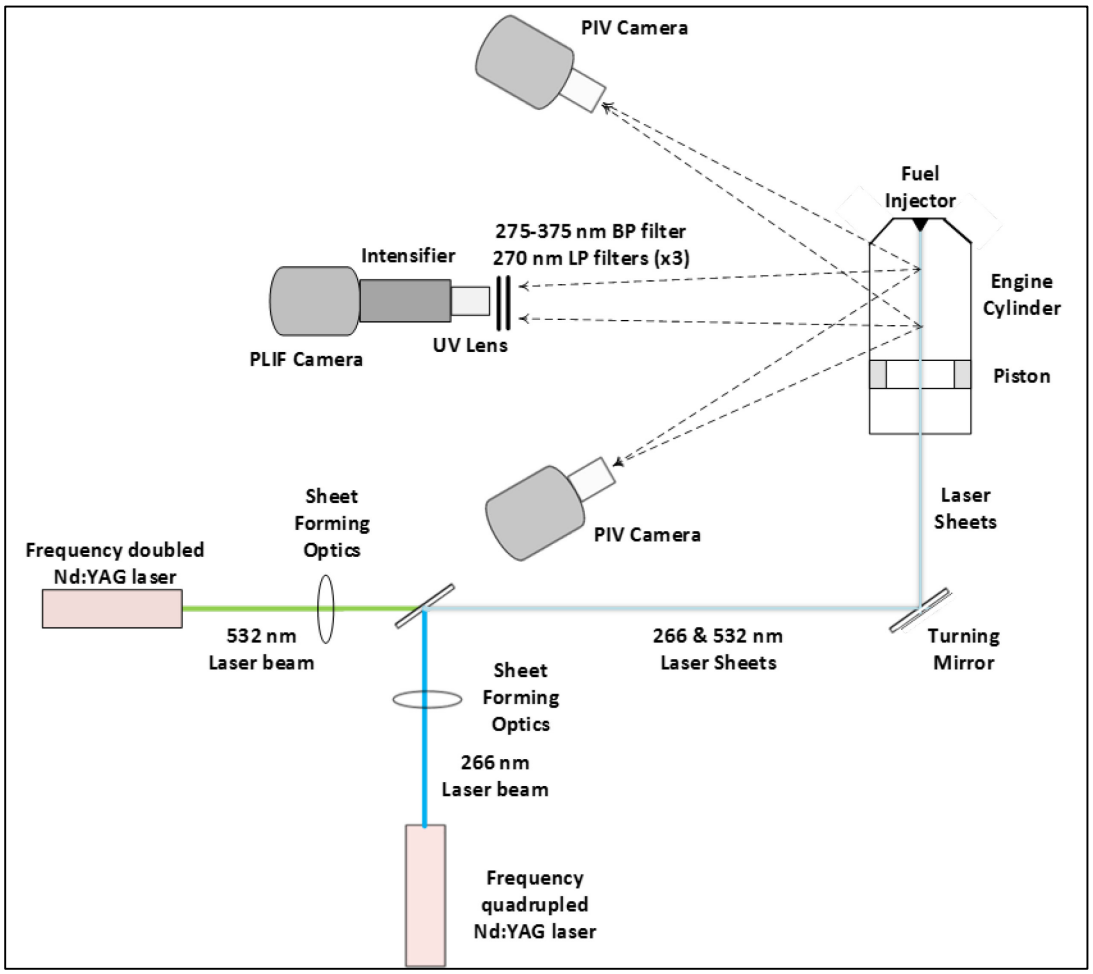

Figure 3-6: Optical imaging setup

A picture of the optical setup from the back (viewing) side of the engine is shown in Figure 3-7 below. The three cameras can be seen near the center of the picture in blue. The PLIF camera in the center has an intensifier mounted to the front of it and is looking at the engine head on. The outer two stereo-PIV cameras are looking at the engine at 15 degree angles (30 degrees total between the two cameras line-of-site).

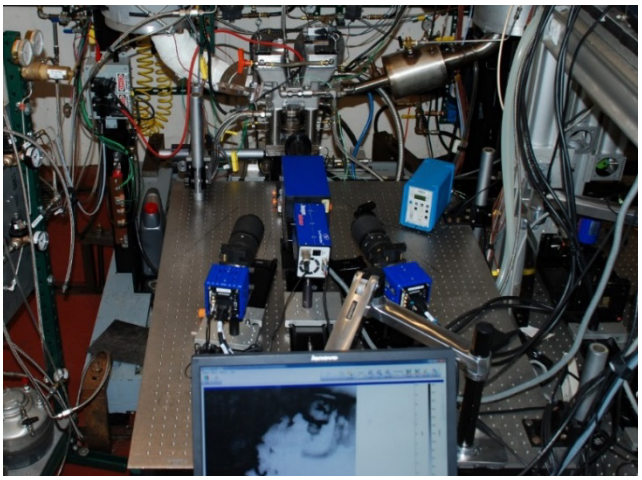

Figure 3-7: Picture of Camera setup

The field-of-view of the PLIF and PIV systems are shown in Figure 3-8 below.

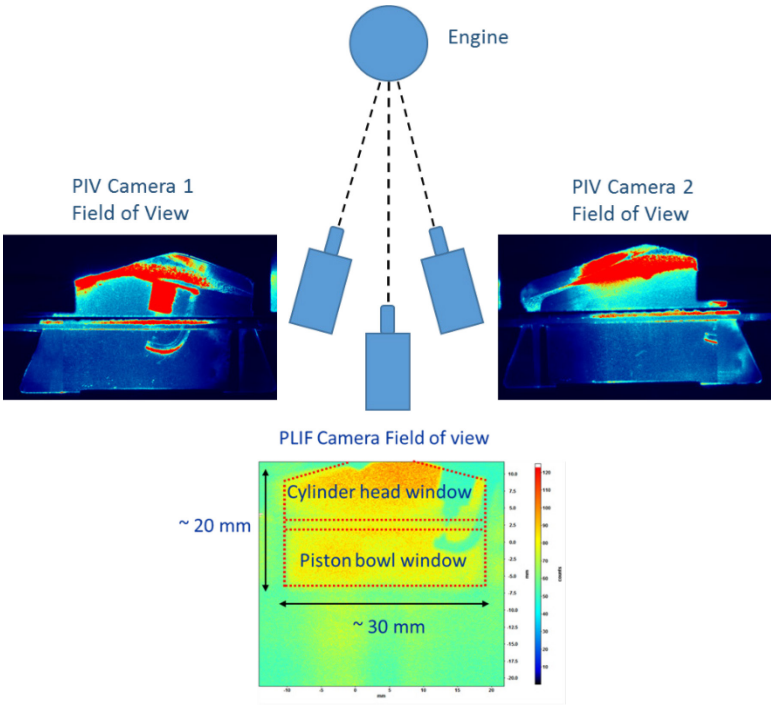

Figure 3-8: Field of view of PLIF and stereo-PIV cameras

These fields of view utilize the entire optically accessible area of the engine which in total is about 30 out of 86 mm of the engines bore. The optical component selection, data collection and post-processing procedures will now be discussed in greater detail.

3.2.1 Optical Components

The first step in the optical data acquisition process was to design and install the two systems. The design was guided by a wealth of literature, documentation and in house experience that existed within the Quantitative Diagnostics Laboratory at the University of Michigan. Proven diagnostic methods were chosen so that little optical diagnostic development was required for the study.

The two Nd:YAG lasers were chosen for use based upon their availability, robustness and ability to deliver the desired wavelengths. An in-line LaVision Energy monitor was installed into the beam path of the UV laser, just upstream of the beam forming optics. The electrical output of the energy meter was recorded by the engines high speed data acquisition system which enabled shot-to-shot energy corrections to be made during PLIF image post-processing.

The sheet forming optics were chosen following the guidelines discussed in Raffel et al. [181] in order to meet the desired sheet dimensions at the engine of 30 mm wide, 0.5 mm thick for the PLIF UV sheet and 1.5 mm thick for the green PIV sheet. For both systems, a pinhole aperture was used directly downstream of the laser to trim off the weak periphery of the laser beams. A combination of a single converging and two diverging spherical lenses were chosen to form the laser sheets.

Appropriate reelection mirrors for the two wavelengths (266 and 532 nm) were chosen to direct and combine the two sheets and a specially coated Bowditch reflection mirror, which can be seen in Figure 3-9, was used to direct the two beams into the engine.

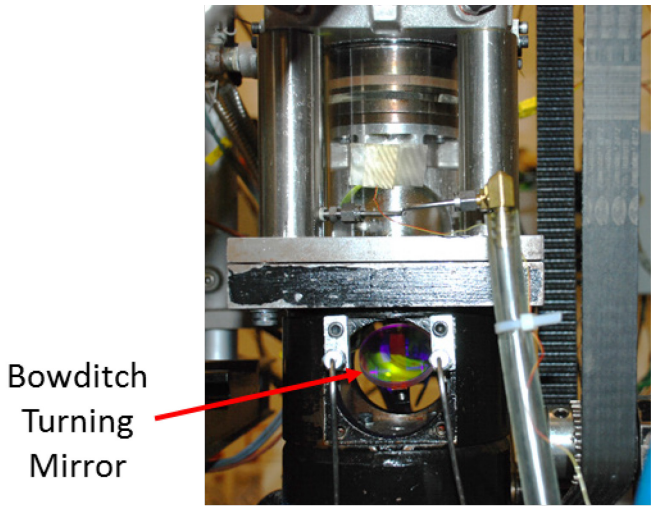

Figure 3-9: Bowditch port turning mirror that reflects laser sheet up into the engines cylinder.

The light collection system (i.e. cameras, lenses, optical filters) were setup on an optical table mounted on the backside of the engine. The PLIF camera viewed the engine head-on and the two stereo-PIV cameras viewed the engine at an included 30 degree angle relative to each other, as was necessary for the system to recognize out-of-plane charge velocities and to correct the in-plane velocities for parallax effects.

The LaVision Imager Intense Flowmaster 3S PLIF camera was mounted directly to a LaVision IRO image intensifier which amplified the weak fluorescent light signal produced by laser excitation into a stronger signal for which the camera could register. A 105 mm, f/2 UV lens was mounted to the intensifier with an appropriate thickness of lens spacers in-between to provide a desirable magnification. A 275-375 nm bandpass (UG-11) filter was mounted in front of the intensifier to limit undesirable light from being collected by the PLIF camera. Two identical 275 nm long-pass filters were also installed in front of the intensifier to limit the intensity of laser light reflection noise registered by the PLIF camera.

The two LaVision Imager s-CMOS cameras were equipped with 200 mm, Nikor AF Micro lenses which were operated at f/22 at a focal length of about 1 meter. They were both fit with Scheimpflug adapters to enable the proper angled focus and 532 nm bandpass filters to

minimize the collection of undesirable light. The small stereo angle of 30 degrees was chosen to provide the two cameras with the maximum field of view inside the engine. However, it is a smaller angle than is typically used for stereo measurements.

The cameras and lasers were wired to and controlled by a LaVision Programmable Timing Unit which was operated by DaVis software on a PC computer. The optical system communicated with the high speed engine data acquisition system so that the optical and mechanical engine data could later be compared in a synchronous manner.

3.2.2 Laser Sheet Locations

The plane of viewing for both the PLIF and PIV techniques was determined by the location of the laser illumination. Remember that the two spatially overlapping laser light sheets (green for PIV, UV for PLIF) were sent into the engine via a reflection mirror in the Bowditch port. The sheets traveled through the engines piston upwards until terminating on the cylinder head itself. The sheet was always setup to be perpendicular to the PLIF cameras field-of-view (normal to the PLIF camera in Figure 3-7) and 15 degrees relative to each of the stereo-PIV cameras.

The light collected, i.e. the scene viewed from both imaging systems originated from only a small portion of the cylinder. The laser sheets volumes were only <1% of the total cylinders volume, so it was crucial that the location of the sheets be chosen wisely so that the region illuminated was interesting (i.e. flames could be visualized in the region during testing).

Under homogeneous-charge condition, the engine flames necessarily propagated throughout the entire cylinder during every fired cycle. Therefore, the choice of location was not critical, as any choice of laser sheet location would have resulted in interesting images. Under stratified-charge condition, the choice of sheet location was much more difficult as the flames were more spatially distributed and different sheet locations offered completely dissimilar perspectives on the stratified-charge combustion events.

Through trial and error testing, two different viewing planes were chosen for this study. Their locations are identified in Figure 3-10 below.

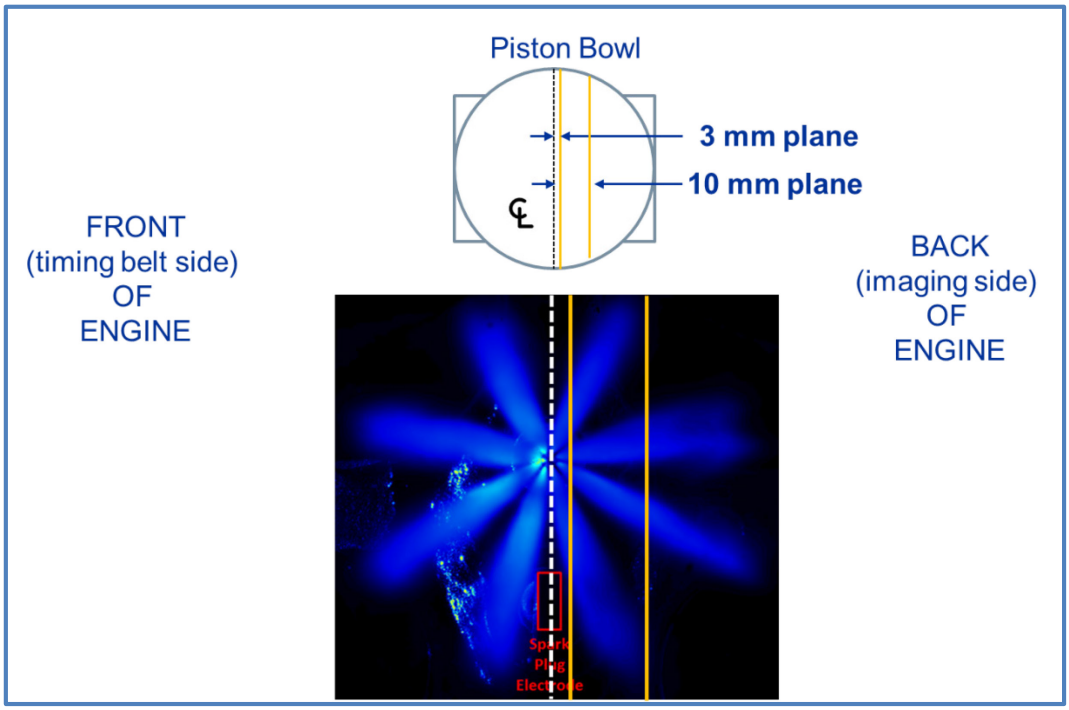

Figure 3-10: Location of laser sheets inside the engines cylinder

The three millimeter offset imaging plane was chosen to be as close to cylinder center as possible, while still managing to avoid impinging the laser sheet upon the spark plug. Imaging was performed at this plane under both the homogeneous and stratified-charge conditions. Under stratified-charge condition it provided a good perspective of one of the ignited (spark plug coincident) fuel plumes and one of the plumes on the opposite side of the engine.

The ten millimeter offset imaging plane was chosen specifically for viewing the stratified-charge condition. Its location provided a different perspective of the stratified combustion event than the three millimeter location. Homogeneous-charge images were not acquired in this plane.

3.2.3 Planar Laser Induced Fluorescent Imaging

Planar Laser Induced Fluorescence (PLIF) images were taken for the purposes of quantifying equivalence ratio distributions (under stratified-charge conditions) and burned/un-burned gas regions. In order to enable the diagnostic, Toluene was added as a 25% by liquid volume fluorescing dopant to iso-octane and the mixture was used to fuel the engine.

Planar Laser Induced Fluorescence (PLIF) techniques have been widely employed within the combustion research community for the purposes of quantifying combustion species and temperatures [182, 183]. Hundreds of peer reviewed articles have been written on the development and utilization of PLIF diagnostics. Toluene has been successfully demonstrated as a fluorescent tracer for in-cylinder temperature and equivalence ratio diagnostics [184, 185]. Therefore, Toluene was chosen for these studies and whenever possible, developed and proven PLIF diagnostic techniques were used.

3.2.3.1 Choice of Toluene as Fluorescing Fuel Dopant

Toluene was chosen as a fluorescing fuel dopant for these studies. It was selected for a few reasons, the greatest of which being that it was demonstrated to be capable of providing a strong, quantifiable fluorescent signals needed to enable the in-cylinder equivalence ratio imaging [184]. Further, it was readily excitable by a frequency quadrupled (266 nm light output) laser which was available for use.

As a common gasoline additive, the addition of Toluene to the previously pure iso-octane fuel mixture did detract from the realism of the engine study. Toluene's most important physical properties, such as its octane rating and volatility are similar to that of iso-octane. Comparisons between the two fuels can be found in the Appendix A.

The exact choice of dopant composition (25% Toluene/75% iso-octane by liquid volume) was determined by trial-and-error experimentation. The mixtures exhibited a high enough dopant concentration to provide a strong signal-to-noise ratio but also small enough concentration avoid excessive attenuation affects.

3.2.3.2 PLIF Image Collection

The PLIF diagnostic was low speed and images were acquired at a temporal rate of one image per every other cycle. At the 1300 RPM conditions tested this resulted in an imaging frequency of about 5.4 Hz. Each image was taken at a single engine position (CAD) during the test with a temporal accuracy of +/- 0.5 CAD of the prescribed timing. Due to limitations in camera memory, engine cleanliness, and safe run time only 100 PLIF images could be acquired per test. The 100 image tests were repeated three times for a total of 300 acquired images per test condition. The engine was necessarily disassembled and cleaned between every imaging test.

The PLIF camera was equipped with an intensifier which was used at a gain of 8 and a gate-width of 50 ns. The short gate width prevented nearly all non-laser induced sources of erroneous light from being registered by the PLIF camera.

PLIF images were acquired under normal engine operating conditions with the engine firing. Immediately after every PLIF imaging test but before bringing the hot engine to rest, a few additional sets of images were acquired for the purpose of correcting and quantifying the images. These additional images were always taken with the engine operating in a motored state.

The first of these additional image sets taken was of the “background”; whereas the term background refers to all undesirable (non-Toluene LIF) signals registered by the camera. These images were acquired with both the fuel and ignition systems disabled. The two largest

contributors to the background signals were solid surface laser reflections and silicon (PIV) seed oil fluorescence.

After the background image was collected, additional “flat field” image sets were taken for the purposes of quantifying the signals from the original PLIF images. The flat-field images were used to create an intensity-to-equivalence ratio scale which could be used to scale the original PLIF images. The flat-field images were taken under homogenous-charge (SOInj at 310 bTDCc) conditions at fixed and known equivalence ratio’s with the ignition system disabled. Under the flat-field image conditions, the Toluene tracer distribution was uniform throughout the cylinder and so the intensity profile through the images tended to look “flat”; hence the choice of terminology.

Laser energy was measured by a laser power meter and recorded on an image-by-image basis. The measurements were used to perform shot-to-shot energy corrections to the PLIF images.

This next sections will discuss the many methods used to process the raw PLIF images into the final products that will be presented in Chapter 5 and 6.

3.2.3.3 Spatial Calibration of PLIF Images

The PLIF images were naturally recorded by the camera as a rectangular 1376 x 1040 pixel map. The pixel map was converted into a spatially correct map by a spatial calibration procedure. The base procedure used was that which is outlined and recommended by LaVision considering the hardware and software (Davis 8.3.0) utilized. However, the challenges of the engine environment and the complexity of the three camera setup complicated the base procedure and some custom procedures had to be established.

The basic spatial calibration approach was to acquire an image of an optical target of known dimensions and to use the scale of the target to scale the image itself. The target used, which

was made by LaVision and can be seen in Figure 3-11, was a plate with every-other dot separated by 5 mm. It was positioned within the engine so that its face was in the location where the laser sheet would normally reside.

The target used for the PLIF calibration was actually designed for calibrating the "3D" stereo-PIV system and as such, it featured two 1.05 mm axially offset planes. The target was overly-complex for the PLIF system but necessary for the stereo PIV calibration. Maintaining a common target allowed the two systems to be calibrated jointly and enabled all three cameras to maintain excellent spatial overlap.

The spatial calibration target itself was too large to fit into the engine; so measures were taken to reproduce the optics of the engine environment (cylinder head windows, cylinder and piston windows) without the entire engine actually being installed in front of the camera. For example, Figure 3-11 below shows an engine mock-up used to acquire a spatial calibration image by mimicking the presence of the cylinder head (and its optical access window) without the bulky head being installed.

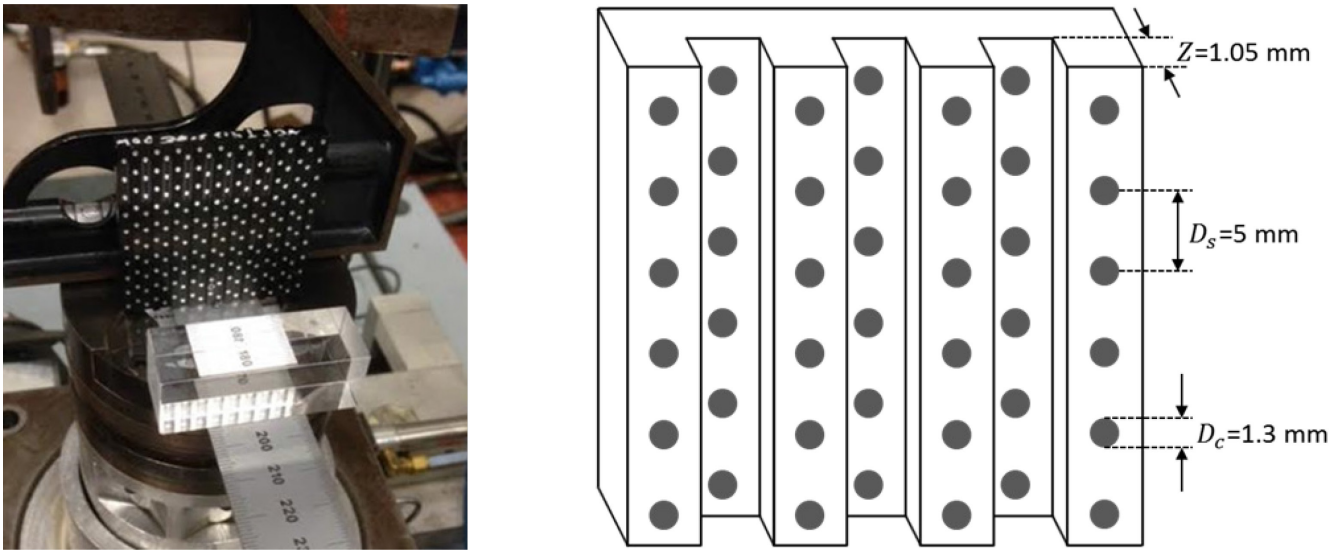

Figure 3-11: Picture of cylinder head mockup and schematic of optical target used for the spatial calibration procedure

Once the calibration images were acquired, procedures suggested by the user's manual for the DaVis software [180] were followed and a pinhole model was selected to map the image and correct for any spatial distortions caused by the optics. An example of a successful calibration result can be seen in Figure 3-12 below.

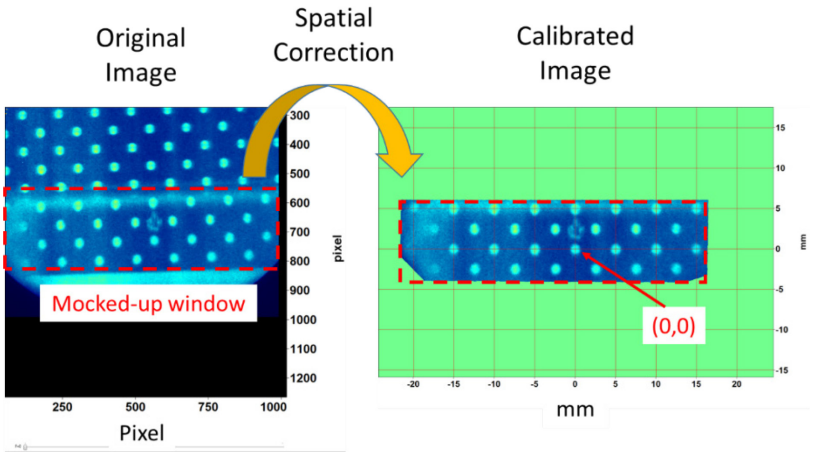

Figure 3-12: Spatial calibration image in both its original and corrected state

The image on the left of Figure 3-12 is as acquired from the target mock-up and the image on the right is post-calibration. Notice the goodness of fit shown by the grid on the calibration image. The stereo-PIV spatial calibration was always performed immediately after the PLIF calibration with the target remaining in place, as will be discussed in greater detail in 3.2.4.2.

3.2.3.4 PLIF Image Equivalence Ratio Quantification

The PLIF images were processed to reveal equivalence ratio distributions. The equivalence ratio quantification was only necessary for the stratified-charge tests. The homogeneous-charge mixtures were already of known and constant composition so the quantitative values of equivalence ratio discovered through quantification were somewhat uninteresting. However, the same quantification procedures, which will be discussed below were applied to all PLIF images in this study.

3.2.3.4.1 Relationship Between Measured Signal Intensity and Equivalence Ratio

Prior to presenting the processing procedures used in this study, a basic introduction to some relevant PLIF quantification theory will first be presented here. The underlying spectroscopic physics that enable quantitative PLIF diagnostics are complex and a complete description of them is beyond the scope of this document. However, readers who seek a more in-depth background on the topic are encouraged to consult any of the many great publications on the topic, including [186-188].

The quantity of photons released from a fluorescent substance is typically referred to as a signal. So long as laser excitation is relatively weak, a LIF signals strength varies proportionally to the power of the laser light used for excitation (P_{laser}), the tracer concentration (n_{tracer}), the absorption cross section, $\sigma_{abs}(\lambda, T)$, which varies with both excitation wavelength and ambient temperature, and the fluorescent quantum yield, $\emptyset_{fl}(\lambda, T, n_i)$, which varies with excitation wavelength, ambient temperature, pressure and the collision frequency (or molecular concentration) with other molecules.

$$S \sim P_{laser} n_{tracer} \sigma_{abs}(\lambda, T) \emptyset_{fl}(\lambda, T, P, n_i)$$

The fluorescent quantum yield of toluene is very sensitive to the local oxygen number density (n_{O_2}) due to a well-documented phenomenon known as oxygen quenching. The fluorescent signal achieved from toluene traced mixture subject to oxygen quenching can be described by [189]

$$S \sim \sigma_{abs}(\lambda, T) \frac{k_{rad} n_{Toluene}}{k_q + k_{q,O_2} n_{O_2}}$$

When $n_{O_2}$is sufficiently strong than the signal achieved from toluene LIF becomes approximately proportional to equivalence ratio.

$$S \sim \frac{n_{Toluene}}{n_{O_2}} \sim \Phi$$

Reboux et al. [184] found this linear relationship to hold true when P_{O_2}>0.6 bar at 296 K. This linear relationship between signal and equivalence ratio is very convenient but not always true. In fact, the linear assumption has been proven to be un-true under some engine like conditions when charge temperatures are sufficiently high [185]. In this study, the linear relationship between S and Φ is assumed.

Following the assumption of Reboux et al.; at fixed temperatures, pressures and species concentrations the relationship between the fluorescent signal recognized from the engine experiments and equivalence ratio can be simply stated as,

$$\Phi = \frac{\Phi_{flatfield}}{I_{flatfield} - I_{background}} (I_{Image} - I_{Background})$$

Where I_{Image} represents the intensity of the PLIF image itself, $I_{Background}$ is the intensity of the background to be subtracted from the PLIF image, and $\frac{\Phi_{flatfield}}{I_{flatfield} - I_{background}}$ is the constant ratio of equivalence ratio to intensity which is drawn from a flat-field image.

This basic linear relationship was used to quantify the measured PLIF intensities in terms of equivalence ratio. However, it could not be directly applied due to the inherent differences in temperature, pressure and molecular concentrations that exist between the $I_{flatfield}$, $I_{Background}$ images and the I_{Image} images. Remember that the former two images were taken under motored and the latter under fired engine conditions. Due to both combustion induced compression and hot residual gas trapping, the charge temperature, pressure and n_{O_2} concentrations were higher under the fired (I_{Image}) conditions than their complimentary motored ($I_{Background}$ and I_{Image}) conditions . Therefore, prior to applying the linear

relationship, intensity corrections were made to the fired (I_{Image}) images to compensate for the mixture state differences.

3.2.3.4.2 Background Image Determination

Background images ($I_{Background}$) were acquired immediately after every PLIF imaging test. The background images provided a good estimate of the unwanted light signals that were present during the PLIF imaging tests. However, the experimentally acquired background images were found to be up to 10% inaccurate in small, select regions. This inaccuracy was acceptable under homogenous-charge condition where the PLIF images where image intensities were only to be qualitatively interpreted as burned/un-burned zones. Therefore, the acquired $I_{Background}$ images were used for the homogeneous-charge test post-processing. However, the inaccuracy was deemed unacceptable under stratified-charge conditions where the PLIF images were to be interpreted quantitatively and so a new, more accurate background correction technique was developed and used for post-processing of the stratified-charge tests.

The cause of the inaccuracy (differences between the measured $I_{Background}$ and the actual background in the PLIF imaging tests) was mostly due to the fact that the $I_{Background}$ images were taken under motored conditions and the I_{Image} images under fired conditions. During fired conditions the engine windows tended to collect soot. During motored conditions the engine windows tended to collect seed oil. In particular, the seed oil showed a tendency to collect on certain regions of the engines windows during the background tests which led to high background signals in the affected regions. Since there was no means of acquiring background images under fired conditions there was no experimental means of rectifying the issue.

Therefore, under stratified-charge conditions, a calculation based correction scheme was devised based upon two different flat-field images ($I_{flatfield,1}$ and $I_{flatfield,2}$). Remember that the two flat-field images were taken at different equivalence ratios (Φ=0.2,0.4).

Assuming a linear relationship between the PLIF signal and equivalence ratio.

$$\Phi_{flatfield} = c\left(I_{flatfield} - I_{Background}\right)$$

Where c is a constant to be solved and $\Phi_{flatfield}$ is the constant, spatially uniform flat-field equivalence ratio. Considering the two flat-fields images and re-arranging the equation yields,

$$I_{\substack{Background \\ (calculated)}} = \frac{\Phi_{flatfield,2}}{\Phi_{flatfield,2} - \Phi_{flatfield,1}} I_{flatfield,1} - \frac{\Phi_{flatfield,1}}{\Phi_{flatfield,2} - \Phi_{flatfield,1}} I_{flatfield,2}$$

Whereas $I_{\substack{Background \\ (calculated)}}$ represents a calculation based background-estimate. This estimate was used to correct the stratified-charge PLIF images.

An example of both a measured and calculated background image is shown in Figure 3-13 below, along with their subsequently processed homogeneous-charge flat-field (combustion free) PLIF images. The Φ=0.34 homogeneous-charge image itself was used as the $I_{flatfield,2}$ in the background image calculation and a leaner (Φ=0.2) flat-field image was used as the complimentary$I_{flatfield,1}$.

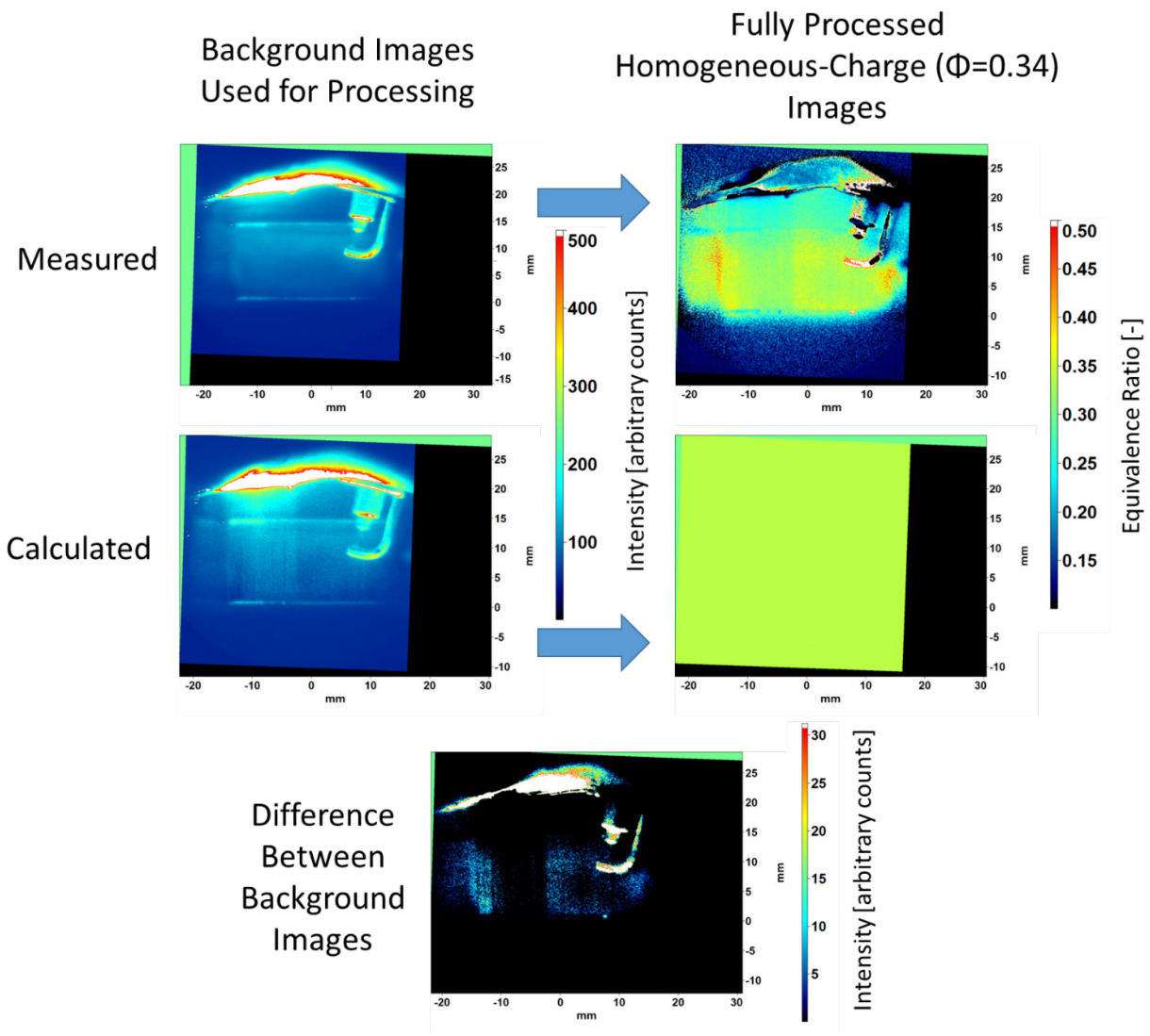

Figure 3-13: Example of measured vs calculated background images and their impact on the processed PLIF results of a very lean (Φ=0.34) homogeneous-charge condition.

Notice that the measured background image led to PLIF quantification errors of up to 50% in select regions of the fully processed image. The calculated background, by definition, produced a perfectly quantified PLIF image. The bottom image in Figure 3-13 shows that difference in intensity between the measured and calculated background images was actually small, only about 10 counts. This small signal difference was significant under such lean homogeneous-charge conditions but much less so under stratified-charge conditions. The measured background inaccuracy under stratified-charge conditions was estimated to lead to < 5% errors in equivalence ratio quantification. However, the calculation based background subtraction

procedure presented here is thought to have largely rectified the issue and reduced the background subtraction error substantially.

3.2.3.4.3 PLIF Image Intensity Corrections

The PLIF images (I_{Image}) were acquired under fired conditions. The flat-field images ($I_{flatfield}$) were taken under motored conditions. Corrections were made to the PLIF images in order to account for the differences in in-cylinder conditions so that accurate equivalence ratio estimates could be made.

Remember that the first intensity correction made to all of the images was a laser energy correction. Within the weak excitation regime the PLIF signal scales with excitation energy,

$$S \sim P_{laser}$$

Since the shot-to-shot laser energy was recorded; all of the images were simply normalized relative to their measured laser energy. This was the first intensity correction to be made.

The difference in in-cylinder condition between the I_{Image} and $I_{flatfield}$ was significant enough to induce 5-50% errors if not properly accounted for, depending on the image timing. Early in the combustion cycle the difference in conditions was relatively minor. For example, at the time of ignition the differences were 0 bar in pressure, 20 C in temperature and 3% in oxygen number density. However, by TDC the differences were 5 bar in pressure, 75 C in temperature and 30% in oxygen number density.

In order to make the proper P, T and n_{O_2} corrections to the PLIF images, the quantities themselves had to be estimated. In-cylinder pressure was the easiest of the quantities to estimate as it was directly measured via the in-cylinder pressure transducer.

Unburned gas in-cylinder temperature estimates were made based upon a GT-Power model that will be discussed in 4.1. The temperature estimate results will also be shown in Figure 4-6. These estimates were verified to be reasonable in comparison to other thermodynamic polytropic-relation based estimates and the uncertainty in the temperature estimates are thought to be about +/- 50 C.

The oxygen number density was estimated based on the other in-cylinder state estimates. Since the in-cylinder oxygen species fraction was weakly dependent on the quantity and composition of trapped residual gasses the trapped residual gas fraction was necessarily estimated. Two methods were used to do so, the first of which was based on the imperial practiced developed by Mrisky et al.. [190] and suggested by Ortiz-Soto et al. [191]. Secondly, GT Power based model estimates were made. Both methods agreed that the trapped residual mass fraction at the start of combustion was 8-14%, depending on the condition.

To compensate for these in-cylinder condition induced differences between the PLIF image intensities and the flat-field images; the two image sets were scaled with respective absorption cross sections, $\sigma_{abs}(\lambda, T)$, fluorescence quantum yields $\emptyset_{fl}(\lambda, T, P, n_i)$ and unburned charge average Toluene number densities.

Absorption cross sections were calculated as a function of temperature based on flow cell measurements taken by Koban et al. [192]. Koban et al. presented the cross sections in the form of a chart. For this study the data was manually extracted and fit with a third order polynomial, as can be seen in Figure 3-14 below.

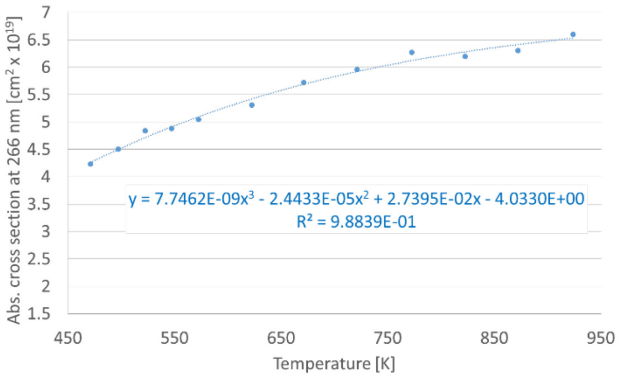

Figure 3-14: Polynomial fit of temperature dependent absorption cross section data provided by Koban et al. [192] for Toluene excited by 266 nm light.

Fluorescent quantum yields ($\emptyset_{fl}$) were estimated based upon a product of correction relations presented by Faust et al. [193] based upon relations originally presented by Koban et al. [194]. These relations consider the temperature, pressure and n_{O_2} dependencies of Toluene fluorescence from a range of 300-1000K and 1-10 bar absolute pressure. The complete relation suggested by Faust et al. is shown in Figure 3-15 below with a sign corrected in red on the B_3 term. This sign error of Faust et al.'s [193] was discovered during this study and is the result of a simple typo. The authors have been informed and they are in the process of making the necessary correction to the publication.

$$\phi_{\text{rel}} \propto \tau_{\text{eff}} \propto \left(\frac{A_1(T)}{1+k_{\text{SV},1}(T)n_{O_2}} + \frac{A_2(T)}{1+k_{\text{SV},2}(T)n_{O_2}}\right) \times \left(B_1(T)\exp\left(-\frac{p_{\text{tot}}}{B_2(T)}\right) + B_3(T)\right)$$

Parameter	Expression
$B_1(T)$	$-8.713 + 0.0574T - 1.22\times10^{-4}T^2 + 1.12\times10^{-7}T^3 - 3.80\times10^{-11}T^4$
$B_2(T)$	$3.32 - 1.39\times10^{-3}T$
$B_3(T)$	$7.76 - 0.0465T + 1.06\times10^{-4}T^2 - 1.06\times10^{-7}T^3 + 3.97\times10^{-11}T^4$

Temperature T is in K

Figure 3-15: Fluorescent quantum yield correction relations provided by [193]

Further, in this study the fluorescent quantum yield relations were extended to higher oxygen concentrations than the relations were designed and validated at. Under some conditions the

$k_{SV,2}$ term, which can be found in its complete form in Koban et al. [194] produced unphysical values. To rectify this issue A_2 was set to zero under conditions when $K_{SV,2}$ was found to be less than or equal to zero. With that, the relations worked well.

After the laser power, pressure, temperature, oxygen number density, Toluene number density corrections had all been made to the PLIF images they could be used in the linear relation to quantify equivalence ratio.

3.2.3.4.4 Equivalence Ratio Quantification (Flat-Field Normalization)

After the PLIF (I_{Image}) and flat-field ($I_{Flatfield}$) images had been laser energy corrected, background subtracted and intensity corrected relative to each other; they were deemed completely corrected and will therefore be labeled here as $I_{\substack{Image \\ Corrected}}$ and $I_{\substack{Flatfield \\ Corrected}}$ respectably.

Considering the corrections the linear image intensity to equivalence ratio equation in 3.2.3.4.1 can then be further reduced to

$$I_{\Phi} = \Phi_{flatfield} \frac{I_{\substack{Image \\ Corrected}}}{I_{\substack{Flatfield \\ Corrected}}}$$

Where I_{Φ} represents the PLIF image which is quantified in terms of equivalence ratio and $\Phi_{flatfield}$ represents the scalar value of the flat-field images homogeneous-charge equivalence ratio.

A visual example of how this equation was applied to the images is shown in Figure 3-16 below.

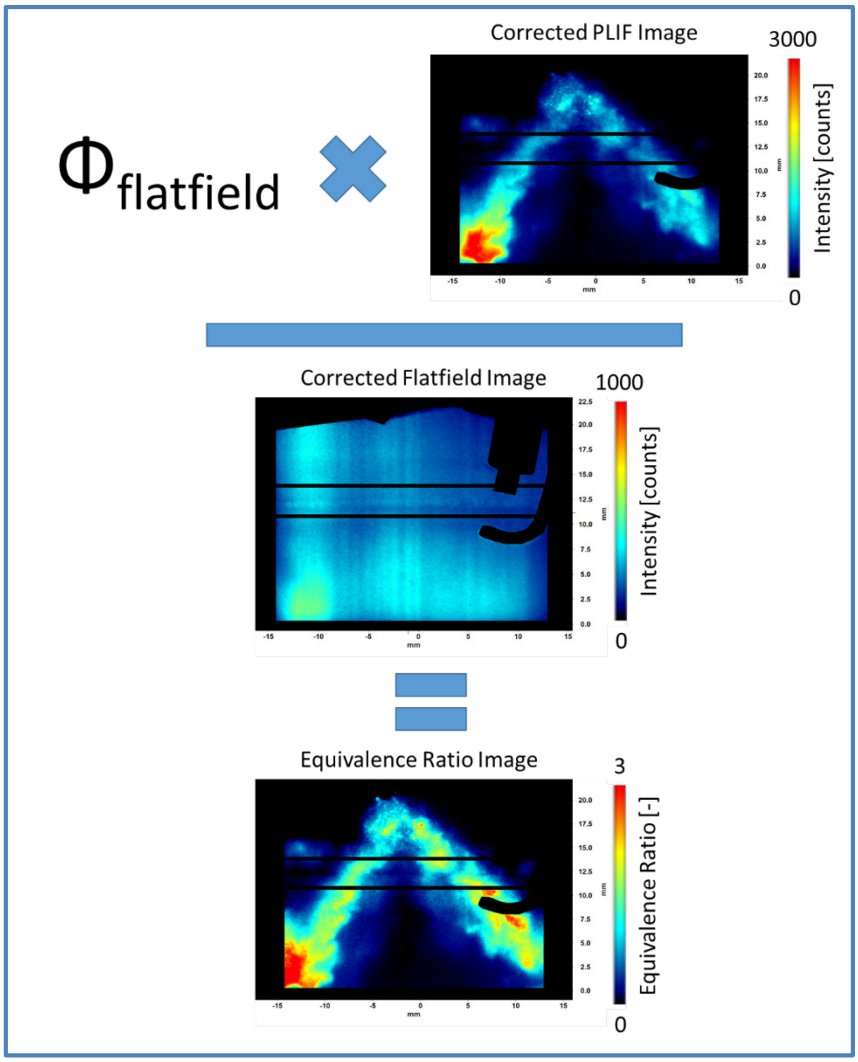

Figure 3-16: Flat-field normalization (equivalence ratio scaling) of PLIF image

The final image in Figure 3-16 is fully quantified in terms of equivalence ratio. It is an example of the final product of the PLIF imaging diagnostic.

The image itself is one of a developing stratified-charge fuel jet. Recognize that a few corrupted regions of the image have been masked out in black. Namely, the engines solid surfaces, such as the cylinder head and spark plug have been blacked out. Two horizontal lines have also been used to cover regions near the cylinder head gasket and piston top. The latter two regions were only slightly corrupted under certain conditions and will be shown unmasked whenever possible.

3.2.3.4.5 PLIF Equivalence Ratio Quantification Uncertainty

Uncertainties in the equivalence ratio measurements arose due to multiple sources of signal bias and noise. Since the PLIF signal strength was sensitive to changes in in-cylinder conditions, such as changes in charge pressures and temperatures, so was the equivalence ratio quantification uncertainty as well. The uncertainty estimate provided here is based upon the in-cylinder conditions for the stratified-charge condition that will be summarized in 4.4.5 that was chosen for the stratified-charge wrinkled-ness study in Chapter 6.

Bias equivalence ratio measurements uncertainties resulted from a combination of cycle-to-cycle fluctuations in in-cylinder state (pressure, temperature and oxygen concentrations), the inexactness of in-cylinder state estimate inaccuracies and the PLIF image correction procedures, and laser beam attenuation effects.

The in-cylinder state based uncertainty was driven by both cycle-to-cycle engine variability and inaccuracies in the state estimation. In-cylinder pressure was well quantified by a pressure transducer but varied from cycle to cycle by as much as 1 out of 20 bar due to the stochastic nature of the stratified-charge combustion. The images were not corrected for the cycle-to-cycle fluctuations. The in-cylinder un-burned gas temperature probably only varied from test-to-test by about +/-30 C but could only be estimated with an accuracy of about +/-50 C. The Oxygen concentration varied about +/- 5% in a linear manner with respect to in-cylinder pressure. Considering the FQR relationships shown in Figure 3-15, the measurement bias uncertainty induced by uncertainty in in-cylinder temperature was about 20%, in Oxygen concentration was about 5% and in pressure was <1%.

Laser beam attenuation affects induced equivalence ratio bias uncertainty. Attenuation magnitudes throughout the cylinder were estimated based upon the Beer-Lambert Law to be less than 1% FSV under typical, liquid-free stratified-charge conditions. When present, liquid fuel would have acted as a strong local beam attenuator. However, liquid fuel conditions were

avoided as much as possible during the study and liquid fuel attenuation effects have therefore been disregarded from this uncertainty estimate.

The accuracy of the intensity correction procedure, including the usage of the relationships presented in Figure 3-15 is inherently uncertain. Less refined versions of the relations were used in an engine [189] and found to be accurate within +/-10%. Because these relationships were used in this study at higher pressures and oxygen concentrations than they were designed for a higher correction induced bias uncertainty of 15% was assumed. Combining all bias uncertainty sources together through a sum-of-square approach yields a total value of 25%.

Noise based equivalence ratio uncertainties arose due to variances in in-cylinder state, laser power and camera/intensifier performance from image to image. In order to assess the noise related uncertainty the flat-field intensities in the piston bowl region of four 100 cycle tests were assessed. Under such combustion-free conditions the in-cylinder state was reliable enough for most bias errors in florescent intensity measurements to be neglected. The COV in image intensity of the four tests measured to be 7%. Therefore, the 95% standard confidence interval of two shot-to-shot measurements, which can be considered the uncertainty, was 14%.

Combining the bias and noise based equivalence ratio uncertainties through the sum-of-square approach yields a total equivalence ratio measurement uncertainty of 29%.

3.2.4 Stereo-Particle Image Velocimetry Imaging

Particle image velocimetry (PIV) is an optical diagnostic technique that relies upon the tracking of flow-born particles to reveal flow velocities, both in magnitude and direction. Typically, PIV diagnostics utilize one camera and a double-pulsed light source to acquire a planar measurement of 2D (in-plane) velocities. In this study, a stereo PIV system was used to make in-cylinder planar 3D (in and out-of-plane) velocity measurements and to track burned/un-burned gas regions.

PIV diagnostics have been widely in use for over 30 years and there are many great references [181, 195-198] that can be consulted for a more in-depth description of the theory and best practices of PIV measurements than can be provided here. PIV was first successfully performed in an optical engine by Reuss et al. [199] in 1989 and has since become a common tool within the engine combustion community [200, 201]. Countless papers have been published on the topic of PIV measurements within engines and progress continues to be made within the field, as is well summarized by Sick et al. [202] in a recent review paper.

The methods and procedures used to perform stereo-PIV measurements in this study will now be discussed. An uncertainty assessment of the PIV measurements is provided at the end of this section.

3.2.4.1 PIV Seeding

Airflow seeding was achieved with the help of a TSI 6-jet atomizer. A fraction of the engines intake airflow was diverted through a TSI 6-jet atomizer on it's way to the engine. The atomizer introduced small (~ 1 μm) silicon oil (Dow Corning 510, Fluid, 50 CST) droplets into the flow which acted as an airflow tracer for the PIV diagnostic. The particle density varied with engine positon (CAD) and condition. However, generally the densities used in these studies were about 10-20 particles per millimeter of field of view, which equals about 7-15 particles per cubic millimeter. The energy content of the particles was negligible (<1%) in comparison with that of the fuel and so the particles are not thought to significantly affect the flames in this study. Seed vs. no-seed engine tests were performed, the results of which verified that the presence of seed oil in this study did not significantly affect the engines performance.

3.2.4.2 Spatial Calibration of PIV Images

The stereo-PIV imaging system required a three dimensional spatial calibration procedure. The calibration procedure had to not only correct the raw images for optical distortions that arose

due to the presence of components such as lenses and windows within the cameras line of site, but it also had to accurately recognize the stereo angle between the two cameras and the effect thereof. Any deficiency in the latter would lead to large errors in the measured velocity fields.

The spatial calibration was performed using the same 3D optical target that was shown in Figure 3-11 and most of the same procedures discussed for the PLIF calibration in 3.2.3.3. The PLIF and PIV images were always calibrated jointly (without the target being moved, utilizing the same optical mockups) to ensure that all cameras shared a single point of origin.

The Scheimpflug adapters that were mounted in-between the cameras and their respective lenses rotated the cameras plane of focus and allowed the camera to focus on the laser sheet (and target) plane, despite the cameras angle relative to it. The Scheimpflug adapter was always optimized just prior to spatial calibration to ensure that the optical target (and later the laser sheet) was well focused throughout the cameras entire field of view.

Images of the calibration target were acquired with both stereo PIV cameras. The images were processed within DaVis software according to procedures recommend by LaVision in the user's manual [180]. The software identified all of the dots on the 3D target and a pin-hole optical model was used to form a spatial grid.

After the calibration process was complete a few different metrics were used to verify the calibrations fidelity. The visual overlap between the spatial grid and the targets dot markers was always verified. An example of such a visual verification is shown in Figure 3-17. These two images represent the overlap of both cameras at different planes (focal lengths). Remember that the optical target itself contained two different planes of dots that were separated in depth by 1.05 mm. Therefore, within each image, half of the dots appear in focus (and well gridded) and the other half out of focus (and un-gridded). Collectively, the two images verify that the spatial calibration provided reasonable results in all three spatial dimensions.

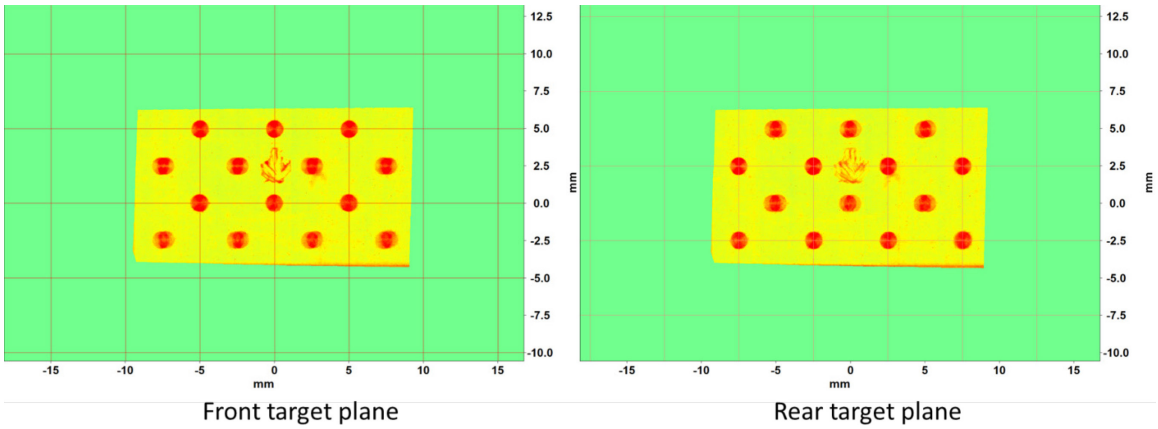

Figure 3-17: Two camera, spatially overlapped stereo particle image velocimetry calibration results for both front and rear target planes.

After identifying good grid-to-dot overlap, the value of the calculated stereo angle would be verified to also be reasonable. Remember that the physical angle between the two cameras relative to the engine was 30 degrees. Therefore, a similar value was expected to be recognized by the calibration model. However, due to optical distortions and refractive affects, the effective stereo angle always registered smaller than the physical angle. For example, in the piston bowl region of the field-of-view the effective stereo angle measured to be 19 degrees, which was reasonable.

The stereo-PIV spatial calibration procedures were performed multiple times to ensure repeatable results. When complete, the spatial calibration parameters were saved and used to spatially correct the raw PIV images and to enable the 3D vector field calculations.

3.2.4.3 Processing of PIV Images into Vector Fields

The PIV velocity fields were calculated from the raw particle images using DaVis commercial software [180]. The many details of PIV processing methods, both current and historical, have

been well documented by Raffel, et al. [181]. Therefore, only a brief description of the process and the relevant processing details will be discussed here.

Within the DaVis software, the parried, temporally-offset double frame images from the two cameras were interrogated in spatially defined window sizes. Within the interrogation windows, two sets of temporally offset double frame images were spatially cross correlated to achieve correlation map results similar to those shown in Figure 3-18. The map was then used to interpret the velocity within the interrogation window. For example, the peak value location within the window could be interpreted as the most significant translation distance of the particles, and based on this and with knowledge of the temporal separation between the two frames, the overall velocity could be recognized. The three dimensional nature of the stereo setup, which necessarily combined the results from both cameras to recognize the in and out-of-plane components of the velocity field, added complexity to the process beyond what was just described. Readers are encouraged to consult any of the following resources for more details on the topic [181, 196, 201].

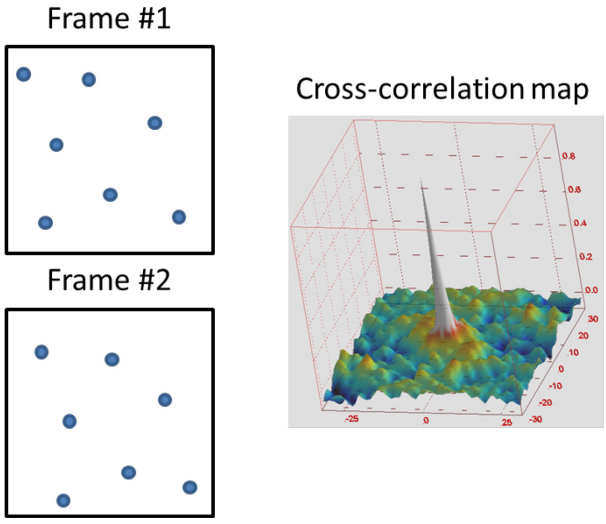

Figure 3-18: Cross-correlation results for two particle images. The correlation images are borrowed from Raffel et al. [181]

Since the correlation and mapping was all done within the DaVis software, only the pre, post and correlation processing parameters were necessarily defined in order to convert the particle images into flow fields. Under homogeneous-charge conditions a sliding background filter was

applied and under stratified-charge conditions no pre-processing was applied prior to the correlation process. The correlation and velocity was performed over a spatial window of 0.5 mm x 0.5 mm for the homogeneous-charge and 0.7 mm x 0.7 mm for the stratified-charge images. After mapping a few procedures were performed to remove any spurious vectors and finalize the velocity field. First, a spatial standard deviation filter was applied to remove vectors of magnitudes differing by greater than three standard deviations from the mean. Similarly, a velocity range filter was then used to get rid of vectors of unreasonably high velocities. Vectors with peak ratios less than 1.4 were also removed. What remained were mostly high fidelity (first and second choice) vectors. Finally, an interpolation procedure was performed in MATLAB to evenly populate the entire PIV field-of-view with vectors.

Example of raw PIV images are shown later in this document in Figure 3-23 and dozens of processed images are shown in sections 5.3.1 and 6.3.1.

3.2.4.4 PIV Uncertainty

The uncertainty in particle-image velocimetry images acquired in this study was assessed by an uncertainty estimate tool built into the Davis's commercial software by LaVision inc. The methods employed by LaVision to estimate PIV uncertainty are based upon the collective research of Douglas et al. [203], Sciacchitano et al. [204], Wieneke et al. [205] and others referenced within their publications. Weineke et al. has published [205, 206] two recent papers on the topic.

The PIV uncertainty was conservatively estimated to be about 1 m/s for in-plane velocities and 5 m/s for out-of-plane velocities. The exact level of uncertainty varied on a test-to-test basis for many reasons; including shot-to-shot difference in seeding density, image quality and in-cylinder flow properties. The exact uncertainty even varied spatially within individual images. Therefore, the value reported above represents a higher end estimate of uncertainty as recognized throughout all testing.

Notice that the out-of-plane velocity component is five times more uncertain than the in plane velocity components. This comes as a natural result of using a tight (30 degree) stereo camera spread angle. The tight angle was chosen at the detriment of the out-of-plane velocity measurements in order to optimize the two cameras perspective on the combustion events. For more information on the relationship between in and out-of-plane error and the stereo-angle, please refer to Prasad [196].

3.2.4.5 Turbulent Flow Field Scale Analysis Technique

This section will summarize the techniques used to estimate turbulent lengths scales, such as the Integral scale and the Taylor microscales from the PIV generated airflow velocity field estimates. Before stating the details of the approach, a brief introduction of integral length scale and Taylor microscale will be provided. However, turbulence and turbulent length scales is a complex topic and if more detailed background on the subject than provided is desired than readers are encouraged to consult any of the following references [102, 207, 208].

In conventional (homogeneous, isotropic) turbulence theory the integral length scale is that which represents some of the largest, most-energetic eddies within a turbulent flow. The integral length scale is often limited by the physical constrain of the environment. In the case such of an engine, this constraint might be the dimensions of combustion chamber or the piston bowl. The Taylor microscale is roughly that for which eddies of equal or smaller diameter undergo significant amounts of viscous dissipation. The Kolmogorov scale represents the smallest turbulent flow length scale for which eddies cannot exist; below which turbulent flow structure are rapidly dissipated by viscosity.

The conceptual framework behind conventional turbulent length scale analysis is built upon the assumption that turbulence occurs in a homogeneous and isotropic manner. The turbulence of engine airflows is very heterogeneous and anisotropic. Flows like this are is still in a state of

discovery and in the absence of better methods the existing, simplified conventional theories were adopted for this study.

The analysis technique for both integral length scale and Taylor microscale relays on the correlation map derived from the PIV velocity fields. A single point correlation is defined as,

$$R_i(x,y) = \frac{\frac{1}{N}\ \sum_{n=1}^{N} U_i(x,y)\ \times\ U_i(x_0,y_0)}{\widetilde{U}_i(x,y)\ \times\ \widetilde{U}_i(x_0,y_0)}$$

where $R_i(x,y)$ is the correlation value of ith component of the turbulent flow field, i. e., the u, v, or w components, at the location of (x,y). $U_i(x,y)$ is the turbulent velocity field which is achieved by subtracting the ensemble-average flow from instantaneous flow. $\widetilde{U}_i(x,y)$ is the root-mean-square (RMS) of turbulent velocity fluctuations, a quantity which will be frequently shown in the results section. (x_0,y_0) is the location of the point of interest and N is the total number of vectors in the velocity field.

The integral length can be calculated based on the autocorrelation function by the following relationship,

$$\Lambda = \int_0^{\infty} R_i(r)dr$$

And the Taylor microscale can be calculated by the following relationship,

$$\lambda_i(x_0,y_0) = [-\frac{1}{2}f''(x_0,y_0)]$$

In this study, the auto-correlation equation was applied to every point in the velocity field for both the u and v (in-plane) velocity components, as is shown in Figure 3-19 below. The z (out-

of-plane) velocity component was neglected for the scale analysis due to its relatively high quantitative uncertainty level.

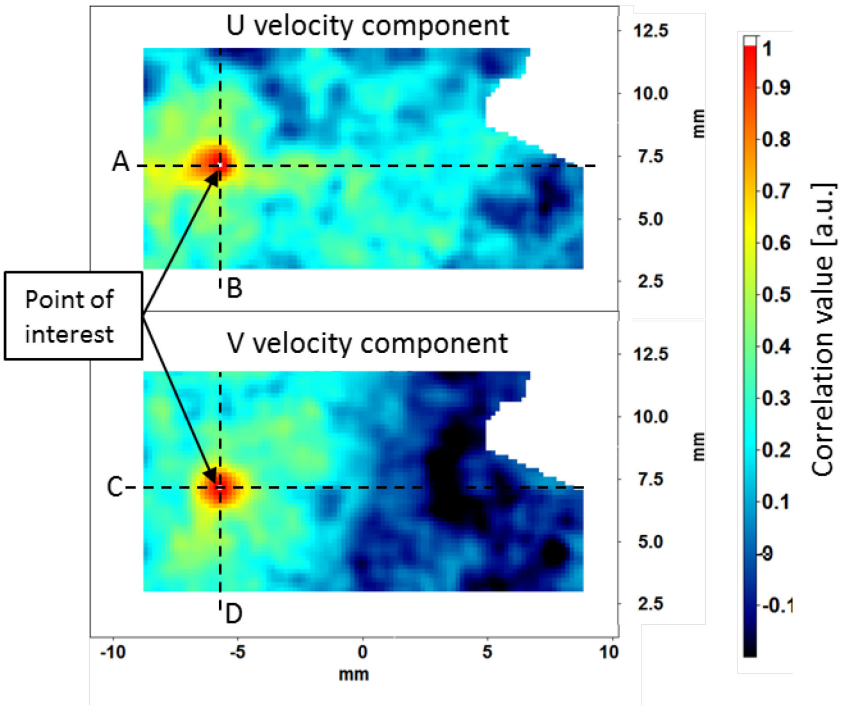

Figure 3-19: Velocity correlation map of in-cylinder flow for one single point with respect to the entire piston bowl region. This figure was produced by Hanyang Zhuang.

From the correlation fields shown in Figure 3-19 the auto-correlation functions (correlation value vs radial distance) were recognized along line profiles in two directions. When the correlation was taken in the same direction as the velocity (x-direction for u, y-direction for v), it represents the longitudinal, and when taken normal to the velocity it represents the transverse correlation. Conventional turbulence theory predicts the transverse integral scales to be half of the longitudinal integral scale. In this study they measured 10-30% lower. For the sake of brevity, only the longitudinal scales will be reported throughout this document.

The auto-correlation functions achieved from the flow fields were somewhat noisy, under-resolved (only 0.7 mm spatial resolution) and sometimes spatially incomplete (i.e. the optical field of view was too small for the correlation to go to zero in every direction) Therefore, curve fitting practices were necessarily employed to interpolate and/or extrapolate the auto-

correlation function as needed to calculate the scales. As can be seen in Figure 3-20 below, exponential functions were used to approximate the two halves of the auto-correlation function for the purpose of calculating the integral scale.

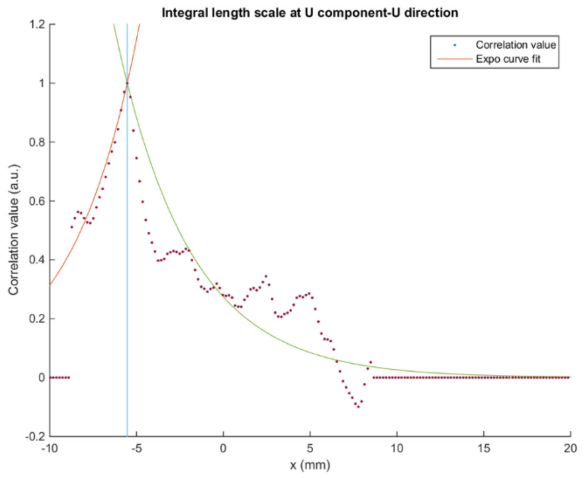

Figure 3-20: Result of fitting an exponential curve to a single-point velocity correlation in order to estimate the integral length scale at that point. This figure was produced by Hanyang Zhuang.

Sometimes, one half of the auto-correlation was discarded from the integral scale calculation due to incompleteness. For example, notice that the failure of the left half of the auto-correlation in Figure 3-20 to approach zero. In such cases, the better half of the correlation was simply mirrored and used for the integral scale calculation.

As is shown in Figure 3-21 below, a second order polynomial was used to fit the auto-correlation function, which provided a convenient means for the second derivatve of the function and subsequently the Taylor microscale to be calculated.

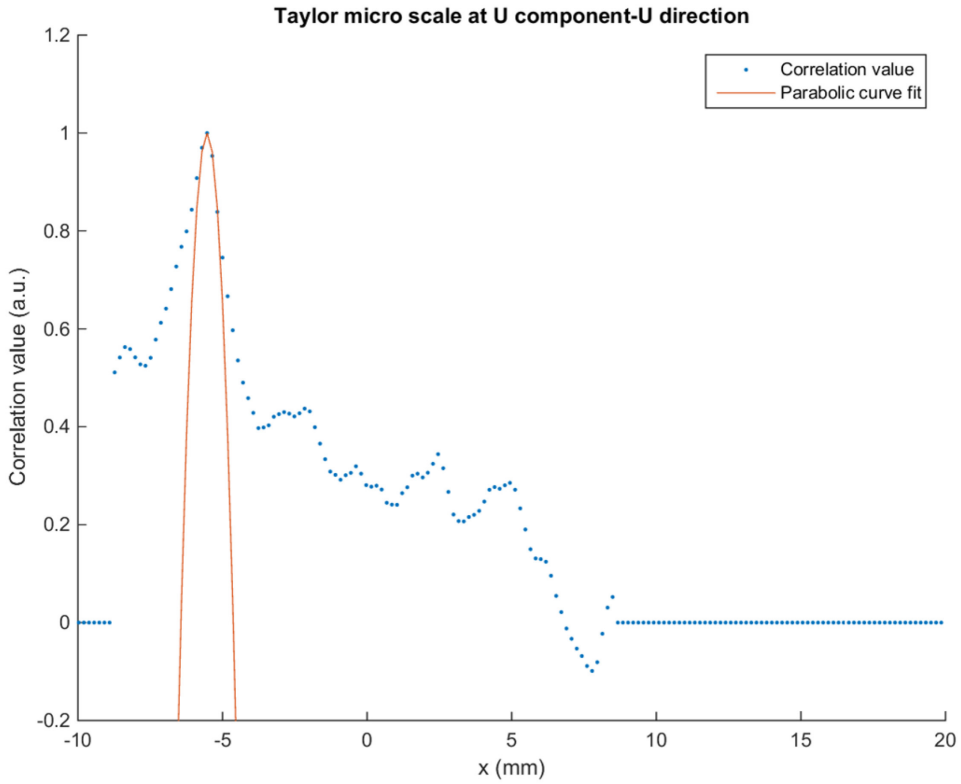

Figure 3-21: Result of fitting a second order polynomial to a single-point velocity correlation in order to estimate the Taylor microscale at that point. This figure was produced by Hanyang Zhuang.

Since the Taylor microscale calculation only required adequate resolution near the point-of-interest, both halves of the correlation were always accepted and used, even when one half of the correlation was incomplete.

Both the integral and Taylor microscales were calculated on point-by-point basis, the final product of which was a spatial map of length scale estimates for every imaging test. More will be discussed on the condensation and interpretation of those maps into single scalar values in sections 5.3.2 and 6.3.2.

From the integral and Taylor microscale estimates the Kolmogrov scale (η) and the turbulent Reynolds numbers (Re_I) were then readily estimated through the following relationships,

$$\lambda = \sqrt{10}\eta^{2/3}\Lambda^{1/3} = \sqrt{10}(Re_l)^{2/3}\Lambda$$

3.2.5 Flame Front Recognition and Analysis

Post-processing methods were developed to identify flame contour based upon the PLIF and stereo-PIV images acquired and to quantify flame wrinkled-ness. This section will describe the development and application of these methods.

3.2.5.1 Homogeneous-Charge Flame Contour Recognition

The homogeneous-charge flame images were truncated into a rectangular region of interest within the cylinder bowl region. That region was then processed into a binary image where the burned (count=0) and unburned (count=1) regions were separate. The basic truncation and binarization procedure is visually summarized in Figure 3-22 below.

Prior to truncation the homogeneous-charge PLIF images were already spatially calibrated, and quantified in terms of equivalence ratio, as has already been discussed in section 3.2.3. The first image (a) in Figure 3-22 is in this pre-processed state. The pre-processed images were then truncated into the field of view shown in Figure 3-22 (b). The truncation was performed in order to ease the spectral analysis process which as will be discussed, favored rectangular fields of view.

Once the region of interest was extracted, a burned-to-unburned gas threshold limit was determined based upon the probability density function of the images pixel intensities. Typically the burned gas showed little to no signal intensity since there was no Toluene present and the unburned gas showed an image count value close to or at the conditions equivalence ratio. As is shown in Figure 3-22 (c), the most probable burned and unburned gas count values were readily recognized form the intensity pdf's. A threshold limit was then set to be half-way

(50%) between the most probable burned and unburned gas counts and the image was binarized accordingly.

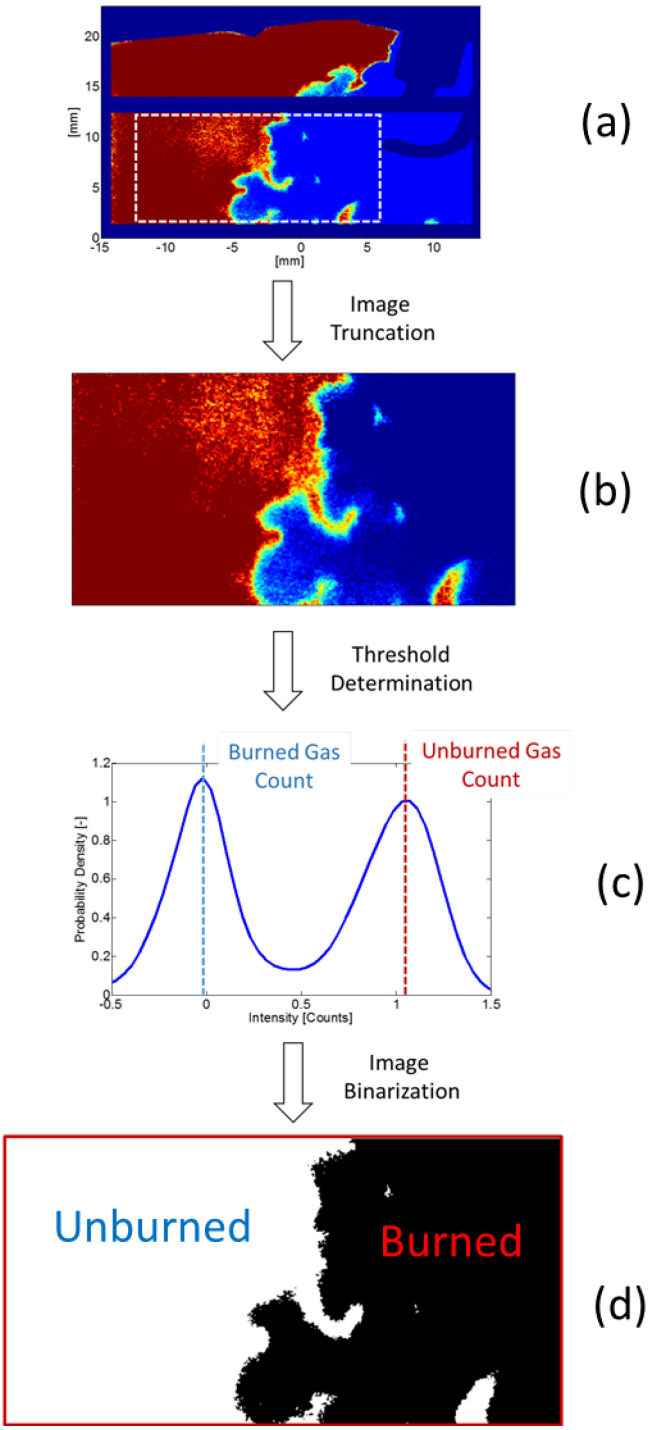

Figure 3-22: Homogeneous-charge flame image truncation and binarization

The flame contours were then recognized on the binary images by a MATLAB based routine as the intersection between the burned and unburned gas zones in the binary images. Very short or border lying flame contour segments were deemed to be noise related and/or non-physical; therefore they were algorithmically recognized and removed. Many contoured homogeneous-charge flame images will be presented later (e.g. Figure 5-3 and Figure 5-5)

3.2.5.2 Stratified-Charge Flame Contour Recognition

The stratified-charge flame contours were recognized through a combination of the PLIF and stereo-PIV results. The PLIF imaging system identified fuel/Φ and the PIV system identified burned gas regions. Flames were identified to exist in regions for which flammable Φ mixtures were actively interacting with burned gas regions.

The first step in the flame contour recognition process was to extract the equivalence ratio and burned gas regions from the PLIF and PIV images. The PLIF equivalence ratio quantification process was performed as discussed at length in 3.2.3.4. Burned gas areas were recognized within the PIV images through a custom dilation/erosion based process; for which the raw PIV images were subjected to the following processes in MATLAB:

- Time-series filtered
- Low intensity regions removal (i.e. particle isolation via thresholding)
- Particle dilation
- Particle joining (i.e. small unburned gas area elimination)
- Image erosion to offset prior dilation

The burned gas areas of both stereo PIV cameras were combined and properly re-gridded to spatially overlap with the equivalence ratio images. Regions of adequate equivalence ratio that were identified to exist within 0.5 mm of burned gas were then recognized within the PLIF images as flame regions. These flammable regions within the PLIF images were then binarized based on the chosen equivalence ratio threshold and a contour was easily fit to binary PLIF border. For the purpose of display, the binary PLIF images were subjected to a 0.5 mm low-

pass spatial filter that was described in 3.2.5.3 prior to contouring. An example of PIV burned gas recognition results and a stratified-charge PLIF image with flame locations identified is shown in Figure 3-23 below.

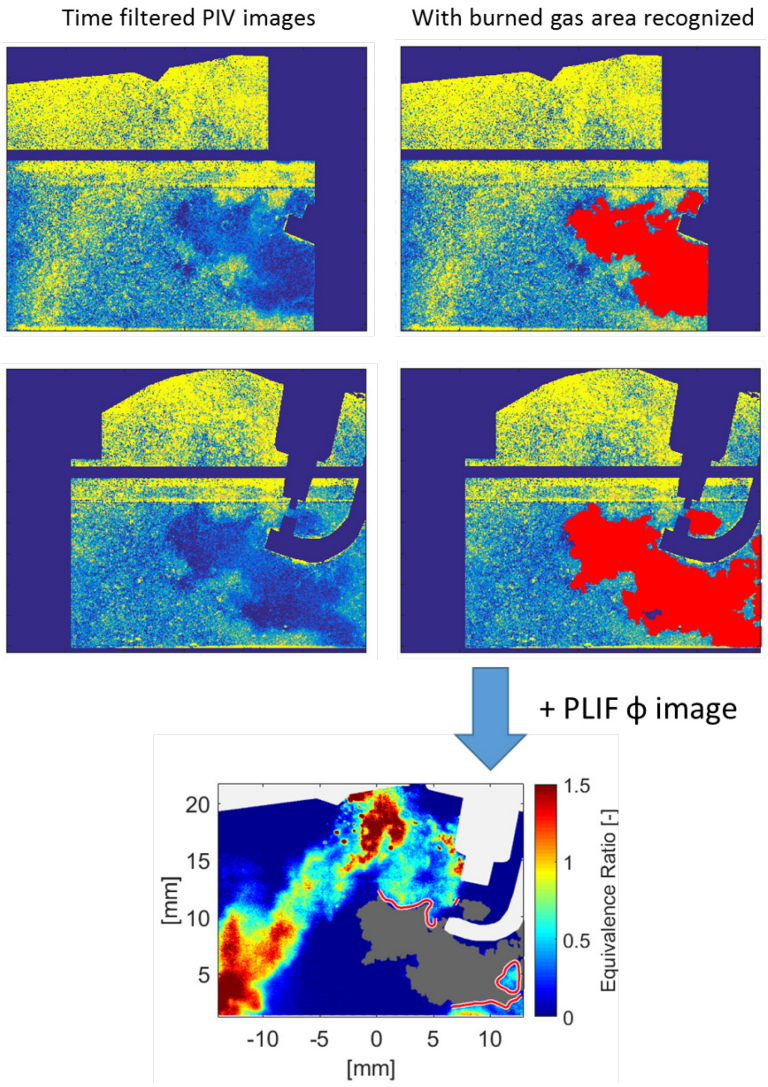

Figure 3-23: An example of the stratified-charge burned gas recognition (from PIV) technique and the result of its combination with the equivalence ratio (from PLIF) images to identify the location of flames. Burned gas regions are shown in gray and flame contours by white traced red lines.

Notice that the burned gas area algorithm identified the particle free image regions well. Also notice that only the flammable regions bordering the burned gas are highlighted in by white-traced-red flame contours. Although the entire flame identification process was algorithmically

automated, ever burned-gas and stratified-charge flame image that was subject to analysis in this study was visually verified to be reasonable.

3.2.5.3 Wrinkled-ness Analysis Technique

Methods were developed to extract both the degree and scale of wrinkling from the binary images and contours. The method utilized a fast Fourier transform (FFT) based algorithm to spectrally separate features of differing spatial scales from within the flames. Based on this, the relative contribution of wrinkles of differing scales towards surface area could be estimated in the form of a wrinkled-ness factor. The technique is applied in this study towards flames and fuel jets. It can generally be applied to any two dimensional topological measurements. However, for the sake of simplicity, the wrinkled-ness analysis here will only be discussed in the context of flame measurements.

Following the basic concepts of the flame surface density model, a PLIF image based wrinkling factor ($\Xi_{measuerd}$) was defined as,

$$\Xi_{measured} = \left[\frac{Turbulent\ Flame\ Perimeter}{"Equivalent\ Laminar"\ Flame\ Perimeter}\right]_{\substack{in\ a \\ 2D\ Flame\ Image}}$$

Remember that according to the FSD model, the wrinkling factor is directly proportional to turbulent flame speed.

$$\Xi \sim \frac{S_T}{S_L^o}$$

Although the definition of Ξ is exact and physically intuitive, the definition chosen for $\Xi_{measured}$ is less so. In order for its value to be determined a somewhat ambiguous “equivalent laminar” flame contour must be defined.

Conceptually, the definition of an "equivalent laminar" flame perimeter (within a 2D image) is only clear for a few canonical flame geometries. For example, for an unrestrained outwardly propagating flame the obvious choice of contour geometry would be a circle of equal burned gas area. However, for an engine flame the choice is more complex. Engine flames are often forced to conform to moving physical boundaries and regularly exhibit open (unclosed) flame contours, typically in the peripheral regions of the chamber whereas all combustibles have been spent.

In this study, a method of quantifying $\Xi_{measured}$ that was originally developed by Ziegler et al. [209] was borrowed and improved upon. The method is driven by the idea that turbulent flame wrinkles and laminar flame structures occur on spatially separable scales and can therefore be partitioned in Fourier space. Therefore, a highly low-pass spatially filtered version of a flame should serve as a decent representation of an equivalent laminar flame that may be used to quantify $\Xi_{measured}$.

For a visual example of the spatial scale separation that may exist between a turbulent flame and it's underlying "equivalent laminar" structure, see Figure 3-24 below. In this image, turbulent wrinkles are clearly visible on the 10^0 mm scale, whereas the flame itself (and its equivalent laminar representation) are on the order of 10^1 mm. Therefore, a 2D low-pass spatial image filter can be designed to remove the 10^0 mm scale wrinkles while leaving the general 10^1 mm flame structure intact. This filtering operation would essentially be an image processing noise reduction process.

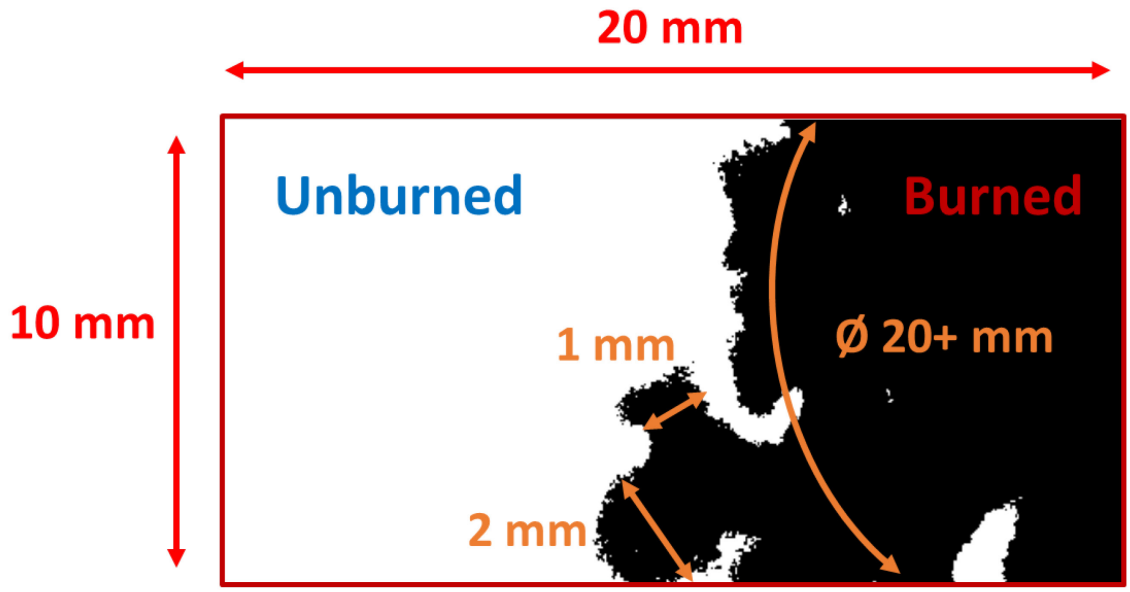

Figure 3-24: Homogeneous engine flame with scales labeled

There are two ways to apply this basic low pass filtering approach. The first way, which was used by Ziegler et al. [209] is to define a flame contour and then to spatial filter to a flame contour itself (filtering of a 2D contour/curve). The second approach, which was used in this study is to filter the entire binary flame image (2D image filtering) and to fit contours as is necessary. The mathematical approach to contour filtering that was demonstrated by Ziegler et al. requires a closed flame contour. The image filtering approach used in this study does not.

Although low pass filtering is very common in the field of digital imaging processing it's typically performed in a qualitative manner. Care was taken to ensure that the spatial filtering was performed in as quantifiable of a manner as possible (i.e. when a filter of a certain spatial scale was applied, wrinkles of that same scale were removed).

The algorithm used to filter the images was MATLAB based and acted best when servicing rectangular or square shaped images. Hence, the motivation for the original PLIF image to be truncated into such sections.

Within the algorithm and prior to spatial filtering, the binary flame image was mirrored horizontally, vertically and diagonally and then padded (zero value pixels added to periphery) as necessary to ensure that the padded image subject to the FFT processing was square. The mirroring step was performed in order to increase the total scale of the flame and reduce the spatial filters natural tendency to erode away at the artificial flame edges that were naturally formed at the flame image boundaries due to truncation. The image padding was done in order to ensure that the spatial filter acted equally (at the same cut-off frequencies) in both spatial dimensions. The padded pixels were far enough separate from the actual field of interest (original image) that the presence of the extra zero value pixels had negligible effect on the actual region of interest. Once mirrored and padded the image was then processed by an FFT based Butterworth low pass filter which was originally coded by Iheme [210]. After filtering, the padded image was truncated back to its original size and field of view. The filtering process often altered the size of the flame. Therefore, the final step in the filtering process was to dilate or erode the flame image as necessary until its burned gas fraction of the filtered image matched that of the original unfiltered image.

As an example of the results achieved, the same flame from Figure 3-24 is shown in Figure 3-25 after being subjected to the filtering process just described. The 0.2 mm filtered contour seen in (a) contains tiny wrinkles that visibly can be recognized to be unphysical (image noise). The 1 mm filtered contour (b) that has been labeled to be the “turbulent” contour appears to contain most of the flames fine physical wrinkling features minus the high spatial frequency components which are likely noise. As the filter scale increases from 1 to 20 mm the wrinkled-ness of the flame decreases. At the 20 mm filtered scale (f), there are no more wrinkles and the contour has been labeled laminar. Although it has not been shown, when a 30 mm or larger scale filter is applied the flame ceases to exist anymore. This maximum filterable scale is related to the size of the flame itself and can be used to provide a rough measurement of the flame’s overall scale.

The choice to title the low spatial frequency representations of flames as “laminar” is technically debatable. However, many previous researchers, including Damköhler in his foundational 1947 publication on the effect of turbulence on flames [211], have used similar terminology [91, 209, 212-214]. Therefore, in order to maintain consistency with the combustion research community the term was adopted for this study.

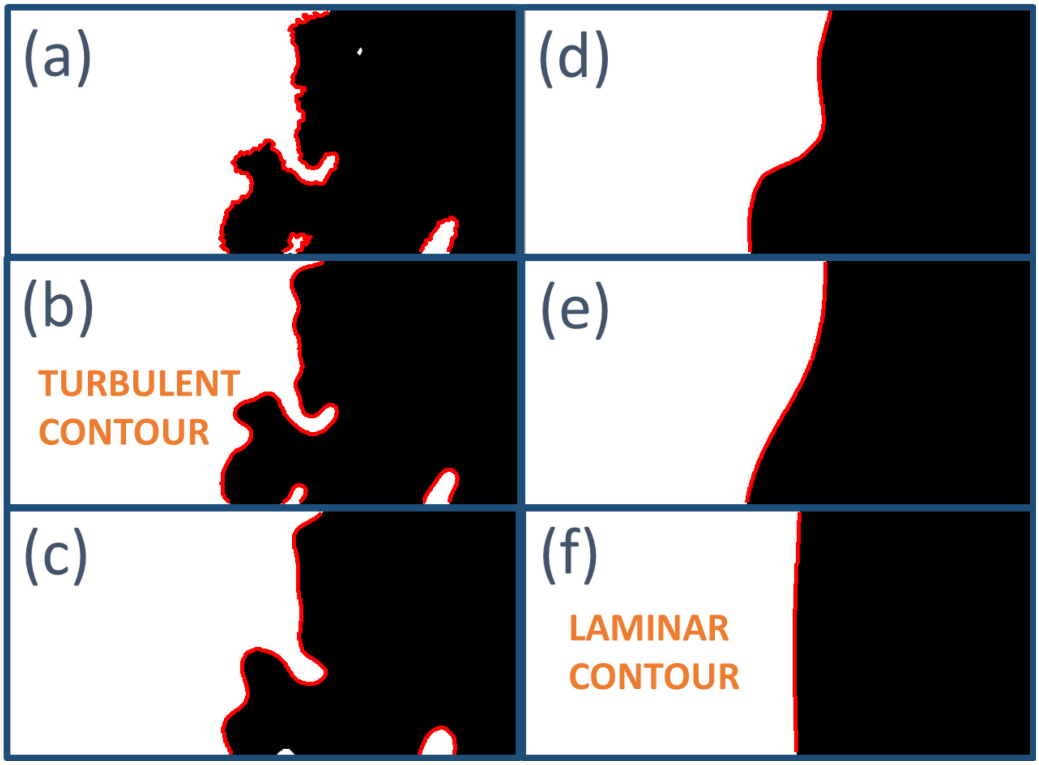

Figure 3-25: Flame after being processed by a low pass spatial frequency of cutoff scales of (a) 0.2 mm, (b) 1 mm, (c) 2 mm, (d) 5 mm, (e) 10 mm, (f) 20 mm.

After spatial filtering, the flame contour lengths were assessed and $\Xi_{measured}$ quantified at the various scales. The filtered images from two of the scales were then chosen to represent the laminar and turbulent contours. The “turbulent contour” filter cut-off frequency was chosen to be 1 mm as it was on scale with the laser sheet thickness (and therefore spatial resolution). The choice of “laminar contour” filter cut-off frequency differed for every test condition. More will be discussed on its choice in the results section.

Due to the definition of spatial frequency in image filtering processes, a filter applied at a given cut-off scale will actually eliminate features that are half the prescribed diametric scale. For example, the 1 mm spatial filter applied in Figure 3-25 (b) will tend to eliminate flame contour wrinkles that are less than or equal to 0.5 mm in diameter. Therefore, in order to eliminate confusion throughout this document the LP filters scales reported in the results sections will be referred to in the context of "minimum wrinkle diameter allowed by LP spatial filter". In this manner, the filter scale can be physically and directly related to wrinkle scales of the flame.

It should be recognized that the filtering process itself was compromised at larger (10+ mm) scales due to the fact that the smallest dimension of the image is 10 mm. The mirroring process enabled the spatial filter to act on spatial scales larger than the actual region of interest. However, there was no way to ensure the fidelity the filtering process performed on scales larger than the field of view. Fortunately, as can be seen by the minimal difference in surface area between (e) and (f) in Figure 3-25, very little surface area is or can be generated at such large spatial scales. Therefore, any large scale infidelities had only a minor effect on the measurements.

With an understanding of how wrinkled-ness was defined and calculated in this study based on PLIF images; the measurement subscript in $\Xi_{measured}$ will be with-held and the wrinkled-ness measurement quantity will simply be signified by Ξ throughout the rest of this document.

Chapter 4: ENGINE PERFORMANCE

The G4VDI engine's hardware and operational strategy was optimized to provide reasonable engine performance under both homogeneous and stratified-charge conditions. This section provides a description of the optimization process and the characterization of the engines resulting performance. The goal of the optimization process was not to achieve production like performance as so much was neither necessary nor possible considering the significant mechanical design limitations imposed by the need for optical engine components. Rather, the goal of was to find an operational strategy that provided suitable production engine-like sprays, flows and flames that were well suited for the study. This was achieved and the final strategies and conditions chosen for the study are summarized.

A GT-Power model was developed and validated to both aid in the optimization of the engine and to provide a means for estimating important engine parameters such as in-cylinder temperatures that could not or were not otherwise measured. The model is also currently aiding in a collaborative effort between the QLDL, General Motors and other universities [215-218] to learn from comparisons made between the G4VDI engine experiments and Large Eddy Simulations. The model, its validation and select results will be presented here.

Before any fired tests were performed for this study the engine's motored performance was characterized and optimized. Engine blow-by rates are typically very large in optical engines. In this study they were reduced as far as possible (estimated <5% by mass) by optimizing a custom single-piece compression ring. GT-Power based estimates will be shown to verify that the G4VDI engines motored performance good.

The engines performance was characterized and optimized under homogeneous-charge and stratified-charge conditions. Acceptable engine performance was achieved and conditions were chosen for the wrinkled-ness studies to follow.

All engine performance results in this document will be presented in the form of indicated (in-cylinder pressure transducer based) values. Due to the many mechanical differences between the single cylinder G4VDI optical engine and conventional automotive engines, brake specific parameters and engine exhaust emissions were not deemed valuable and were not quantified. Heat transfer and blow-by were not considered or compensated for in the indicated in-cylinder pressure based parameter calculations. More details on the in-cylinder based pressure indicated calculation algorithms can be found in the Combustion Analysis Systems (CAS) user's manual [219] which was produced by A&D Technologies.

4.1 GT Power Model Development, Validation and In-cylinder State Predictions

A GT Power model was developed and used to verify engine performance and to predict un-measured engine parameters, such as in-cylinder temperatures. The models development, validation and usage will be discussed here.

The G4VDI GT Power models code was developed by Dr. Xiaofeng Yang and Dr. Tang-Wei Kuo from General Motors based upon an extensive mechanical measurements and characterization of the G4VDI engine hardware. The model was refined and validated based upon experimental data acquired during this study.

All of the relevant intake, exhaust and engine hardware were measured and their dimensions were translated to the model. Flow-bench testing was performed on the cylinder head in order to quantify valve discharge coefficients and effective swirl and tumble ratios. Temperature, flow rate and high speed (CAD resolved) pressure measurements were acquired at a variety of

engine speeds and loads and used to validate and refine the model. A schematic of the model is shown in Figure 4-1 below.

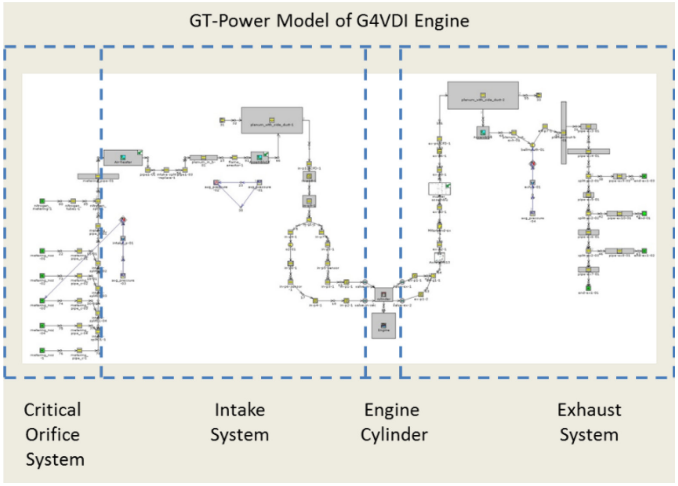

Figure 4-1: GT-Power Engine Model of the G4VDI Engine that was designed in collaboration with General Motors [ref].

With very little tuning, the model proved capable of reproducing the respiratory pressure dynamics of the intake and exhaust systems very well. For example, Figure 4-2 and Figure 4-3 below demonstrate the excellent agreement between the experimentally measured and GT-Power predicted pressure dynamics that occurred in the G4VDI engine under motored, 1300 RPM, 95 kPa MAP conditions. For this same condition the engine airflow rate was also predicted by the model with only a 5% inaccuracy.

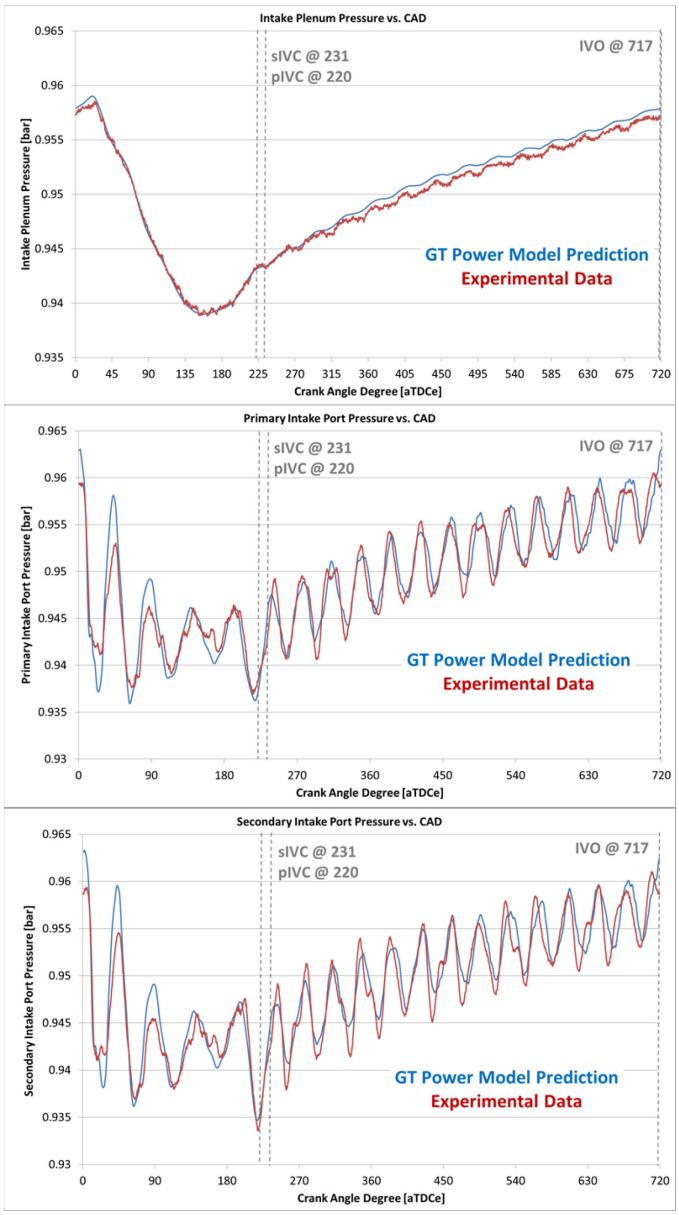

Figure 4-2: Experimentally measured and GT-power estimates of intake port and plenum pressures vs. crank angle degree at 1300 RPM, 95 kPa MAP and 45 C engine temperature.

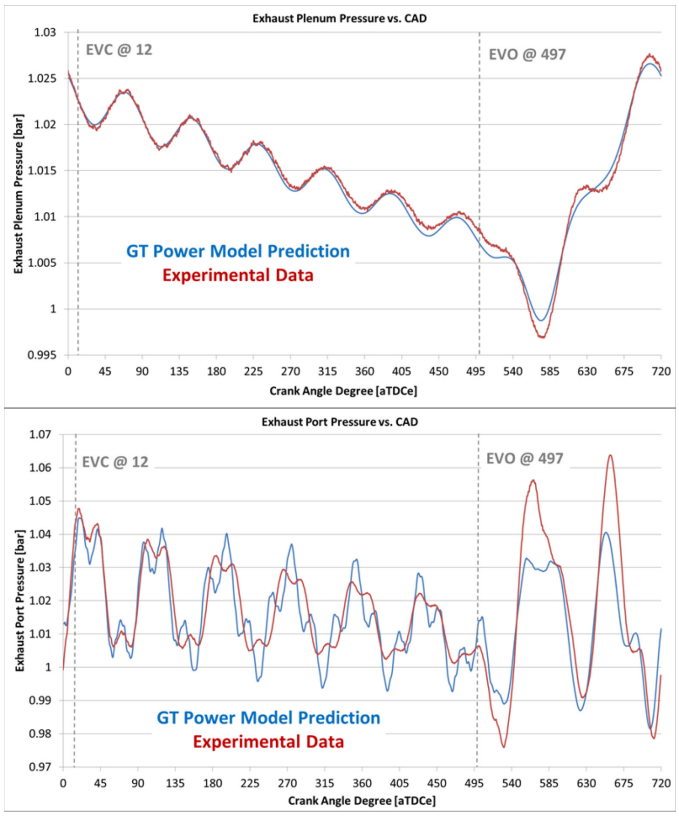

Figure 4-3: Experimentally measured and GT-power estimates of exhaust port and plenum pressures vs. crank angle degree at 1300 RPM, 95 kPa MAP and 45 C engine temperature.

In-cylinder pressures were estimated by GT-Power using an un-tuned Woshni heat transfer model. In-cylinder pressure comparisons between the experiment and model for a motored, 95 kPa intake MAP condition is shown below in Figure 4-4.

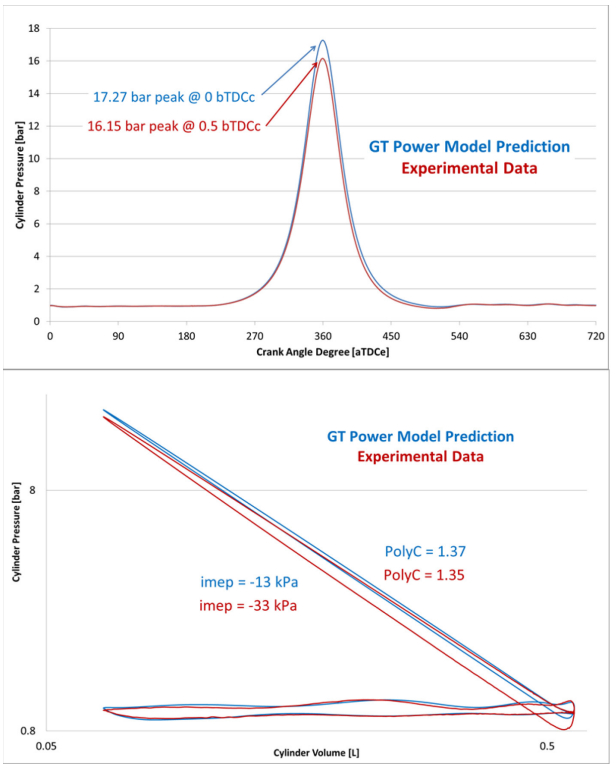

Figure 4-4: Experimentally measured and GT-power estimates of in-cylinder pressure data vs. crank angle degree (a) and cylinder volume (b) with the engine operating at a motored state at 1300 RPM, 95 kPa MAP and 45 C engine temperature.

The GT-Power predicted in-cylinder pressure estimates preceded the engines compression ring design and was used as an experimental design target. The engines compression ring-set was modified and only deemed adequate when the engines in-cylinder pressure traces agreed as well as shown in Figure 4-4.

In Figure 4-4 (a), notice that the experimentally measured peak pressures are little lower than the GT-Power predicted pressures. Also in (b), notice that the experimental power loop and its associated negative value of IMEP is also larger than the predicted values. This difference is thought to be primarily due to blow-by which was unaccounted for in the model. A thermodynamic estimate of the difference between the two pressure traces suggests that the degree of blow-by in these conditions is < 5% the in-cylinder charge by mass. Under fired conditions the compression rings are thought to seal even better and the blow-by is expected to be much less. Therefore, blow-by induced GT-Power modeling errors were accepted.

A simple Wiebe function based combustion model was implemented using measured experimental parameters (CA50 and CA10-90 timings) and a Wiebe coefficient ranging from 2-3, depending on the condition. The results of an in-cylinder pressure experiment to model comparison at a Φ=1 condition (same one chosen for this study) is shown in Figure 4-5 below.

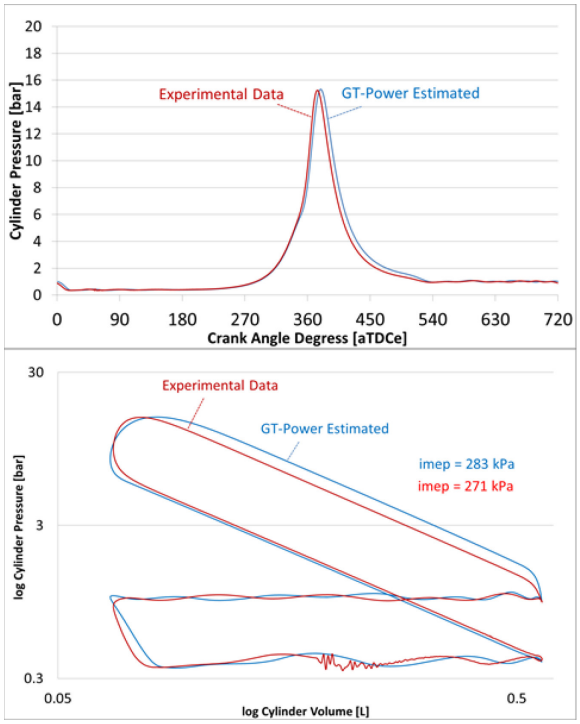

Figure 4-5: Experimentally measured and GT-power estimates of in-cylinder pressure data vs. crank angle degree (a) and cylinder volume (b) with the engine operating at a fired state at 1300 RPM, 40 kPa MAP, 45 C engine temperature, Φ=1 and a spark timing of 27 bTDCc.

The agreement shown in Figure 4-5 was regarded as good and acceptable and the model was used as a tool to predict parameters such as trapped residual fractions and in-cylinder temperatures. The model was further validated at other operating conditions, including the stratified-charge conditions, the results of which will be withheld for the sake of brevity. However, the degree of agreement between the model and the experiment was similar under other conditions as well.

Once validated, the model was used as a tool to estimate un-measured in-cylinder parameters such as un-burned gas charge temperatures, which are shown in Figure 4-6 below, and trapped

residual gas fraction, so that the PLIF images could be better quantified in terms of equivalence ratio.

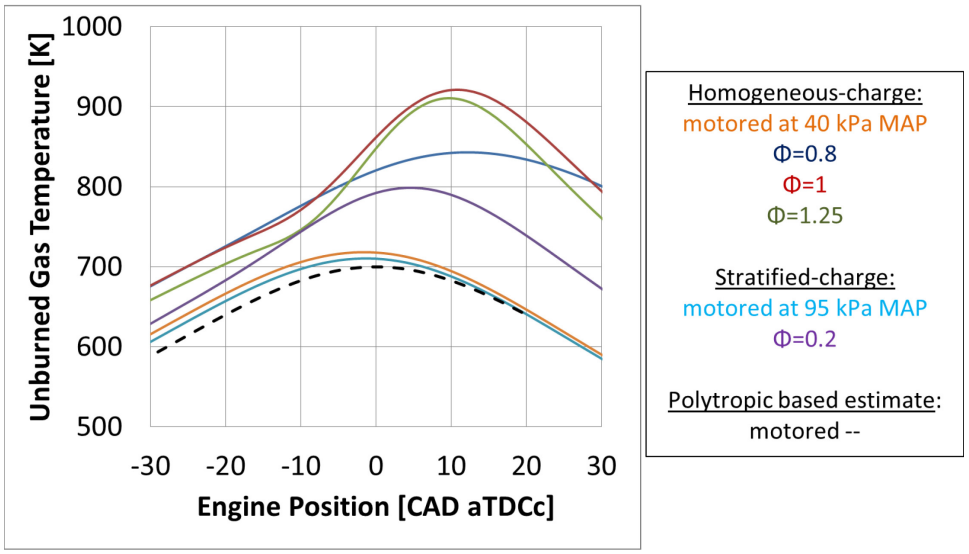

Figure 4-6: In-cylinder temperature estimates for engine conditions chosen for use in this study.

The in-cylinder temperature estimates calculated by GT power were verified reasonable in comparison to estimates provided by the basic polytropic relationship,

$$T_{CAD} = T_{CAD,ref}\left(\frac{V_{CAD,ref}}{V_{CAD}}\right)^{PolyC-1}$$

The results of which are also included in Figure 4-6. Therefore, the GT Power results were accepted and used throughout this study.

4.2 Fuel Injector Selection and Targeting

An 8-hole, 90 degree included angle injector was chosen for use. The injector was targeted so that two of its fuel jets were centered around and "straddling" the spark plug. The injector was chosen based upon the results of a spray imaging study and trial-and-error stratified-charge engine testing.

The design requirements for a spray-guided stratified-charge fuel injector are stringent. In order to be successful, a SGSC fuel injector must create a rich fuel mixture ($\Phi \sim 2+$) local to the spark plug to ensure robust ignition and a leaner but still strong mixture (probably $\Phi \sim 1$) throughout the rest of the bulk charge to promote a healthy and clean main burn. Favorable pairing between the fuel injector with the combustion system (cylinder head, piston bowl, etc.) is just as critical towards the strategies success as the selection of the injector itself. Accepting the scope the SGSC engine design challenge, only modest efforts were made in this study to optimize hardware.

There are two basic approaches to targeting a multi-hole fuel spray in a SGSC engine. The first approach is to target a single fuel jet directly at the spark plug. This strategy was formerly employed in the G4VDI engine by Peterson et al. [23, 39, 220-222] with relative success. The second approach, which was employed in this study is to "straddle" the spark plug with two of the jets, as can be seen in Figure 4-8. The latter approach was favored for reasons relating to spark plug durability, cleanliness and general commercial feasibility.

A few different fuel injectors were considered for this study. Imaging tests were performed to determine the promise of each one. In the process, a 3D plenoptic technology based imaging diagnostic was developed [178, 179] and used to aid in the eventual choice of an 8-hole, 90 degree included angle injector. As can be seen in the Mie scattering images shown in Figure 4-7 below, the periphery of the fuel spray generated by the injector targeted the base of the spark plug electrode while avoiding bulk liquid spray-to-plug impingement

.

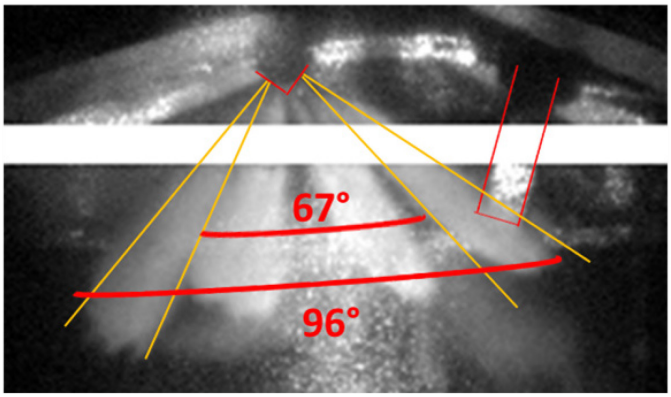

Figure 4-7: Fuel spray image taken during engine operation to assess the spray angle of the injector and the sprays targeting relative to the spark-plug. The spray was illuminated by a frequency doubled Nd:YAG laser. The image was taken with a high speed Phantom V7.1 camera from the backside of the engine (imaging side in Figure 3-6).

With the assisstance of the Mie scattering diagnostic system shown in Figure 4-8, the spray was targeted to straddle the spark plug symetrically (+/- 3 degrees).

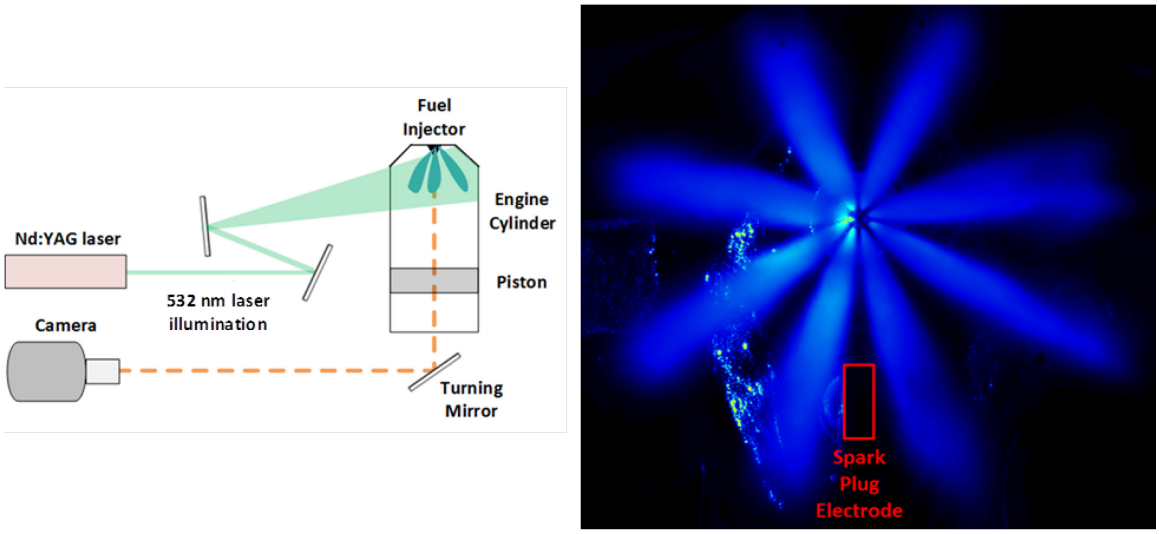

Figure 4-8: Laser induced Mie-scattering setup (a) and fuel spray image (b) under quiescent conditions demonstrating the “straddled” spray targeting strategy. The image is a 50 injection average.

With this injector targeting, two of the eight fuel jets traveled within close enough proximity of the spark plug to be ignited. Most of the fuel charge targeted the piston bowl so that after the combustion began within one or two of the spark-plug adjacent fuel jets the others were also within close enough vicinity to eventually ignite as well.

4.3 Homogeneous-Charge Engine Performance

In order to determine the best engine test conditions for use in the homogeneous-charge wrinkled-ness study, the G4VDI engines performance was characterized over a range of homogeneous-charge conditions. The following engine parameters were held constant throughout all of the characterization testing,

Table 4-1: Homogeneous-charge operational parameters which were held constant during optimization testing

Intake Manifold Absolute Pressure [kPa]	40
Exhaust Manifold Absolute Pressure [kPa]	101.5
Engine Coolant Temperature [C]	45
Intake Air Temperature [C]	45
Engine Speed [RPM]	1300
Injection Pressure [MPa]	12
Start of Injection Timing [bTDCc]	310
Fuel Composition [-]	100% Iso-Octane

Three different comparable homogeneous-charge conditions of differing equivalence ratio (lean, rich and stoichiometric) were desired. Ideally, the lean and the rich mixtures would be as far from stoichiometric as possible as to maximize their thermo-diffusive property differences. However, far off-stoichiometric mixtures and very lean mixtures in particular don't burn well. Therefore, the choice in exact stoichiometry for the lean and rich conditions was necessarily a compromise between mixture composition separation and combustion stability.

With all the parameters listed in Table 4-1 being held constant, there were three engine variables that could be swept: ignition timing, swirl-valve position (in-cylinder swirl level) and equivalence ratio. The strategy employed for choosing the best three homogeneous-charge conditions was to first optimize the stoichiometric (Φ=1) condition and then to accept the ignition timing and swirl-valve position for the two off-stoichiometric conditions. The exact choice of equivalence ratio for the off-stoichiometric conditions was then based on the results of an equivalence ratio sweep.

Maintaining the swirl valve setting and ignition timing for all three (lean, stoichiometric and rich) homogeneous-charge condition provided less-then-optimal engine performance for the off-stoichiometric conditions. However, it ensured that the in-cylinder conditions were similar for all three mixtures at the start of ignition which enabled fair early flame development comparisons to be made between the three conditions.

The two primary metrics used for grading engine performance were indicated mean effective pressure (IMEP) and the coefficient of variance of indicated mean effective pressure (COV of IMEP). Neglecting pumping or frictional losses (which are comparable for all three homogeneous-charge conditions), IMEP are indicative of the engines work output and higher numerical values are generally favorable. COV of IMEP values are indicative of variability in the engines work output and lower numerical values are favorable. Typical production engine values of COV of IMEP are < 2% and values above 5% are usually considered unacceptable by commercial standards.

CA50 values will be shown throughout this section as a general reference for combustion phasing. A common rule of thumb in engine research is that homogenous-charge engines operate at their optimum when CA50 occurs between 5-10 CAD aTDCc.

As has been previously mentioned, emissions measurements were not performed and the engines pollutant emission levels were not considered when optimizing the engine or choosing conditions for further study.

4.3.1 Stoichiometric (Φ=1) Engine Performance Optimization

Engine performance was optimized under stoichiometric homogeneous-charge conditions. Ignition timing sweeps were performed under both high (swirl-valve closed) and low (swirl-valve fully open) in-cylinder swirl conditions. The results of an ignition sweep for the low-swirl condition can be seen in Figure 4-9 below.

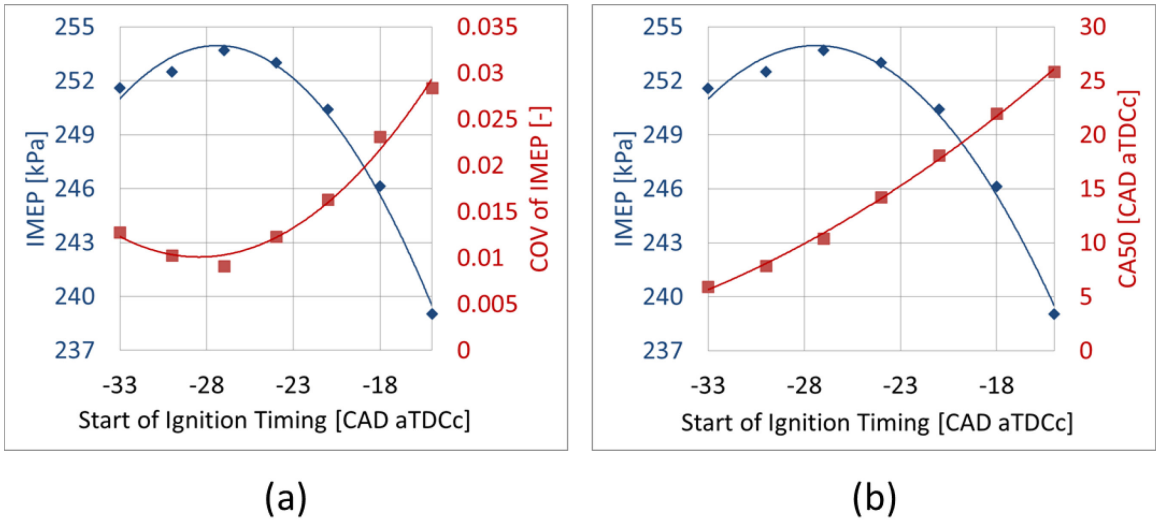

Figure 4-9: (a) Engine performance (IMEP and COV of IMEP) vs. start of ignition timing and (b) Combustion phasing (CA50) vs. start of ignition timing under low swirl, homogeneous, 40 kPa MAP, Φ=1 conditions.

The optimal Φ=1, low-swirl operation can be recognized to occur with a start of ignition timing of 27 bTDCc. At this timing the IMEP is at its maximum and the COV of IMEP is at its minimum. The CA50 at this ignition timing is 10 aTDCc, which is reasonable.

The results of an ignition sweep for the high-swirl condition can be seen in Figure 4-10 below.

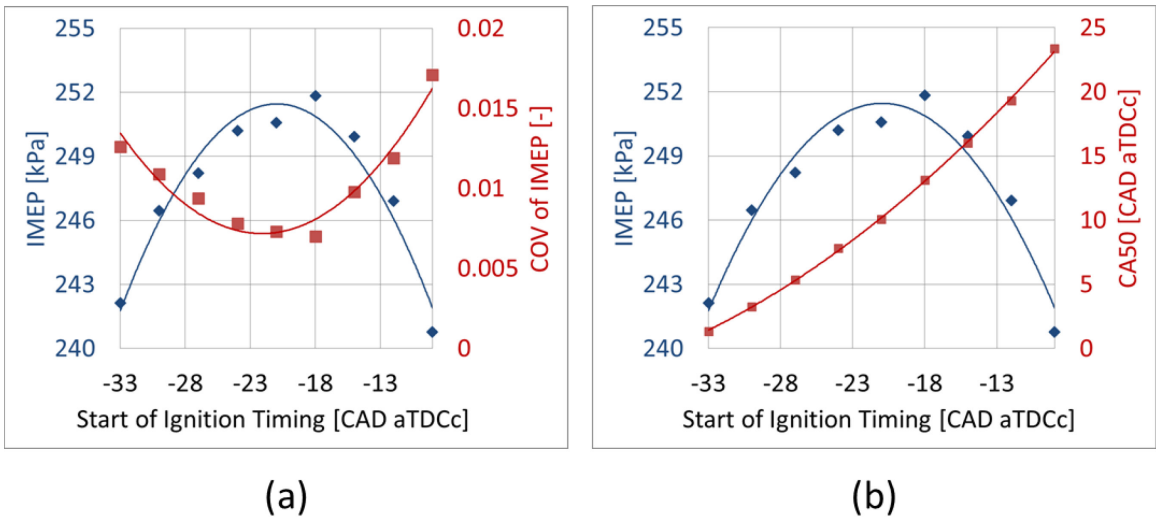

Figure 4-10: (a) Engine performance (IMEP and COV of IMEP) vs. start of ignition timing and (b) Combustion phasing (CA50) vs. start of ignition timing under high swirl, homogeneous, 40 kPa MAP, Φ=1 conditions.

The optimal Φ=1, high-swirl operation can be recognized to occur at a start of ignition timing of about 21 bTDCc. At this timing the IMEP is at its maximum and the COV of IMEP is at its minimum. The CA50 at this ignition timing is about 8 aTDCc, which is reasonable.

Due to lower its flame speeds, the optimum low-swirl conditions demanded six extra degrees of ignition advance relative to the high swirl condition. The optimal high and low swirl conditions both produced a work output of 250 kPa IMEP at excellent, production-like, < 1% COV of IMEP levels of variance. Either one of the two (high or low swirl) optimal Φ=1 conditions would have made excellent test conditions for the wrinkled-ness study. For reasons to be discussed later, the low swirl condition was chosen.

4.3.2 Off-stoichiometric Homogeneous Charge Mapping

The engines performance at a variety of off-stoichiometric homogenous-charge mixtures was tested at the conditions listed in Table 4-1 with the swirl valve fully open and the start of ignition timing set at 27 bTDCc (as was prescribed by Φ=1 optimization results).

The engine performance results for both 20% (Φ=0.8 and 1.25) and 30% (Φ=0.7 and 1.4) off-stoichiometric mixtures are shown in Table 4-2 below.

Table 4-2: Engine performance under off-stoichiometric homogeneous charge conditions at 1300 RPM, low-swirl, 40 kPa MAP, fixed spark timing of 27 bTDCc.

	IMEP [kPa]	COV of IMEP [-]	CA50 [CAD aTDCc]
Φ=0.7	70% misfires, not worth reporting		
Φ=0.8	191	0.11	18
Φ=1	254	0.01	10
Φ=1.25	251	0.01	7
Φ=1.4	248	0.01	9

Under the rich conditions tested the engines IMEP output remained similar and steady at a low COV of IMEP levels of 1% for all tests. The output and variability of the engine was perfectly acceptable up to the richest condition (Φ=1.4) shown in Table 4-2.

Engine performance was far worse under the lean conditions tested. The engines output decreased by 30% between Φ=1 and Φ=0.8, 20% of which can be attributed to the decreased

fuel loading alone. At Φ=0.8 the engines COV of IMEP measured to be about 10% which was about as high as was considered to be experimentally acceptable. Therefore, as the leanest desirable condition, Φ=0.8 was as one of the two off-stoichiometric conditions chosen for the wrinkled-ness study.

The Φ=1.25 (20% excess fuel) rich mixture was a natural complement to the Φ=0.8 (20% excess air) lean mixture. Therefore, the Φ=1.25 condition was chosen as the second off-stoichiometric condition for the wrinkled-ness study.

4.3.3 Homogeneous-Charge Operational Conditions Chosen for the Wrinkled-ness Study

Three final homogeneous-charge operational conditions were chosen for use the wrinkled-ness study based on the engine performance characterization results just presented in 4.3.1 and 4.3.2. A summary of the operational parameters for the final conditions is provided in Table 4-3 below.

Table 4-3: Homogeneous-charge operating condition

Intake Manifold Absolute Pressure [kPa]	40
Exhaust Manifold Absolute Pressure [kPa]	101.5
Engine Coolant Temperature [C]	45
Intake Air Temperature [C]	45
Engine Speed [RPM]	1300
Injection Pressure [MPa]	12
Start of Injection Timing [bTDCc]	310
Fuel Composition [-]	25% Toluene / 75% Iso-Octane (by liq. vol.)
Swirl Valve Position [-]	Open (Low in-cylinder swirl)
Start of Ignition Timing [bTDCc]	27

Most, but not all of the parameters listed in Table 4-3 match those that were either used or determined during the characterization studies of 4.3.1 and 4.3.2, with the notable exception of fuel composition. The fuel mixture was changed for the wrinkled-ness study from pure iso-octane to a 25% Toluene / 75% iso-octane by liquid volume mixture. The Toluene enabled the PLIF diagnostic.

A summary of the indicated engine performance for the three homogenous-charge conditions used in the wrinkled-ness study are listed in Table 4-4 below.

Table 4-4: Engine performance of three chosen homogeneous-charge conditions

	Equivalence Ratio [-]	Injected Fuel Mass [mg/cycle]	Ignition Timing [CAD bTDCc]	IMEP [kPa]	COV of IMEP [-]	CA50 [CAD aTDCc]
Lean	0.80	7.1	27	204	0.09	21
Stoichiometric	1.00	8.9	27	275	<0.01	8
Rich	1.25	11.1	27	290	<0.01	7

The indicated heat release rates and burn fractions for the three conditions, which will be referred to later in Chapter 5 are shown below in Figure 4-11.

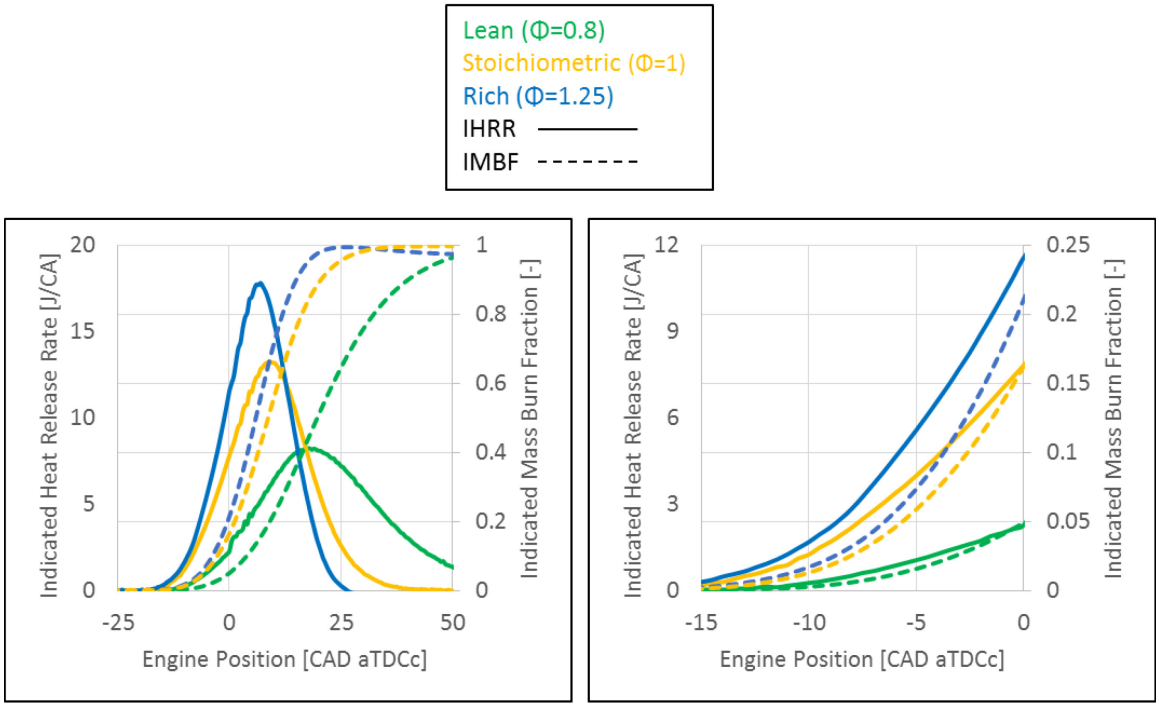

Figure 4-11: Indicated heat release rate and burn fraction for the homogeneous-charge conditions shown throughout entire cycle and throughout a sub-portion (imaged time) of the engine cycle.

Lewis number estimates and Markstein lengths measurements for both iso-octane and Toluene are included in Appendix A. The rich (Φ=1.25) mixtures used was thermo-diffusively unstable and the lean (Φ=0.8) mixtures stable. The range of equivalence ratio's spans most of that for which might be relevant in application. The fuel mixture utilized (75% iso-octane/25% Toluene) was gasoline-like. Therefore, the three homogeneous-charge conditions chosen here were ideally suited for interrogating thermo-diffusive instability effects under production like engine conditions.

4.4 Stratified Engine Performance

In order to determine the best engine test condition for use in the stratified-charge wrinkled-ness study, the G4VDI engines performance was characterized over a range of stratified-charge conditions. The following engine parameters were held constant throughout all of the characterization testing,

Table 4-5: Stratified-charge operational parameters which were held constant during engine performance optimization testing.

Intake Manifold Absolute Pressure [kPa]	95
Exhaust Manifold Absolute Pressure [kPa]	101.5
Engine Coolant Temperature [C]	45
Intake Air Temperature [C]	45
Engine Speed [RPM]	1300
Injection Pressure [MPa]	12
Fuel Composition [-]	100% Iso-Octane
Injected Fuel Mass [mg/cycle]	9.0
Global Equivalence Ratio [-]	0.30

The injected fuel mass of 9 mg per cycle was chosen to match the fueling rate of the homogeneous-charge, Φ=1 condition. The engine was operated at a high intake MAP of 95 kPaa which is typical for SI engines operating at wide-open throttle. However, the overall engine load remained low (2.5-3 bar IMEP). The global equivalence ratio of 0.3 was well below the fuels lean flammability limit and so the success of the SGSC strategy depended upon favorable partial fuel/air premixing and partially-premixed combustion.

Only one stratified-charge condition was needed for the wrinkled-ness study. However, it was challenging to identify even a single condition that featured both good engine performance and

optical visibility (i.e. adequately low levels of in-cylinder soot production). This section will begin by first focusing on engine performance optimization under the operational restrictions listed in Table 4-5 but will then move on to discuss operational compromises that were necessarily made (namely, a reduction in fueling rate) to limit in-cylinder sootiness.

Adjustable engine operating parameters included injection timing, ignition timing, and swirl valve position. The strategy employed for choosing the best performing stratified-charge condition was to first determine the best temporal phasing between the fuel spray and ignition by sweeping injection-to-ignition timings and then to determine the optimal combustion phasing by sweeping injection timings (at a fixed injector-to-ignition delay). Both the injector-to-ignition and injection timing sweeps were performed under swirl valve open (low-swirl) and swirl valve closed (high-swirl) conditions to also assess the impact of in-cylinder swirl on the SGSC engines performance.

The same indicated metrics used in 4.3 of IMEP, COV of IMEP and CA50 were used to grade the engines performance. The final condition that was selected for the wrinkled-ness testing will be presented and discussed at the end of this section.

4.4.1 Injection to Ignition Delay Mapping

The delay between start of injection (SOInj) and start of ignition (SOIgn) was optimized under SGSC conditions at a fixed SOInj timing of 25 bTDCc. The sweeps were performed under both high (swirl-valve closed) and low (swirl-valve fully open) in-cylinder swirl conditions. The results of an ignition sweep for both the low and high swirl conditions can be seen in Figure 4-12 below. There, 200 engine cycle averaged IMEP values are shown in blue, COV of IMEP values in red and miss-fire and partial burn free COV of IMEP values in green. Partial burns were defined as cycles that achieved less than half of the test average IMEP.

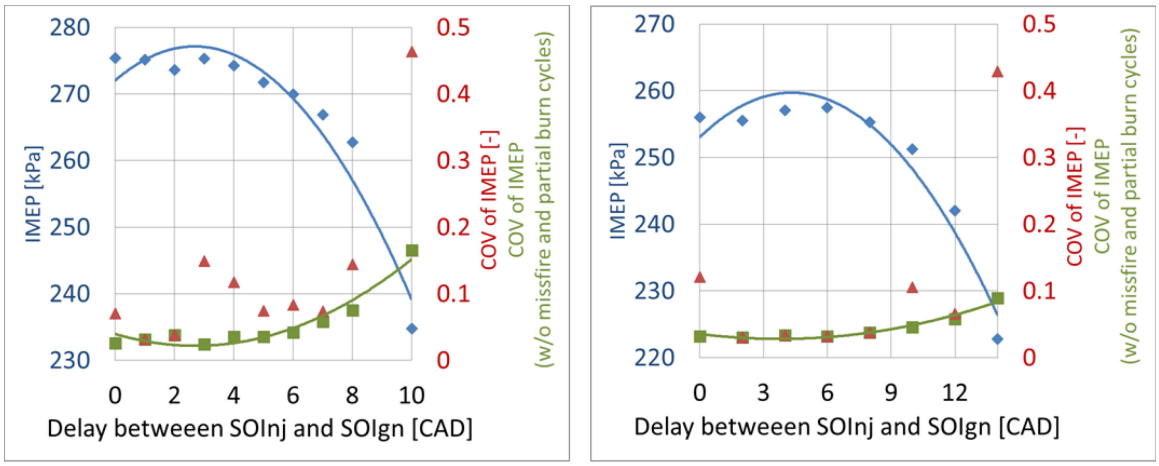

(a) Low in-cylinder swirl (b) High in-cylinder swirl

Figure 4-12: Engine performance (IMEP and COV of IMEP) vs. delay between start of injection and start of ignition under (a) low swirl and (b) high swirl, stratified, Φ=0.30 conditions.

For both high and low swirl conditions the engines performance demonstrated an impressive insensitivity to SOInj to SOIgn timing so long as the delay was shorter than 6 CAD. IMEP trends show that shorter (0-4 CAD) delays were marginally favorable under low swirl conditions. Whereas under high swirl conditions all of the delays ranging from 0-8 CAD provided identical results both in terms of IMEP output and variability. The level of IMEP variability for both low and high swirl conditions was very good for a SGSC engine. However, the rate of misfires of about once or twice per every thousandth cycles would need to be resolved if the engine were production bound. The conditions that lead to such misfires have been well described by Peterson et al. [39].

In order to gauge the effect of SOInj to SOIgn timing on combustion phasing the low and high swirl IMEP results are shown in Figure 4-13 below with CA50 values on the secondary axis instead of variability.

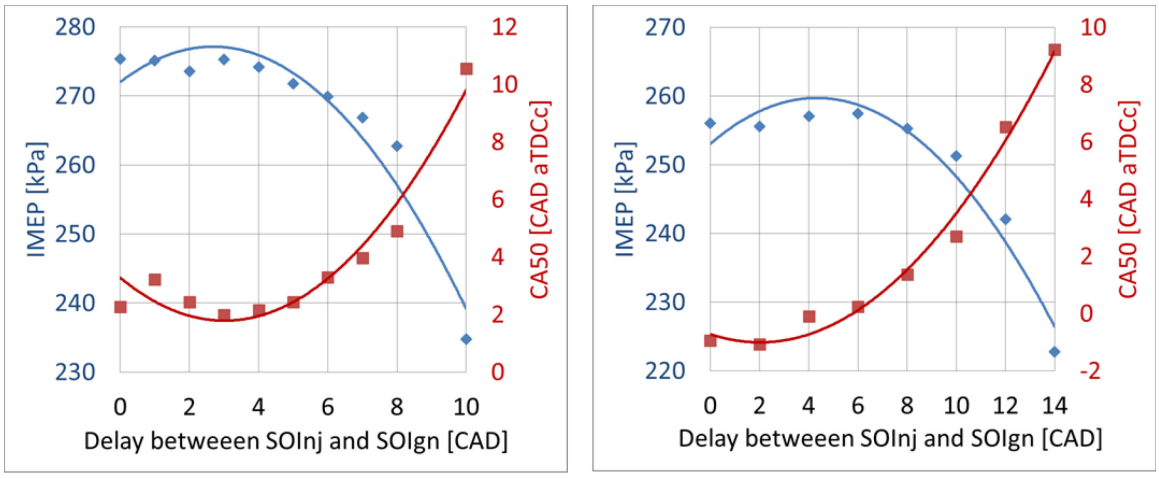

(a) Low in-cylinder swirl (b) High in-cylinder swirl

Figure 4-13: Engine performance (IMEP) and combustion phasing (CA50) vs. delay between start of injection and start of ignition under (a) low swirl and (b) high swirl, stratified, Φ=0.30 conditions.

The results in Figure 4-13 show that combustion phasing in unaffected by the SOInj to SOIgn delay so long as the delay is under 5 CAD's in length. From this it can be recognized that under low swirl conditions lengthier SOInj to SOIgn delays resulted in faster burn rates. The same cannot be said under high swirl condition where combustion phasing scaled linearly with SOInj to SOIgn for all delays less than 9 CAD's. It can also be recognized that the high swirl burn rates were relatively insensitive to SOInj to SOIgn delays over that same large range.

Based on the results in Figure 4-12 and Figure 4-13 a SOInj to SOIgn delay of 3 CAD was chosen for the wrinkled-ness study.

4.4.2 Injection Timing (Combustion Phasing) Mapping

Using a fixed SOInj to SOIgn delay of 3 CAD an injection timing sweep was performed in order to optimize combustion phasing within the engine cycle. The impact of start of injection timing on engine performance (IMEP and COV of IMEP) and combustion phasing (CA50) for both the low and high swirl conditions can be seen in Figure 4-14 below.

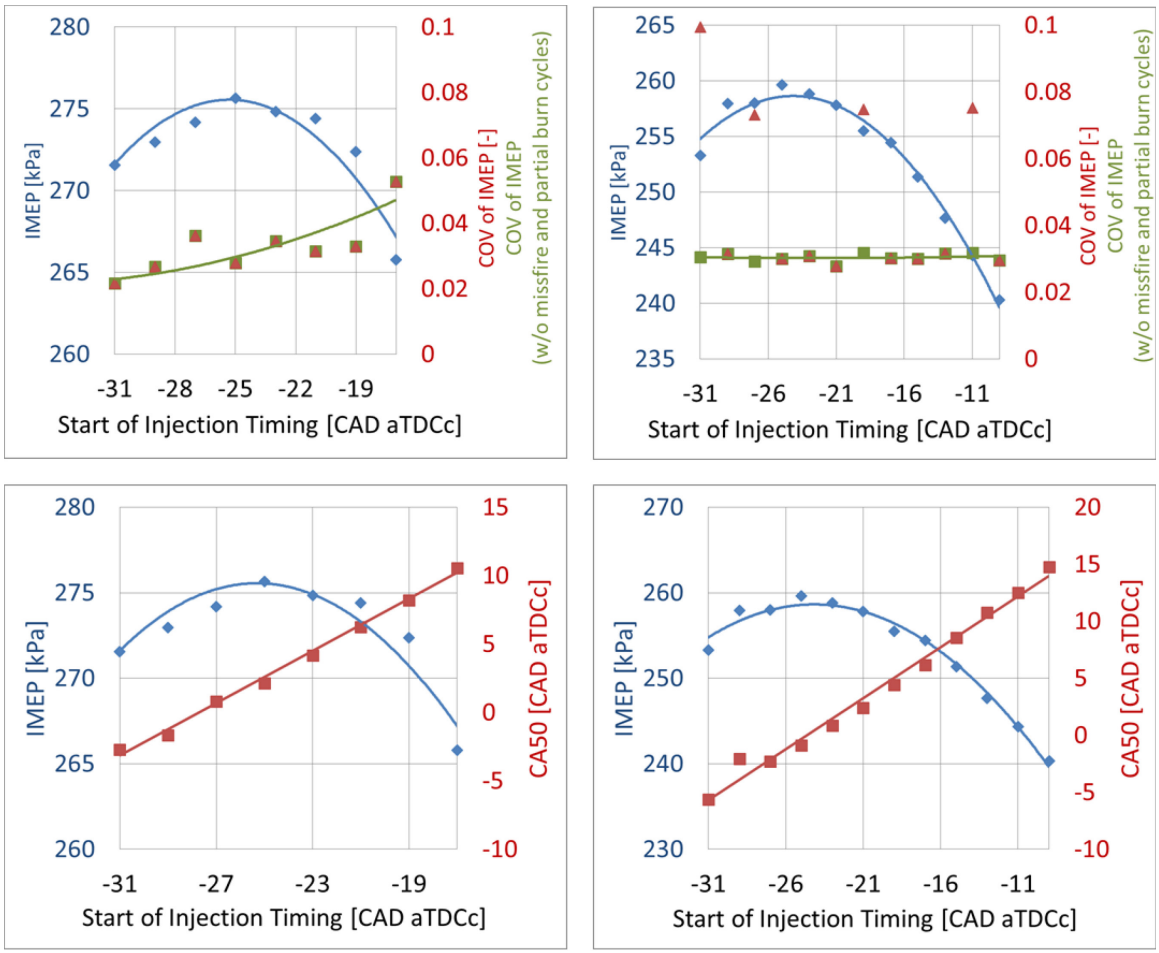

(a) Low in-cylinder swirl (b) High in-cylinder swirl

Figure 4-14: Engine performance (IMEP and COV of IMEP) vs. delay between start of injection timing under (a, top) low swirl and (b, top) high swirl. Combustion phasing (CA50) vs. start of injection timing under (a, bottom) low swirl and (b, bottom) high swirl under stratified, 95 kPa MAP, Φ=0.30 conditions with the SOInj to SOIgn delay fixed at 3 CAD.

Optimum engine output (IMEP) occurred with a start of injection timing of 25 CAD under both low and high swirl conditions. At this optimum timing the CA50 values were 0 and 2 CAD aTDCc respectably, which is very early in comparison to the optimum homogeneous-charge phasing.

Under optimal low swirl conditions the engine achieved 275 kPA IMEP at a COV of 3%. Under optimal high swirl conditions the engine achieved 260 kPa IMEP also at a COV of IMEP of 3%. These performances are excellent.

4.4.3 Stratified-Charge vs Homogeneous-Charge Engine Performance

The motivation for and the challenges of enabling SGSC strategies can be recognized by comparing the results of the optimized homogeneous-charge (Φ=1) and stratified-charge strategies. Since both optimizations were performed at the same mass fuel rate of 9 mg/cycle the engine outputs provided by both strategies can be directly compared.

Due to its high (un-throttled-like) intake MAP, the pumping losses (PMEP) for the stratified-charge condition was small at only 12 kPa. The pumping losses for the homogeneous-charge conditions were much higher at 60 kPa. Subtracting the pumping losses from the indicated outputs yields the net outputs (NMEP = IMEP-PMEP), the net mean effective pressures of the stratified and homogeneous-charge conditions measured to be 252 and 192 kPa respectively. Therefore, at the same 9 mg/cycle fueling rate, the stratified-charge strategy demonstrated a 30% increase in indicated net output relative to the homogeneous-charge strategy. This dramatic efficiency improvement demonstrates the benefit of the SGSC strategies.

The engine output variability (COV of IMEP) was 1% for the homogeneous-charge and 3% for the stratified-charge strategies, both of which are acceptably low. However, the stratified-charge strategy exhibited misfires at a rate of about 1/1000 cycles which would be commercially unacceptable. Reducing miss-fire and partial-burn cycles remains a challenge under SGSC conditions.

As promising as the stratified-charge engines indicated engine performance was at the 9 mg/cycle fueling rate; the soot levels produced by the engine were unacceptably high. Therefore, as will be discussed in the next section, SGSC soot-reduction strategies were necessarily implemented and they were done at the detriment of engine performance. The excellent SGSC engine performance results that were just shown illustrate the promise of the SGSC strategy. The soot issues to be shown demonstrates one of the greatest remaining challenges that the SGSC strategy still has to overcome. Considered collectively, the results in

this engine performance section do a good job at illustrating both the motivation for and continued research on the topic of SGSC engines.

4.4.4 Soot Reduction Measures

Despite demonstrating such promising indicated engine performance, the engine produced unacceptably high levels of soot under the optimal stratified-charge condition identified in 4.4.1 and 4.4.2. So much so that the engines optical access windows were blackening, as is show in Figure 4-15 below, too rapidly for high quality optical studies to be performed. Therefore, the root cause of the sootiness was investigated and an alternative, but similar final operating condition was chosen for use in the stratified-charge wrinkled-ness study.

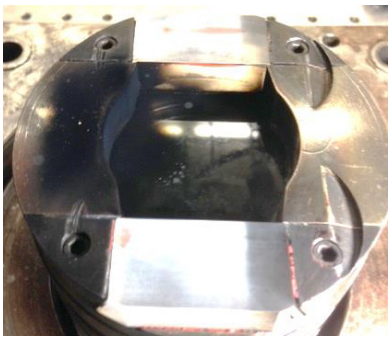

Figure 4-15: Blackened piston after a few minutes of engine operation under optimal indicated engine performance stratified-charge conditions at a fueling rate of 9 mg/cycle.

A brief imaging study was performed in an attempt to recognize the root cause of the excessive soot formation. A high speed Phantom 1610 camera was used to view the engines natural (un-filtered) luminescence from the same backside perspective shown for the PLIF camera in Figure 3-6. The camera was equipped with an unfiltered 200 mm visible lens and was operated with 50 µs exposures at a rate of one image every 0.5 CAD. The signals measured by the camera resulted from two main in-cylinder sources; combustion luminosity and soot incandescence. The latter produced signals were an order of magnitude larger and so the strong luminosity

signals could be recognized as being soot born. The luminosity imaging results can be seen in Figure 4-16 below.

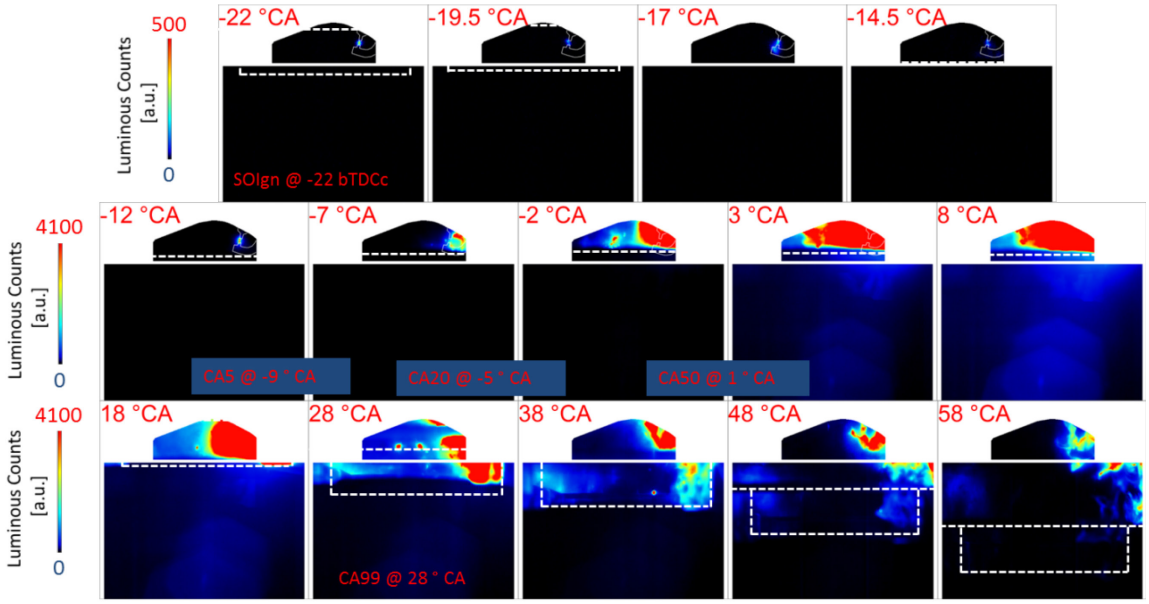

Figure 4-16: High speed natural luminescence images of a typical stratified combustion event occurring under the optimal low-swirl conditions. The locations of the piston top and the piston window have been identified in the images by dotted white lines.

Notice that from the cameras perspective, most of the stratified-combustion luminosity emanated from the right side of the bowl. This is the same region of the piston bowl that can be recognized as blackened in Figure 4-15. Although this observation in itself is unsurprising, the long-lasting nature of the luminosity is. The luminescence persisted beyond 58 CAD aTDCc and it appeared to track with the engines solid surfaces. Its continuation well beyond the indicated end of combustion (CA99) suggested that the late luminosity was emanating from only a small quantity of fuel. So much is consistent with the nature of liquid pools fires (from liquid-fuel to solid surface impingement), as is described by Drake et al. [223].

Mie-scattering studies were performed in order to assess the liquid length and potential solid surface impingement characteristics of the fuel spray. A green Nd:YAG laser beam was used to illuminate the liquid fuel spray in the 10 mm offset plane shown in Figure 3-10 under motored,

stratified-charge conditions. Despite the planar nature of the measurement technique, the sprays scattering was strong enough to illuminate liquid throughout much of the cylinder. Since liquid length is known to be highly sensitive to engine temperature (and subsequently injected fuel temperature since the injector was mounted directly inside the cylinder head), tests were performed at two different temperatures; 45 C (as originally prescribed for the optimization study) and a much higher 90 C. The spray penetration results can be seen in Figure 4-17 below. The images shown were taken at 15 bTDCc which is 10 CAD after the start of injection.

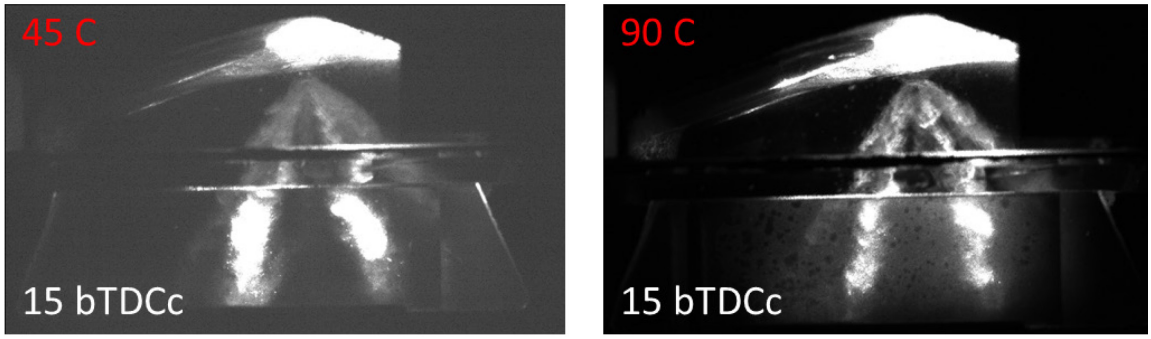

Figure 4-17: Mie scattering images of fuel-spray penetration of the G4VDI engine under stratified-charge, SOInj=25 bTDC, 1300 RPM, 95 kPaa intake MAP, low-swirl conditions at a fueling rate of 9 mg/cycle at two different engine temperatures.

Figure 4-17 clearly shows that the liquid fuel spray was penetrating all the way to the pistons solid surfaces even at high (90C) engine temperatures. Such spray impingement is known lead to thin fuel surface deposits that only contain only small quantities of fuel but are capable of producing large quantities of soot [224].

Due to the right leaning angle of the fuel injection, the right region of the cylinder that demonstrated the highest affinity to soot is also where the liquid spray is most physically constrained and likely to impinge. Due to its close vicinity to the spark plug, it is also one of the earliest burning regions in the engine liquid depositions within were unlikely to have had enough time to vaporize and mix to acceptable equivalence ratio levels.

After recognizing that excessive liquid fuel spray impingement was the likely cause of the stratified-charge soot issue efforts were made to mitigate the issue. Modest efforts were made to adjust in-cylinder conditions, such as pressures, temperatures and swirl levels to reduce spray penetration. Such efforts did not yield significant improvements in the quantity of soot deposited on the optical windows. Advanced injection strategies, such as the utilization of multiple fuel injections and/or high dilution rates promise a means for improvement [16]. However, the enablement of such strategies is beyond the scope of this study.

One of the most effective means of reducing soot formation within an engine is to lower the engines load (less fuel tends to produce less soot). Remember that the stratified-charge fueling rate of 9 mg/cycle was only chosen to match that of the homogeneous-charge, Φ=1 condition. Doing so enabled the operational mode engine performance comparisons presented in 4.4.3 to be made. However, for the sake of the wrinkled-ness study such a high fueling rate was not necessary.

Therefore, in order to reduce the soot level of the engine under stratified-charge conditions the fueling rate was reduced to 6.3 mg/cycle (Φ=0.2) for the wrinkled-ness study. The reduction in fueling did not provide soot free engine operation but it did mitigate the problem enough for the engines windows to remain acceptably clean over the duration of a stratified-charge imaging test. The piston windows remained cleaner under low rather than high-swirl conditions so low-swirl conditions were chosen for the wrinkled-ness study. In order to maintain consistency between the tests, low-swirl conditions were also accepted for the homogeneous-charge wrinkled-ness study conditions as well.

Despite the reduction in fueling rate; other previously optimized engine conditions such as start of injection and start of ignition timings proved to remain acceptable and were maintained. Although the reduction in fueling rate provided relief from sootiness it did so at the detriment of engine performance. IMEP decreased from 275 kPa to 175 kPa, as might be expected. However, the COV of IMEP increased dramatically from 3% to 12%. Therefore, the low fueling

rate condition chosen for the wrinkled-ness test may best be described as a rough idle condition. However, as will later be recognized, the test condition proved excellent for studying in-cylinder flame wrinkling.

4.4.5 Stratified-Charge Operational Condition Chosen for Wrinkled-ness Study

Three final stratified-charge operational conditions chosen for use the wrinkled-ness study based on the engine performance characterization results just presented. A summary of the operational parameters for the final conditions is provided in Table 4-6 below.

Table 4-6: Stratified-charge operating condition

Intake Manifold Absolute Pressure [kPa]	95
Exhaust Manifold Absolute Pressure [kPa]	101.5
Engine Coolant Temperature [C]	45
Intake Air Temperature [C]	45
Engine Speed [RPM]	1300
Start of Ignition Timing [CAD bTDCc]	22
Start of Injection Timing [CAD bTDCc]	25
Injection Pressure [MPa]	12
Fuel Composition [-]	25% Toluene/75% Iso-Octane
Injected Fuel Mass [mg/cycle]	6.3
Global Equivalence Ratio [-]	0.20
Indicated Mean Effective Pressure [kPa]	175

The indicated heat release rates and burn fractions for the chosen stratified charge condition, which will be referred to later in Chapter 6 are shown below in Figure 4-18.

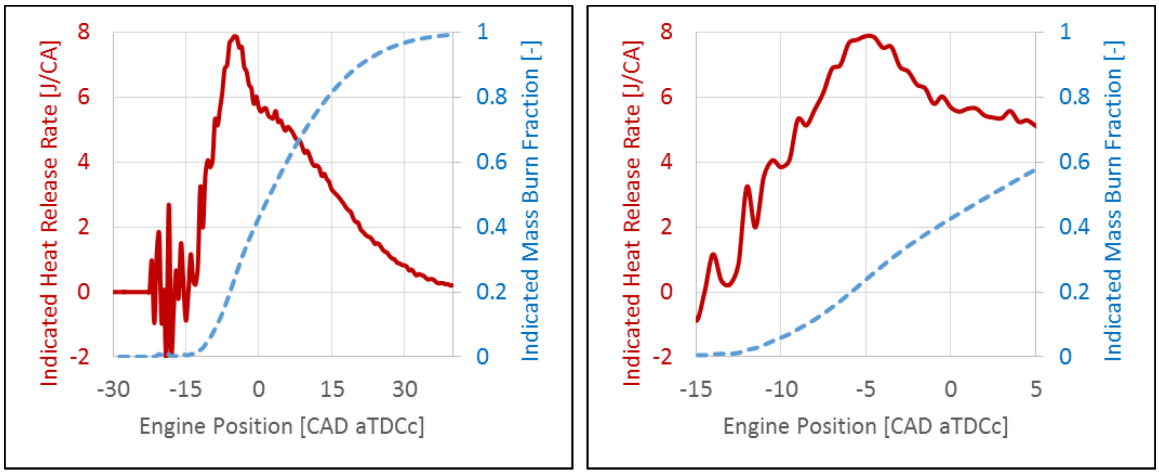

Figure 4-18: Indicated heat release rate and burn fraction for the stratified-charge condition shown throughout entire cycle and throughout a sub-portion (imaged time) of the engine cycle.

Chapter 5: HOMOGENEOUS-CHARGE FLAME WRINKLING STUDY

The G4VDI engine was operated under the homogeneous-charge conditions shown in Table 4-3 for the three air/fuel mixtures (Φ=0.8, 1, 1.25) listed there. These three mixtures exhibit very different thermo-diffusive (Lewis number) properties. PLIF and PIV images were taken at image timings ranging from 15 bTDCc to 0 bTDCc in 5 CAD increments. These image timings provided a view of the early flame development process. Basic flame properties, such as turbulent flame speeds and wrinkled-ness were estimated based on an in-cylinder pressure analysis. Flame wrinkled-ness and the relative contribution of wrinkles of varying scales towards the total wrinkled-ness was quantified from the PLIF images. In-cylinder charge-flow velocities and turbulent length scales were extracted from the PIV images.

In this section, the pressure, PLIF and PIV based results are all combined to provide conclusions regarding the relative importance of the physical processes that drove the early homogenous-charge flame wrinkle development process in this study. From this, guidance will be offered to those currently developing early flame development models for homogeneous-charge IC engines. Further, the results presented here serve as a source for comparison with the stratified-charge results to come.

5.1 In-cylinder Pressure Based Estimates of Flame Wrinkling

An in-cylinder pressure measurements analysis was performed in order to estimate in-cylinder charge burn rates and subsequently global flame speeds and flame wrinkled-ness factors for all three fuel/air mixtures. The estimates provide a means to validate the PLIF based wrinkled-ness

measurement technique. They also provide wrinkled-ness estimates for the mid-to-late burn portions of the engine cycle where the optical measurements could not be made due to field-of-view limitations.

The flame speed estimates were made by processing the measured indicated mass burn fraction profiles to estimate the diametrical growth of the flames based upon the assumption that the flames expanded spherically within the engine. The spherically propagating assumption is reasonable when the flame is small but progressively less accurate as the flame grows larger. Therefore, the absolute quantitative accuracy of the in-cylinder pressure based estimates of flame speed and wrinkled-ness factors is questionable; especially when applied to large 20+ mm diameter flames which would regularly interact with the engines solid surfaces.

Fortunately, the bias errors induced by the spherical assumption affect the results of all three mixtures in a similarly manner. Therefore, qualitative mixture-to-mixture comparisons can accurately be made based upon the estimates provided in this section. Further, the spherically propagating assumption is reasonable enough at small flame diameters to warrant a quantitative comparison with the some of the early flame development results from the optical wrinkled-ness measurements that will be presented in 5.2.

Based on the spherically propagating model, the flame burning speed was simply found by the flames radial expansion rate according to the definitions defined by Heywood [5]. Comparable laminar flame speeds were estimate by performing CHEMKIN-PRO [225] laminar flame speed calculations using the 323 species gasoline mechanism developed by Mehl et al. [226]. The thermodynamic states chosen for the calculations were based upon in-cylinder pressures and the temperature estimates shown in section 4.1. The wrinkling factor was then found as the quotient of the pressure estimated flame speed to the CHEMKIN-PRO calculated laminar flame speed.

In-cylinder heat release analyses are inherently inaccurate at really low burn fractions. Therefore, very small radius wrinkled-ness factors will not be reported here. The minimum burn fraction range that will be reported here was chosen to overlap with the maximum burn fraction range to be reported in optical wrinkled-ness results, as to provide a means for comparison.

The wrinkled-ness estimate results are shown in Figure 5-1 below. As can be seen, the wrinkled-ness factor, which provides an estimate of $\frac{S_t}{S_l}$ remains relatively constant at about 2 to 2.5 for all three mixtures over the range of data shown. The range of data (burned gas radius size range) shown on the x-axis was chosen to represent 7-25% mass burn fraction flames. The wrinkling factors in the first half of the figure (15-30 mm flame diameter) can be compared to the 5 bTDC rich and stoichiometric tests as well as the 0 bTDCc lean imaging tests that will later be shown in 5.2.1 and 5.2.2.

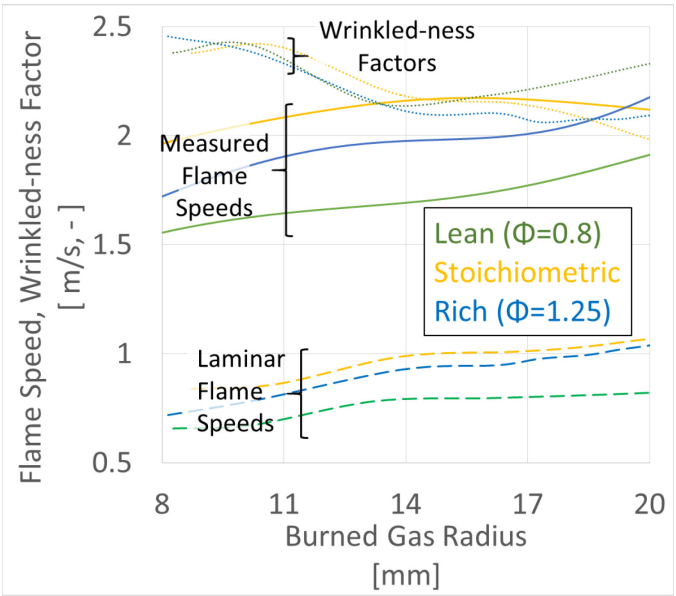

Figure 5-1: Estimated wrinkled-ness factors, flame speeds and laminar flame speeds for homogeneous-charge engine tests.

Notice that the estimated wrinkling factors are very similar for the three mixtures throughout the entire range of data shown. Therefore, during the times for which the in-cylinder pressure based wrinkled-ness estimates were made (mid-cycle, CA7-75), the inherent differences in thermo-diffusive instabilities between the three mixtures (Le > 3 for lean, Le < 1 for rich) did not cause differences in flame speed or wrinkled-ness.

These in-cylinder pressure based results show that during the bulk of the engine's burn cycle (CA7-75) the three mixtures achieved similar levels of flame wrinkled-ness. During this mid-cycle flame development period, none of the three mixtures demonstrated a propensity or resistance to wrinkling beyond that of their peers. However, the pressure based analysis was incapable of providing results during the most crucial time in the combustion cycle, the early (CA0-10) flame development period. The optical results to follow will provide just that, flame wrinkled-ness results from the early flame development period for all three mixtures.

5.2 Homogeneous-Charge PLIF Results

PLIF images were acquired under all three homogeneous-charge conditions (Φ=0.8,1,1.25) at three different image timings. The timings were temporally spaced in 5 CAD increments to provide a view of the early flame growth of the mixtures. During the image timing the flames grew from about 1-7% mass burn fractions. From comparing the three mixtures that are known to differ in propensity to wrinkle due to their inherent differences in thermo-diffusive (Lewis number) instabilities, insights were gained into the role (or lack thereof) that such instabilities during the early flame development period of a 75% iso-octane/25% toluene (gasoline-like) fueled homogeneous-charge engine under low load conditions.

The results of nine total test conditions (three Φ's, three timings) will be presented here. Each test condition was repeated three times. Test-to-test repeatability will be demonstrated.

All of the tests were performed with the laser sheet (imaging) plane at the 3 mm offset location shown in Figure 3-10. This location was near cylinder center and passed as close to the spark plug as possible without direct impingement.

Prior to the results presented here, the homogeneous-charge PLIF images were all processed according the procedures described in 3.2.5.1 and 3.2.5.3. From this, binary, spatially filtered versions of the images along with their complementary flame contours were achieved. The flame contour lengths were then measured over a range of spatial filter scales. The turbulent and laminar contours length were then defined and their wrinkled-ness factors (Ξ) were calculated.

Qualitative flame image and contour results will be presented in 5.2.1. Then quantitative flame wrinkled-ness results will then be presented in 5.2.2. These results will later be combined with the homogeneous-charge PIV results in 5.3 and conclusions will be drawn about the homogeneous-charge wrinkled-ness study in 5.4. The results and conclusions from this chapter will later be compared against the stratified-charge results.

5.2.1 Flame images and contours

In this section, the fidelity of the flame contour recognition and processing procedures will be demonstrated. Some fully processed flame images will be shown and qualitative comparisons will be made between the flame results of the three different (Φ=0.8,1,1.25) conditions. These results will lead right into the next section (5.2.2) where wrinkled-ness values will be quantified and quantitative conclusions will be drawn.

As was discussed in 3.2.5.3, all of the flame images were subject to low-pass spatial filtering in the Fourier domain over a wide range of filter scales. In order to define wrinkled-ness values, spatial scales had to be chosen to define the turbulent and laminar flame fronts by. The laminar flame front resulted from a highly filtered image (all wrinkles removed) and the turbulent flame

from a lightly filtered image (only noise removed). Physically, the definition of the turbulent flame front is well defined. The laminar, as it's being defined here, is not. The definition of an equivalent laminar flame front assumes an inherent seperability of turbulent (wrinkled) flame topology features from laminar ones. Such a separation scale is not fundamentally defined. Therefore, as will be shown, best practices had to be reasoned for selecting a proper laminar spatial filter scale.

The turbulent contour was discovered by subjecting the raw image to a low pass filtered image which removed wrinkles smaller than 0.5 mm. Remember that filters of a given scale only remove wrinkles at half of their scale. Since the laser sheet itself was 0.5 mm thick, smaller spatial features were assumed to be non-physical (measurement noise).

There might have been sub-half-millimeter wrinkles present during the tests that were not resolved by the imaging system. However, It will be shown later that such sub-half-millimeter wrinkles did not play a prominent role in the early development of the homogeneous-charge flames observed in this study and that the neglect thereof was reasonable.

Since the size of every flame realization was different, the best choice of spatial filter scale for the laminar (Ξ=1) contours was made on an image-by-image basis. In order to determine the best laminar filter scale, every flame image was filtered over an ever increasing range of scales, beginning at the 0.5 mm wrinkle scale that was prescribed for the turbulent contour and proceeding upwards until the largest possible filterable scale was reached. This maximum filterable wrinkle scale was typically 10-15 mm and beyond that any increase in spatial filter scale resulted in the total removal of the flame from the image. This limiting scale, which I will refer to as the largest filterable scale, was extracted from the images as property which was used to help specify the laminar flame filter scale value. The exact threshold for the laminar filter scale was targeted to be 85% of the maximum filterable scale. This choice was made retro-actively (after filtering was complete), so an exact 85% filter scale threshold was not applied; rather the average flame length for the filter scales ranging between 80-90% was taken to be an

estimate of the laminar flame length. Considering the uncertainty in the averaging, affectively, the laminar low-pass filter scale threshold was applied at 85 +/- 3% of the maximum filterable scale.

To demonstrate the insensitivity of the equivalent laminar flame length measurement to choice of scale threshold, an example of flame length vs. low pass filter scale for 100 stoichiometric images is shown in Figure 5-2 below. The absolute flame lengths and the maximum-filterable scales can both vary by a factor of two or more, therefore the values on both axes have been normalized by their respective maximums on an image-by-image basis. The 85% laminar filter scale threshold is shown by a vertical red line.

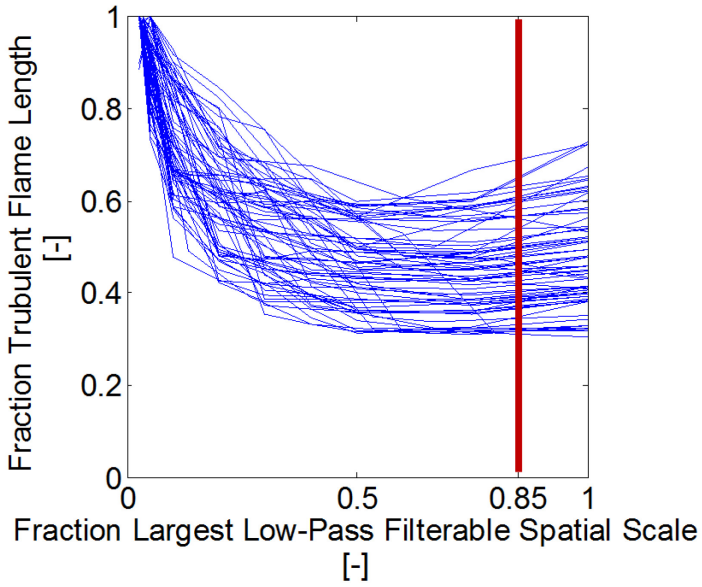

Figure 5-2: Flame length vs. spatial filter scale for 100 different stoichiometric, 5 bTDCc images. Both the flame lengths and filter scales have been normalized by their respective maximums (turbulent flame length and maximum filterable scale)

Notice that most of the flame lengths change very little between 50-100% of the maximum filterable scale. This trend will be seen to hold true for all tests. Therefore, the choice of filter scale for defining the laminar flame contour did not have to be exact in order to achieve quality flame length estimates. Based on a trial and error threshold analysis, a 10% change in threshold value results in approximately +/- 4% in absolute flame length. Since the threshold was applied

uniformly to all data sets, the 4% threshold induced uncertainty affected all of the tests in a similar manner and should have no bearing on a qualitative analysis.

The maximum filterable scales were always found to be smaller than the total expected flame size (based on comparison with the in-cylinder pressure analysis). The discrepancy between the flames diametric size and their maximum filterable size is expected for two reasons. Firstly, the limited optical field of view (20 mm x 10 mm) of the imaging system prevented the entire flame from being viewed at once. Secondly, the apex of flame rarely passes through the laser sheet and so the flames were naturally truncated due to the planar nature of the measurement. Therefore, when interpreting Ξ results, it should be recognized that the largest reported (laminar) scale will not necessarily be in good agreement with the total flame size; it tends to be a fraction thereof.

It is possible that the Ξ values reported in this study are slightly biased low due to the imaging system's inability to resolve of larger scale (10+ mm) wrinkling affects. However, as the asymptotic-like behavior of turbulent flame length vs filtered scale in Figure 5-2 suggests, there is little reason to suspect that such large scaler wrinkles contributed a significant amount of wrinkled-ness to the flames imaged in this study.

A few examples of fully processed rich, stoichiometric and lean flame images along with their turbulent (red) and equivalent laminar (cyan) contours are shown in Figure 5-3, Figure 5-4 and Figure 5-5 below.

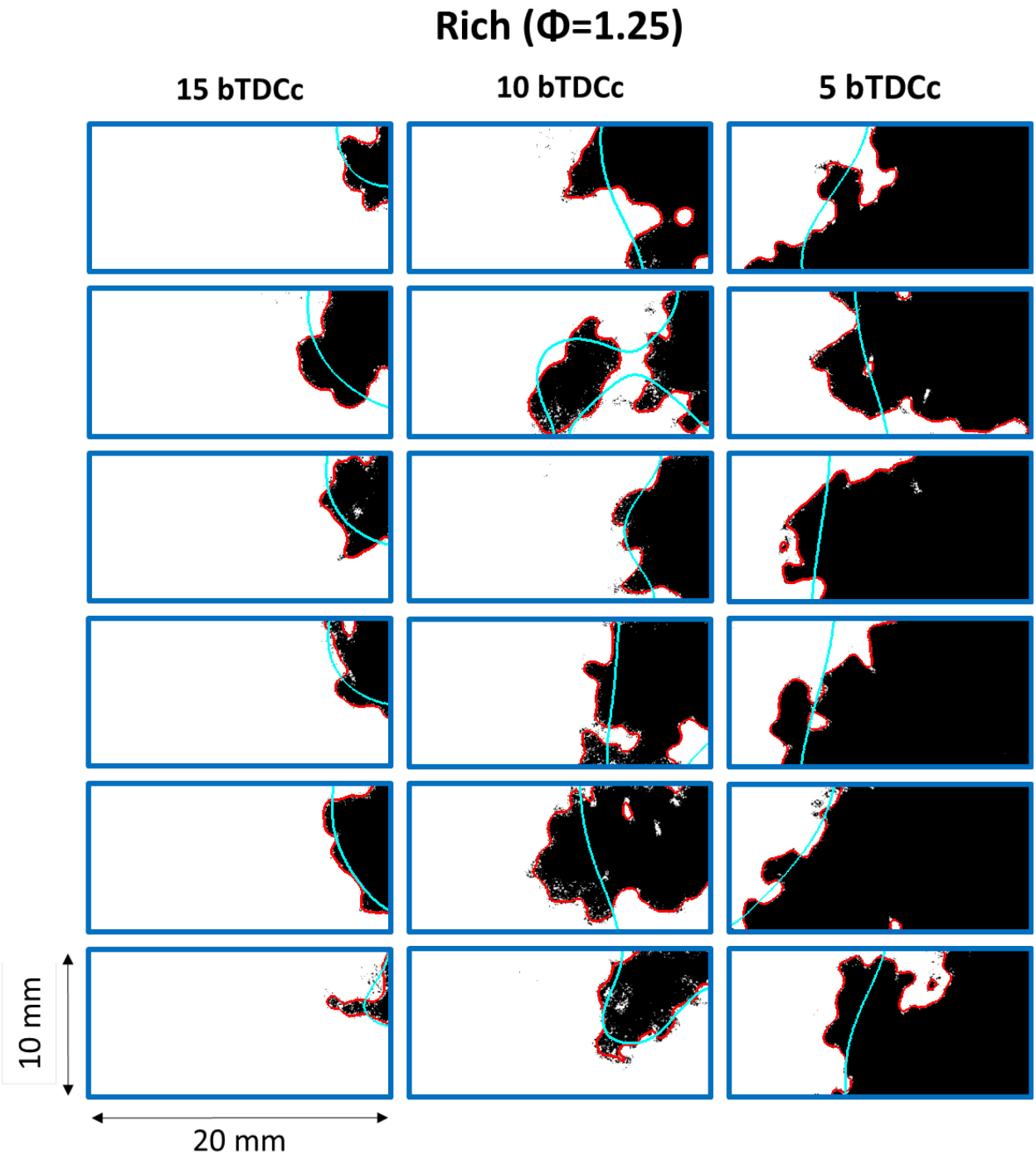

Figure 5-3: Examples of turbulent (red) and equivalent laminar (cyan) contours on homogeneous-charge rich (Φ=1.25) flames. Burned gas regions are shown in black and unburned gas regions in white.The eighteen images displayed were chosen at random.

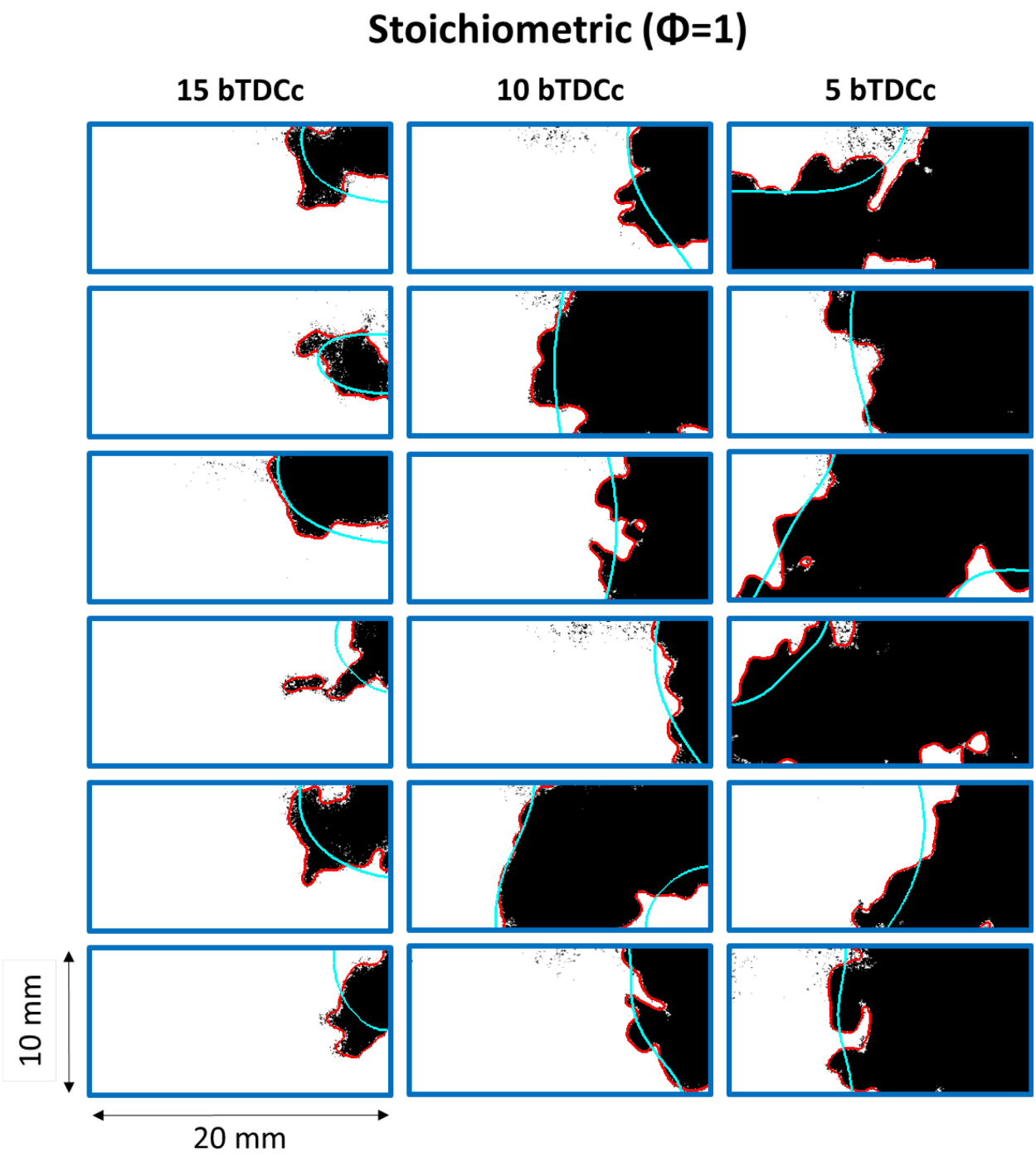

Figure 5-4: Examples of turbulent (red) and equivalent laminar (cyan) contours on homogeneous-charge stoichiometric (Φ=1) flames. Burned gas regions are shown in black and unburned gas regions in white. The eighteen images displayed were chosen at random.

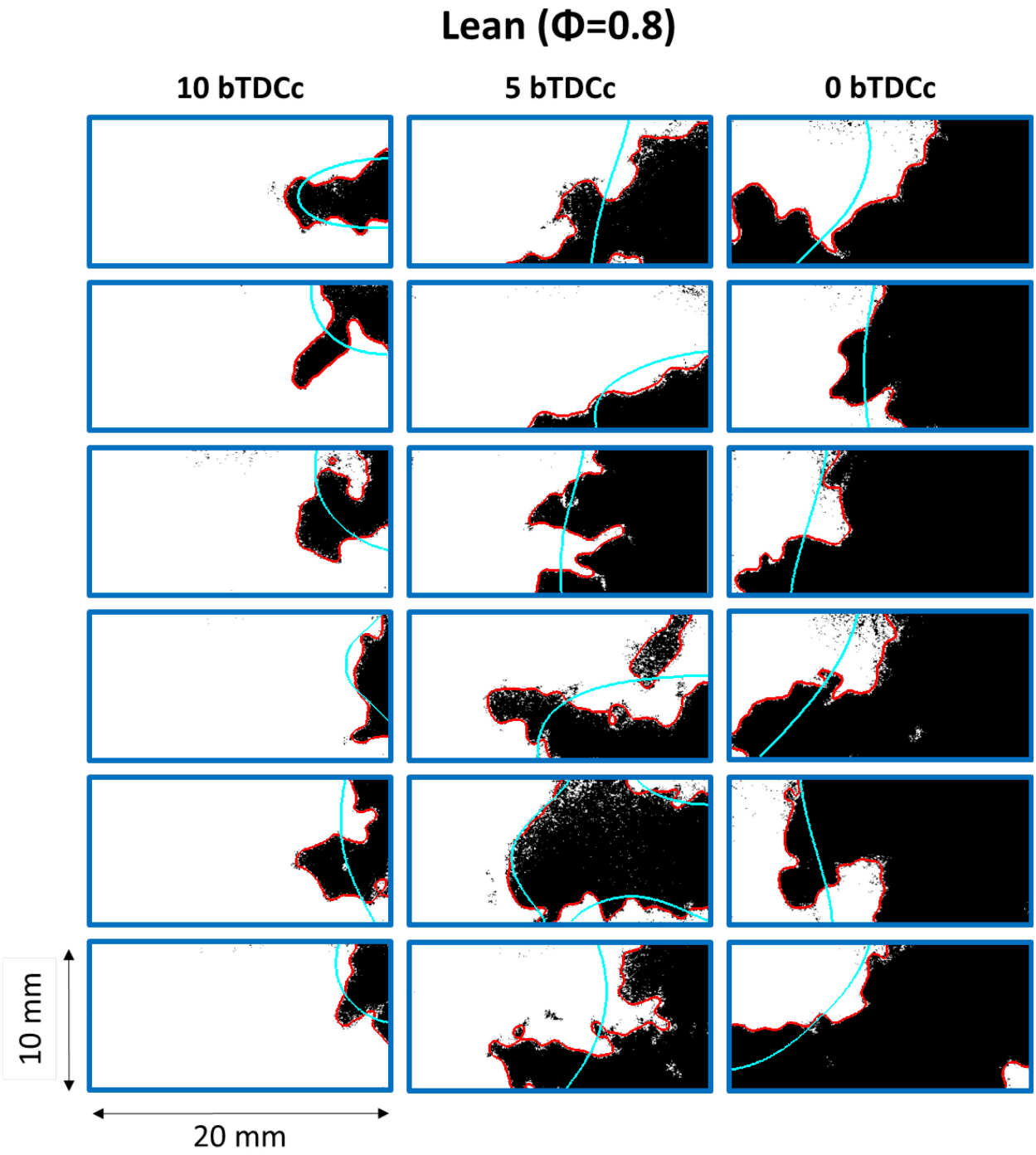

Figure 5-5: Examples of turbulent (red) and equivalent laminar (cyan) contours on homogeneous-charge lean (Φ=0.8) flames. Burned gas regions are shown in black and unburned gas regions in white. The eighteen images displayed were chosen at random.

Visually, notice that the rich and stoichiometric flames appear to grow at a similar rate from 15 bTDCc until 5 bTDCc. Also notice that they start their growth sequence at the same time (15 bTDCc) and at a similar size. The in-cylinder pressure analysis shown in Figure 5-1 supports the conclusion that the stoichiometric and rich flames propagate at a similar speed during the early flame growth period tested.

Visually, the lean flames also appear to grow from a similar size and at a similar rate to its richer counterparts. However, they do so at a delayed starting time (10 bTDCc instead of 15 bTDCc). The apparent similarity in growth rate between the lean flames and their richer counterparts is misleading as it was shown in Figure 5-1 that the lean flames propagated significantly slower than their counterparts. Remember that the burned gas size recognized by the PLIF imaging system is not an exact indicator of overall flame size. Therefore, no conclusions about flame size should be drawn from the images in these three sequences alone.

Nonetheless, in terms of the spatial development of the flames, the three sequences shown are similar enough to warrant a visual comparison. In doing so, the first thing to notice is that wrinkled-ness of the flames in all three sequences look very similar. So much so that an unbiased observer would be unable to identify which flame resulted from which air/fuel mixture.

The second thing to notice is the common burn path for the three mixtures. All of the flames began their propagation in what appears as the upper right (spark plug side) of the images. The in-cylinder tumble airflow tended to direct the early flame kernels from the upper right corner towards the center of the field of view. The flames tended to follow the tumble flow across the face of the piston bowl before eventually turning upwards towards the rest of the unburned gas charge. Clearly, the bulk in-cylinder flow velocity was high enough to direct the early flame kernels. Many previous researchers have recognized the ability of strong in-cylinder flows to convect small flame kernels long distances across combustion chamber during the ignition delay period. The images in Figure 5-3, Figure 5-4, Figure 5-5 and many more not shown,

suggest that such that the kernels in this study were only modestly directed. Most began rapidly visible growth (CA2+) within 10 mm of the spark plug electrode.

The third and most important thing to notice from this sequence is that the turbulent and laminar flame contours identified by the technique developed for this study produced physically reasonable results. The red turbulent flame contours track all of visible flames features well. With some imagination, the laminar flame contours can also be recognized to be free of wrinkles but still reassembling the original flame. The algorithm even produced good results under complex conditions, such as multiple or broken flame fronts. So much has not been demonstrated by any other contour/spatial filtering based wrinkled-ness quantification method in the past.

5.2.2 Homogeneous-Charge Flame Wrinkled-ness

The primary goal of the homogeneous-charge test presented here was to characterize the wrinkled-ness development process of the early flames created by the three different mixtures; both for the purpose of assessing the impact of the mixtures differing thermo-diffusive properties but also as a baseline for comparison with the stratified-charge flame results which will be presented in Chapter 6.

In this section, the quantitative homogeneous-charge flame wrinkled-ness results will be presented. Not only will the wrinked-ness values for all of the conditions be shown, but the scales for which the wrinkled-ness developed will also be evaluated.

The wrinkled-ness characterization results for three (repeat) rich, 5 bTDCc (~CA7) tests are shown below in Figure 5-6 as a plot of flame wrinkled-ness vs filter scale.

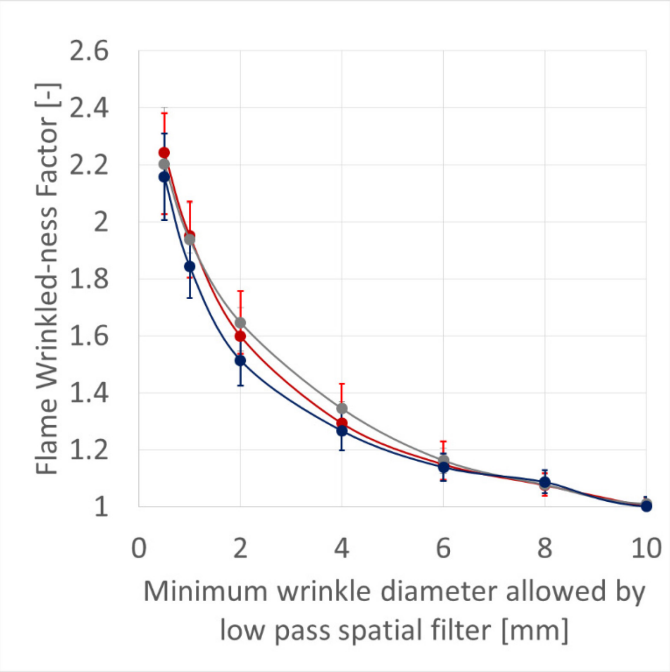

Figure 5-6: Flame wrinkled-ness factor vs. minimum wrinkle diameter allowed by low pass spatial filter for three different, 100 engine cycle, 5 bTDCc tests, under homogeneous-charge, rich conditions.

Notice the low test-to-test variability in the mean that is demonstrated in Figure 5-6. Standard 95% uncertainty estimates suggest that the uncertainty in the single test 100 cycle wrinkled-ness measurements were was about +/-10%. The mean values for all three tests differed by less than 5% over the entire range of filtered spatial scales. The optical wrinkled-ness quantification process proved reliable, repeatable and acceptably certain.

Figure 5-6 shows that about 50% of the rich flames wrinkled-ness generation (and flame surface area) was created by 0.5-2 mm diameter wrinkles, about 40% by 2-6 mm diameter wrinkles and only about 10% due to larger wrinkles. Therefore, nearly all of the turbulent flame surface area generation in the rich, 5 bTDCc tests occurred due to wrinkle formation on the 0.5-6 mm wrinkle diameter scales.

The total wrinkled-ness factor for the rich 5 bTDCc condition, which can be recognized as the wrinkled-ness value measured at the smallest (0.5 mm wrinkle diameter) filtered scale, is about 2.2. This value is in excellent agreement with the in-cylinder pressure and CHEMKIN-PRO based

wrinkled-ness estimates previously presented in Figure 5-1. As this section progresses, many more wrinkled-ness values will be presented that can be similarly compared back the estimates in Figure 5-1. By doing so it can be recognized that the optical wrinkled-ness estimates are in good agreement with the in-cylinder pressure based estimates.

To begin comparing the three different mixtures (Φ=0.8,1,1.25), Figure 5-7 shows flame wrinkled-ness vs spatial filter scale results at comparable timings; a rich 10 bTDCc test is shown in red, a stoichiometric 10 bTDCc test is shown in blue and a lean 5 bTDCc test is shown in green. The mass fraction burn for the three tests is about 2 (+/- 1) %. Therefore, the mean flame sizes in the tests are expected to be similar (~ 10-20 mm in diameter) and the three conditions are ripe for comparisons.

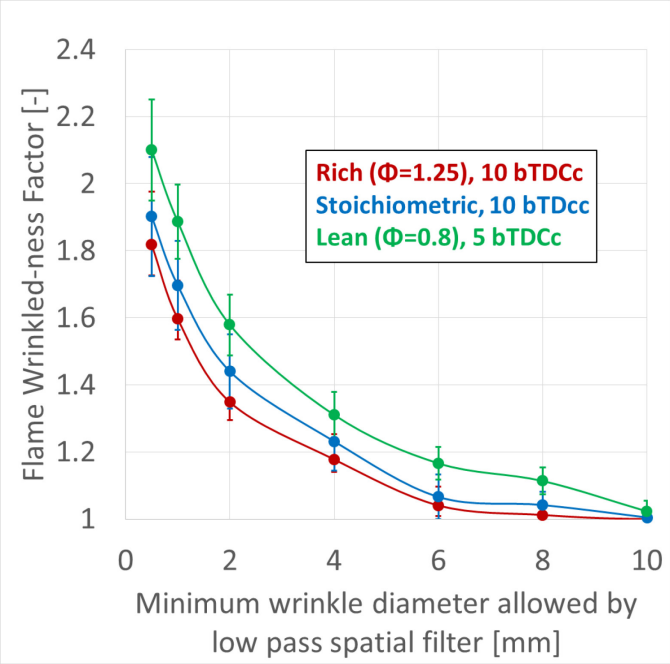

Figure 5-7: Flame wrinkled-ness factor vs. minimum wrinkle diameter allowed by low pass spatial filter for three different, 100 engine cycle, tests, under homogeneous-charge, rich ,stoichiometric and lean conditions at 10 bTDCc, 10 bTDCc and 5 bTDCCc timings respectively. The timings were chosen to so that the mass burn fraction (~2%) and flame size of all three mixtures were comparable.

The trends in Figure 5-7 show that the rich flames wrinkled the least, but not statistically significantly less than the stoichiometric test. The lean test wrinkled the most (Ξ=2.1), but only marginally so in comparison to the rich and stoichiometric tests (Ξ=1.85). This wrinkled-ness trend is counter to what might be expected considering the thermo-diffusive instability differences between the three mixtures. The Lewis number of lean mixture was the highest and the rich mixture the lowest, so acting based upon its own natural instabilities alone, the rich mixture was expected to wrinkle the most.

For both the stoichiometric and rich tests, 50% of the wrinkled-ness was generated by 0.5-2 mm diameter wrinkles and nearly all of the remaining entire remaining 50% was created by 2-6 mm diameter wrinkles. Unlike the previously reported rich, 5 bTDCc conditions showed in Figure 5-6 and the lean condition, the rich and stoichiometric tests showed a negligible amount of wrinkling on the 6-10 mm scales.

The extra 10% wrinkled-ness that the lean mixture showed in Figure 5-7 relative to its stoichiometric and rich counterparts can almost solely be attributed to its increased level of large (6+ mm) diameter scale wrinkling. Remember that the test image timings selected for comparison in Figure 5-7 were chosen in order to provide similar flame progress in terms of burned gas fraction but in order to do so, the lean flame mixture was necessarily allowed an extra 5 CAD (64 μs) to develop. The extra time that the lean mixture was provided might explain its marginally higher degree of wrinkled-ness.

The rich 5 bTDCc test results previously shown in Figure 5-6 can be directly compared to the rich 10 bTDCc tests in Figure 5-7. The only difference between the two conditions was the imaging timing. During the 5 CAD's that separated the two tests, the flame developed 20% more wrinkled-ness. At least half of the acquired wrinkled-ness occurred due to 6+ mm wrinkles forming. This result, combined with the lean flame result discussed in the previous paragraph, suggest that the early flame wrinkling process observed in this study was unstable

with respect to time and that small (0.5-6 mm) wrinkles tended to form more rapidly than large (6+ mm) wrinkles.

The total wrinkled-ness results for all three mixtures (lean, stoichiometric, rich) for all three imaging times are displayed in the two figures below. Mean wrinkled-ness vs. engine position is shown in Figure 5-8 and mean wrinkled-ness vs. indicated mass burn fraction in Figure 5-9.

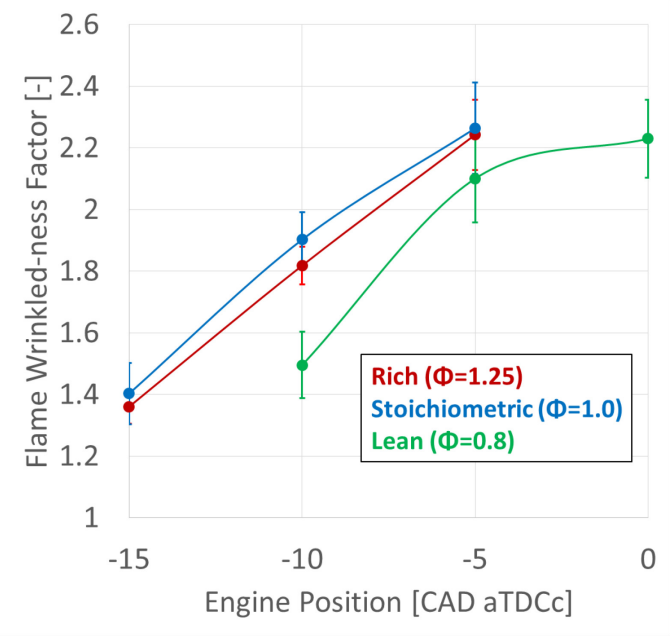

Figure 5-8: Wrinkled-ness vs. Engine position for all three equivalence ratios. The error bars represent the standard 95% CI for the sample mean.

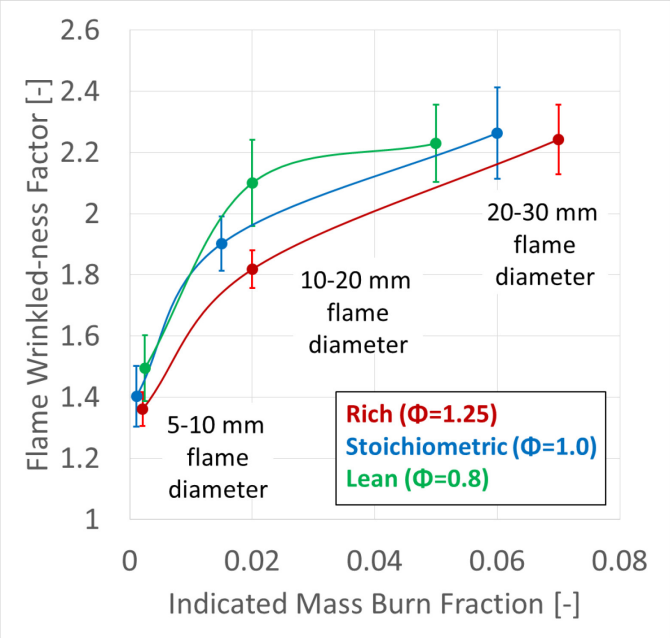

Figure 5-9: Wrinkled-ness vs. Indicated mass burn fraction for all three equivalence ratios. The vertical error bars represent the standard 95% CI for the sample mean. The exact uncertainty of the indicated mass burn fraction estimates cannot be provided but is approximately 0.01.

Figure 5-8 shows that on a time basis, the lean mixture is slower to develop wrinkled-ness than the rich or stoichiometric condition. The rich and stoichiometric mixtures develop wrinkled-ness at a very similar rate. Remember that the lean mixtures exhibit a much lower flame speed and is therefore much slower to develop in size as well. For example, at 10 bTDCc, the lean flames are only about 5-10 mm in diameter whereas the rich and stoichiometric flames are about 10-20 mm. For this reason, it is probably unfair to compare the development of the three air/fuel mixtures on a time (or CAD) basis.

Figure 5-9 shows wrinkled-ness vs. indicated mass burn fraction which scales with flame size. When viewed this way, all three mixtures develop wrinkled-ness at a similar rate and approach a like magnitude of Ξ~2.2 by CA7. Remember that the wrinkled-ness estimate findings in 5.1 suggested that mid-cycle (CA7-CA75) flame wrinkled-ness was quasi-steady and similar at about Ξ~2-2.5 for all three mixtures. Therefore, although the imaging system was limited to viewing only a small percentage of the total combustion process (CA1-7), most of the flame wrinkled-

ness development that occurred was captured by the diagnostic and can be recognized in Figure 5-9.

The highly transient wrinkle development phase of all three mixtures was long and continued for the first 20-25 CAD's (256-320 μs) after start of ignition. Considering that the combustion durations (CA10-90) themselves were of similar temporal length (25-40 CAD), it is of little surprise that engine combustion phasing is so strongly dependent on the early flame development phase.

Somewhat surprisingly, despite the inherent differences in thermo-diffusive stability between the three air/fuel mixtures, none of the early flames generated within the mixtures demonstrated either a propensity or resistance to wrinkling beyond that of their peers. Therefore, in this homogeneous-charge engine flame study, thermo-diffusive (Lewis number based) natural instabilities affects did not play a prominent role in the early flame wrinkled-ness development process.

5.3 Homogeneous-Charge Stereo PIV Results

The homogeneous-charge stereo particle image velocimetry (PIV) results will now be presented. The homogeneous-charge PIV results serve as a compliment to the previously presented PLIF results; both of which will be combined in 5.4 to draw conclusions.

Prior to any of the results presented in this section, the homogeneous-charge PIV data was processed from its raw form into vector fields according to the procedures discussed in 3.2.4. The PIV results will be presented in two separate sub-sections. In the first section titled flow fields will present the measured flow and turbulent velocity fluctuation fields. In the second section the turbulent length scales of the flow will be analyzed. Collectively, these two sections provide an overall characterization of the in-cylinder flow properties

The results in this section are based upon a set of motored engine tests under stoichiometric (Φ=1) conditions. The engine was operated as it normally would under fired conditions; that is at 1300 RPM, 40 kPA intake MAP, 45 C engine and intake temperatures and with early (310 bTDCc) fuel injection. However, ignition was neglected so that the charge wouldn't burn. This enabled clean (flame free) PIV measurements to be under conditions that resembled those that of the homogeneous-charge flame wrinkled-ness tests discussed in 5.2.1 and 5.2.2.

5.3.1 Flow-Field Results

Ensemble average flow fields for all image timings (15, 10, 5, 0 bTDCc) are shown in Figure 5-10 below. The top image in the figure shows the 15 bTDCc vector field with one of the two stereo-PIV cameras field of view in the background for reference. Remember that the stereo PIV cameras necessarily viewed the laser sheet (imaging) plane from an angle. Hence, the atypical (angled) view of the cylinder head as a whole.

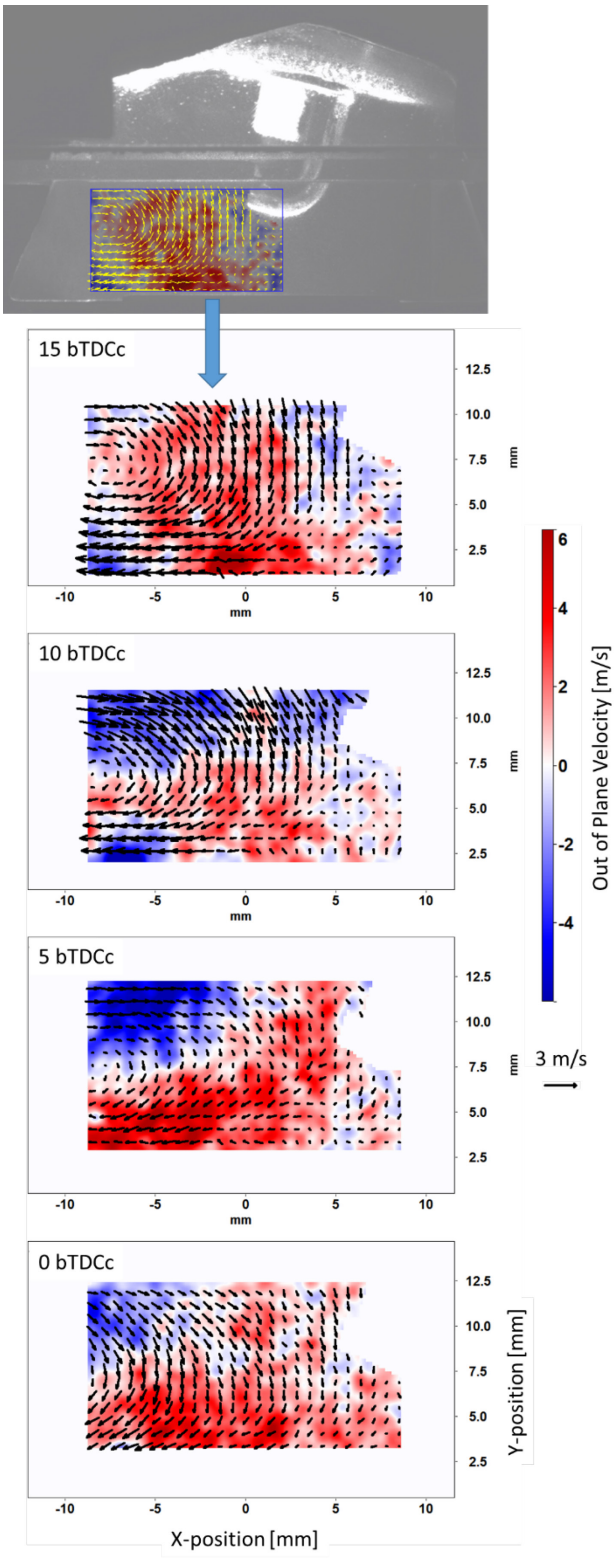

Figure 5-10: Homogeneous-Charge Planar 3D Flow Velocity Fields (40 cycle averages)

The spatial average of the ensemble averaged x and y velocity components (i.e. the average in plane velocities) were on the order of 2 m/s. The velocities were highest early in the cycle (15 bTDCc) and lowest later in the cycle (0 bTDCc). Turbulent viscous dissipation is responsible for the losses in flow velocity that occurred between the two timings.

The clockwise nature of the engines in-cylinder tumble flow can clearly be recognized in the test mean flow fields shown in Figure 5-10. A nearly 10 mm in diameter clockwise rotating vortical structure is visible in the left half of the earlier (15 to 5 bTDCc) test average images.

The out-of-plane (z) velocities measured to be about 4 m/s on average. This is about twice that of the in-plane velocities. However, remember that due to the tight angle between the two cameras (30 degrees) that the out-of-plane velocity measurements were +/- 5 m/s uncertain. Qualitatively, Figure 5-10 shows that the spark plug lies right along the breaking surface of a tumble structure; whereas most of the flow below (piston side) the plug is directed out-of-plane and most of the flow on or above the height of the spark plug is directed in-plane.

Five individual cycle flows-field were chosen at random and are displayed in Figure 5-11 below.

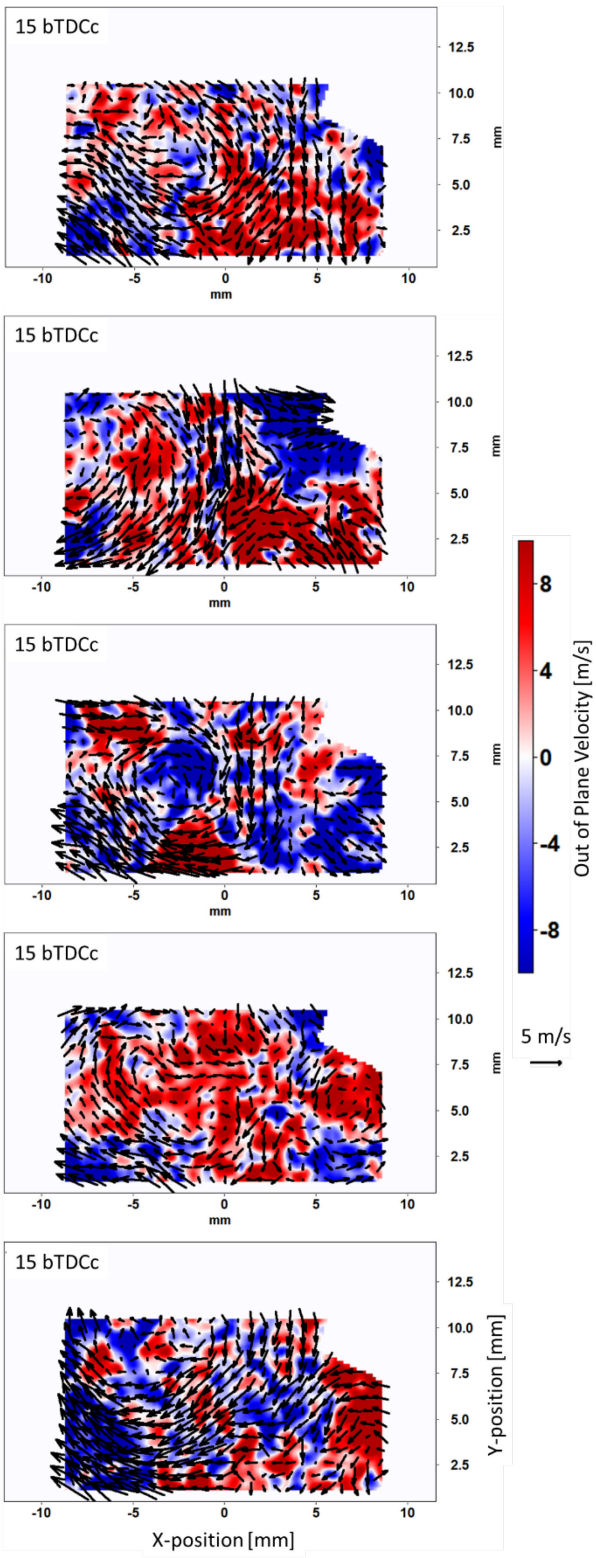

Figure 5-11: Homogeneous-Charge Planar 3D Flow Velocity Field Examples (Single Shot Images)

Notice that the individual cycle flow field velocities are about 50% higher than were recognized in the ensemble average fields. Turbulent velocity fluctuations are responsible for the balance between the two. Generally, the same in-plane tumble flow structure can be seen within all of the individual images. Vortices as large as 10 mm in diameter can be visually recognized and so it is reasonable to expect that the Integral length of the turbulent in-cylinder flow is of a similar size.

There are a lot of small scale structures visible in the out-of-plane flow velocity distributions (red and blue shaded regions within Figure 5-11) which are not thought to be physical. Once again, remember the in and out of plane velocity measurements were inherently highly uncertain. The individual cycle out-of-plane velocity distributions are thought to be too uncertain to warrant a detailed analysis or conclusions.

The chaotic nature of the in-cylinder flow is demonstrated in the root-mean-square turbulent fluctuation velocity fields shown in Figure 5-12 below.

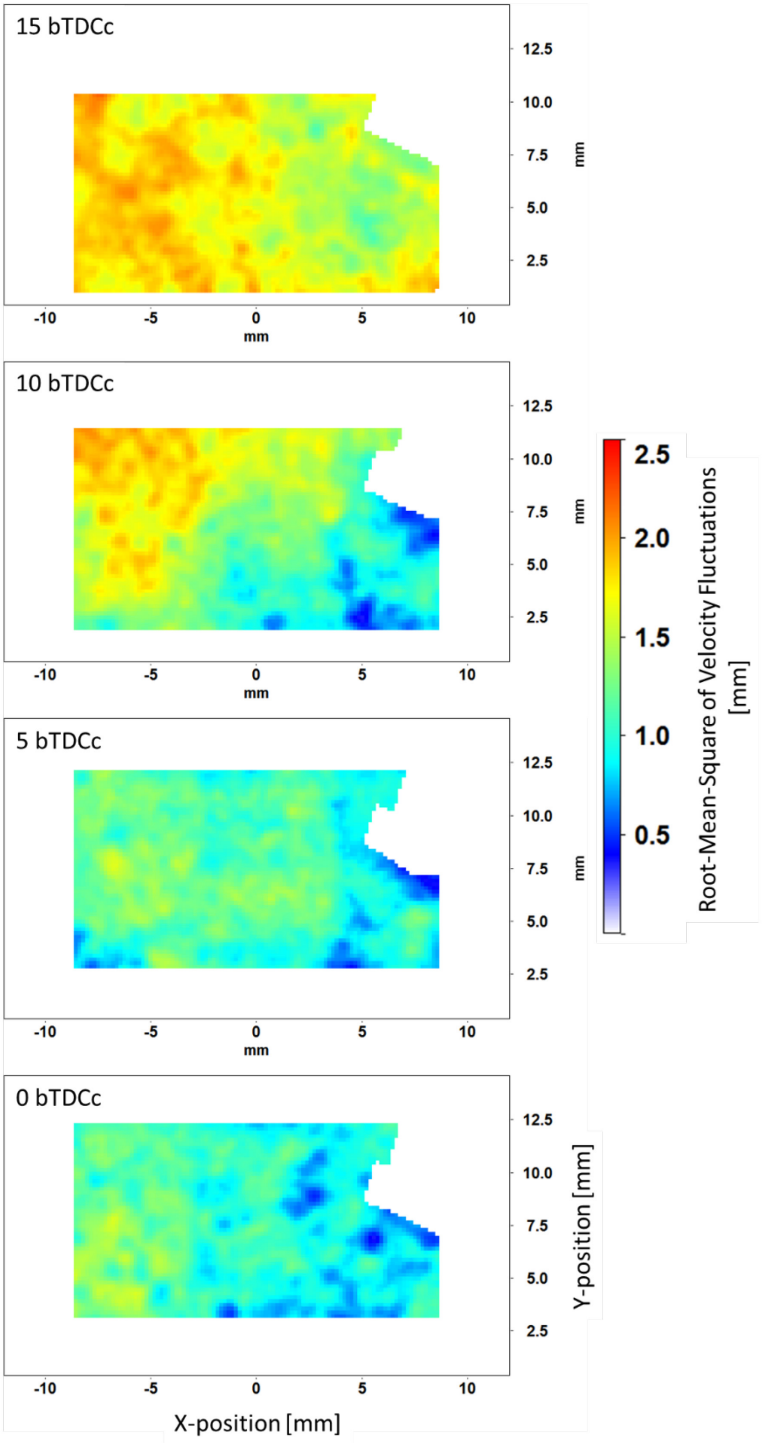

Figure 5-12: Root-mean-square of velocity fluctuations of the homogeneous-charge in-cylinder flow calculated based upon in-plane velocity components from 40-cycle tests.

Notice that the RMS velocity fluctuations (1-2 m/s) are of a similar magnitude as the average flow velocities (1-3 m/s) shown in Figure 5-10. Therefore, the turbulence intensity values

throughout the field of view range from about 50-100%. In comparison with other common turbulent flow applications, such as flows though turbines or pipes, these intensities are extremely high, perhaps an order of magnitude larger than typical. However, it will later be shown that the Reynolds number of the in-cylinder flow is also very low (~250) and the application traditional turbulence concepts such as turbulent intensity may not be appropriate.

Nonetheless, the in-cylinder flow is both directed and variable at a magnitude of approximately 2 m/s. Also remember that the developed (CA7+) in-cylinder flame velocities were estimated to be approximately 1.5-2 m/s. During the early flame development period that was optically investigated the flames propagated even slower. Therefore, the engine flames were highly susceptible to chaotic flow manipulation and bulk convection, especially when they were small.

Having recognized the basic feature of the in-cylinder flow field, the turbulent length scales results will now be presented.

5.3.2 Turbulent Length Scale Results

The homogeneous-charge PIV measurements were processed according to the procedures discussed in 3.2.4.3. From this, estimates of the turbulent in-cylinder charge-flow scales were made according to the procedures discussed in 3.2.4.5, the results of which will be presented here.

Prior to presenting the scale results, it should be recognized that the small scale (Taylor and Kolmogorov) measurements come with a large amount of uncertainty that arises for a number of reasons; including the finite 0.6 mm resolution of the PIV system and the anisotropy of the flow itself. It is reasonable to expect that the Taylor scale estimates are accurate within about a factor or two and the Kolmogorov a factor of five.

The integral length scales and Taylor microscales were measured in both the X (cylinder radial) and Y (cylinder axial) directions and their spatial distributions are shown separately from 15 to 0 bTDCc in Figure 5-13 and Figure 5-14 below.

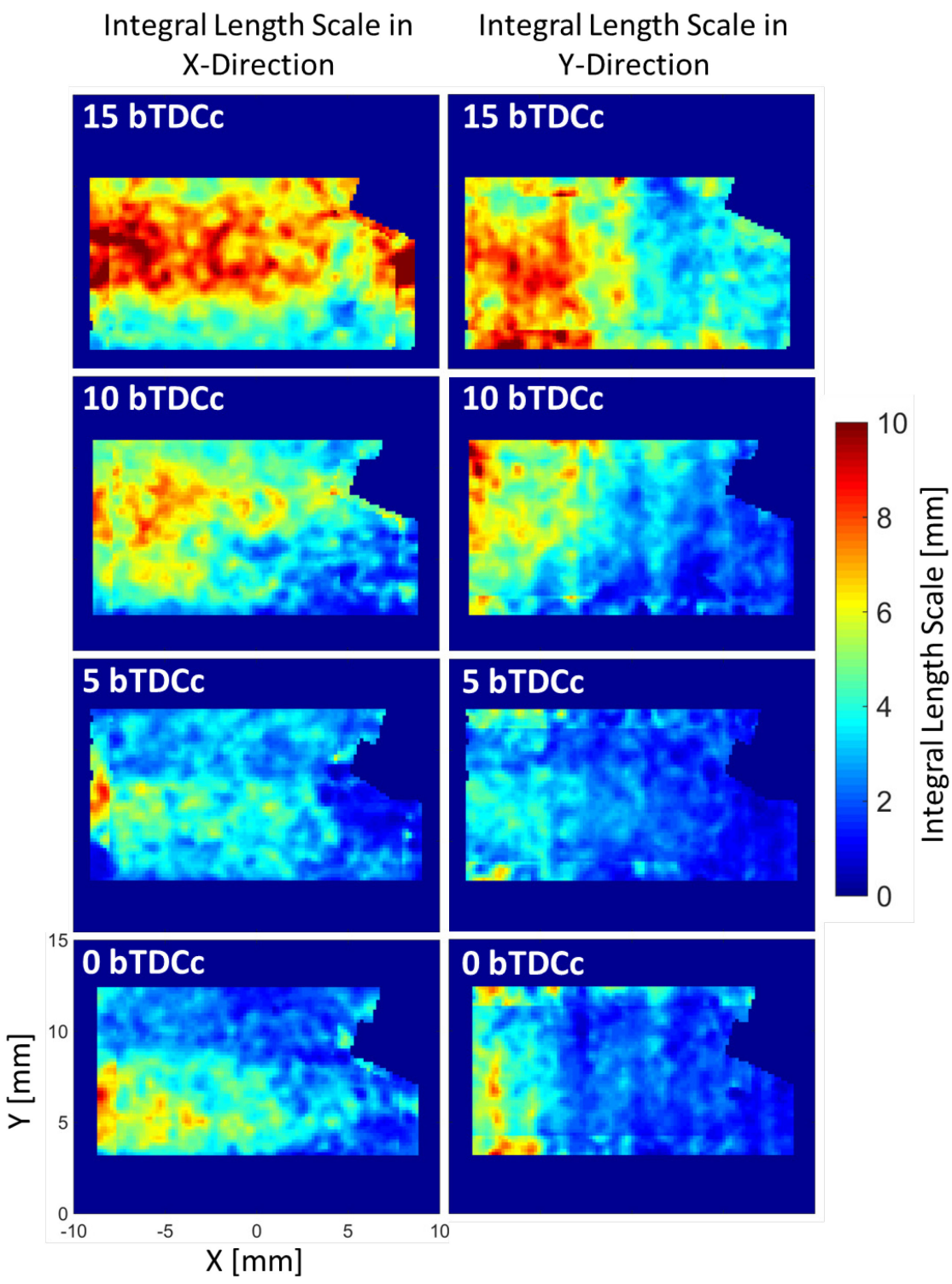

Figure 5-13: Integral length scale distribution in piston bowl. The measurements were taken during 100 engine cycle, Φ=1, homogeneous-charge, spark-disabled (motored) tests at image timings of rom 15, 10, 5 and 0 bTDCc.

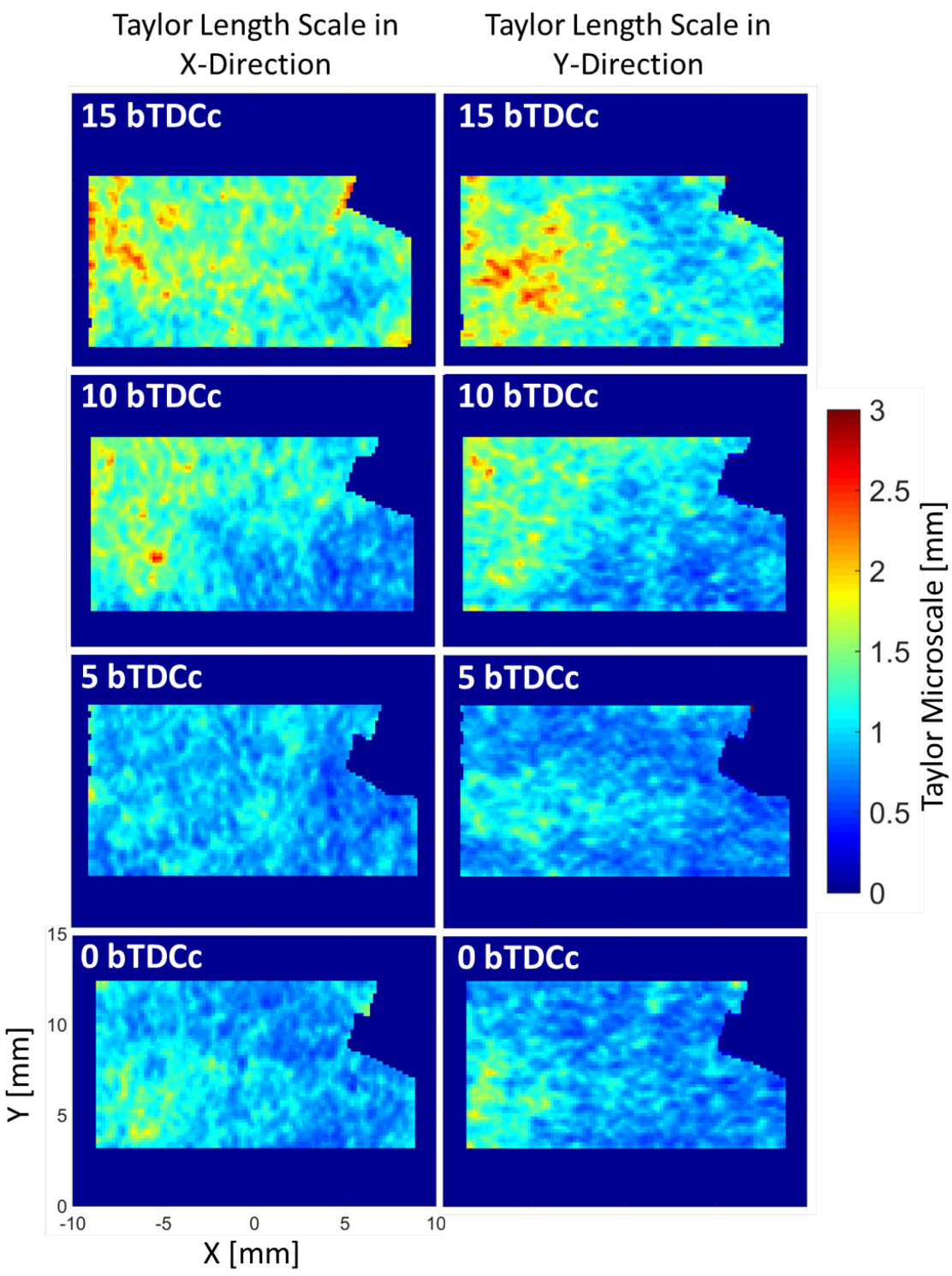

Figure 5-14: Taylor length scale distribution in piston bowl. The measurements were taken during 100 engine cycle, Φ=1, homogeneous-charge, spark-disabled (motored) tests at image timings of rom 15, 10, 5 and 0 bTDCc.

This spatially resolved length-scale presentation style shown in Figure 5-13 and Figure 5-14 is rather atypical as turbulent length scales are usually quantified as a singular property value. However, in this study the spatial variances in measured flow scales were recognized to be as large as fivefold. Much of the variance in the measured scales is thought to be due to the anisotropy of the flow itself. Therefore, the turbulent length scales measured in this study will continue to be treated as they were displayed in Figure 5-13 and Figure 5-14, as spatially distributed properties.

Notice that both the integral scales and the Taylor microscales generally decrease between 15 and 0 bTDCc. This decrease in scale is due to compressive effect of the piston on the in-cylinder charge. More specifically, as the piston moves towards TDC the spatial dimension of the cylinder charge itself reduces and the turbulent flow structures are forced to package themselves into smaller spaces.

Quantitatively, the integral length scales measured 3-8 mm and the Taylor microscales 0.5-2 mm depending on the in-cylinder location. Qualitatively, the Taylor microscales tend to measure about a fourth of the size of the integral length scales. Similar overall and relative length scale magnitudes have been observed in other engine studies [227, 228].

The distribution for both the X and Y direction integral scales and Taylor microscales that were shown in Figure 5-13 and Figure 5-14 are shown in a different form, as statistical probability density functions (pdf's) in Figure 5-15 below.

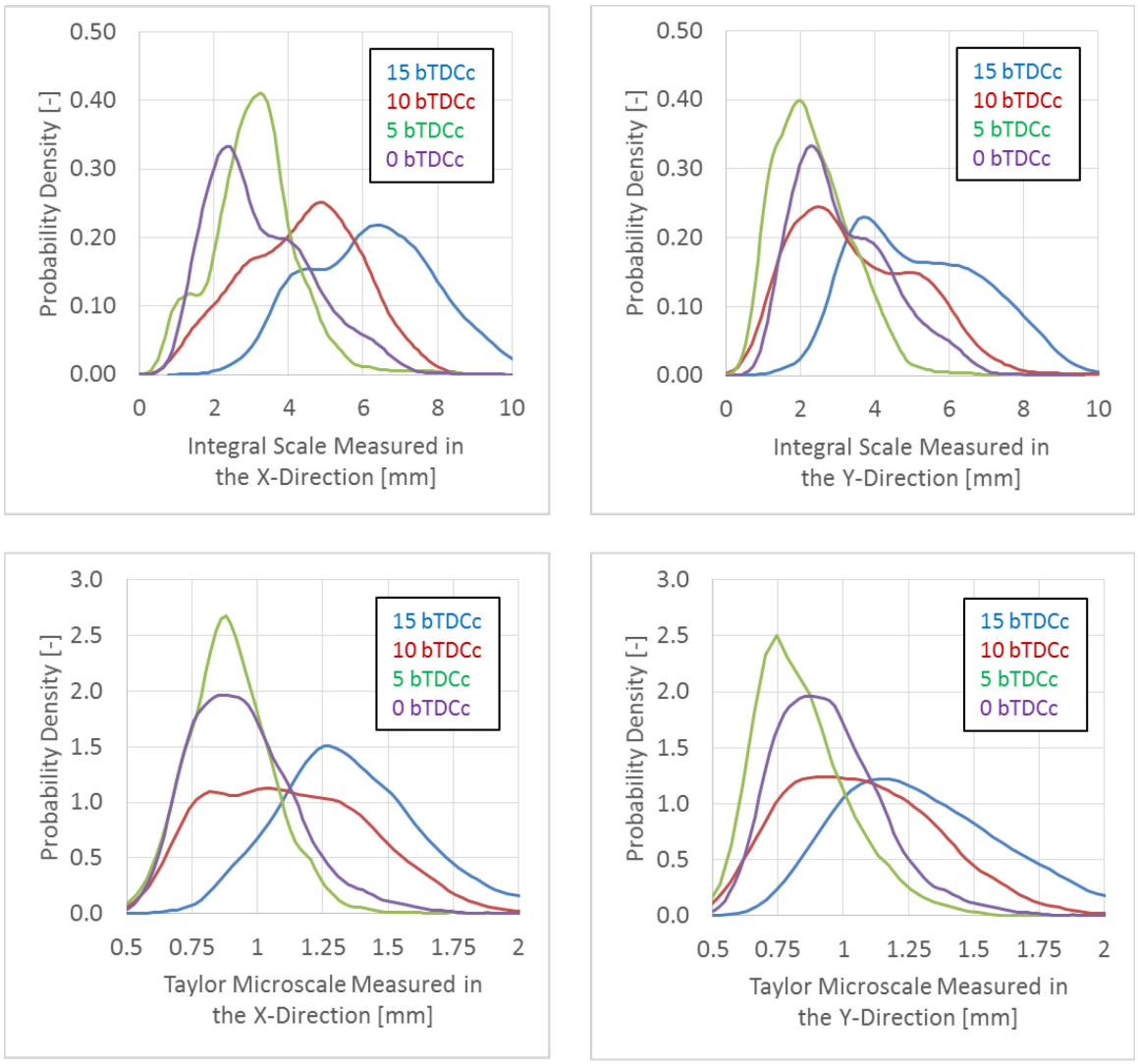

Figure 5-15: Probability density distribution of the homogenous-charge integral length scales and Taylor microscales as measured in the X and Y-directions throughout the entire field-of-view for the same tests shown in Figure 5-13.

The pdf distributions of the scales are wide. The confidence intervals suggest that 95% of the spatial length scale values measured within +/- 50% of the spatial mean. This large spread in the distribution is thought to be due mostly to the anisotropy of the flow itself. Hence, no single value could characterize the flow scale values any better than within about a factor of two.

Accepting the anisotropy, the spatial average flow scales and their respective standard 95% confidence intervals are shown in Figure 5-16 below.

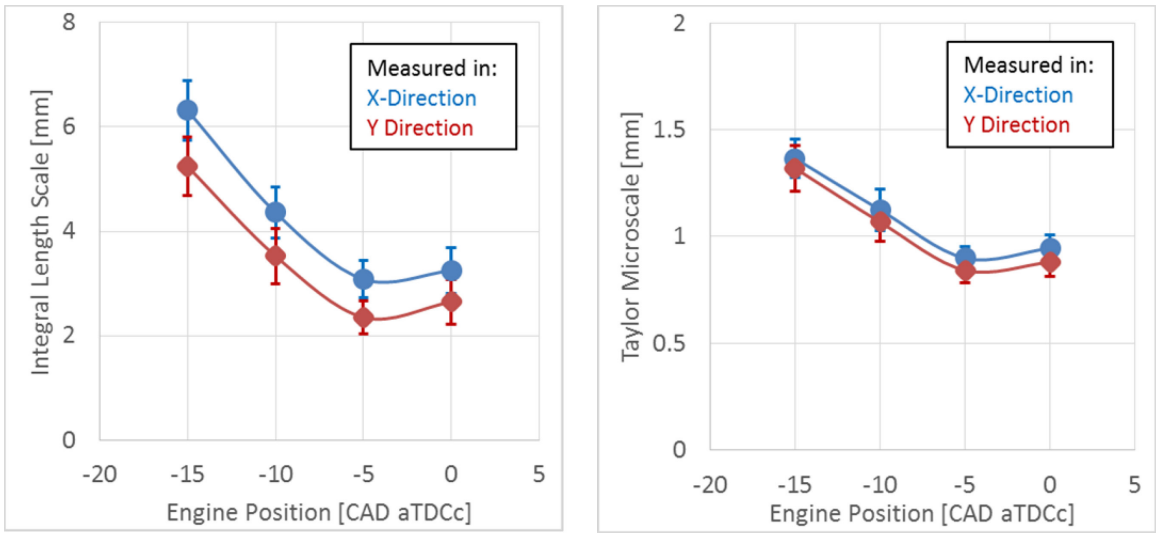

Figure 5-16: Spatial mean homogeneous-charge integral length and Taylor microscales (throughout entire field-of-view) vs. engine position as measured in both the x and y directions for same 100 cycle tests shown in Figure 5-13. The error bars represent the standard 95% confidence interval in the mean.

The spatial mean integral scale begins at about 6 mm at 15 bTDCc and drops to about 3 mm by 5 bTDC. The spatial mean Taylor microscale begins at about 1.5 mm at 15 bTDCc and drops to about 0.75 mm by 5 bTDCc. Both scales remain nearly constant between 5 and 0 bTDCc; a time for which the piston moves very little and much of the turbulent kinetic energy that was once provided by the intake jet flow has already dissipated.

Based on the integral and Taylor scale values shown above, the turbulent Reynolds number at 15 bTDCc is about 250 and the Kolmogorov length scale is about 0.1 mm. At 5 or 0 bTDCc the turbulent Reynolds number is the same but the Kolmogorov length scale is about 0.05 mm. These measured scales can now be used to help interpret some of the previously presented homogenous-charge flame wrinkled-ness results.

5.4 Homogeneous-Charge Conclusions

Early flame development and charge-flows were observed within the cylinder of an optically accessible DISI engine that was operated under homogeneous-charge spark-ignited conditions.

Planar laser induced fluorescence (PLIF) images were acquired and used to identify and track flame fronts. The PLIF images were processed to reveal flame wrinkled-ness and to determine the scales for which flame wrinkling occurred. Particle image velocimetry (PIV) was used to track in-cylinder charge-flow. The PIV images were processed to reveal charge-flow velocities and to characterize the length scales of the turbulent in-cylinder flow. From this study, the following can be concluded,

1. By the end of the early flame development period (CA1-CA7), the flames from all three mixtures showed similar levels of wrinkled-ness.

2. From about CA10 until CA75, there was no in-cylinder pressure based evidence to suggest that the flames from any of the three mixtures acquired excessive wrinkled-ness relative to its peers. There was no evidence to suggest a sudden onset of wrinkled-ness (or rapid growth of cellular structures) occurred for any of the three mixtures at any time during the tests.

3. Over the optically observed duration (approximately CA1→7), on average, the flames from the stoichiometric (Φ=1) and rich (Φ=1.25) homogenous-charge mixtures developed wrinkled-ness at a similar rate. Flames from the lean (Φ=0.8) mixtures developed wrinkled-ness at a slower temporal rate. However, on a per-size basis, the lean flames developed wrinkled-ness faster than the stoichiometric and rich mixtures. The developmental differences between the lean and richer flames can probably be attributed to the relative differences in their laminar flame speeds.

4. Despite the inherent differences in thermo-diffusive stability of the three air/fuel mixtures, none of the mixtures demonstrated a propensity or resistance to wrinkling beyond that of their peers. Relative to flow induced wrinkling affects, natural instabilities did not demonstrate an impactful role in the early homogeneous-charge flame wrinkled-ness development processes.

5. 0.5-6 mm wrinkles were responsible for the bulk (90+%) of the wrinkled-ness recognized by all three mixtures at all engine timings. Throughout the tests, the spatial average in-cylinder integral scales measured to be 3-6 mm and the Taylor scales 0.75-1.5 mm. Therefore, the flames predominately wrinkled on the same scales as the turbulent in-cylinder flow and turbulent flame-to-flow interactions are thought to be responsible for the bulk of the flame wrinkled-ness development observed in this study.

6. Small flame wrinkles formed faster than large flame wrinkles. Total flame wrinkled-ness was dependent on both flame-to-flow interaction time and overall flame scale/size.

Based on the conclusions above, this homogeneous-charge study has demonstrated the dominant ability of in-cylinder flow to wrinkle early homogeneous-charge 75% Iso-Octane/25% Toluene flames on scale with the in-cylinder flow (Taylor→integral scale) completely independent of the mixtures natural tendency to promote or resist wrinkling based on its thermo-diffusive properties. Being that the engine conditions chosen for this study exhibited relatively low in-cylinder turbulence intensities levels relative to many typical conditions (such as higher engine speeds), flame-to-flow interaction based wrinkling is expected play a more dominant role in driving the early flame wrinkling process under most homogeneous-charge spark-ignited engine conditions.

Some comparisons can be made between this study and others. For example, Aleiferis et al. [229] performed an in cylinder flow and wrinkle scale analysis in a homogeneous-charge engine and discovered similar integral scale length magnitudes and trends. They utilized a qualitative Fourier wrinkled-ness analysis technique and identified a similar range of flame wrinkle scales (0.75-5 mm diameter). Their technique did not allow for wrinkled-ness or the relative contribution of different scales to be quantified so no such comparisons can be made. However, the generally good agreement between the findings of this study in their own in terms of wrinkle and flow scales, despite the inherent differences in engine geometry, speaks well for the large scale applicability of both studies.

Brequigney et al. [230] studied thermo-diffusive effects in a lean burn SI engine using three fuels of differing thermo-diffusive properties: iso-octane, methane and propane. They characterized flame wrinkled-ness under very similar operational conditions to those of this study. Brequigney et al. recognized flame topological effects within their engine with they attributed to thermo-diffusive instabilities. More specifically, they noted a marginal increase in flame wrinkled-ness from methane and propane mixtures relative to an iso-octane mixture. Remember that no similar thermo-diffusive instability effects could be recognized in this study. However, the method for which thermo-diffusive instabilities were introduced into the two studies were different (fuel vs. equivalence ratio variations). Therefore, care should be taken when extending the conclusions drawn from this study with regards to the insensitivity of homogeneous-charge engine flame wrinkled-ness to thermo-diffusive instabilities towards engines operating on significantly different fuels, such as methane and propane. The choice of fuel composition and equivalence ratios for this study were selected to be production (gasoline) like. As such, the conclusions drawn are thought to be relevant towards conventional (gasoline fueled) automotive SI engines.

Considering the conclusions above, some guidance can be offered to those modeling early flame development in homogeneous-charge engines. Since most of the early flame wrinkling observed in this study occurred on scale with the Taylor microscale, spatial resolution can best be prescribed to capture the physics occurring around this scale. For example, in this study, the Taylor microscale (and the most prominent wrinkling scale) was measured to be about 0.5 mm. Therefore, a complementary Large Eddy Simulation model best consider physically resolving the flow structures at or below the 0.5 mm scale. If that same model were to want to resolve the finer (and most important) features of the flame topology then the grid spacing would have to be about an order of magnitude smaller than the Taylor scale to resolve the smaller wrinkles. Considering that the Taylor scale decreases with engine speed a physically accurate engine flame topology simulation would demand grid spacing on the order of 0.01 mm, far finer than what is currently practical for engine design purposes.

If non-physical sub-scale/empirical wrinkled-ness models are to be developed or used they should necessarily depend strongly upon flame-to-flow interaction times and scales. So long as the fuel in use is similar to that of this study, the model should display a weak or negligible dependency on thermo-diffusive instability based physics.

Chapter 6: STRATIFIED-CHARGE FLAME WRINKLING STUDY

The G4VDI engine was operated under the stratified-charge condition listed in Table 4-6. PLIF and PIV images were taken at image timings ranging from 12.5 bTDCc to 5 aTDCc in two imaging planes. The images timings provided a view of the early-to-mid cycle (CA1-50) flame development process for four out of eight of the stratified-charge fuel jets. Flames were identified from a combination of equivalence ratio (Toluene PLIF) and burned gas (stereo-PIV) information. Flame wrinkled-ness and the relative contribution of wrinkles of varying scales towards the total wrinkled-ness was quantified from the PLIF images. In-cylinder charge-flow velocities and turbulent length scales were extracted from the PIV images.

In this section, the pressure, PLIF and PIV based results are all combined to provide conclusions regarding the relative importance of the physical processes that drove the stratified-charge flame wrinkle development process in this study. From this, guidance will be offered to those currently developing early flame development models for stratified-charge IC engines. Further, the results presented here serve as a source for comparison with the homogeneous-charge results and comparisons of the two studies will be made in the conclusions of this section.

6.1 Stratified-Charge Combined PLIF/PIV Imaging Results

A combination of the PLIF and stereo-PIV results were used to characterize the in-cylinder equivalence ratio distribution, burned gas area and flame locations for the stratified-charge images taken in both of the optical imaging planes described in 3.2.2. The procedures used to

process the images from their raw form into these quantities were described in 3.2. Further, the stratified engine operational condition itself was described in 4.4.5.

The optical imaging results are shown in Figure 6-1 through Figure 6-9 below. The first five image panels in the sequence were acquired from in the three millimeter offset imaging plane at engine timings 12.5, 10, 5, 0 and -5 bTDCc. The last four image panels were acquired in the ten millimeter offset imaging plane at engine timings of 10, 5, 0, -5 bTDCc. The start of imaging timing of 12.5 bTDCc was chosen because it was the earliest liquid-fuel free and subsequently equivalence ratio quantifiable timing possible. All of the panels are composed of twelve individual cycle images that were chosen from a much larger set of 300 images.

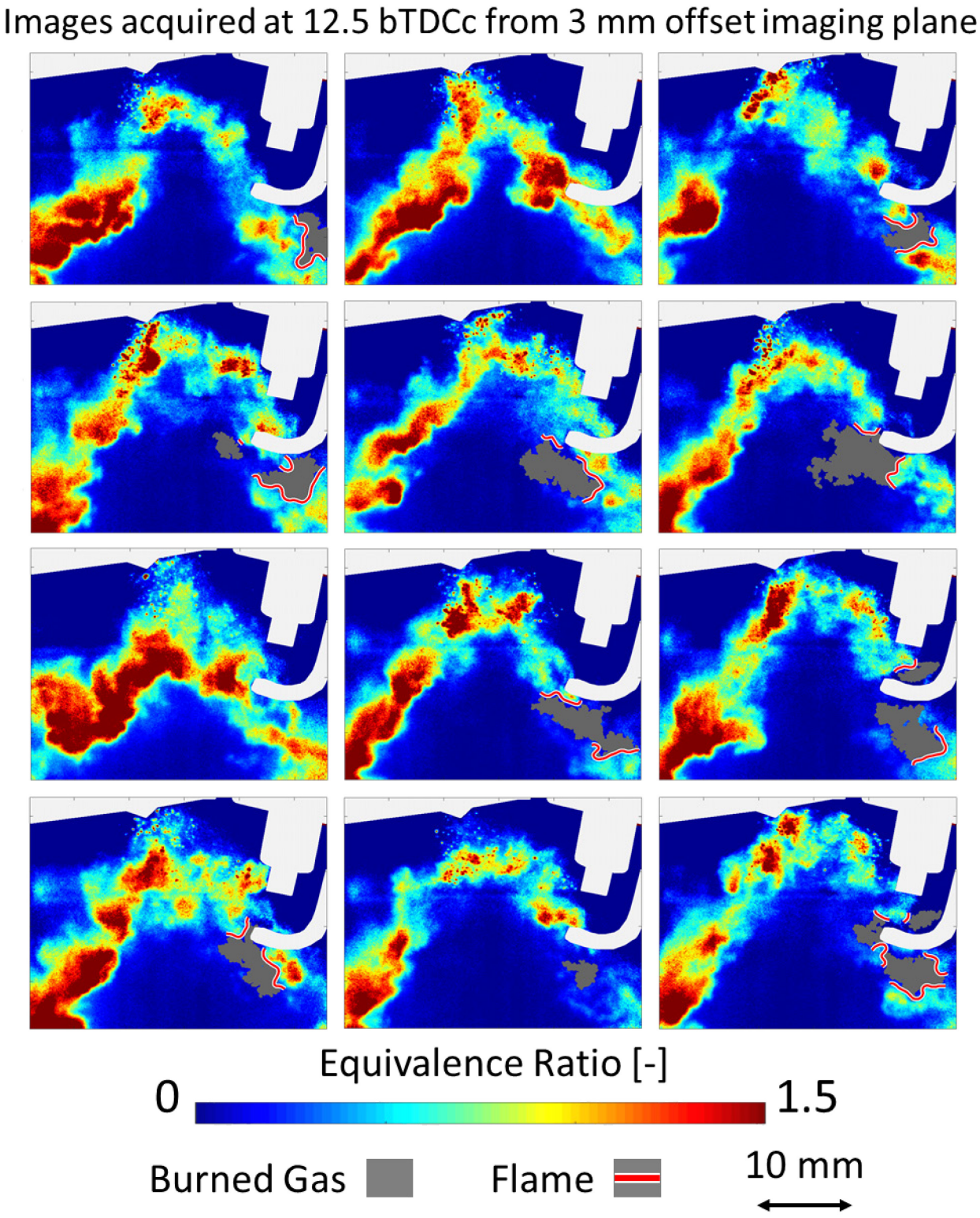

Figure 6-1: Stratified-charge engine combustion images from 3 mm offset imaging plane taken at 12.5 bTDCc.

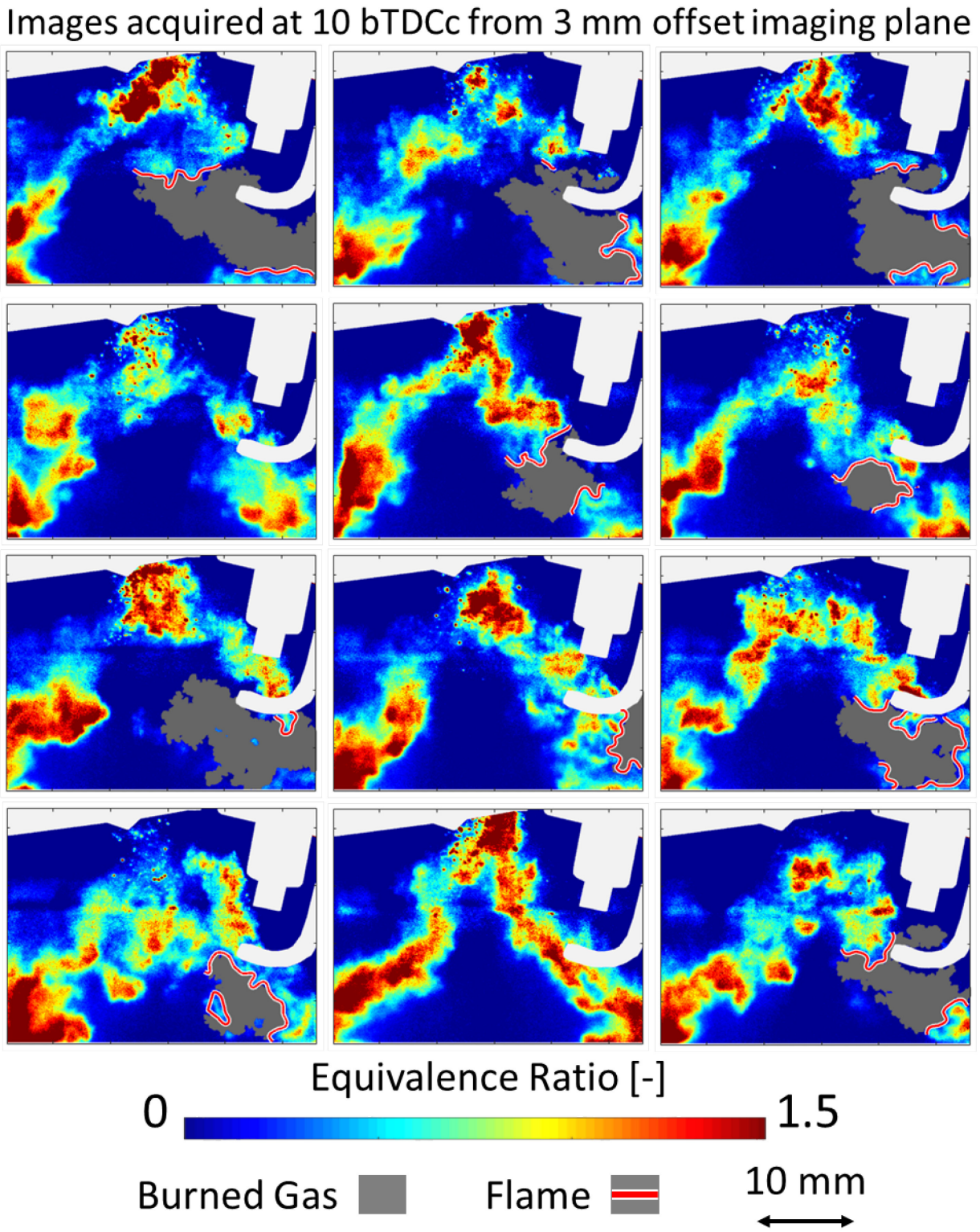

Figure 6-2: Stratified-charge engine combustion images from 3 mm offset imaging plane taken at 10 bTDCc.

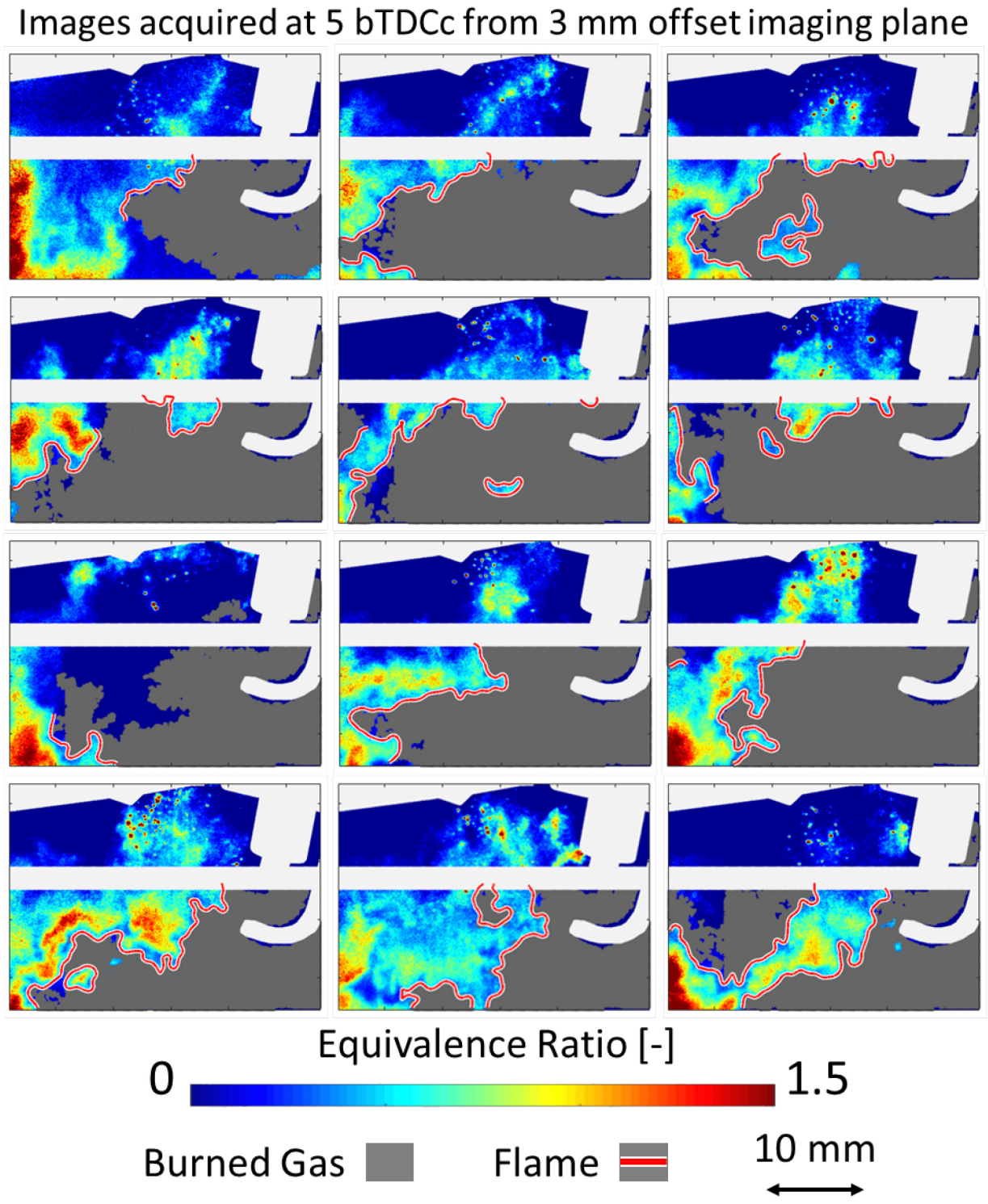

Figure 6-3: Stratified-charge engine combustion images from 3 mm offset imaging plane taken at 5 bTDCc.

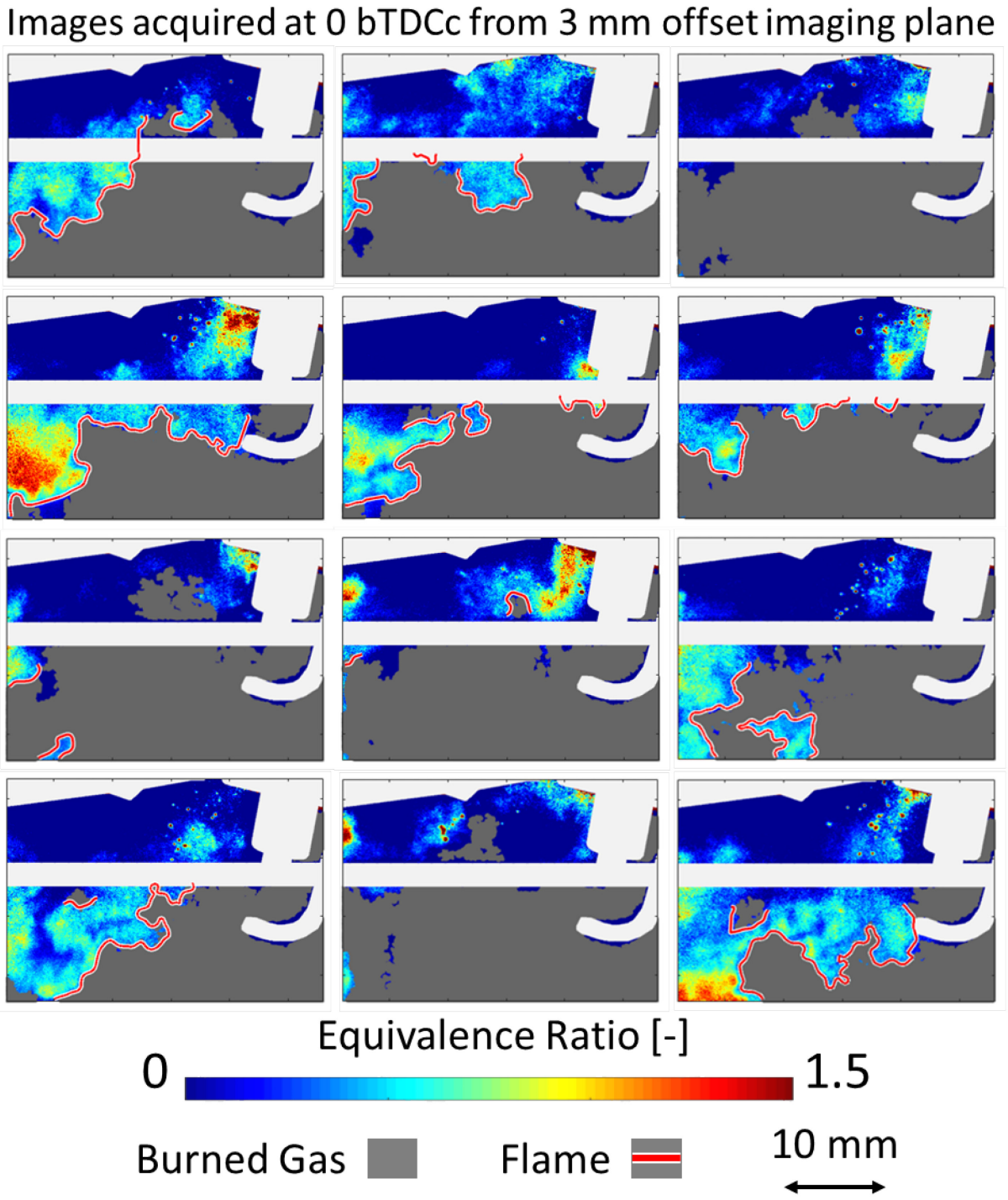

Figure 6-4: Stratified-charge engine combustion images from 3 mm offset imaging plane taken at 0 bTDCc.

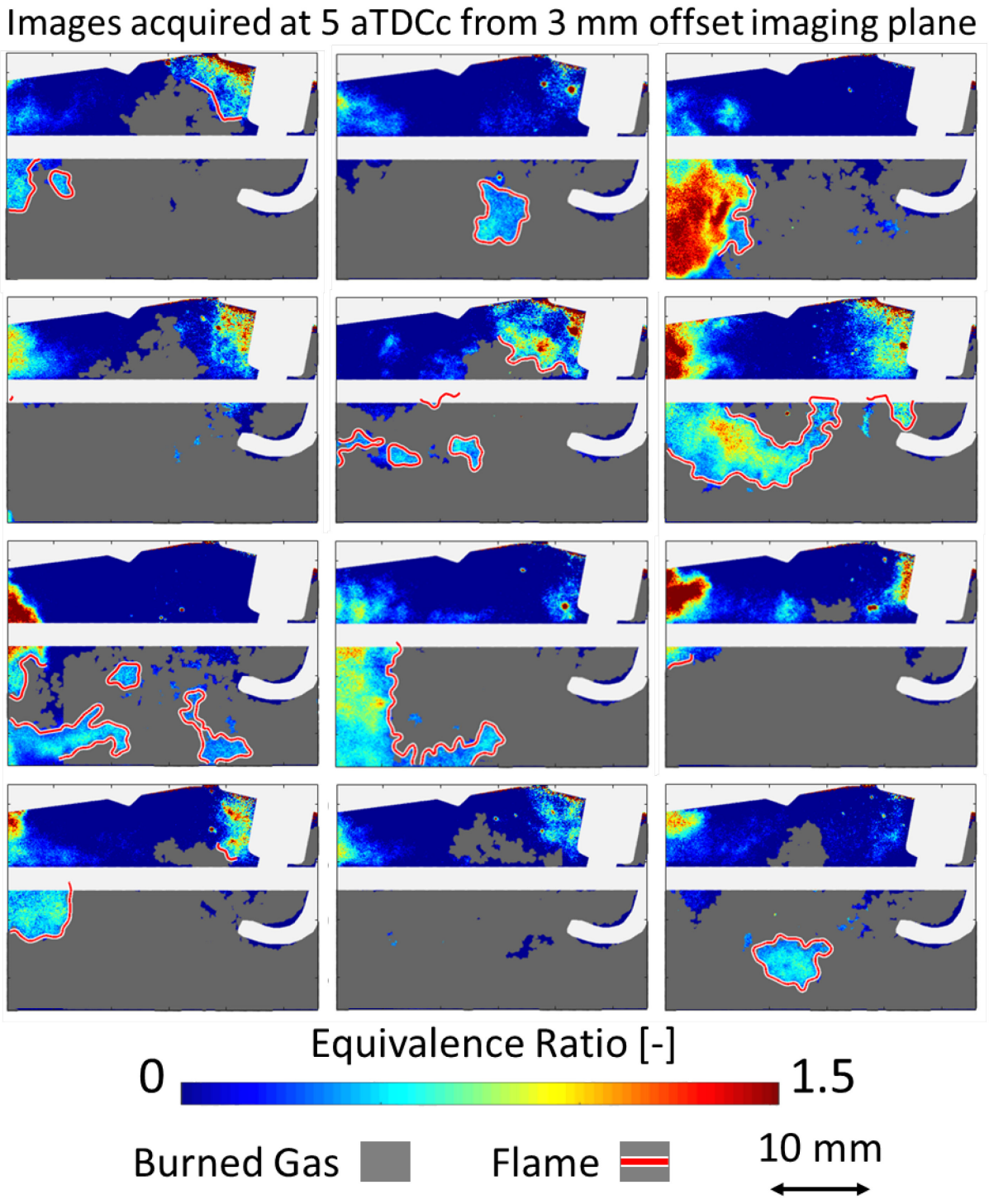

Figure 6-5: Stratified-charge engine combustion images from 3 mm offset imaging plane taken at 5 aTDCc.

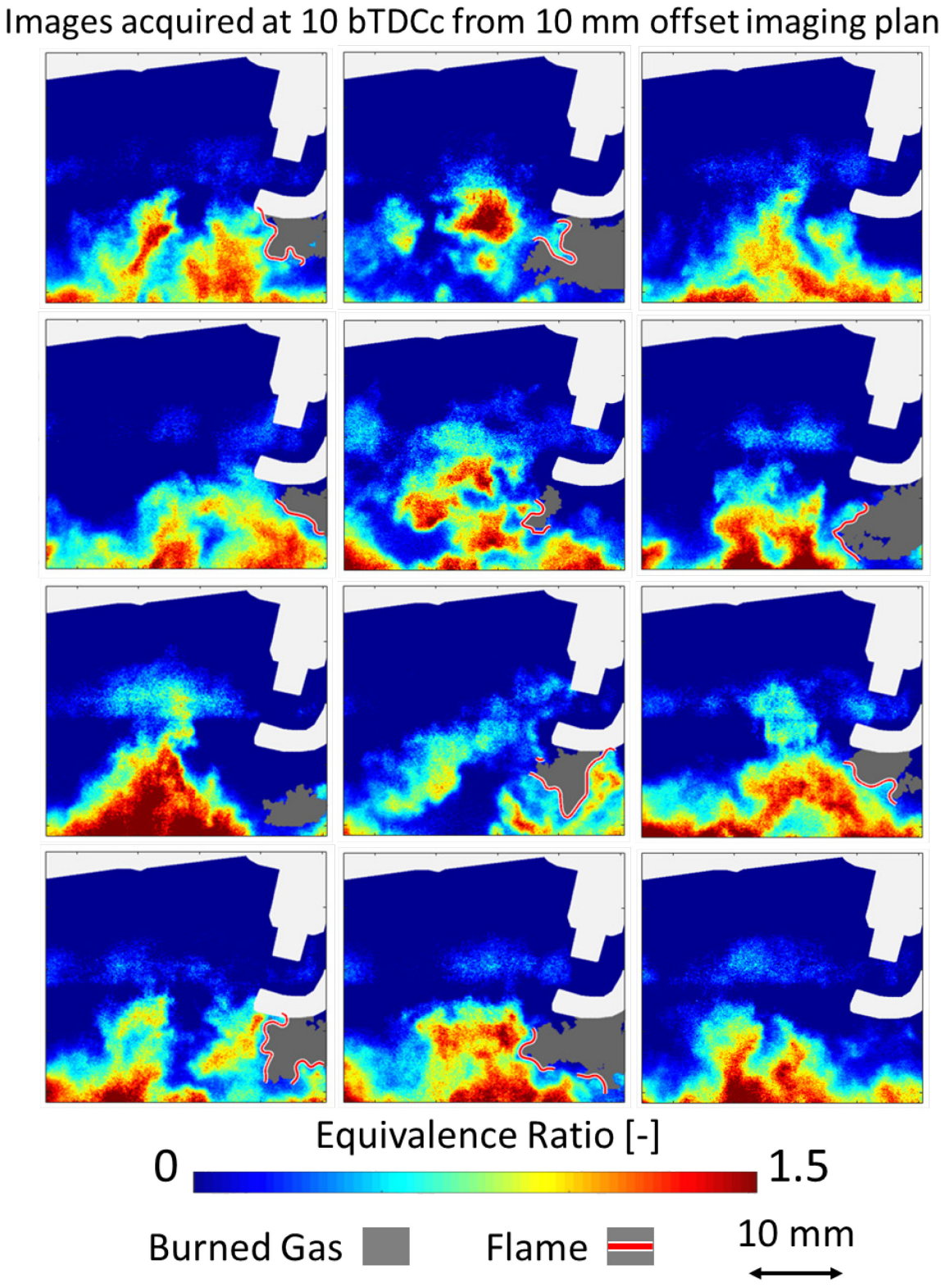

Figure 6-6: Stratified-charge engine combustion images from 10 mm offset imaging plane taken at 10 bTDCc.

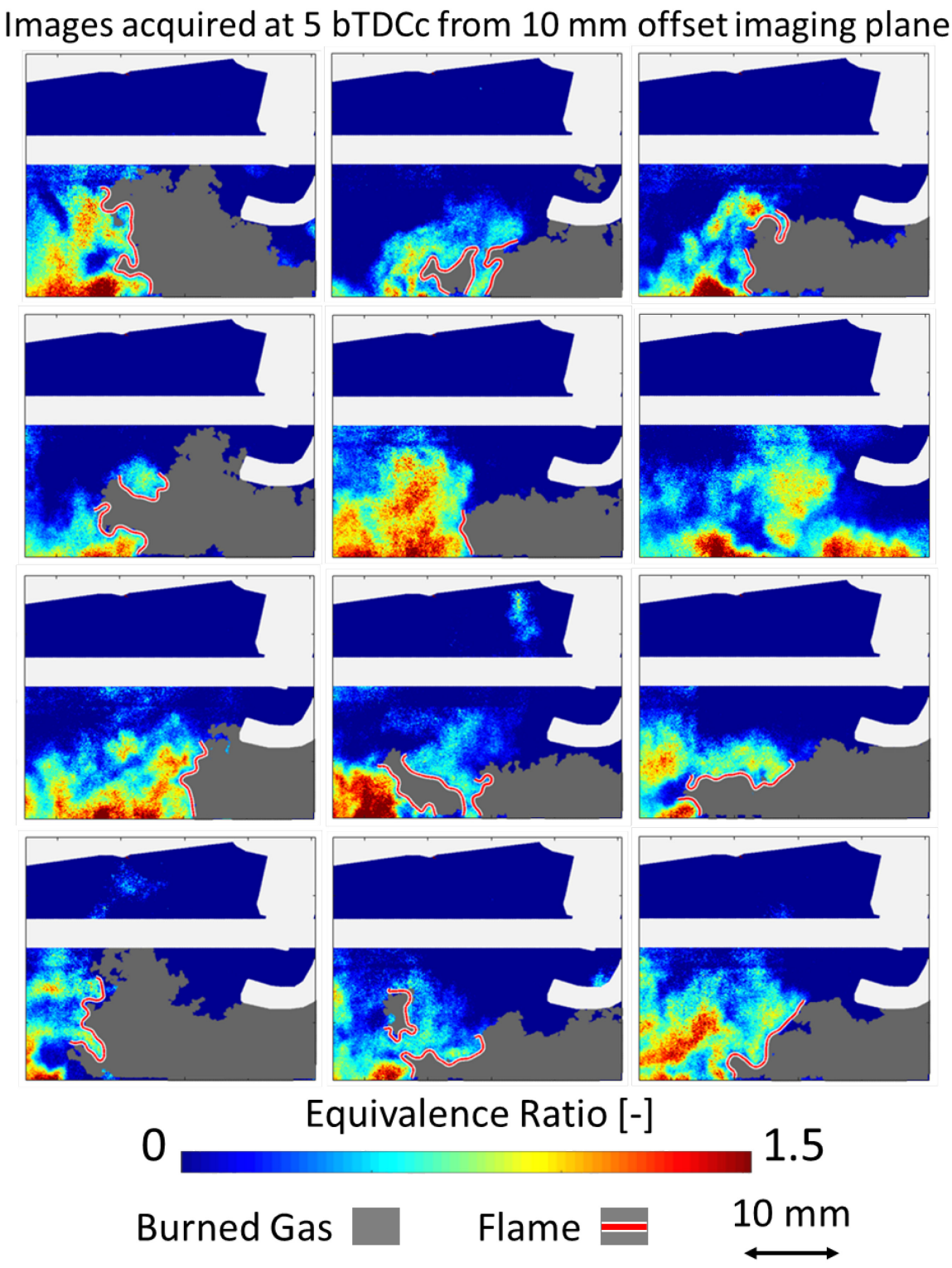

Figure 6-7: Stratified-charge engine combustion images from 10 mm offset imaging plane taken at 5 bTDCc.

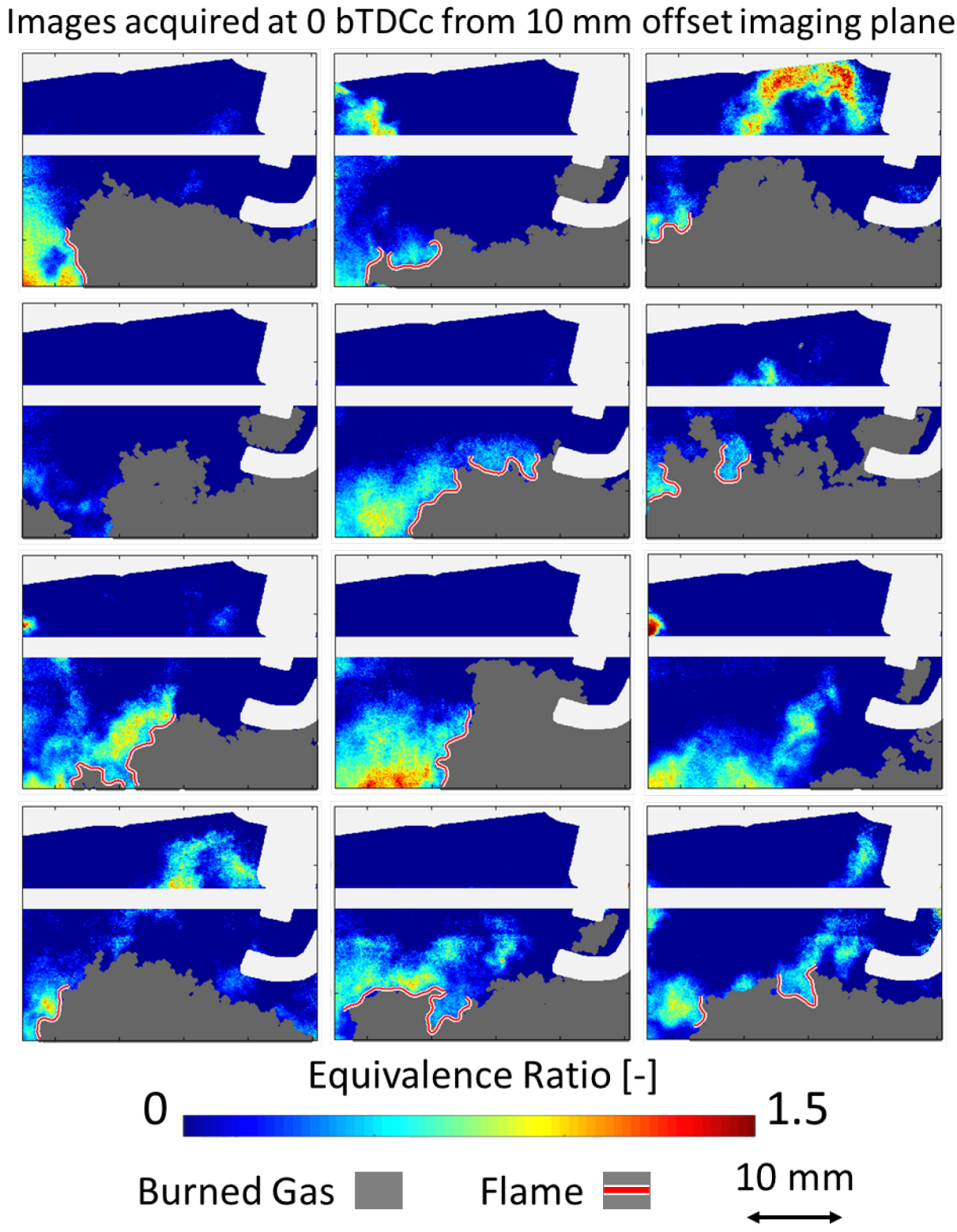

Figure 6-8: Stratified-charge engine combustion images from 10 mm offset imaging plane taken at 0 bTDCc.

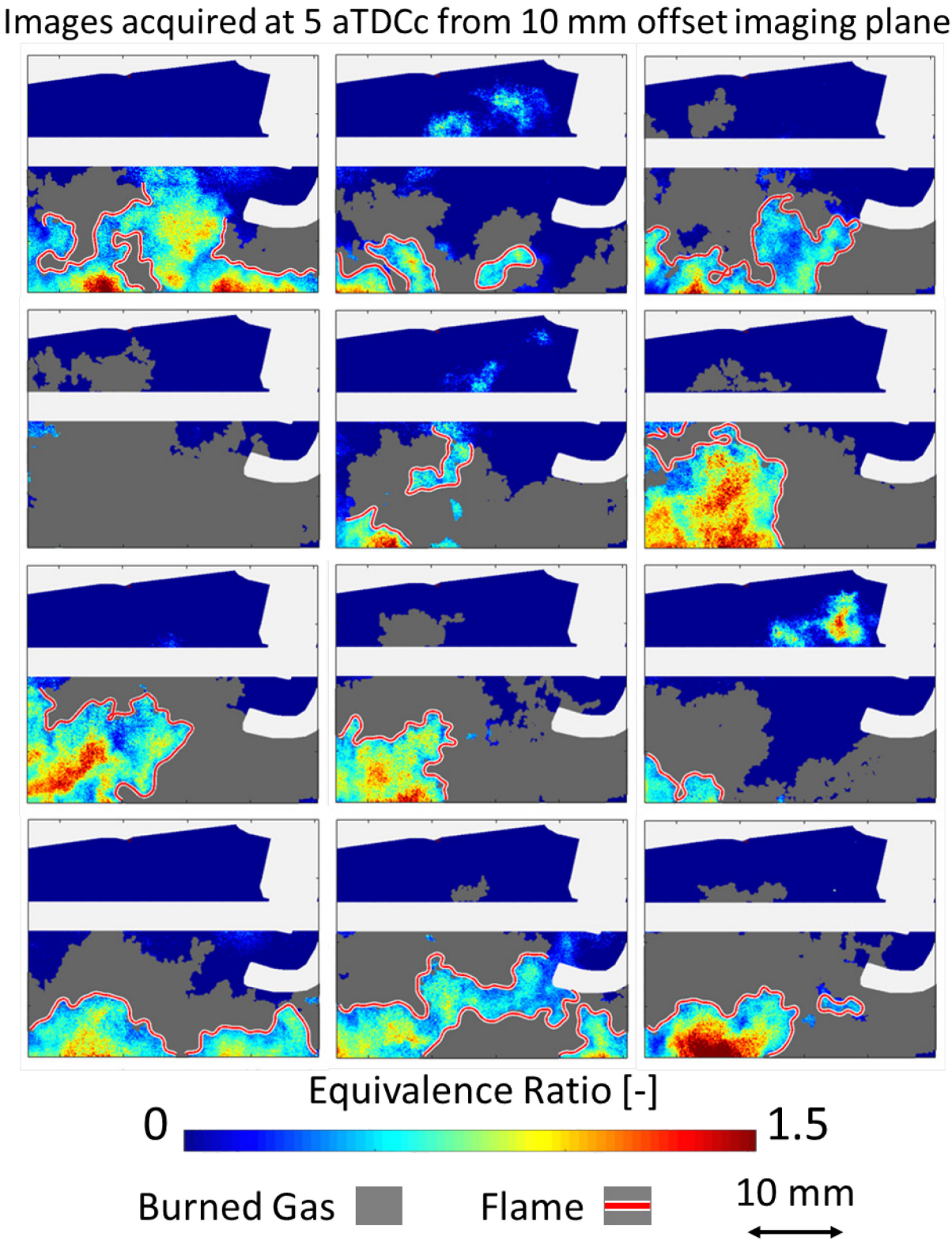

Figure 6-9: Stratified-charge engine combustion images from 10 mm offset imaging plane taken at 5 aTDCc.

The flame development as viewed in both planes will now be discussed both in the context of SGSC engines and in terms of flame and flow wrinkled-ness.

The two fuel plumes visible within the three millimeter offset plane (Figure 6-1 to Figure 6-5) were separated by 135 degrees. The right fuel plume was one of two straddling jets that was directly ignitable by the spark plug. The second directly ignitable fuel plume was not visible in this study.

As can be seen in Figure 6-1 and Figure 6-2, the right plume of the three millimeter imaging plane typically ignited and developed sizeable flames by 10 bTDCc. However, sometimes the spark plug failed to directly ignite it. For example, in the images shown in Figure 6-1 (1,2), (3,1) and (4,2) combustion cannot be recognized at all. Counter to the appearance of failure in these three images, the engine cycles that they were acquired from burned quite well and yielded a respectable 196, 197 and 205 kPa IMEP's. Apparent well igniting mixtures sometimes failed to burn well. For example, the early flame visible in (3,3) of Figure 6-1 appears healthy but it's engine cycle yielded a partial burn and only registered 130 kPa IMEP.

In the case of the well burning apparent ignition just discussed, the successful ignition and flame spread within the second un-visualized straddling fuel plume likely made up for the observed deficiency. In the case of partial burns, sluggish combustion was responsible for the deficiency. Sluggish combustion was recognized to occur and cause partial burns either during the early portion of the cycle (CA0-8) and/or late in the burn cycle (CA75-90). The causes for slow combustion at these two very different periods in the engine cycle were probably different. Complete engine misfires were rare under stratified-charge conditions and mid-cycle (CA10-75) combustion tended to occur in a much more robust and repeatable manner than the early and late burn portions of the cycle. A detailed justification for these assessments is provided in Appendix C.

Six out of the eight of the fuel plumes, including the left most plume seen in the three millimeter plane were ignited indirectly by flame spread and/or interaction with hot burned gasses. Due to the low speed nature of the optical imaging measurements the difference between spread and burned gas ignition within each image could not be definitively recognized. However, considering the visible spatial separation between fuel jets and the general mobility of the burned gas clouds it is likely that some of the flame spread from jet-to-jet occurred due to interaction between hot burned gas and the fuel jet. Such a mode of flame spread would rely on low Oxygen concentration ignition physics that aren't typically captured by conventional homogeneous-charge engine flame propagation computational models.

The spark plug tended to ignite the three millimeter right plume somewhat centrally. The early flame propagation generally traversed both axially and transversely through the jet but the strong guidance of the jet usually forced the burning charge down into the bowl where it tended to remain for the portion of the combustion process visualized. The prominent effect of the in-cylinder flows tumble can be recognized in the flames strong tendency to travel from the right (ignited) towards the left side of the bowl. Late in the cycle (5 aTDCc) portions of the jet could sometimes be recognized to be recirculating back into the cylinder head region. Much of the combustion activity observed in this study occurred within close vicinity to the piston bowl and it is clear that a good understanding of flame/fuel jet-to-bowl interactions will be pre-requisite to the successful development of predictive SGSC engine models. It is also clear that despite the high momentum of the fuel jet, in-cylinder flow strongly influences the development of stratified-charge flames throughout the course of the combustion cycle.

Often, some of the fuel injected at the end of the fuel injected period appeared to linger on its way into the bowl and was often still visible to be high in the cylinder at 0 bTDCc while much of the rest of the fuel charge was already being burned within the piston bowl region. The fate of this small quantity of fuel is uncertain and should be investigated in future as it has the potential to lead to unwanted exhaust hydrocarbon emissions.

Normally, most of the right three millimeter plume was burned by 5 bTDC and combustion of the left plume followed from about 5 bTDCc to 5 aTDCc. The left plume was mostly consumed by spatially divided inwardly propagating flames. After such flames were established (i.e. the flame had spread all the way across the surface of the divided fuel charge), the inwardly propagating flames could only decrease in size until the charge was consumed. In terms of wrinkled-ness development, the inwardly propagating flames observed here should exhibit different natural tendencies than the outwardly propagating flames that were recognized under homogeneous-charge conditions. For example, by definition, such inwardly propagating flames must approach a laminar-like (Ξ=1) topology as they decreasing to minimum size as small flames simply cannot support wrinkles. Dissimilarly, outwardly propagating flames can maintain a high degree of wrinkled-ness all the way up until extinction. Generally, within the images shown this trend can be recognized as very small flames are visibly less wrinkled than their larger counterparts.

The viewing perspective of the ten millimeter offset plane was much different than that of the three millimeter plane. The two ten millimeter plane fuel plumes that can be seen in Figure 6-6 through Figure 6-9 were separated by 45 degrees from each other and they straddled the two three millimeter plane plumes previously shown. The two ten millimeter plane plumes were targeted with a large out-of-plane velocity relative to the field of view and the jets generally traversed through (towards viewer) the laser sheet plane with some of the charge potentially recirculating back towards bowl center (away from viewer) later in the viewing cycle.

The rather violent impact between the two ten millimeter plane plumes and the piston bowl is evident in Figure 6-6. Complex mixing structures can be seen rising above the zone of impact and the interaction with the bowl causes the two jets to spread and sometimes join along the bowl surface. The bowl charge created by the two ten millimeter offset plumes impacting the piston was usually indirectly ignited sometime between 10-5 bTDCc, after which they tended to burn from right to left and from cylinder bottom upwards. This burn pattern is consistent with

the most probable ignition source (the right plume in the three millimeter imaging plane) and the direction of the in-cylinder tumble flow.

The images shown in Figure 6-6 through Figure 6-9 provide a rare and detailed view of mid-cycle bowl-constrained stratified-charge combustion. An entire spectrum of flames, ranging from small to large and rich to lean can be seen burning within the images. The flames appear highly wrinkled and corrugated. Highly rich and lean fuel mixture zones can be seen burning. The rich products generated within the rich combustion zones were likely followed by trailing diffusion flames. Rich mixtures tended to collect and burn close to the piston surface.

Collectively, the complexity and variability shown by the fuel jets and stratified-charge flames in Figure 6-1 through Figure 6-9 is staggering. It is self-evident that the predictive success of any computation attempting to model such flames will depend strongly on the models ability to capture the both the stochastic nature of the fuel jet, flow and flame physics as well as jet-to-jet and jet-to-solid surface interactions.

In terms of wrinkled-ness; visually, it is challenging to recognize any general trends in wrinkled-ness for the larger (5+ mm scale) flames shown throughout the nine image panels. Therefore, in order to better understand the stratified-charge wrinkled-ness development the same quantitative wrinkled-ness characterization technique used to study homogeneous-charge flame wrinkled-ness in Chapter 5 will now be used to analyze the stratified-charge flames.

6.2 Stratified-Charge Wrinkled-ness Results

Stratified-charge flame wrinkled-ness was studied by applying the same FFT based low pass spatial filtering technique to the stratified-charge optical results as was outlined in 3.2.5.3 and applied to achieve the homogeneous-charge wrinkled-ness results in Chapter 5. The first step in the wrinkled-ness analysis process was to recognize the location of the stratified-charge flames. A combination of the PLIF and PIV images were used to do so, the details of which were

discussed in 3.2.5. After recognizing the locations of the stratified-flames, the sub-regions of the PLIF images were algorithmically extracted in binary form and subjected to the complete FFT filtering process previously described. Two examples of such sub-region extractions are shown in Figure 6-10 below.

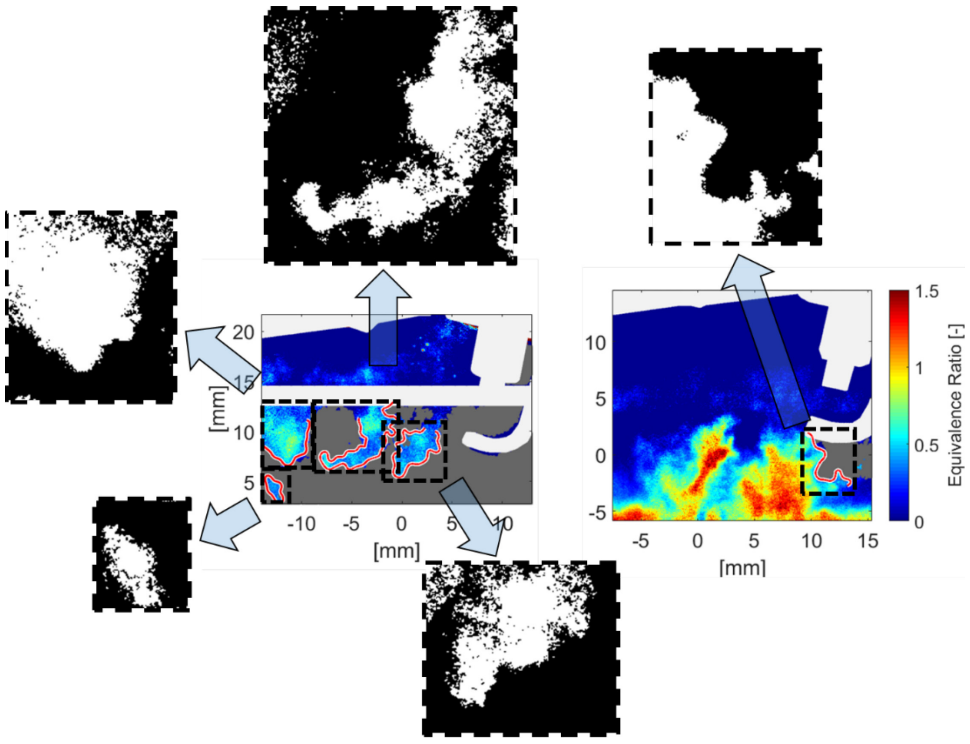

Figure 6-10: Example of stratified-charge flame front extraction technique.

As can be seen in Figure 6-1, it was common for a single stratified-charge image to yield a few flame sub-images. Sometimes the flame extraction regions were within close enough vicinity to each other that some spatial overlap between the sub-images was necessary. However, in order to avoid “double counting” flames during the wrinkled-ness assessment, sub-image spatial area overlap was limited to 0.5 mm in scale and when necessary, flame sub-sections were truncated in size to meet the imposed criterion. If the truncation resulted in more than 2 mm of loss from the overall flame size then the larger of the two full, un-truncated spatially-overlapped flame images was selected for further use and the smaller was discarded from the analysis.

Since the physics of the SGSC flames are so closely coupled with that of the jet itself, the fuel jet (full PLIF) images were also binarized and submitted to the same FFT analysis. The threshold used to binarize the fuel jet was ϕ=0.45, which is the approximate value of the lower confidence interval of the lean flammability limit of iso-octane (ϕ~0.6). An example sequence of such binary fuel jet images which were acquired from the three millimeter imaging plane are shown in Figure 6-11 below.

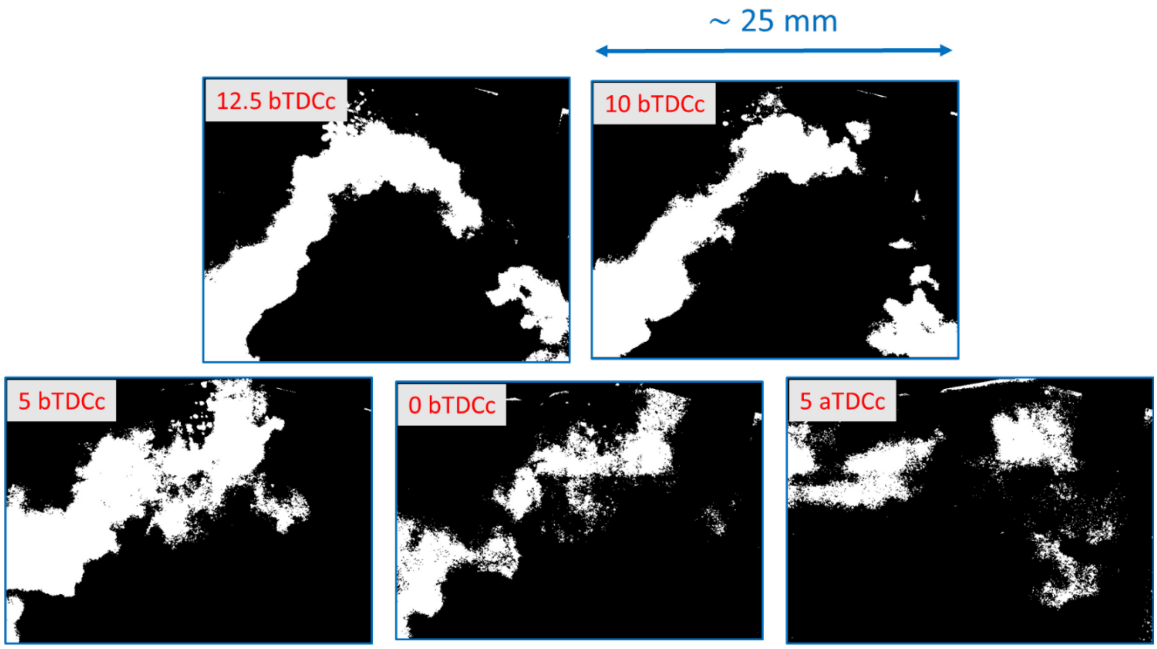

Figure 6-11: Binary image of flammable region of fuel mixture extracted from PLIF images acquired in the 3 mm imaging plane.

The results of both the stratified-charge flame and jet wrinkled-ness analyses are shown side-by-side in Figure 6-12 below for both of the imaging planes. The flame wrinkled-ness values displayed are averages of a few hundred flame images and the fuel jet results of the average of one hundred jet images. The error bars represent the standard 95% confidence interval of the reported mean values.

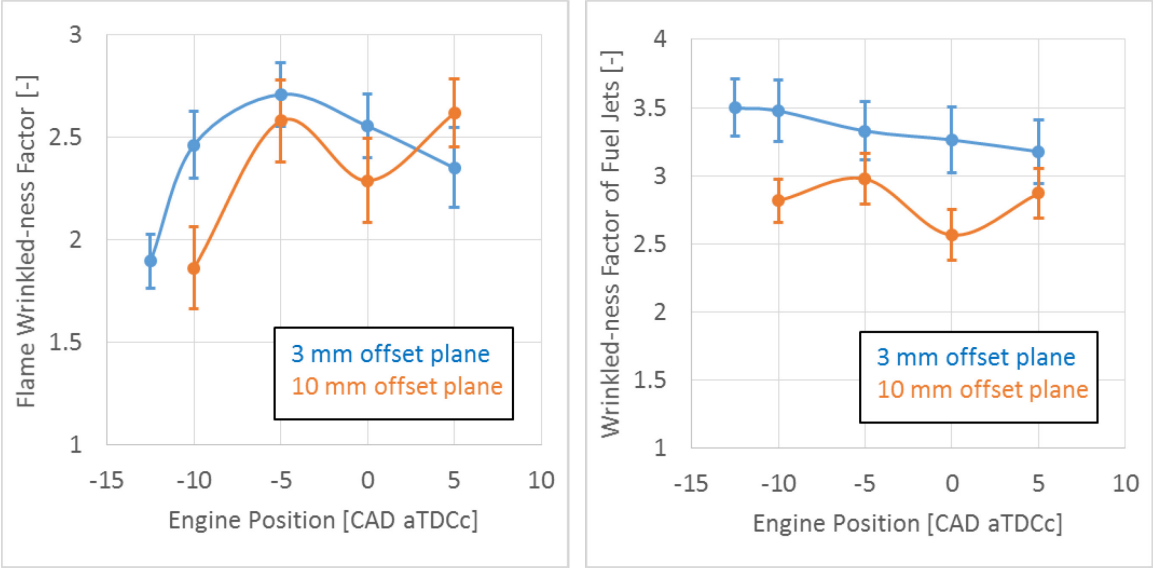

Figure 6-12: Mean wrinkled-ness of the stratified-charge flames and the flammable regions of the fuel jets shown vs engine position (CAD) as measured from a few hundred images in both the 3 and 10 mm imaging planes. The error bars represent the standard sample 95% confidence interval in the mean reported values.

The three millimeter imaging plane flame results in Figure 6-12 show that flame wrinkled-ness increased to peak from 12.5 to 5 bTDCc and depleted thereafter. Remember that the SOIgn timing was 22 bTDCc but that the flame kernels tended to remain very small until 12.5 bTDCc. The small flames (CA~2) observed at 12.5 bTDCc demonstrated an impressive wrinkled-ness of Ξ~2. Extrapolating the wrinkled-ness trend backwards in time to Ξ=1 provides an estimate of the total flame wrinkled-ness development time, from laminar to peak, of about 15 CAD (2 ms). This duration of development is similar to what was recognized for the homogeneous-charge flames in this study.

The stratified-charge flame wrinkled-ness development trends for the two different imaging planes were similar from 10 and 0 bTDCc but differed slightly from 0-5 aTDCc. Unlike the three millimeter plane flames, which showed a definitive reduction in wrinkled-ness following 5 bTDCc, the ten millimeter plane flames showed a decrease from 5 to 0 bTDCc followed by a marginal increase from 0-5 aTDCc. The uptick in wrinkled-ness exhibited by the ten millimeter imaging plane flames was mirrored the complimentary fuel jet wrinkled-ness measurements, which is of little surprise as most of the jet is itself burning at 5 aTDCc. It is possible that the

increase in wrinkled-ness that occurred in the ten millimeter plane flames was related to the strong bowl-to-jet and flame interactions that were occurring around the time of imaging. However, considering the uncertainty bands of the measurements, investigations into the cause of the uptick were not considered warranted.

The ten millimeter plane flames managed to maintained near-peak levels of wrinkled-ness for longer than the three millimeter plane flames. If viewed later into the cycle, it is suspected that the ten millimeter plane flames would have followed a similar path of reduced wrinkled-ness as their inwards consumption approached completion.

The wrinkled-ness results acquired from both imaging planes show that the fuel jets maintained a pretty high degree of wrinkled-ness (Ξ=2.5 to 3.5) at all times. The overall magnitude of wrinkled-ness observed in the stratified-charge tests was about 25% higher than those recognized under homogeneous-charge conditions (Figure 5-9). However, caution should be employed when comparing the absolute values of wrinkled-ness between the two studies. Remember that the spatial resolution of the wrinkled-ness (PLIF) diagnostic was limited to 0.5 mm by the laser sheet thickness. Under homogeneous-charge conditions the effect of sub-half-millimeter wrinkles was reasoned to be small by comparing the optically characterized wrinkled-ness results in 5.2.2 with in-cylinder pressure based wrinkled-ness estimates in 5.1. However, a similar analysis and reasoning could not be applied under stratified-charge conditions and it is likely that the absolute value of the stratified-charge wrinkled-ness values reported here are bias low due to the measurement techniques neglect of sub-half-millimeter diameter wrinkles. Although this bias should not detract from the qualitative comparisons made within this section, it does hinder fair comparisons between the stratified and homogeneous-charge studies. Recognizing that the absolute stratified-charge wrinkled-ness values are likely bias low, it can still be definitively concluded that the stratified-charge flames measured in this study were significantly more wrinkled than their homogeneous-charge counterparts presented in Chapter 5.

The relationship between the overall size and wrinkled-ness of the stratified-charge flames measured in this study was investigated, the results of which can be seen in Figure 6-13 below.

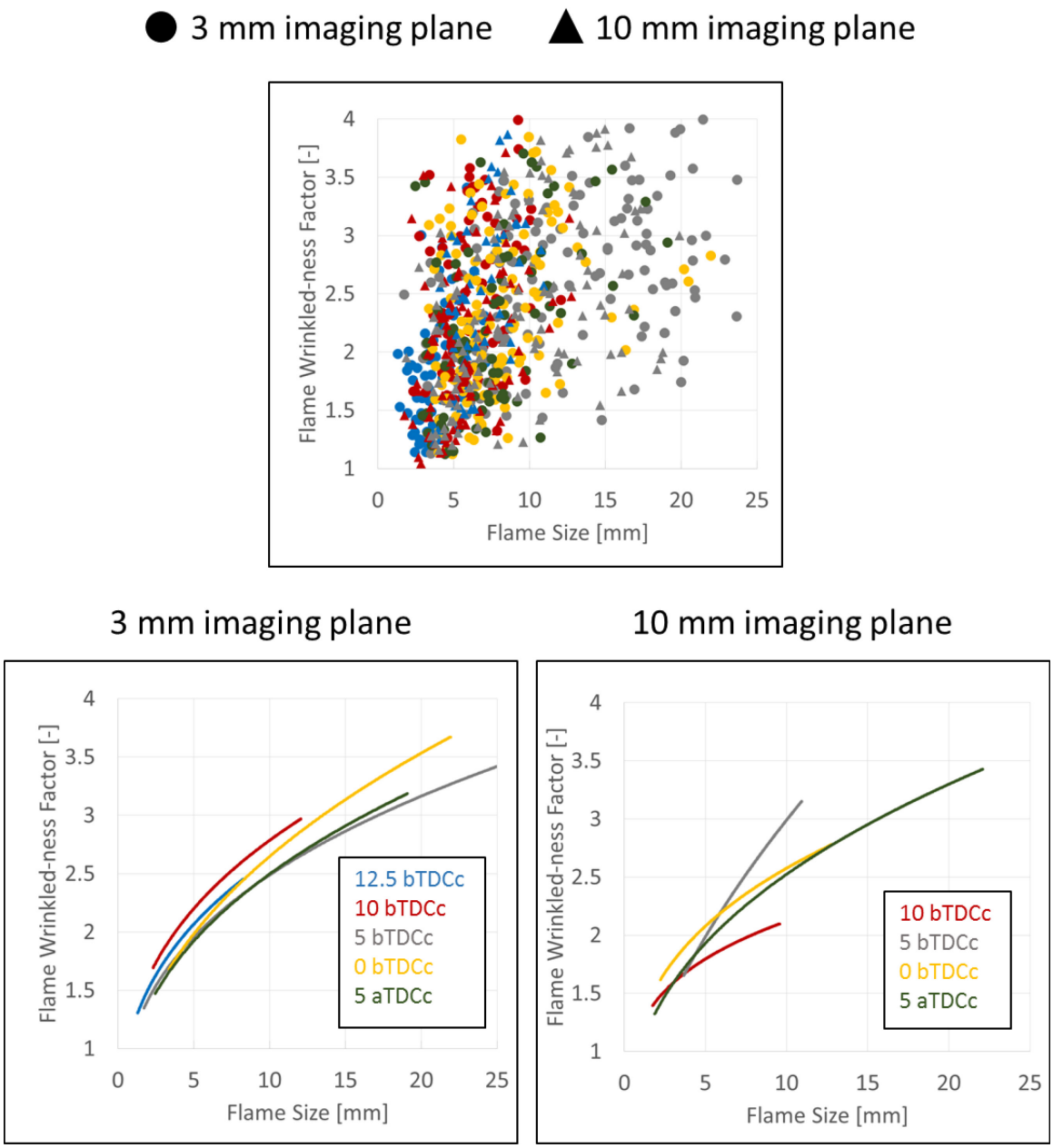

Figure 6-13: Stratified-Charge flame wrinkled-ness vs flame size from tests in both the 3 and 10 mm offset imaging planes. The bottom two figures were acquired by applying power series fits on a per image timing basis to the same raw wrinkled-ness vs. flame size data shown in the top figure.

The top scatter plot in Figure 6-13 includes a 100 cycle tests worth of flame wrinkled-ness vs size data from all nine combinations of image timings viewing planes. The two bottom figures show a power fit of the data points for the two imaging planes separately. The flame size reported in the figure was defined to be the diagonal of the flames extractable area (i.e. smallest rectangular area that a flame contour could be enclosed within). This flame size definition was chosen to be fair to ovular, straight and tortuous flame contours alike.

Figure 6-13 shows that larger flames tend to be more wrinkled than smaller flames. All of the flames, other than the early ones recognized in the ten millimeter imaging planes, approached the wrinkled-ness values of the jet itself as they grew to their maximum sizes. These results are consistent with the fact that the flame topology had to approach the fuel jets topology with increasing size as at the largest scale, as the topology of the two were by definition one and the same when the flame was fully developed (i.e. when the flame was large enough that the entire jet was engulfed in flames).

Peak stratified-charge flame wrinkled-ness occurred at the same engine timing of 5 bTDCc as the engines peak indicated heat release rate (see Figure 4-18). This makes sense as flame surface area, which is the primary driver of the heat release rate (see 2.2.2.4), increases proportionally with flame wrinkled-ness.

The relationship between flame front equivalence ratio and wrinkled-ness of the flames measured in this study was investigated. A scatter plot of test normalized flame front equivalence ratio vs. wrinkled-ness is shown in Figure 6-14 below. The equivalence ratios shown were extracted from a 0.1-0.6 mm region downstream of the flames. Due to the finite laser sheet thickness and the chosen regions close vicinity to the flame itself, the PLIF signals measured and equivalence ratios registered were bias low of true. A complete set of three and ten millimeter flame data from all engine timings was included in the scatter plot along with linear fits of there data. The R^2 values of the fits are also reported.

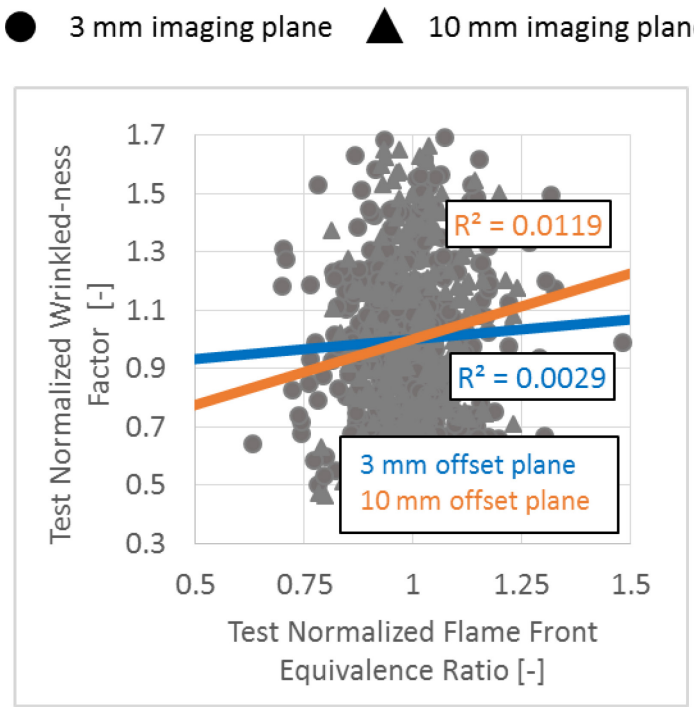

Figure 6-14: Test normalized wrinkled-ness factor vs. flame front equivalence ratio for flames at all tested engine timings in both imaging planes.

The near zero R^2 values signify a lack of correlation between the stratified-charge flame wrinkled-ness and flame front equivalence ratio measurements. The data was further investigatd on a per imaging timing basis and with equivalence ratios being drawn from regions of different standoff distance from the flame. No evidence could be found to suggest that stratified-charge flame wrinkled-ness and flame front equivalence ratio correlated during the test. This suggests that equivalence ratio effects, such as those which might be caused by thermo-diffusive instabilities and/or gradients therein, probably played a secondary role in the stratified-charge flame development process. However, more testing would be required to say so conclusively.

In order to assess the individual contribution of wrinkles of differing scales towards the total wrinkled-ness of the flames and fuel jets, the wrinkled-ness vs. spatial filter scale trends are shown in Figure 6-15 below for all engine timings and both imaging planes.

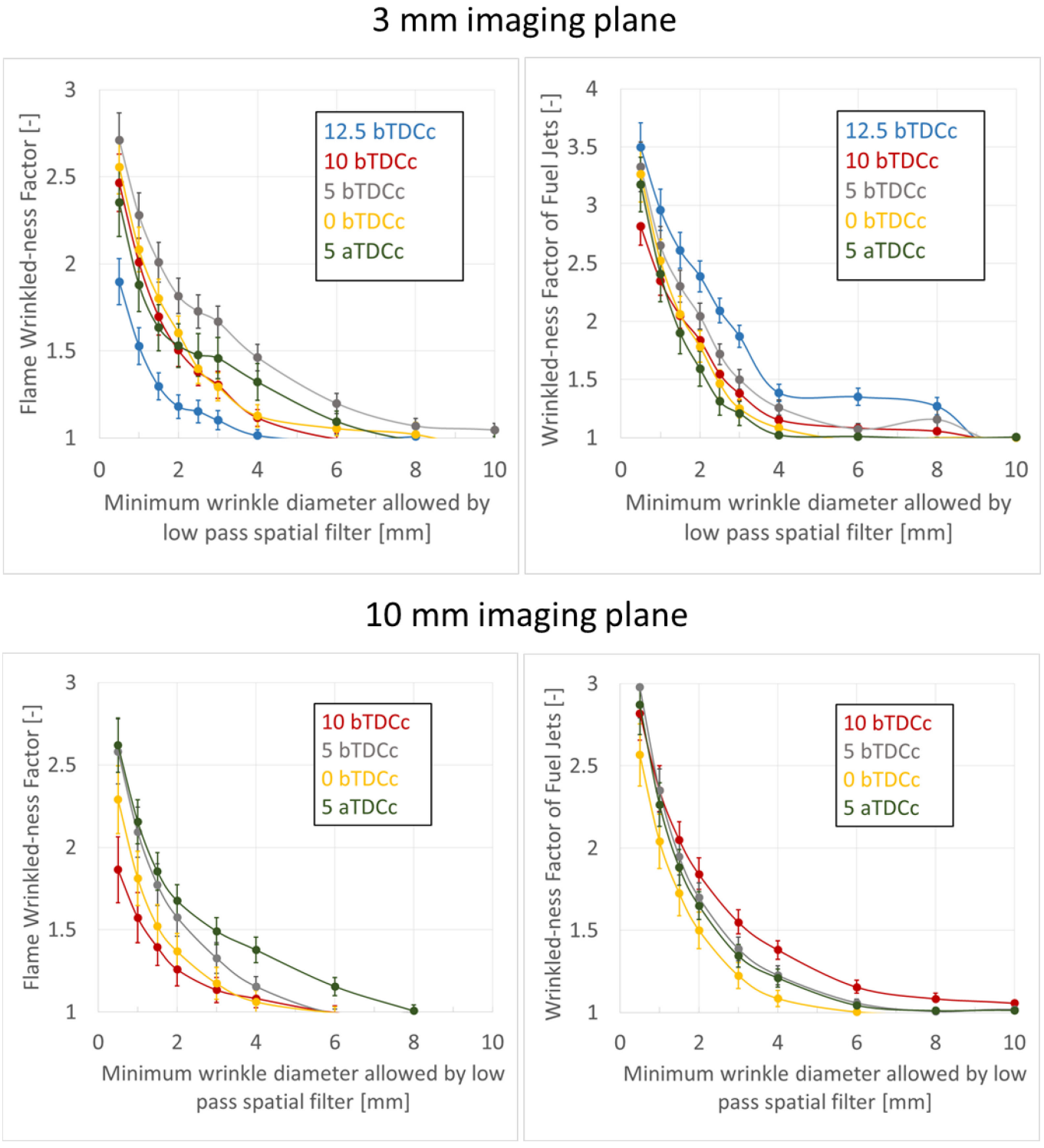

Figure 6-15: Average wrinkled-ness vs. low pass spatial filter scale for both the flames and the flammable regions of the fuel jets as measured in the 3 mm and 10 mm imaging planes.

Independent of viewing plane or engine timing; about half of the stratified-charge flame wrinkled-ness recognized could be attributed to 0.5-2 mm diameter wrinkles. The other half was due to 2-4 or 2-6 mm diameter wrinkles, depending on the timing of the image. Generally, the images that featured the largest flames (such as 5 bTDCc in the three millimeter plane and 5 aTDCc in the ten millimeter plane) also featured the largest contribution of larger (4+ mm) scale wrinkles.

Most of the wrinkled-ness recognized for the fuel jet also occurred on the same scales, with about half of the wrinkled-ness being generated by 0.5-2 mm diameter wrinkles and the other half generated by 2-6 mm diameter wrinkles. Much unlike the flames, the larger wrinkle scales (4+ mm) played a more prominent role in generating wrinkled-ness early in the cycle for the fuel jet and wrinkled-ness continually decreased throughout the engine cycle, particularly on the larger scales. This decrease in large scale wrinkling can be attributed to the fact that the jets generally decreased in overall size both due to jet breakup and combustion.

6.3 Stratified-Charge PIV Results

The stratified-charge stereo particle image velocimetry (PIV) results will now be presented. The stratified-charge PIV results serve as a compliment to the previously presented PLIF results; both of which will be combined in 6.4 to draw conclusions.

The stratified-charge PIV data was processed from its raw form into vector fields according to the procedures discussed in 3.2.4. The PIV results will be presented in two separate sub-sections. In the first section the measured flow and turbulent velocity fluctuation fields will be shown. In the second section the turbulent length scales of the flow will be analyzed. Collectively, these two sections provide an overall characterization of the in-cylinder flow properties to be compared with the measured scales of stratified-charge flame and fuel jet wrinkled-ness.

The results in this section are based upon a set of motored engine tests under stratified-charge conditions. The engine was operated as it normally would under fired conditions; that is at 1300 RPM, 95 kPA intake MAP, 45 C engine and intake temperatures and with fuel injection starting at 25 bTDCc. However, ignition was withheld so that the charge didn't burn. This enabled clean (flame free) PIV measurements to be under conditions that resembled those of the stratified-charge flame wrinkled-ness tests discussed in 5.2.1 and 5.2.2.

6.3.1 Flow-Field Results

Ensemble average flow fields acquired from both imaging planes for all image timing are shown in Figure 6-16 below.

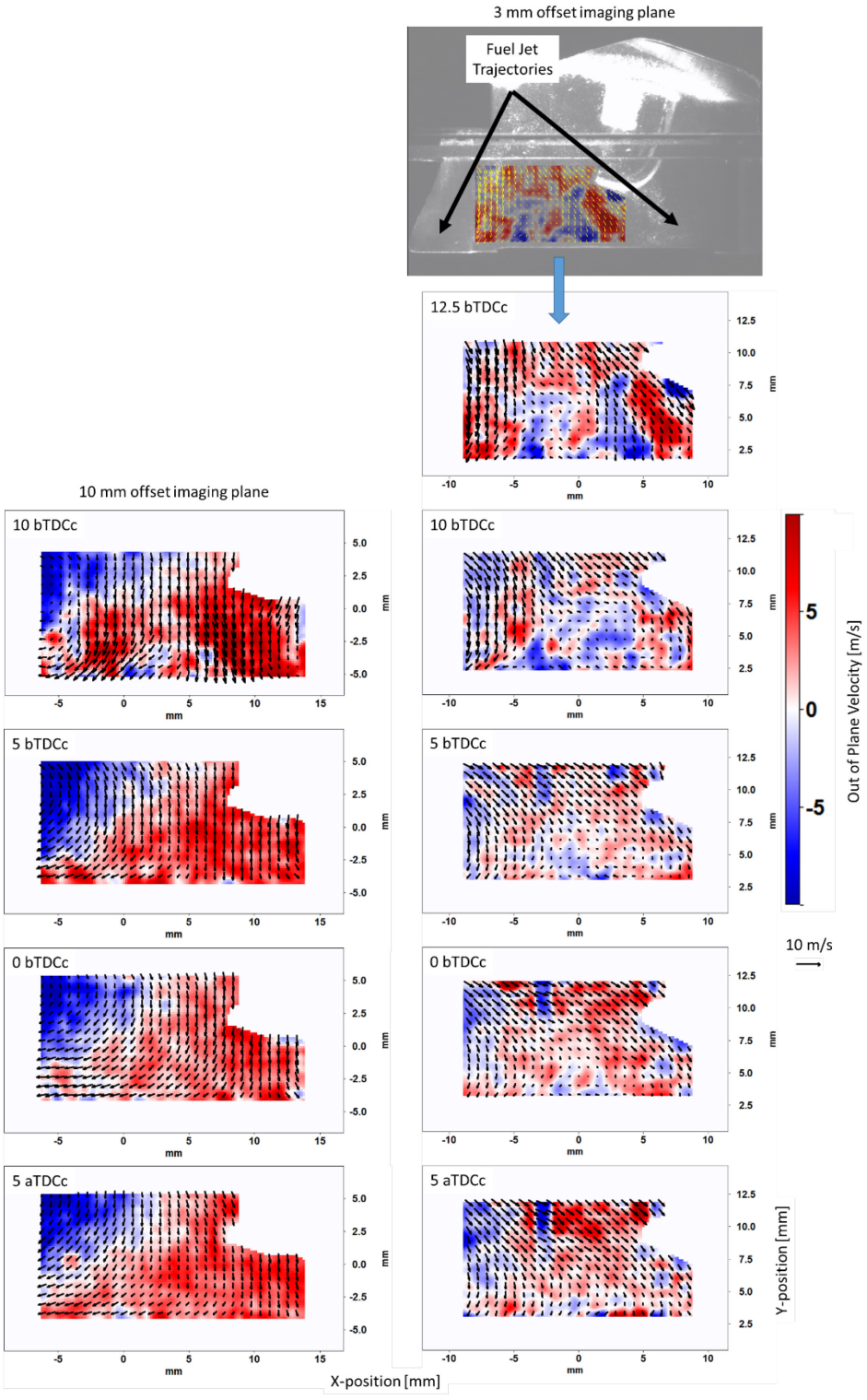

Figure 6-16: Stratified-Charge Planar 3D Flow Velocity Fields (40 cycle averages)

The ensemble mean in-plane flow velocities were on the order of 5 m/s and the out of plane velocity about 10 m/s. The strong out-of-plane velocities observed in both imaging planes is due to a combination of the penetrating fuel jets and the in-cylinder swirl velocity.

The ten millimeter offset imaging plane flow fields indicate strong, persisting out-of-plane flow velocities in the regions of the impinging fuel jets and in-plane velocities that both coincide with the jets and the counterclockwise in-cylinder tumble motion. The in-plane flow visible in the upper left of the ten millimeter plane images in Figure 6-16 is likely a reaction to the jets penetration and also natural consequence of the in-cylinder swirl flow motion.

The profile of the two penetrating fuel jets visible in the three millimeter plane can be recognized in the early images of Figure 6-16 by the downward directed in-cylinder flow on both sides of the images and the strong out-of-plane velocities. The central region of the images captures flow recirculation occurring between the two jets. The out-of-plane velocity components of the three millimeter plane primarily indicates out-of-plane velocities. However, a variety of small scale flow structures are visible within the out-of-plane velocity fields that are unlikely to be physical. Remember that the out-of-plane velocity components were about +/- 5 m/s uncertain which is of similar velocity magnitude to those finer flow structures.

The in-cylinder flow was highly stochastic and the individual cycle flow fields usually differed greatly from the ensemble averages. Five example single shot flow field results are shown in Figure 6-17 below for both imaging planes.

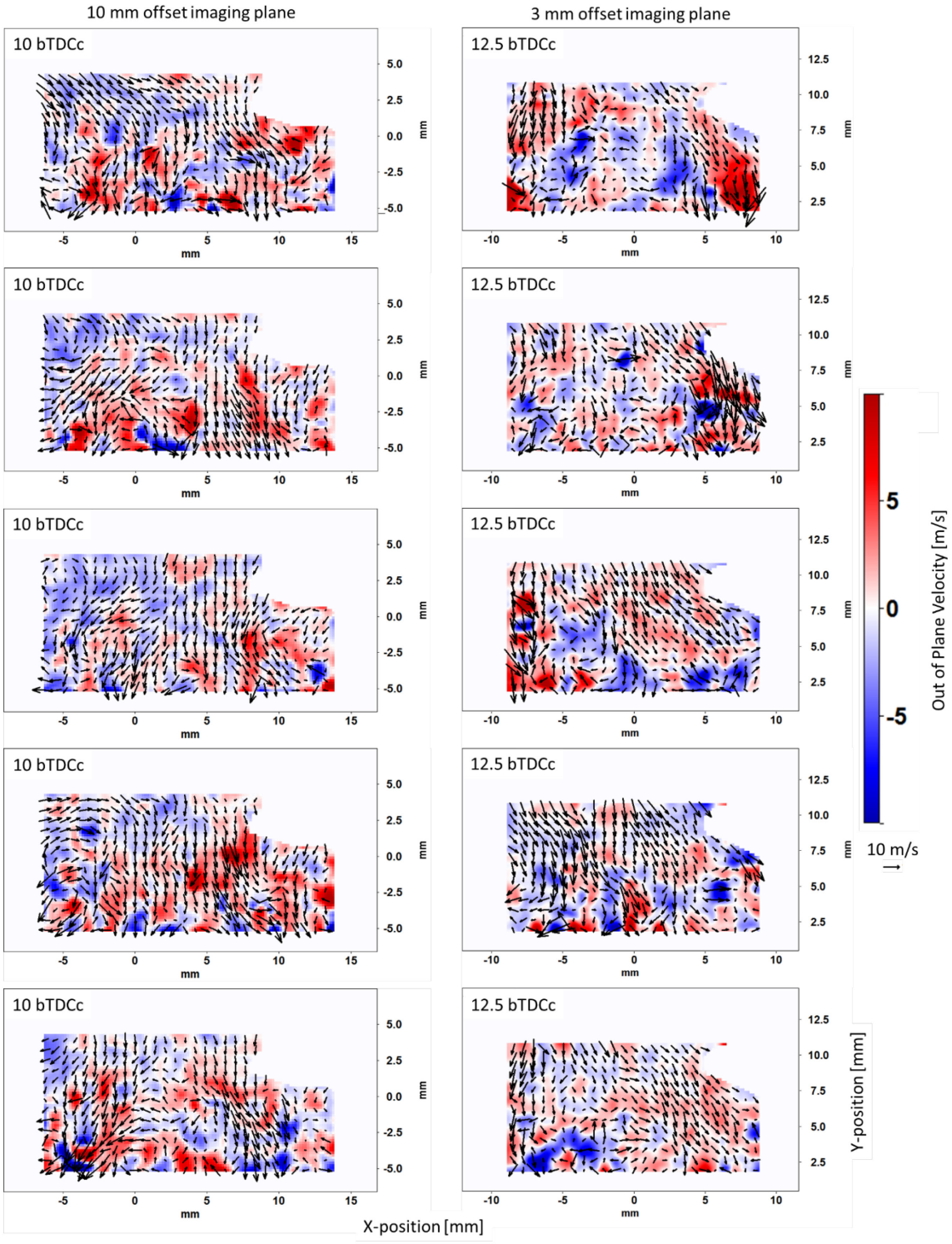

Figure 6-17: Stratified-Charge Planar 3D Flow Velocity Field Examples

Notice that the spatial average flow velocities shown in Figure 6-17 were about twice as large as the ensemble averages shown in Figure 6-16. This difference is due to turbulent fluctuations. The RMS velocity fluctuation fields are shown in Figure 6-18 below.

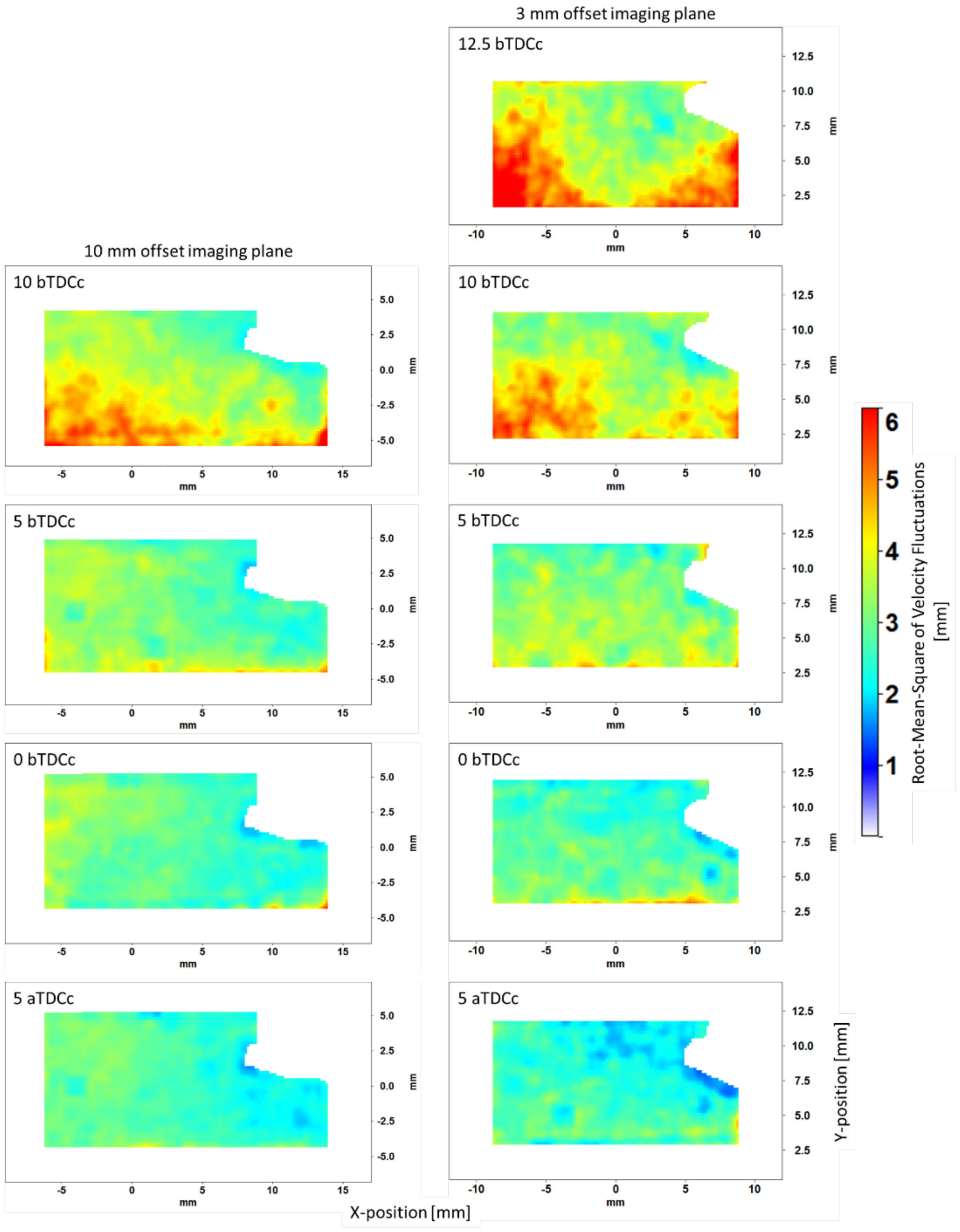

Figure 6-18: Root-mean-square of velocity fluctuations of the stratified-charge in-cylinder flow calculated based upon in-plane velocity components from 40 cycle tests.

Figure 6-18 verifies that the root-mean-velocity fluctuations are indeed on par in magnitude with the ensemble average velocities, which indicate a turbulence intensity of roughly 100%.

The turbulent fluctuations were strongest in the bowl region earlier in the cycle (12.5 and 10 bTDCc) in the regions where the jet impacted the piston bowl most prominently. The effect of SGSC fuel sprays on in-cylinder flow and combustion was studied by Zeng et al. [231, 232] and Sjoberg et al. [233] and was therefore not investigated further in this study. However, the amount of turbulence produced by the jet's interaction with the bowl was undoubtedly large enough to affect the combustion process.

6.3.2 Turbulent Length Scale Results

The stratified-charge turbulent in-cylinder flow length scale results will now be presented in the same manner as they were in 5.3.2 for the homogeneous-charge results. That is, the scales will be recognized as spatially distributed properties and both the spatial distribution and the mean values of the integral and Taylor microscale measures will be presented.

The probability density function of the integral and Taylor microscales are shown in Figure 6-19 below. The probability is calculated by performing a statistical analysis on length scales calculated at points throughout the entire field of view. The most probable scales are those which are most likely to be encountered, if one were to choose a single point measurement within the combustion chamber. The spread in the distributions is a good measure of the un-certainty of the measurement and/or the inaccuracy of the isotropic length scale concepts within the engine environment. For the sake of brevity, only the three millimeter offset plane probability distributions are displayed.

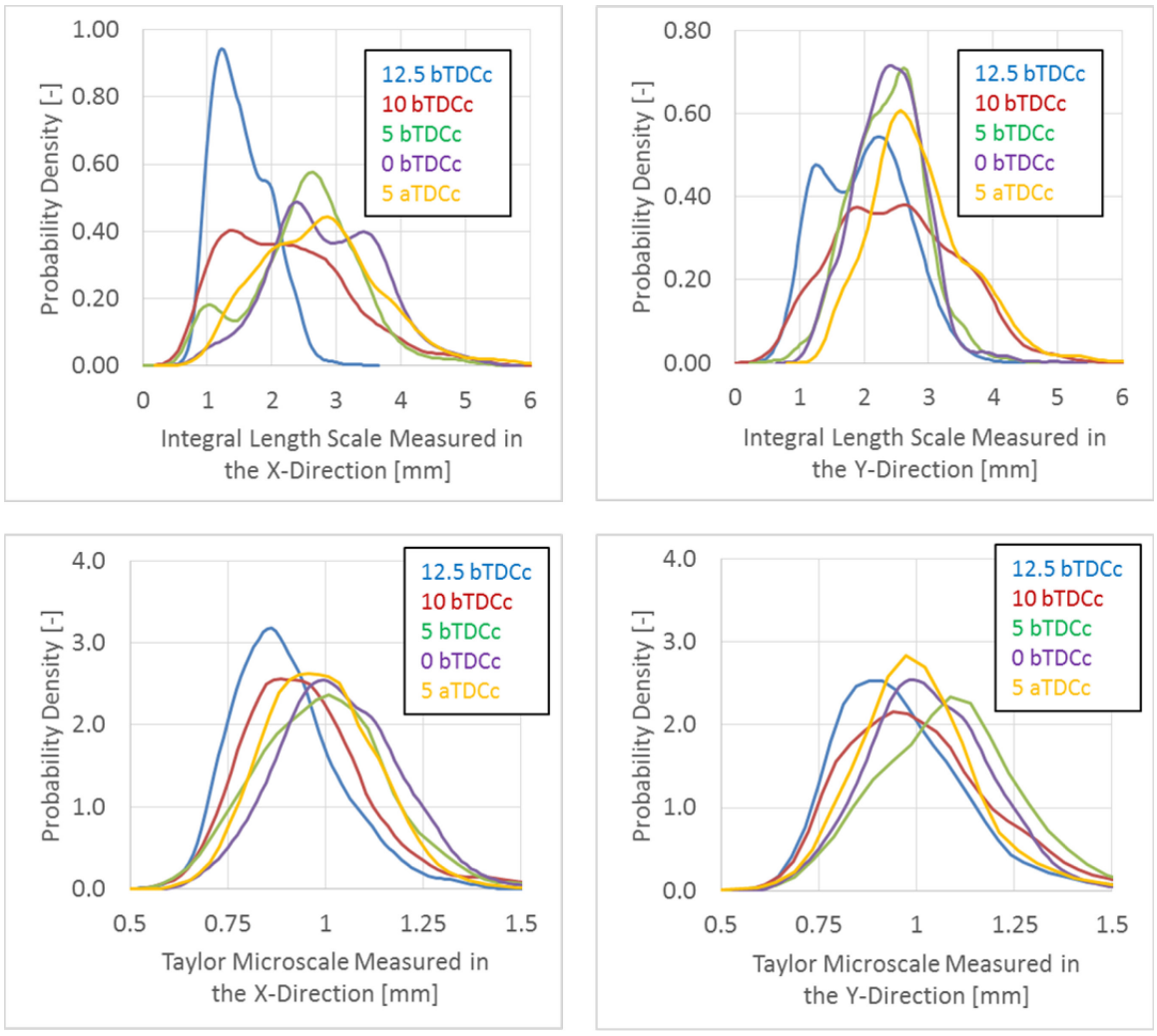

Figure 6-19: Probability density distribution of the stratified-charge integral scales and Taylor microscales as measured in the X and Y directions in the 3 millimeter offset imaging plane.

Further, the spatial mean stratified-charge integral and Taylor microscales vs. engine position for both planes in the x and y directions are shown in Figure 6-20 below.

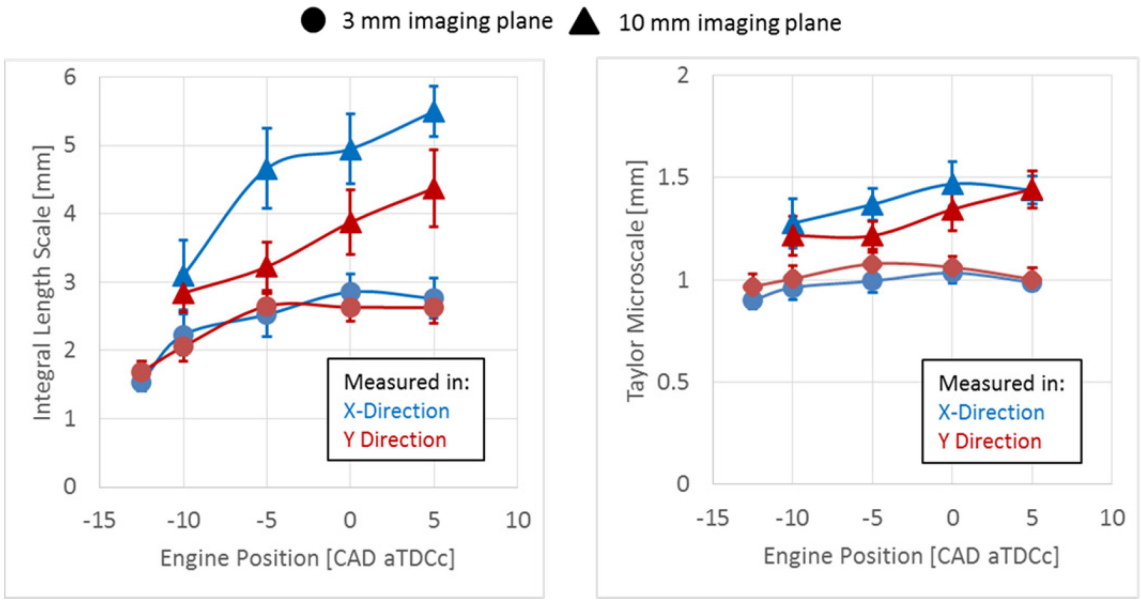

Figure 6-20: Spatial mean stratified-charge integral and Taylor microscales (throughout entire field-of-view) vs. engine position as measured in both the x and y directions for both imaging planes. The error bars represent the standard 95% confidence interval in the mean.

The spatial mean integral length scale measurements results ranged from 1.5 to 5 mm, depending on the direction, imaging plane and engine timing. Counter to what is normally recognized (within homogeneous-charge engines) the integral scale grew larger throughout the cycle as the fuel jet momentum and in-cylinder turbulence dissipated. The probability distribution functions for the integral length scales, shown in Figure 6-19 often show a bimodal nature. That is, there are often two scales separated by a 1-3 mm. The smaller of the two separate scales is more reflective of the highly turbulent near-fuel jet and near-bowl regions and the larger of the bulk flow.

The spatial mean Taylor microscale measurement results ranged from 1 to 1.5 mm, which is probably high of true; particularly at the earlier engine timings where the integral scale measured of a similar magnitude. Remember that the spatial resolution of the PIV imaging system under stratified-charge conditions was about 0.6 mm. Therefore, the Taylor scale measurements were likely resolution limited. In order to verify the reasonability of the Taylor microscale estimates shown in Figure 6-20 empirical calculations were performed based upon isotropic turbulent relations listed in Lumley et al.'s book [234]. These relations utilized

previously reported integral length scales sand RMS velocities. The relations predict Taylor microscale lengths ranging 0.3 to 1.5 mm, depending on the engine timing and exact choice of scale parameters used. Considering both methods of measurement, it can be fairly concluded that the Taylor microscale under the stratified-charge conditions measured to be between 0.1 and 1.5 mm over the course of the engine tests.

Based on the integral and Taylor scale values shown above, the turbulent Reynolds number throughout the tests was about 200 and the Kolmogorov length scale ranged from 0.05 to 0.1 mm, with the larger values occurring later in the cycle. These measured scales can now be used to help interpret some of the previously presented stratified-charge flame wrinkled-ness results.

6.4 Stratified-Charge Conclusions

Flame, fuel jet and flow development were observed within the cylinder of an optically accessible DISI engine that was operated under spray-guided stratified-charge spark-ignited conditions. Planar laser induced fluorescent (PLIF) images were combined with PIV images to identify flame fronts. The images were processed to reveal flame wrinkled-ness and to determine the scales for which flame wrinkling occurred. Particle image velocimetry (PIV) was used to track in-cylinder charge-flow. The PIV images were processed to reveal charge-flow velocities and to characterize the length scales of the turbulent in-cylinder flow. From this study, the following can be concluded,

1. Stratified-charge flame wrinkled-ness was always observed to be unsteady, increasing from the first appearance of the flame until at or around the timing of the peak heat release rate and then reducing sometime after.

2. The wrinkled-ness reduction that occurred later in the engine cycle was largely the result of large scale (4+ mm) wrinkle loss. This loss might be attributed to the flames

natural tendency to reducing in overall scale with time due to reactant consumption and the flames inwardly propagating nature.

3. Independent of engine timing or the plane of viewing, stratified-charge flames tended to increase in wrinkled-ness with overall flame size.

4. Despite efforts, no correlation was found between stratified-charge flame wrinkled-ness and average flame front equivalence ratio. This inconclusively suggests that equivalence ratio relative topological effects, such as those related to thermo-diffusive stability gradients played a secondary role in the wrinkle development process of the SGSC engine flames observed.

5. 0.5-6 mm wrinkles were responsible for the bulk (90+%) of the wrinkled-ness recognized at all engine timings. Throughout the tests, the spatial average in-cylinder integral scales measured to be 1.5-6 mm and the Taylor scales were estimated to be 0.3-1.5 mm. Therefore, the flames predominately wrinkled on the same scales as the turbulent in-cylinder flow and turbulent flame-to-flow interactions are thought to be responsible for the bulk of the flame wrinkled-ness observed.

6. The stratified-charge flames generally exhibited higher levels of wrinkled-ness than the homogenous-charge flames studied in Chapter 5, the full extent of which could not be quantified due to the probable existence of sub-image resolution (< 0.5 mm diameter) wrinkles under the highly turbulent stratified-charge condition.

7. The flammable regions of the stratified-charge fuel jet tended to exhibit a higher level of wrinkled-ness than flames that were consuming them. The stratified-charge flames approached a similar level of wrinkled-ness as they grew to similar scales as the jet. However, by definition, at the flames maximum size the jet and flame contour surfaces become one and the same.

8. The stratified-charge fuel jets were observed to continually reduce in wrinkled-ness throughout the course of the engine combustion cycle approaching that of the flames. The flames likely contributed to their reduction by both reducing the overall size of the jets and by consuming their finer peripheral features.

This is the first study of its kind to explicitly measure stratified-charge flame wrinkled-ness within an engine. As such, there are no prior publications to serve as a basis for direct comparison of the wrinkled-ness results. However, Dahms et al. [29, 174, 176] made a few observations that are further confirmed by this study. Namely, Dahms et al. [29] empirically reasoned that SGSC engine flames should be insensitive to diffusive-instability based wrinkling phenomenon and this study supports that theory. Also, Dahms et al. provided a detailed description of a highly wrinkled, tumble driven SGSC flame development process which is also consistent with what was observed in section 6.1 of this study.

The conclusions from both the homogeneous-charge and stratified-charge wrinkled-ness studies will now be combined in Chapter 7 to answer the research questions originally posed in the introduction.

Chapter 7: CONCLUSIONS

Conclusions with regards to the stratified-charge and homogeneous-charge studies have already been provided in 5.4 and 6.4. Therefore, this section will be devoted to directly answering the questions originally proposed in the introduction, plus one additional question with regards to future stratified-charge engine combustion research.

Do thermo-diffusive instabilities play an important role in the early flame wrinkled development process in homogeneous-charge engines?

Not in the engine tests performed in this study. A flame wrinkled-ness characterization was performed in an optical engine under homogeneous-charge conditions. The wrinkled-ness of three mixtures of differing composition (ϕ=0.8,1,1.25) and thermo-diffusive stability were monitored during the early flame development period. None of the three mixtures demonstrated an affinity to promote or resist flame wrinkling beyond that of its peers.

What flow scales have the greatest influence over homogeneous-charge engine flame topology?

In the engine tests performed in this study, nearly all of the homogeneous-charge flame wrinkling was observed to have occurred on diametric scales ranging from the integral scale down to the to the Taylor microscale of the flow, with the smallest scale wrinkles contributing the most towards flame surface area generation. Under the low-load 1300 RPM engine conditions tested, these scales measured approximately 0.5 and 6 mm respectively. A

quantification of the total wrinkled-ness contributed by wrinkles of differing diametric scale is provided in 5.2.2.

How steady is the early flame wrinkled-ness process under homogeneous-charge conditions? Not very in the engine tests performed in this study. A flame wrinkled-ness characterization was performed in an optical engine under homogeneous-charge conditions. The wrinkled-ness of three mixtures of differing composition (ϕ=0.8,1,1.25) and thermo-diffusive stability were monitored during the early flame development period. Wrinkled-ness was observed to develop over a lengthy (15 CAD at 1300 rpm) period of time with small wrinkles forming faster than large wrinkles.

Do equivalence ratio based flame instability effects, such as those caused by thermo-diffusive instabilities play an important role in the wrinkle development process in stratified-charge engines?

The results of the engine tests performed in this study inconclusively suggests not. A flame and fuel jet wrinkled-ness and flame front equivalence ratio characterization was performed in an optical engine under stratified-charge conditions. Flames were analyzed at various times within the engine cycle from two different imaging perspectives and no correlation could be found between flame wrinkled-ness and flame front equivalence ratio.

What flow scales have the greatest influence over stratified-charge flame topology?

In the engine tests performed in this study, nearly all of the stratified-charge flame wrinkling was observed to have occurred on diametric scales ranging from the integral scale down to the to the smallest measureable scale of the flow, with the smallest measureable (0.5 mm diameter) wrinkle scales contributing the most towards flame surface area generation. Under the low-load 1300 RPM engine conditions tested, these scales measured to be approximately 0.5 and 4 mm respectively. Being that the Taylor microscale is estimated to be no lower than

0.3 mm and the flames thermal thickness was estimated to be on the order of 0.1 mm itself, the existence of unrecognized (sub-image resolution) 0.1-0.5 millimeter diametric scale wrinkles is possible but the existence of sub-tenth-of-a millimeter wrinkles is unlikely. A quantification of the total wrinkled-ness contributed by wrinkles of differing diametric scale is provided in 6.2.

How are the flame wrinkled-ness development processes similar and different under spray-guided stratified-charge engine conditions from that of conventional homogeneous-charge engine conditions?

In the study performed here, the flame wrinkled-ness development process observed under both homogeneous and stratified-charge engine operational modes proved to be driven by flame-to-flow interactions. The contribution of Taylor microscale to integral length sized wrinkles towards overall flame wrinkled-ness was prominent under both combustion modes. Small wrinkles, at or around the size of the Taylor microscale produced the lion's share of recognized wrinkled-ness under both combustion modes.

The stratified-charge engine flames experienced generally higher levels of wrinkled-ness than the homogeneous-charge engine flames. This increase in wrinkled-ness might be expected based on the relatively larger RMS turbulent velocity fluctuations recognized under stratified-charge conditions (Figure 6-18) in comparison to the homogeneous-charge conditions (Figure 5-12).

The homogeneous-charge flame wrinkled-ness process was driven by in-cylinder airflow-to-flame interactions and the dominant scales of wrinkled-ness based flame surface area generation coincided with the scales of the airflow. The stratified-charge process was driven by fuel jet-to-flame interactions and as the stratified-charge flame increased in size its topology naturally approached that of the jets.

The outwardly propagating homogeneous-charge engine flames developed wrinkled-ness early in the engine cycle and maintained a semi-steady level of wrinkled-ness throughout much of the mid-to-late engine cycle. The stratified-charge flames developed wrinkled-ness early in the engine cycle but then necessarily reduced in wrinkled-ness as the flame decreased in overall scale, as might be expected based on their inwardly propagating nature.

Wrinkled-ness aside, how are the flame spread processes different under spray-guided stratified-charge engine conditions from that of conventional homogeneous-charge engine conditions?

Stratified-charge and homogeneous-charge engine flames spread and propagate in a very different manner and a few notable differences were recognized in this study. Homogeneous-charge engine flames propagate outwardly and generally maintain continuity between regions of combustion. Stratified-charge flames tend to propagate inwardly and along multiple spatially separated flame fronts at once. Jet-to-jet flame spread in the stratified-charge environment is likely to occur via a combination of homogeneous-like flame propagation or by burned-gas-to-flammable mixture interaction. The latter is an ignition process that contains physics not often considered in the homogeneous-charge engine combustion models.

If fine scale flame topology is so important, is it worthwhile attempting to resolve topological flame features or should they be subject to sub-grid modeling for the foreseeable future?

To answer this question, consider this study as an example. Under both homogenous-charge and stratified-charge conditions at least half of the flame wrinkled-ness was observed to be due to 0.5-2 mm diameter wrinkles and the rest due to 2-6 mm wrinkles. Recognizing that it probably takes about ten points to define a wrinkle; 0.05 mm grid spacing would be required to completely resolve most of the wrinkling, a 0.2 mm grid spacing would be required to resolve about half of the surface area generating wrinkles and a 0.6 mm grid spacing would be too course to resolving any of the turbulent features of the flame. A lot of 3D engine models

currently employ grid spacing on the order of 0.5 mm. As a better understanding of flame wrinkling physics comes to be, such models might benefit greatly by introducing finer grids. Even a modest decrease in grid spacing, perhaps from 0.6 to 0.2 mm, might relieve the burden of an inherently inaccurate sub-grid topology model greatly. However, due to computation limitations; flame topology physics will remain a subject of sub-grid modeling for some time to be.

Based upon this work, what suggestions can be made for future topics of advanced engine combustion research, particularly with regards to spray-guided stratified-charge flame topology and strategies?

A lot more might be learned about stratified-charge engine flame topological development if similar imaging studies were performed but with higher speed optical diagnostics. Increased imaging rates would allow for the progression of flames within individual engine cycles to be monitored, which might help to pinpoint some more of the critical flow and mixture field features that drive the flames topology. Further, studies of the sort might also lead to the recognition of mixture and flow strategies that are generally favorable for the SGSC strategy itself.

It would also be valuable for similar imaging studies to be performed with increased spatial resolution to gauge the effect of sub-half-millimeter wrinkles on overall flame wrinkled-ness. Such small wrinkles might play an important role in promoting surface area growth under stratified-charge conditions.

Further, the flame-to-flow interactions that occur in the stratified-charge and other advanced engine environments are complex enough that they might best be understood with the assistance of more fundamental testing performed within simplified test environments. For example, the interactions that occur between fuel sprays/jets, flames and solid surfaces in SGSC engines would probably be best investigated in a constant volume vessel under semi-realistic

engine-like conditions. Optical engine experiments, such as what was just presented, provide a much needed real world context to the engine combustion community but cannot reproduce the controllability of diagnostic abilities of simplified experimental environments. The task of developing advanced engines and models to forward promising concepts such as SGSC demand strong collaborations between computational modelers and experimentalists of all sorts, including those working within production-like metal and optical engines but also those working within more fundamental combustion research environments. Collectively, progress on the subject is guaranteed and success in enabling a few partially premixed advanced combustion strategies, whether it be SGSC or others, is likely.

APPENDICES

Appendix A: Properties of Iso-octane and Toluene

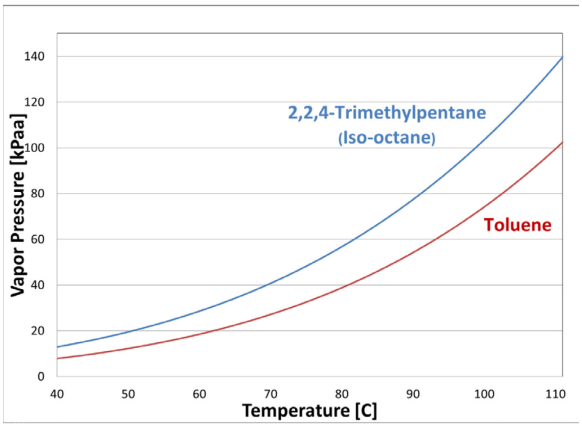

Appendix Figure A-1: Vapor pressure vs. temperature for Iso-octane and toluene [235].

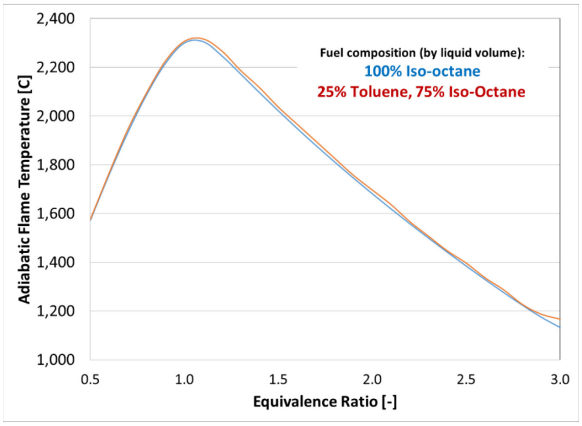

Appendix Figure A-2: CHEMKIN-PRO [236] based estimates of adiabatic flame temperature vs. equivalence ratio for pure Iso-octane and 25% toluene/75% iso-Octane fuel mixtures by liquid volume.

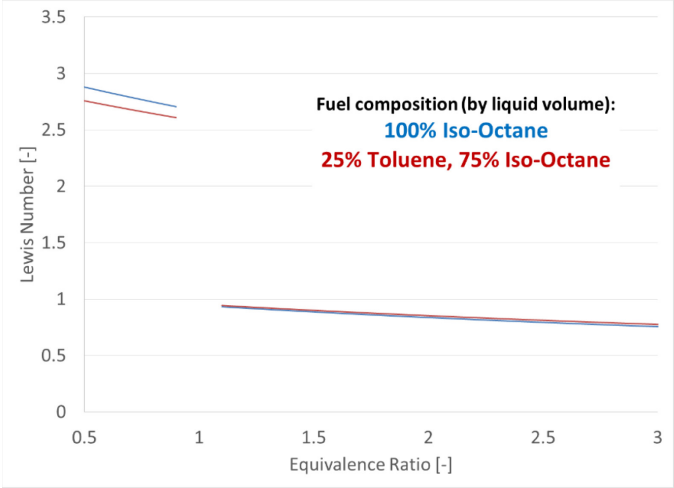

Appendix Figure A-3: Lewis number vs. equivalence ratio for pure iso-octane and a 25% Toluene, 75% iso-octane (by liquid volume) fuel mixture. The Lewis number values were calculated based upon thermal and diffusive properties estimated by CHEMKIN-PRO software [236].

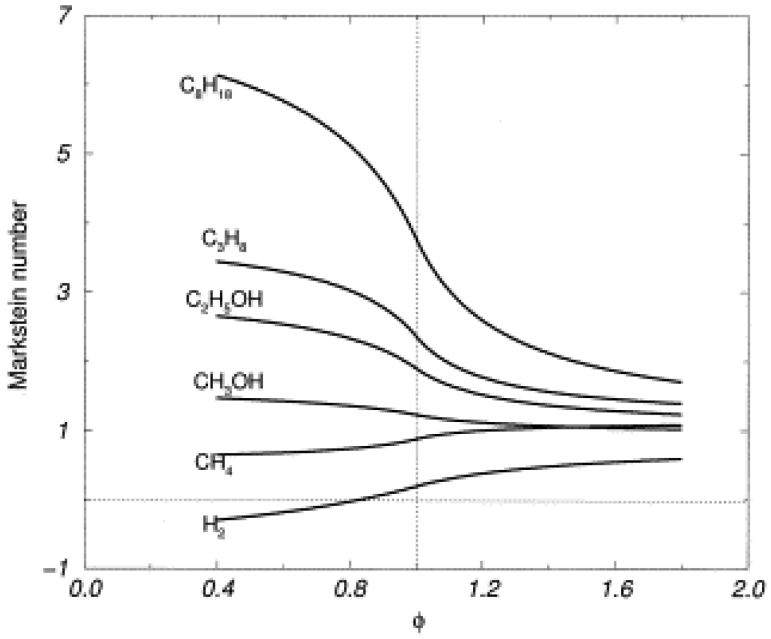

Appendix Figure A-4: Markstein number vs. equivalence ratio estimates for various fuels including pure iso-octane. This figure was originally produced and published by Bechtold et al. [237].

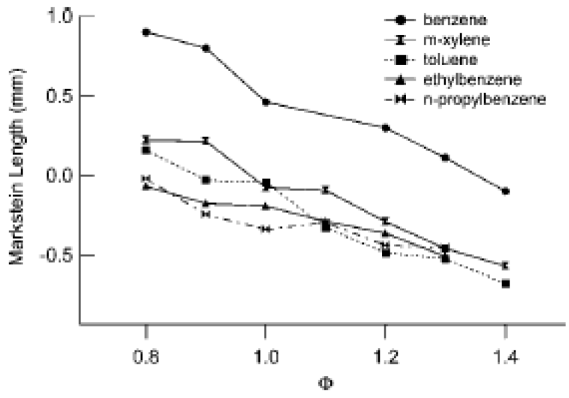

Appendix Figure A-5: Markstein length vs equivalence ratio for various aromatic fuels including toluene at 450 K and 3 bar total pressure. This figure was originally produced and published by Johnston et al. [238].

Appendix B: Effect of Toluene Dopant on Engine Performance

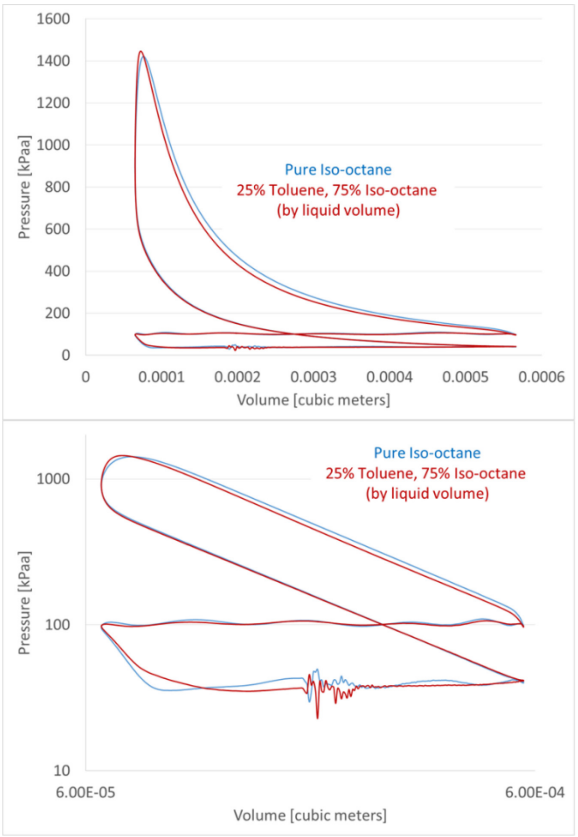

Appendix Figure B-1: PV Diagrams for pure iso-octane and toluene doped fuel mixtures at same homogeneous-charge, Φ=1 operational condition plotted on both (a) normal and (b) logarithmic scales.

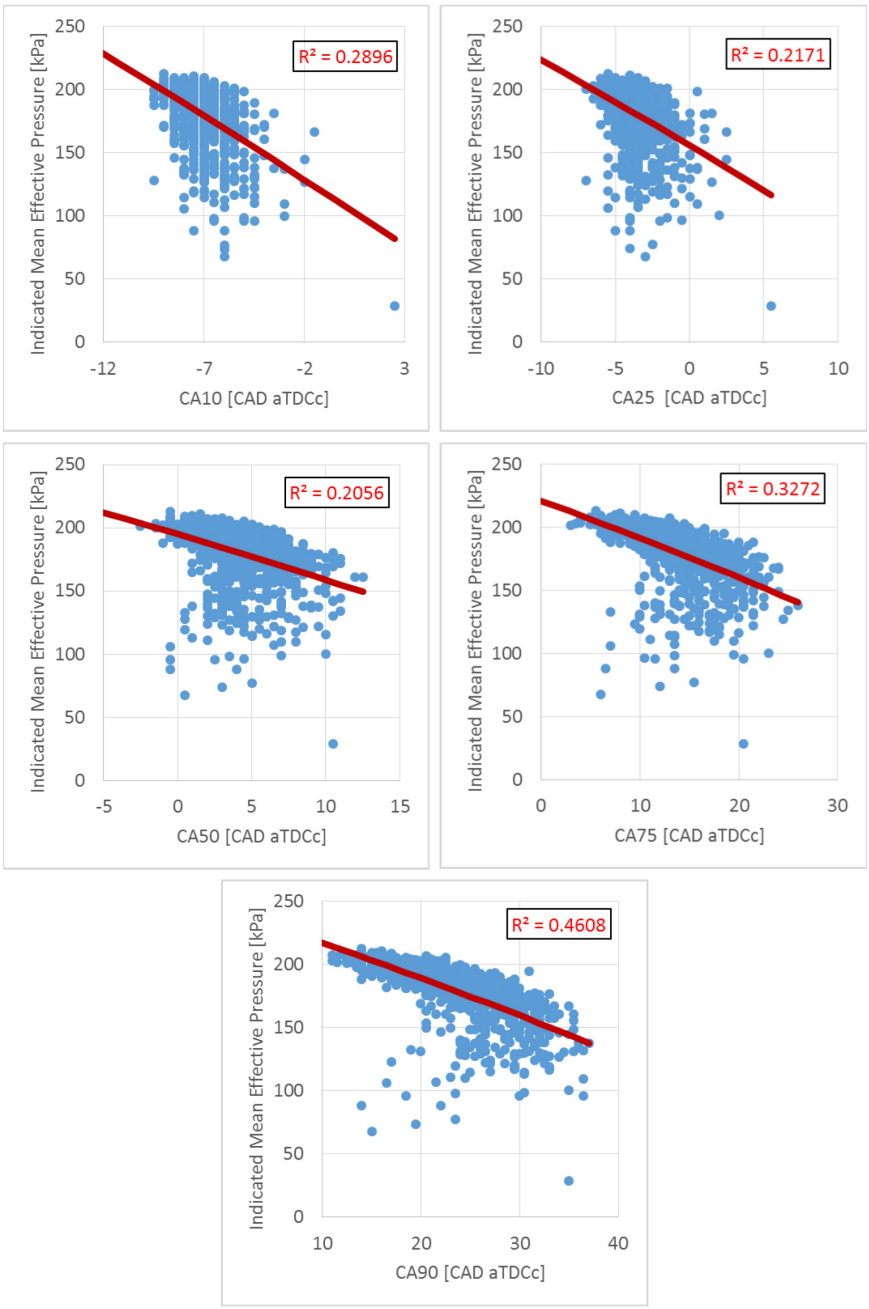

Appendix Figure C-1: Engine performance (IMEP) vs. combustion phasing (CAxx) for 1050 cycles of the stratified-charge condition used for the wrinkled-ness study fit with second order polynomials. Notice that combustion phasing weakly, but definitively correlates with IMEP output. CA75 and CA90 correlated best. Cycles that were slowed or delayed to burn generally yielded low values of IMEP.

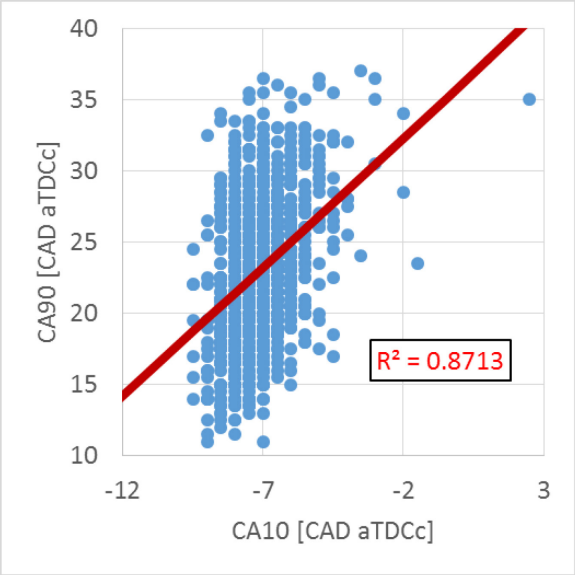

Appendix Figure C-2: CA90 vs CA10 for 1050 cycles of the engine operating under the SGSC conditions used for the wrinkled-ness study. The strong correlation between CA10 and CA90 implies that cycles that start out slow end late. In the previous set of figures, it was recognized that late ending cycles yielded low IMEP outputs. Therefore, cycles that started out slow tended to also yield low IMEP outputs (i.e. resulted in partial-burns) and sluggish charge ignition/early-burn was a source of variability and a cause for some of the partial burn cycles observed.

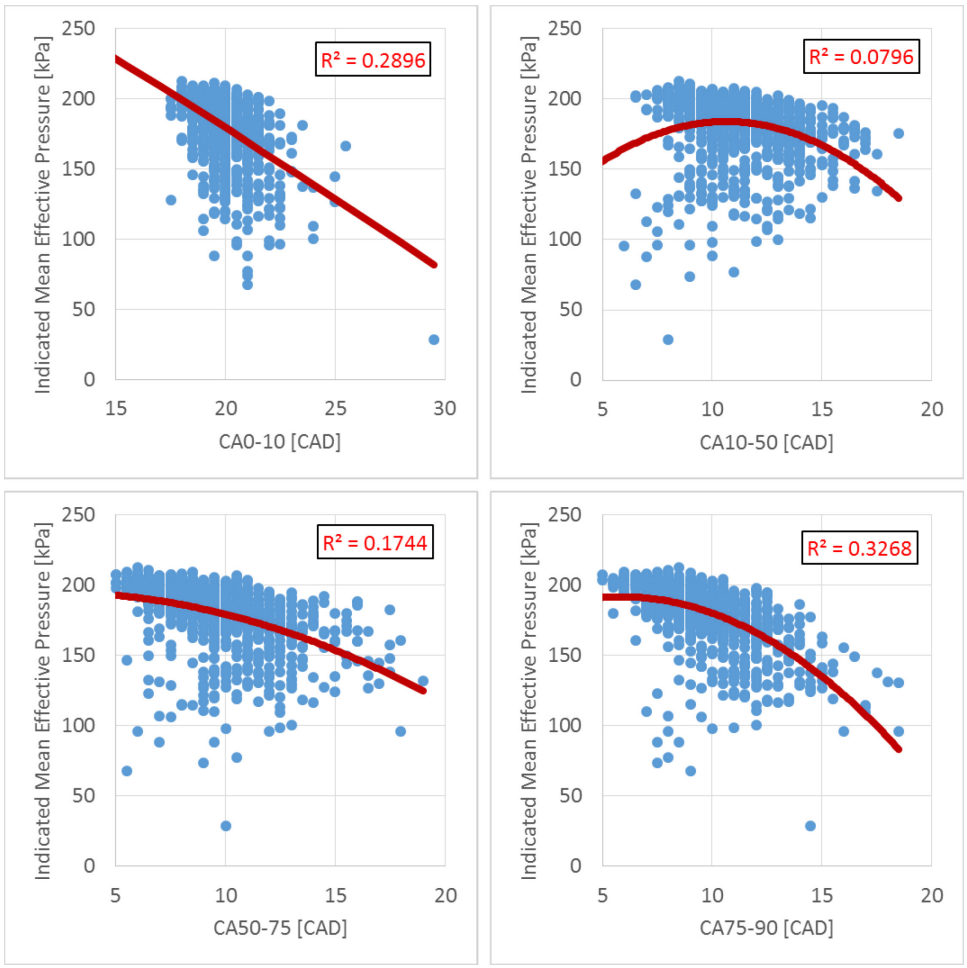

Appendix Figure C-3: Burn-durations (CAxx-CAxx) vs. Engine performance under the SGSC conditions used for the wrinkled-ness study. Notice that both early (CA0-10) and late (CA75-90) burn durations correlate weakly with IMEP. Generally, longer burn durations yielded lower values of IMEP output.

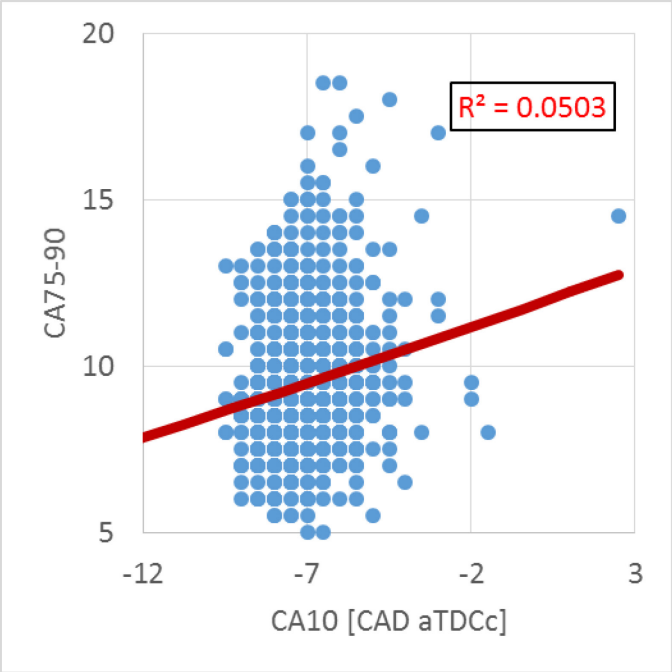

Appendix Figure C-4: CA10 vs. CA75-90 burn duration. Notice that there is no correlation between early combustion phasing (CA10) and the late combustion burn duration (CA75-90). Also remember that it was just shown that lengthy late cycle combustion burn durations generally led to reduced IMEP output. Therefore, poor late cycle flame propagation/spread was a source of variability and a cause for some of the partial burn cycles observed.

Appendix D: Imaging System Rates, Resolutions and Uncertainties

Imaging rate = one image per every-other-cycle (~5 Hz)

Spatial resolution = limited to 0.5 mm by laser sheet thickness

Quantitative accuracy in Φ = 25%
Quantitative precision in Φ = 14%
Total uncertainty in Φ = 29%

Appendix Figure D-1: Imaging rate, spatial resolution and uncertainty of the planar laser induced fluorescence equivalence ratio (Φ) diagnostic.

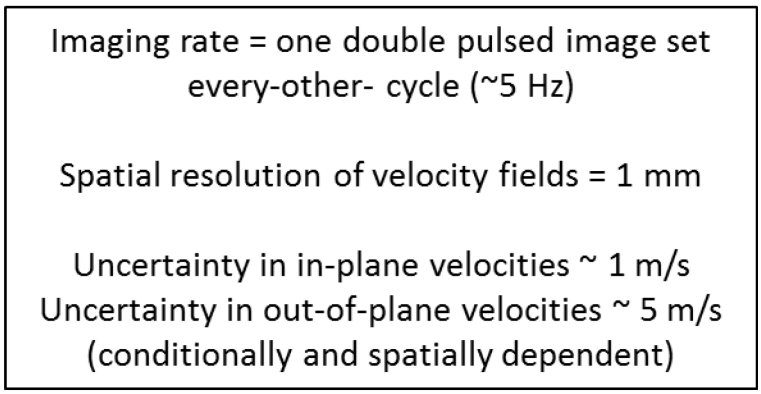

Appendix Figure D-2: Imaging rate, spatial resolution and uncertainty of the stereo particle image velocimetry diagnostic.

BIBLIOGRAPHY

1. Economic, U.N.D.o. and S. Affairs, *World Population to 2300*. 2004: New York: United Nations, Department of Economic and Social Affairs.
2. Administration, U.S.E.I. *International Energy Statistics*. 2013; Available from: http://www.eia.gov/.
3. Gerard, D. and L.B. Lave, *Implementing technology-forcing policies: The 1970 Clean Air Act Amendments and the introduction of advanced automotive emissions controls in the United States.* Technological Forecasting and Social Change, 2005. **72**(7): p. 761-778.
4. Bilger, R.W., et al., *Paradigms in turbulent combustion research.* Proceedings of the Combustion Institute, 2005. **30**(1): p. 21-42.
5. Heywood, J.B., *Internal combustion engine fundamentals*. Vol. 930. 1988: McGraw-Hill New York.
6. Stone, R., *Introduction to internal combustion engines.* 1985.
7. Pulkrabek, W.W., *Engineering fundamentals of the internal combustion engine*. Vol. 2. 2004: Pearson Prentice Hall New Jersey.
8. Teh, K., S. Miller, and C. Edwards, *Thermodynamic requirements for maximum internal combustion engine cycle efficiency. Part 1: optimal combustion strategy.* International Journal of Engine Research, 2008. **9**(6): p. 449-465.
9. Teh, K., S. Miller, and C. Edwards, *Thermodynamic requirements for maximum internal combustion engine cycle efficiency. Part 2: work extraction and reactant preparation strategies.* International Journal of Engine Research, 2008. **9**(6): p. 467-481.
10. Dunbar, W. and N. Lior, *Sources of combustion irreversibility.* Combustion Science and Technology, 1994. **103**(1-6): p. 41-61.
11. Borgnakke, C. and R.E. Sonntag, *Fundamentals of thermodynamics*. 2013, Hoboken, NJ: Wiley. xvii, 894 p.
12. MacLean, H.L. and L.B. Lave, *Evaluating automobile fuel/propulsion system technologies.* Progress in energy and combustion science, 2003. **29**(1): p. 1-69.
13. Reitz, R.D., *Directions in internal combustion engine research.* Combustion and Flame, 2013. **160**(1): p. 1-8.
14. Drake, M.C. and D.C. Haworth, *Advanced gasoline engine development using optical diagnostics and numerical modeling.* Proceedings of the Combustion Institute, 2007. **31**(1): p. 99-124.
15. Drake, M.C., T.D. Fansler, and A.M. Lippert, *Stratified-charge combustion: modeling and imaging of a spray-guided direct-injection spark-ignition engine.* Proceedings of the Combustion Institute, 2005. **30**(2): p. 2683-2691.
16. Alkidas, A.C., *Combustion advancements in gasoline engines.* Energy Conversion and Management, 2007. **48**(11): p. 2751-2761.

17. Alkidas, A.C. and S.H. El Tahry, *Contributors to the Fuel Economy Advantage of DISI Engines Over PFI Engines*. 2003, SAE International Technical Paper No. 2003-01-3101.
18. Zhao, F., M.-C. Lai, and D.L. Harrington, *Automotive spark-ignited direct-injection gasoline engines.* Progress in energy and combustion science, 1999. **25**(5): p. 437-562.
19. M.C. Drake, D.T.F., T.D. Fansler. *Advanced Diagnostics For Minimizing Hydrocarbon Emissions From A Direct-Injection Gasoline Engine*. in *Proc. Combust. Inst.* 1996.
20. Kašpar, J., P. Fornasiero, and N. Hickey, *Automotive catalytic converters: current status and some perspectives.* Catalysis Today, 2003. **77**(4): p. 419-449.
21. Park, C., et al., *Emission Characteristics of Gasoline and LPG in a Spray-Guided-Type Direct Injection Engine*. 2013, SAE International Paper Number 2013-01-1323.
22. Akihama, K., et al., *Mechanism of the Smokeless Rich Diesel Combustion by Reducing Temperature*. 2001, SAE International Technical Paper No. 2001-01-0655.
23. Peterson, B. and V. Sick, *High-speed flow and fuel imaging study of available spark energy in a spray-guided direct-injection engine and implications on misfires.* International Journal of Engine Research, 2010. **11**(5): p. 313-329.
24. Smith, J., et al., *A Comparison of Spray-Guided Stratified-Charge Combustion Performance with Outwardly-Opening Piezo and Multi-Hole Solenoid Injectors.* SAE Int. J. Engines, 2011. **4**(1): p. 1481-1497.
25. Chen, H., D.L. Reuss, and V. Sick, *Analysis of misfires in a direct injection engine using proper orthogonal decomposition.* Experiments in fluids, 2011. **51**(4): p. 1139-1151.
26. Law, C.K., *Combustion physics*. 2006: Cambridge University Press.
27. Johansson, A.N., S. Hemdal, and P. Dahlander, *Experimental Investigation of Soot in a Spray-Guided Single Cylinder GDI Engine Operating in a Stratified Mode*. 2013, SAE International Technical Paper No. 2013-24-0052.
28. Siebers, D. and B. Higgins, *Flame Lift-Off on Direct-Injection Diesel Sprays Under Quiescent Conditions*. 2001, SAE International Technical Paper No. 2001-01-0530.
29. Dahms, R.N., Fansler, T.D., Drake, M.C., Kuo, T.-W., and Peters, N., *Understanding ignition phenomena in spray-guided gasoline engines using high-speed imaging and the extended spark-ignition model SparkCIMM. Part B: Importance of molecular fuel properties in early flame front propagation.* Combustion and Flame, 2011. **158**: p. 2245-2260.
30. Lacour PhD, C. and C. Pera, *An Experimental Database Dedicated to the Study and Modelling of Cyclic Variability in Spark-Ignition Engines with LES*. 2011, SAE International Technical Paper No. No. 2011-01-1282.
31. Westrate, B., et al., *Dynamometer Development Results for a Stratified-Charge DISI Combustion System*. 2002, SAE International Technical Paper No. 2002-01-2657.
32. Keck, J.C., J.B. Heywood, and G. Noske, *Early flame development and burning rates in spark ignition engines and their cyclic variability*. 1987: Society of Automotive Engineers Warrendale, PA.
33. Chen, H., et al., *A practical guide for using proper orthogonal decomposition in engine research.* International Journal of Engine Research, 2013. **14**(4): p. 307-319.
34. Chen, H., D.L. Reuss, and V. Sick, *On the use and interpretation of proper orthogonal decomposition of in-cylinder engine flows.* Measurement Science and Technology, 2012. **23**(8): p. 085302.
35. Chen, H., M. Xu, and D.L. Hung, *Analyzing In-Cylinder Flow Evolution and Variations in a Spark-Ignition Direct-Injection Engine Using Phase-Invariant Proper Orthogonal Decomposition Technique*. 2014, SAE Technical Paper No. 2014-01-1174.

36. Chen, H., et al., *Cycle-to-cycle variation analysis of early flame propagation in engine cylinder using proper orthogonal decomposition.* Experimental Thermal and Fluid Science, 2014. **58**: p. 48-55.
37. Chen, H., et al., *Proper orthogonal decomposition analysis of fuel spray structure variation in a spark-ignition direct-injection optical engine.* Experiments in Fluids, 2014. **55**(4): p. 1-12.
38. Zeng, W., M. Sjöberg, and D.L. Reuss, *Combined effects of flow/spray interactions and EGR on combustion variability for a stratified DISI engine.* Proceedings of the Combustion Institute, 2015. **35**(3): p. 2907-2914.
39. Peterson, B.R., *High-Speed Fuel And Flow Imaging To Investigate Misfires In A Spray-Guided Direct-Injection Engine*, in *Mechanical Engineering*. 2010, University of Michigan.
40. Piock, W.F., et al., *Ignition Systems for Spray-Guided Stratified Combustion.* SAE Int. J. Engines, 2010. **3**(1): p. 389-401.
41. Dec, J.E., *A Conceptual Model of DI Diesel Combustion Based on Laser-Sheet Imaging**. 1997, SAE International Technical Paper No. 970873.
42. Gatowski, J.A., J.B. Heywood, and C. Deleplace, *Flame photographs in a spark-ignition engine.* Combustion and Flame, 1984. **56**(1): p. 71-81.
43. Withrow, L. and G.M. Rassweiler, *Studying engine combustion by physical methods a review.* Journal of Applied Physics, 1938. **9**(6): p. 362-372.
44. Bowditch, F.W., *A New Tool for Combustion Research A Quartz Piston Engine*. 1961, SAE International Technical Paper No. 610002.
45. Fansier, T., et al., *Local fuel concentration, igiation and combustion in a stratified charge spark ignited direct injection engine spectroscopic, imaging and pressure-based measurements.* International Journal of Engine Research, 2003. **4**(2): p. 61-86.
46. Fansler, T., et al. *Fuel-spray and spark-plug interactions in a spray-guided direct-injection gasoline engine*. in *7th international symposium on internal combustion diagnostics. Baden-Baden*. 2006.
47. Deschamps, B., R. Snyder, and T.A. BARITAUD, *Effect of flow and gasoline stratification on combustion in a 4-valve SI engine.* SAE transactions, 1994. **103**(4): p. 1483-1494.
48. Hentschel, W., *Optical diagnostics for combustion process development of direct-injection gasoline engines.* Proceedings of the combustion institute, 2000. **28**(1): p. 1119-1135.
49. Itoh, T., et al., *A study of mixture formation processes in direct injection stratified charge gasoline engines by quantitative laser-induced fluorescence imaging and the infrared absorption method.* International Journal of Engine Research, 2006. **7**(5): p. 423-434.
50. Richter, M., et al., *Investigation of the Fuel Distribution and the In-cylinder Flow Field in a Stratified Charge Engine Using Laser Techniques and Comparison with CFD-Modelling*. 1999, SAE International Technical Paper No. 1999-01-3540.
51. Shingne, P., et al., *Turbocharger matching for a 4-cylinder gasoline HCCI engine using a 1D engine simulation*. 2010, SAE Technical Paper No. 2010-01-2143.
52. Shingne, P.S., et al., *A Comparison of Valving Strategies Appropriate For Multimode Combustion Within a Downsized Boosted Automotive Engine—Part I: High Load Operation Within the Spark Ignition Combustion Regime.* Journal of Engineering for Gas Turbines and Power, 2014. **136**(10): p. 101507.
53. Gerow, M.S., et al., *A Comparison of Valving Strategies Appropriate for Multimode Combustion Within a Downsized Boosted Automotive Engine—Part II: Mid Load Operation Within the SACI Combustion Regime.* Journal of Engineering for Gas Turbines and Power, 2014. **136**(10): p. 101508.

54. Gorzelic, P., et al. *A low-order HCCI model extended to capture SI-HCCI mode transition data with two-stage cam switching*. in *ASME 2014 Dynamic Systems and Control Conference*. 2014. American Society of Mechanical Engineers.
55. Kong, S.-C., Z. Han, and R.D. Reitz, *The development and application of a diesel ignition and combustion model for multidimensional engine simulation*. 1995, SAE Technical Paper.
56. Kume, T., Iwamoto, Y., Iida, K., Murakami, M. et al., *Combustion Control Technologies for Direct Injection SI Engine.* SAE Technical Paper 960600, 1996.
57. Karl G, K.R., Bargende M., *Analysis of a direct injected gasoline engine.* SAE Technical Paper, No. 970624, 1997.
58. Lückert, P., et al., *The new V6 gasoline engine with direct injection by Mercedes-Benz.* MTZ worldwide, 2006. **67**(11): p. 2-6.
59. Pausas, J.G. and J.E. Keeley, *A burning story: the role of fire in the history of life.* BioScience, 2009. **59**(7): p. 593-601.
60. Lipatnikov, A., *Fundamentals of Premixed Turbulent Combustion*. 2012: CRC Press.
61. Law, C.K., *Combustion at a crossroads: Status and prospects.* Proceedings of the Combustion Institute, 2007. **31**(1): p. 1-29.
62. Sweeney, M.S., S. Hochgreb, and R.S. Barlow, *The structure of premixed and stratified low turbulence flames.* Combustion and Flame, 2011. **158**(5): p. 935-948.
63. Warhaft, Z., *Passive scalars in turbulent flows.* Annual Review of Fluid Mechanics, 2000. **32**(1): p. 203-240.
64. Mura, A., V. Robin, and M. Champion, *Modeling of scalar dissipation in partially premixed turbulent flames.* Combustion and Flame, 2007. **149**(1–2): p. 217-224.
65. Peters, N., *Turbulent combustion*. 2000: Cambridge university press.
66. McAllister, S. and J.-Y. Chen, *Mechanical Engineering: Fundamentals of Combustion Processes*. 2011: Springer.
67. Natanzon, M.S., F. Culick, and Knovel, *Combustion instability*. Neustoĭchivost' goreniia.English. 1999, Reston, Va.: American Institute of Aeronautics and Astronautics. xxviii, 258 p.
68. Poinsot, T. and D. Veynante, *Theoretical and numerical combustion*. 2005: RT Edwards Incorporated.
69. Warnatz, J., U. Maas, and R.W. Dibble, *Combustion: physical and chemical fundamentals, modeling and simulation, experiments, pollutant formation*. 2006: Springer.
70. Stiesch, G., *Modeling engine spray and combustion processes*. 2003: Springer Berlin.
71. Broustail, G., et al., *Experimental determination of laminar burning velocity for butanol and ethanol iso-octane blends.* Fuel, 2011. **90**(1): p. 1-6.
72. Zeldovich, Y.B. and D. Frank-Kamenetskii, *A theory of thermal propagation of flame.* Zh. Fiz. Khim, 1938. **12**(1): p. 100-105.
73. Kee, R., et al., *CHEMKIN Release 4.1.* Reaction Design, San Diego, CA, 2006.
74. Curran, H.J., et al., *A comprehensive modeling study of iso-octane oxidation.* Combustion and flame, 2002. **129**(3): p. 253-280.
75. Côme, G.M., et al., *Computer-aided design of gas-phase oxidation mechanisms—Application to the modeling of n-heptane and iso-octane oxidation.* Symposium (International) on Combustion, 1996. **26**(1): p. 755-762.
76. Jia, M. and M. Xie, *A chemical kinetics model of iso-octane oxidation for HCCI engines.* Fuel, 2006. **85**(17–18): p. 2593-2604.
77. Fieweger, K., R. Blumenthal, and G. Adomeit, *Self-ignition of SI engine model fuels: a shock tube investigation at high pressure.* Combustion and Flame, 1997. **109**(4): p. 599-619.
78. Davis, S.G. and C.K. Law, *Laminar flame speeds and oxidation kinetics of iso-octane-air and n-heptane-air flames.* Symposium (International) on Combustion, 1998. **27**(1): p. 521-527.

79. Vagelopoulos, C.M., F.N. Egolfopoulos, and C.K. Law, *Further considerations on the determination of laminar flame speeds with the counterflow twin-flame technique.* Symposium (International) on Combustion, 1994. **25**(1): p. 1341-1347.
80. Law, C. and C. Sung, *Structure, aerodynamics, and geometry of premixed flamelets.* Progress in Energy and Combustion Science, 2000. **26**(4): p. 459-505.
81. Echekki, T. and J.H. Chen, *Unsteady strain rate and curvature effects in turbulent premixed methane-air flames.* Combustion and Flame, 1996. **106**(1–2): p. 184-202.
82. Haq, M.Z., et al., *Wrinkling and curvature of laminar and turbulent premixed flames.* Combustion and Flame, 2002. **131**(1–2): p. 1-15.
83. Markstein, G.H., *Nonsteady flame propagation*. Vol. 75. 1964: Pergamon.
84. Bechtold, J.K. and M. Matalon, *The dependence of the Markstein length on stoichiometry.* Combustion and Flame, 2001. **127**(1–2): p. 1906-1913.
85. Bradley, D., et al., *The Measurement of Laminar Burning Velocities and Markstein Numbers for Iso-octane–Air and Iso-octane–n-Heptane–Air Mixtures at Elevated Temperatures and Pressures in an Explosion Bomb.* Combustion and Flame, 1998. **115**(1–2): p. 126-144.
86. Halter, F., T. Tahtouh, and C. Mounaïm-Rousselle, *Nonlinear effects of stretch on the flame front propagation.* Combustion and Flame, 2010. **157**(10): p. 1825-1832.
87. Brequigny, P., et al., *Impact of Fuel Properties and Flame Stretch on the Turbulent Flame Speed in Spark-Ignition Engines*. 2013, SAE International Technical Paper No. 2013-24-0054.
88. Borghi, R., *On the structure and morphology of turbulent premixed flames*, in *Recent advances in the Aerospace Sciences*. 1985, Springer. p. 117-138.
89. Shepherd, I., et al., *Premixed flame front structure in intense turbulence.* Proceedings of the Combustion Institute, 2002. **29**(2): p. 1833-1840.
90. Fox, M. and F. Weinberg, *An experimental study of burner-stabilized turbulent flames in premixed reactants.* Proceedings of the Royal Society of London. Series A. Mathematical and Physical Sciences, 1962. **268**(1333): p. 222-239.
91. Driscoll, J.F., *Turbulent premixed combustion: Flamelet structure and its effect on turbulent burning velocities.* Progress in Energy and Combustion Science, 2008. **34**(1): p. 91-134.
92. Abdel-Gayed, R.G. and D. Bradley. *Dependence of turbulent burning velocity on turbulent reynolds number and ratio of flaminar burning velocity to RMS turbulent velocity*. in *Symposium (International) on Combustion*. 1977. Elsevier.
93. Shepherd, I.G. and R.K. Cheng, *The burning rate of premixed flames in moderate and intense turbulence.* Combustion and Flame, 2001. **127**(3): p. 2066-2075.
94. Deschamps, B., et al. *Surface density measurements of turbulent premixed flames in a spark-ignition engine and a Bunsen-type burner using planar laser-induced fluorescence*. in *Symposium (International) on Combustion*. 1996. Elsevier.
95. Pope, S., *The evolution of surfaces in turbulence.* International journal of engineering science, 1988. **26**(5): p. 445-469.
96. Steinberg, A.M., *The Dynamics Of Turbulent Premixed Flames: Mechanisms And Models For Turbulence-Flame Interaction*, in *Aerospace Engineering*. 2009, The University of Michigan. p. 308.
97. Duclos, J.M., D. Veynante, and T. Poinsot, *A comparison of flamelet models for premixed turbulent combustion.* Combustion and Flame, 1993. **95**(1): p. 101-117.
98. Darrieus, G., *Propagation d'un front de flamme.* La Technique Moderne, France, 1938.
99. Landau, L., *On the theory of slow combustion.* Acta Physicochim. URSS, 1944. **19**(1): p. 77-85.
100. Matalon, M., *Intrinsic flame instabilities in premixed and nonpremixed combustion.* Annu. Rev. Fluid Mech., 2007. **39**: p. 163-191.

101. Jomaas, G., C. Law, and J. Bechtold, *On transition to cellularity in expanding spherical flames.* Journal of fluid mechanics, 2007. **583**: p. 1-26.
102. Pope, S.B., *Turbulent flows*. 2000: Cambridge university press.
103. Gülder, Ö.L. and G.J. Smallwood, *Inner cutoff scale of flame surface wrinkling in turbulent premixed flames.* Combustion and Flame, 1995. **103**(1–2): p. 107-114.
104. Takeno, T., M. Murayama, and Y. Tanida, *Fractal analysis of turbulent premixed flame surface.* Experiments in Fluids, 1990. **10**(2-3): p. 61-70.
105. Renard, P.H., et al., *Dynamics of flame/vortex interactions.* Progress in Energy and Combustion Science, 2000. **26**(3): p. 225-282.
106. Peters, N. and F. Williams. *Premixed combustion in a vortex*. in *Symposium (International) on Combustion*. 1989. Elsevier.
107. Wu, M.-S. and J.F. Driscoll, *A numerical simulation of a vortex convected through a laminar premixed flame.* Combustion and Flame, 1992. **91**(3–4): p. 310-322.
108. Poinsot, T., D. Veynante, and S. Candel. *Diagrams of premixed turbulent combustion based on direct simulation*. in *Symposium (International) on Combustion*. 1991. Elsevier.
109. Patnaik, G. and K. Kailasanath. *A computational study of local quenching in flame-vortex interactions with radiative losses*. in *Symposium (International) on Combustion*. 1998. Elsevier.
110. Rutland, C.J. and J.H. Ferziger, *Simulations of flame-vortex interactions.* Combustion and Flame, 1991. **84**(3–4): p. 343-360.
111. Katta, V. and W. Roquemore. *Vortex-flame interactions in premixed jet flames*. in *AIAA, Aerospace Sciences Meeting and Exhibit, 33 rd, Reno, NV*. 1995.
112. Vassilicos, J.C. and N. Nikiforakis, *Flamelet-vortex interaction and the Gibson scale.* Combustion and Flame, 1997. **109**(3): p. 293-302.
113. Roberts, W.L. and J.F. Driscoll, *A laminar vortex interacting with a premixed flame: Measured formation of pockets of reactants.* Combustion and Flame, 1991. **87**(3): p. 245-256.
114. Poinsot, T., D. Veynante, and S. Candel, *Quenching processes and premixed turbulent combustion diagrams.* Journal of Fluid Mechanics, 1991. **228**(561-606): p. 230.
115. Roberts, W.L., et al., *Images of the quenching of a flame by a vortex—To quantify regimes of turbulent combustion.* Combustion and Flame, 1993. **94**(1): p. 58-69.
116. Nye, D.A., et al., *Flame stretch measurements during the interaction of premixed flames and Kármán vortex streets using PIV.* Combustion and Flame, 1996. **105**(1–2): p. 167-179.
117. Driscoll, J.F., et al., *The strain exerted by a vortex on a flame—determined from velocity field images.* Combustion Science and Technology, 1994. **96**(4-6): p. 213-229.
118. Pindera, M.Z. and L. Talbot, *Flame induced vorticity: Effects of stretch.* Symposium (International) on Combustion, 1988. **21**(1): p. 1357-1366.
119. Mueller, C.J., et al., *Vorticity generation and attenuation as vortices convect through a premixed flame.* Combustion and Flame, 1998. **112**(3): p. 342-358.
120. Mueller, C.J., et al., *Effects of unsteady stretch on the strength of a freely-propagating flame wrinkled by a vortex.* Symposium (International) on Combustion, 1996. **26**(1): p. 347-355.
121. Sinibaldi, J.O., et al., *Suppression of flame wrinkling by buoyancy: the baroclinic stabilization mechanism.* AIAA journal, 1998. **36**(8): p. 1432-1438.
122. Buckmaster, J., et al., *Combustion theory and modeling.* Proceedings of the Combustion Institute, 2005. **30**(1): p. 1-19.
123. Echekki, T. and E. Mastorakos, *Turbulent combustion modeling: Advances, new trends and perspectives*. Vol. 95. 2011: Springer.
124. Haworth, D.C., *A Review of Turbulent Combustion Modeling for Multidimensional In-Cylinder CFD*. 2005, SAE International Technical Paper No. 2005-01-0993.
125. Williams, F. and J. Buckmaster, *The mathematics of combustion.* SIAM, Philadelphia, 1985. **97**.

126. Weller, H., *The development of a new flame area combustion model using conditional averaging.* Thermo-fluids section report TF, 1993. **9307**.
127. Herweg, R. and R. Maly, *A fundamental model for flame kernel formation in SI engines.* SAE transactions, 1992. **101**(3): p. 1947-1976.
128. Bray, K. and J. Moss, *A unified statistical model of the premixed turbulent flame.* Acta Astronautica, 1977. **4**(3): p. 291-319.
129. Bray, K., P.A. Libby, and J. Moss, *Flamelet crossing frequencies and mean reaction rates in premixed turbulent combustion.* Combustion Science and Technology, 1984. **41**(3-4): p. 143-172.
130. Marble, F.E. and J.E. Broadwell, *The coherent flame model for turbulent chemical reactions*. 1977, DTIC Document.
131. Gouldin, F., K. Bray, and J.-Y. Chen, *Chemical closure model for fractal flamelets.* Combustion and flame, 1989. **77**(3): p. 241-259.
132. Bray, K. and N. Peters, *Laminar flamelets in turbulent flames.* Turbulent reacting flows, 1994: p. 63-113.
133. Meneveau, C. and T. Poinsot, *Stretching and quenching of flamelets in premixed turbulent combustion.* Combustion and Flame, 1991. **86**(4): p. 311-332.
134. Duclos, J., D. Veynante, and T. Poinsot, *A comparison of flamelet models for premixed turbulent combustion.* Combustion and flame, 1993. **95**(1): p. 101-117.
135. Poinsot, T. *Using direct numerical simulations to understand premixed turbulent combustion*. in *Symposium (International) on Combustion*. 1996. Elsevier.
136. Cant, R., S. Pope, and K. Bray. *Modelling of flamelet surface-to-volume ratio in turbulent premixed combustion*. in *Symposium (International) on Combustion*. 1991. Elsevier.
137. Veynante, D., et al. *Experimental analysis of flame surface density models for premixed turbulent combustion*. in *Symposium (International) on Combustion*. 1996. Elsevier.
138. Mantel, T. and R. Borghi, *A new model of premixed wrinkled flame propagation based on a scalar dissipation equation.* Combustion and Flame, 1994. **96**(4): p. 443-457.
139. Hélie, J. and A. Trouvé, *A modified coherent flame model to describe turbulent flame propagation in mixtures with variable composition.* Proceedings of the Combustion Institute, 2000. **28**(1): p. 193-201.
140. Kioni, P.N., et al., *Flame spread in laminar mixing layers: The triple flame.* Combustion and Flame, 1993. **95**(3): p. 276-290.
141. Buckmaster, J., *Edge-flames.* Progress in energy and combustion science, 2002. **28**(5): p. 435-475.
142. Im, H.G. and J.H. Chen, *Effects of flow strain on triple flame propagation.* Combustion and Flame, 2001. **126**(1–2): p. 1384-1392.
143. Dold, J., *Flame propagation in a nonuniform mixture: analysis of a slowly varying triple flame.* Combustion and Flame, 1989. **76**(1): p. 71-88.
144. Plessing, T., et al., *An experimental and numerical study of a laminar triple flame.* Combustion and Flame, 1998. **115**(3): p. 335-353.
145. HARTLEY, L.J. and J. Dold, *Flame propagation in a nonuniform mixture: analysis of a propagating triple-flame.* Combustion science and technology, 1991. **80**(1-3): p. 23-46.
146. Ruetsch, G., L. Vervisch, and A. Linán, *Effects of heat release on triple flames.* Physics of Fluids, 1995. **7**(6): p. 1447-1454.
147. Chung, S., *Stabilization, propagation and instability of tribrachial triple flames.* Proceedings of the Combustion Institute, 2007. **31**(1): p. 877-892.
148. Veynante, D., et al., *Triple flame structure and diffusion flame stabilization.* 1995.
149. Favier, V. and L. Vervisch, *Edge flames and partially premixed combustion in diffusion flame quenching.* Combustion and Flame, 2001. **125**(1–2): p. 788-803.

150. Lyons, K., et al., *On flame-edge propagation.* Flow, Turbulence and Combustion, 2008. **80**(3): p. 405-410.
151. Upatnieks, A., et al., *Liftoff of turbulent jet flames—assessment of edge flame and other concepts using cinema-PIV.* Combustion and flame, 2004. **138**(3): p. 259-272.
152. Vena, P.C., et al., *Equivalence ratio gradient effects on flame front topology in a stratified iso-octane/air turbulent V-flame.* Proceedings of the Combustion Institute, 2011. **33**(1): p. 1551-1558.
153. Marzouk, Y., A. Ghoniem, and H. Najm, *Dynamic response of strained premixed flames to equivalence ratio gradients.* Proceedings of the Combustion Institute, 2000. **28**(2): p. 1859-1866.
154. Kang, T. and D.C. KYRITSIS, *Methane flame propagation in compositionally stratified gases.* Combustion science and technology, 2005. **177**(11): p. 2191-2210.
155. Galizzi, C. and D. Escudié. *Turbulent stratified V-shaped flames: Experimental analysis of the flame front topology*. in *Proceedings*. 2005.
156. Kang, T. and D.C. Kyritsis, *A combined experimental/computational investigation of stratified combustion in methane–air mixtures.* Energy Conversion and Management, 2007. **48**(11): p. 2769-2774.
157. Kang, T. and D.C. Kyritsis, *Phenomenology of methane flame propagation into compositionally stratified, gradually richer mixtures.* Proceedings of the Combustion Institute, 2009. **32**(1): p. 979-985.
158. Anselmo-Filho, P., et al., *Experimental measurements of geometric properties of turbulent stratified flames.* Proceedings of the Combustion Institute, 2009. **32**(2): p. 1763-1770.
159. Vena, P.C., et al., *Structure of a Partially Premixed Iso-Octane/Air Turbulent V-Flame*. 2009, SAE International Technical Paper No. 2009-01-2655.
160. Pires Da Cruz, A., A. Dean, and J. Grenda, *A numerical study of the laminar flame speed of stratified methane/air flames.* Proceedings of the Combustion Institute, 2000. **28**(2): p. 1925-1932.
161. Garrido-Lopez, D. and S. Sarkar, *Effects of imperfect premixing coupled with hydrodynamic instability on flame propagation.* Proceedings of the Combustion Institute, 2005. **30**(1): p. 621-628.
162. Galizzi, C. and D. Escudié, *Experimental analysis of an oblique laminar flame front propagating in a stratified flow.* combustion and flame, 2006. **145**(3): p. 621-634.
163. Haworth, D., et al., *Numerical simulation of turbulent propane–air combustion with nonhomogeneous reactants.* Combustion and Flame, 2000. **121**(3): p. 395-417.
164. Bray, K., P. Domingo, and L. Vervisch, *Role of the progress variable in models for partially premixed turbulent combustion.* Combustion and Flame, 2005. **141**(4): p. 431-437.
165. Domingo, P., L. Vervisch, and K. Bray, *Partially premixed flamelets in LES of nonpremixed turbulent combustion.* Combustion Theory and Modelling, 2002. **6**(4): p. 529-551.
166. Domingo, P., L. Vervisch, and J. Réveillon, *DNS analysis of partially premixed combustion in spray and gaseous turbulent flame-bases stabilized in hot air.* Combustion and Flame, 2005. **140**(3): p. 172-195.
167. Libby, P.A. and F.A. Williams, *A presumed PDF analysis of partially premixed turbulent combustion.* Combustion Science and technology, 2000. **161**(1): p. 351-390.
168. Ribert, G., M. Champion, and P. Plion, *Modeling turbulent reactive flows with variable equivalence ratio: application to the calculation of a reactive shear layer.* Combustion Science and technology, 2004. **176**(5-6): p. 907-923.
169. Robin, V., et al., *A multi-Dirac presumed PDF model for turbulent reactive flows with variable equivalence ratio.* Combustion science and technology, 2006. **178**(10-11): p. 1843-1870.

170. Veynante, D., et al., *Coherent Flame Model for Non-Uniformly Premixed Turbulent Flames*, in *Turbulent Shear Flows 7*. 1991, Springer. p. 367-378.
171. Baritaud, T.A., J.M. Duglos, and A. Fusco, *Modeling turbulent combustion and pollutant formation in stratified charge SI engines.* Symposium (International) on Combustion, 1996. **26**(2): p. 2627-2635.
172. Duclos, J. and M. Zolver. *3D modeling of intake, injection and combustion in a DI-SI engine under homogeneous and stratified operating conditions*. in *The Fourth Internationa Symposium COMODIA*. 1998.
173. Colin, O., A. Benkenida, and C. Angelberger, *3D modeling of mixing, ignition and combustion phenomena in highly stratified gasoline engines.* Oil & gas science and technology, 2003. **58**(1): p. 47-62.
174. Dahms, R.N., et al., *Detailed Simulations of Stratified Ignition and Combustion Processes in a Spray-Guided Gasoline Engine using the SparkCIMM/G-Equation Modeling Framework.* SAE Int. J. Engines, 2012. **5**(2): p. 141-161.
175. Dahms, R.N., et al., *Understanding ignition processes in spray-guided gasoline engines using high-speed imaging and the extended spark-ignition model SparkCIMM. Part A: Spark channel processes and the turbulent flame front propagation.* Combustion and Flame, 2011. **158**(11): p. 2229-2244.
176. Dahms, R., et al., *Modeling ignition phenomena in spray-guided spark-ignited engines.* Proceedings of the Combustion Institute, 2009. **32**(2): p. 2743-2750.
177. Cundy, M.E., *Development of high-speed laser diagnostics for the investigation of scalar heterogeneities in engines*. 2012, General Motors.
178. Chen, H., P.M. Lillo, and V. Sick, *Three-dimensional spray–flow interaction in a spark-ignition direct-injection engine.* International Journal of Engine Research, 2015: p. 1468087415608741.
179. Lillo, P.M., M.L. Greene, and V. Sick, *Plenoptic single-shot 3D imaging of in-cylinder fuel spray geometry.* Zeitschrift für Physikalische Chemie, 2015. **229**(4): p. 549-560.
180. LaVision, *DaVis* 2016.
181. Raffel, M., et al., *Particle image velocimetry: a practical guide*. 2013: Springer.
182. Eckbreth, A.C., *Laser diagnostics for combustion temperature and species*. Vol. 3. 1996: CRC Press.
183. Wolfrum, J., *Laser diagnostics in combustion.* Applied Physics B: Lasers and Optics, 1990. **50**(6): p. 439-440.
184. Reboux, J., D. Puechberty, and F. Dionnet, *A New Approach of Planar Laser Induced Fluorescence Applied to Fuel/Air Ratio Measurement in the Compression Stroke of an Optical S.I. Engine*. 1994, SAE International.
185. Schulz, C. and V. Sick, *Tracer-LIF diagnostics: quantitative measurement of fuel concentration, temperature and fuel/air ratio in practical combustion systems.* Progress in Energy and Combustion Science, 2005. **31**(1): p. 75-121.
186. Daily, J.W., *Laser induced fluorescence spectroscopy in flames.* Progress in Energy and Combustion Science, 1997. **23**(2): p. 133-199.
187. Demtröder, W., *Laser spectroscopy: basic concepts and instrumentation*. Vol. 3. 2004: Springer.
188. Dreizler, A., V. Sick, and J. Wolfrum, *Applied laser spectroscopy in technical combustion systems.* Berichte der Bunsengesellschaft für physikalische Chemie, 1997. **101**(5): p. 771-782.
189. Koban, W., et al., *Predicting LIF signal strength for toluene and 3-pentanone under engine-related temperature and pressure conditions.* Proceedings of the Combustion Institute, 2005. **30**(1): p. 1545-1553.
190. Yun, H. and W. Mirsky, *Schlieren-streak measurements of instantaneous exhaust gas velocities from a spark-ignition engine*. 1974, SAE Technical Paper No. 741015.

191. Ortiz-Soto, E.A., J. Vavra, and A. Babajimopoulos, *Assessment of residual mass estimation methods for cylinder pressure heat release analysis of HCCI engines with negative valve overlap.* Journal of Engineering for Gas Turbines and Power, 2012. **134**(8): p. 082802.
192. Koban, W., et al., *Absorption and fluorescence of toluene vapor at elevated temperatures.* Physical chemistry chemical physics, 2004. **6**(11): p. 2940-2945.
193. Faust, S., et al., *Temperature, pressure, and bath gas composition dependence of fluorescence spectra and fluorescence lifetimes of toluene and naphthalene.* Applied Physics B, 2013. **110**(1): p. 81-93.
194. Koban, W., et al., *Oxygen quenching of toluene fluorescence at elevated temperatures.* Applied Physics B, 2005. **80**(6): p. 777-784.
195. Adrian, R.J. and J. Westerweel, *Particle image velocimetry*. 2011: Cambridge University Press.
196. Prasad, A.K., *Stereoscopic particle image velocimetry.* Experiments in fluids, 2000. **29**(2): p. 103-116.
197. Willert, C.E. and M. Gharib, *Digital particle image velocimetry.* Experiments in fluids, 1991. **10**(4): p. 181-193.
198. Westerweel, J., *Fundamentals of digital particle image velocimetry.* Measurement science and technology, 1997. **8**(12): p. 1379.
199. Reuss, D.L., et al., *Instantaneous planar measurements of velocity and large-scale vorticity and strain rate in an engine using particle-image velocimetry*. 1989, SAE Technical Paper No. 890616.
200. Reuss, D.L., et al., *Particle image velocimetry measurements in a high-swirl engine used for evaluation of computational fluid dynamics calculations*. 1995, SAE Technical Paper No. 952381.
201. Schiffmann, P., et al., *High-speed Three-component Flow Imaging in an Optical Engine.* 2012.
202. Sick, V., M.C. Drake, and T.D. Fansler, *High-speed imaging for direct-injection gasoline engine research and development.* Experiments in fluids, 2010. **49**(4): p. 937-947.
203. Neal, D.R., et al., *Collaborative framework for PIV uncertainty quantification: the experimental database.* Measurement Science and Technology, 2015. **26**(7): p. 074003.
204. Sciacchitano, A., et al., *Collaborative framework for PIV uncertainty quantification: comparative assessment of methods.* Measurement Science and Technology, 2015. **26**(7): p. 074004.
205. Wieneke, B. *Generic a posteriori uncertainty quantification for PIV vector fields by correlation statistics*. in *17th international symposium on applications of laser techniques to fluid mechanics (Lisbon, Portugal)*. 2014.
206. Wieneke, B. and A. Sciacchitano. *PIV uncertainty propagation*. in *11th Int Symp on PIV-PIV15*. 2015.
207. Batchelor, G.K., *The theory of homogeneous turbulence*. 1953: Cambridge university press.
208. Davidson, P.A., *Turbulence: an introduction for scientists and engineers*. 2015: Oxford University Press.
209. Ziegler, G., et al., *Cycle-resolved two-dimensional flame visualization in a spark-ignition engine*. 1988, Society of Automotive Engineers, Warrendale, PA.
210. Iheme, L.O. *Butterworth Bandpass Filter*. 2011 [cited 2015; Available from: https://www.scribd.com/doc/51981950/Frequency-Domain-Bandpass-Filtering-for-Image-Processing.
211. Damköhler, G., *The effect of turbulence on the flame velocity in gas mixtures.* 1947.
212. zur Loye, A.O. and F.V. Bracco, *Two-Dimensional Visualization of Premixed-Charge Flame Structure in an IC Engine - SP-715*. 1987, SAE International Technical Paper No. 870454.
213. Gülder, Ö.L., et al., *Flame front surface characteristics in turbulent premixed propane/air combustion.* Combustion and Flame, 2000. **120**(4): p. 407-416.

214. Filatyev, S.A., et al., *Measured properties of turbulent premixed flames for model assessment, including burning velocities, stretch rates, and surface densities.* Combustion and Flame, 2005. **141**(1–2): p. 1-21.
215. Schiffmann, P., et al., *TCC-III Engine Benchmark for Large-Eddy Simulation of IC Engine Flows.* Oil & Gas Science and Technology, 2016. **71**(1).
216. Sick, V., et al. *A common engine platform for engine LES development and validation*. in *International Conference on Large-Eddy Simulation for Internal Combustion Engine Flows (LES4ICE), Rueil-Maimaison, France, November*. 2010.
217. Schiffmann, P., et al., *An Integrated Experimental and Simulation Study of Cycle-to-Cycle Variations in a Homogeneous-Charge Spark-Ignition Engine.*
218. Abraham, P.S., et al., *Flow-pattern switching in a motored spark ignition engine.* International Journal of Engine Research, 2015: p. 1468087414565400.
219. Technology, A.D., *Phoenix Combustion Analysis Software (CAS) 4.0 Reference Manual*. 2009.
220. Peterson, B. and V. Sick, *Simultaneous flow field and fuel concentration imaging at 4.8 kHz in an operating engine.* Applied Physics B, 2009. **97**(4): p. 887-895.
221. Peterson, B., D.L. Reuss, and V. Sick, *On the ignition and flame development in a spray-guided direct-injection spark-ignition engine.* Combustion and Flame, 2014. **161**(1): p. 240-255.
222. Peterson, B., D.L. Reuss, and V. Sick, *High-speed imaging analysis of misfires in a spray-guided direct injection engine.* Proceedings of the Combustion Institute, 2011. **33**(2): p. 3089-3096.
223. Drake, M.C., et al., *Piston fuel films as a source of smoke and hydrocarbon emissions from a wall-controlled spark-ignited direct-injection engine*. 2003, SAE Technical Paper.
224. Stojkovic, B.D., et al., *High-speed imaging of OH* and soot temperature and concentration in a stratified-charge direct-injection gasoline engine.* Proceedings of the Combustion Institute, 2005. **30**(2): p. 2657-2665.
225. Kee, R.J., F.M. Rupley, and J.A. Miller, *Chemkin-II: A Fortran chemical kinetics package for the analysis of gas-phase chemical kinetics*. 1989, Sandia National Labs., Livermore, CA (USA).
226. Mehl, M., et al., *An approach for formulating surrogates for gasoline with application toward a reduced surrogate mechanism for CFD engine modeling.* Energy & Fuels, 2011. **25**(11): p. 5215-5223.
227. Han, Z. and R.D. Reitz, *Turbulence Modeling of Internal Combustion Engines Using RNG κ-ε Models.* Combustion Science and Technology, 1995. **106**(4-6): p. 267-295.
228. Fraser, R., et al., *Preliminary turbulence length scale measurements in a motored IC engine*. 1986, Princeton Univ., Princeton, NJ.
229. Aleiferis, P.G. and M.K. Behringer, *Flame front analysis of ethanol, butanol, iso-octane and gasoline in a spark-ignition engine using laser tomography and integral length scale measurements.* Combustion and Flame, 2015. **162**(12): p. 4533-4552.
230. Brequigny, P., et al., *Thermodiffusive Effect on the Flame Development in Lean Burn Spark Ignition Engine*. 2014, SAE International Technical Paper 2014-01-2630.
231. Zeng, W., M. Sjöberg, and D. Reuss, *Using PIV Measurements to Determine the Role of the In-Cylinder Flow Field for Stratified DISI Engine Combustion.* 2014.
232. Zeng, W., M. Sjöberg, and D.L. Reuss, *PIV examination of spray-enhanced swirl flow for combustion stabilization in a spray-guided stratified-charge direct-injection spark-ignition engine.* International Journal of Engine Research, 2014: p. 1468087414564605.
233. Sjöberg, M., W. Zeng, and D. Reuss, *Role of engine speed and in-cylinder flow field for stratified and well-mixed disi engine combustion using e70.* SAE International Journal of Engines, 2014. **7**(2014-01-1241): p. 642-655.
234. Tennekes, H. and J.L. Lumley, *A first course in turbulence*. 1972: MIT press.

235. Linstrom, P.J. and W. Mallard, *NIST Chemistry webbook; NIST standard reference database No. 69.* 2001.
236. Design, R., *CHEMKIN 10131.* San Diego, 2013.
237. Bechtold, J. and M. Matalon, *The dependence of the Markstein length on stoichiometry.* Combustion and flame, 2001. **127**(1): p. 1906-1913.
238. Johnston, R. and J. Farrell, *Laminar burning velocities and Markstein lengths of aromatics at elevated temperature and pressure.* Proceedings of the combustion institute, 2005. **30**(1): p. 217-224.